N°d'ordre NNT : 2018LYSE1303

THESE de DOCTORAT DE L'UNIVERSITE DE LYON
opérée au sein de
l'Université Claude Bernard Lyon 1

Ecole Doctorale N° 162
MECANIQUE, ENERGETIQUE, GENIE CIVIL, ACOUSTIQUE

Spécialité de doctorat : TRAITEMENT DE SIGNAL/IMAGE ET ACOUSTIQUE

Soutenue publiquement le 14/12/2018, par :
Emilia Bădescu

High-frame rate ultrasound methodologies for cardiac applications

---

Devant le jury composé de :

Nadjia Kachenoura	Chargée de recherche HdR, Inserm / Université Paris Sud	Rapporteur
Jan d'Hooge	Professeur, Katholieke Universiteit Leuven	Rapporteur
Ling Tong	Ingénieur de recherche, Supersonic Imaging	Examinatrice
Olivier Basset	Professeur, Université Claude Bernard Lyon 1	Examinateur
Hervé Liebgott	Professeur, Université Claude Bernard Lyon 1	Directeur de thèse
Denis Friboulet	Professeur, INSA Lyon	Co-directeur
Damien Garcia	Chargé de recherche, Inserm / Insa Lyon	Invité

UNIVERSITE CLAUDE BERNARD - LYON 1

Président de l'Université	**M. le Professeur Frédéric FLEURY**
Président du Conseil Académique	M. le Professeur Hamda BEN HADID
Vice-président du Conseil d'Administration	M. le Professeur Didier REVEL
Vice-président du Conseil Formation et Vie Universitaire	M. le Professeur Philippe CHEVALIER
Vice-président de la Commission Recherche	M. Fabrice VALLÉE
Directeur Général des Services	M. Alain HELLEU

COMPOSANTES SANTE

Faculté de Médecine Lyon Est – Claude Bernard	Directeur : M. le Professeur J. ETIENNE
Faculté de Médecine et de Maïeutique Lyon Sud – Charles Mérieux	Directeur : Mme la Professeure C. BURILLON
Faculté d'Odontologie	Directeur : M. le Professeur D. BOURGEOIS
Institut des Sciences Pharmaceutiques et Biologiques	Directeur : Mme la Professeure C. VINCIGUERRA
Institut des Sciences et Techniques de la Réadaptation	Directeur : M. le Professeur Y. MATILLON
Département de formation et Centre de Recherche en Biologie Humaine	Directeur : Mme la Professeure A-M. SCHOTT

COMPOSANTES ET DEPARTEMENTS DE SCIENCES ET TECHNOLOGIE

Faculté des Sciences et Technologies	Directeur : M. F. DE MARCHI
Département Biologie	Directeur : M. le Professeur F. THEVENARD
Département Chimie Biochimie	Directeur : Mme C. FELIX
Département GEP	Directeur : M. Hassan HAMMOURI
Département Informatique	Directeur : M. le Professeur S. AKKOUCHE
Département Mathématiques	Directeur : M. le Professeur G. TOMANOV
Département Mécanique	Directeur : M. le Professeur H. BEN HADID
Département Physique	Directeur : M. le Professeur J-C PLENET
UFR Sciences et Techniques des Activités Physiques et Sportives	Directeur : M. Y.VANPOULLE
Observatoire des Sciences de l'Univers de Lyon	Directeur : M. B. GUIDERDONI
Polytech Lyon	Directeur : M. le Professeur E.PERRIN
Ecole Supérieure de Chimie Physique Electronique	Directeur : M. G. PIGNAULT
Institut Universitaire de Technologie de Lyon 1	Directeur : M. le Professeur C. VITON
Ecole Supérieure du Professorat et de l'Education	Directeur : M. le Professeur A. MOUGNIOTTE
Institut de Science Financière et d'Assurances	Directeur : M. N. LEBOISNE

Abstract

Echocardiography is the most widely used imaging modality for assessing cardiac morphology and function. It does provide a non-invasive tool in diagnosis and assessment of heart diseases and it allows, in addition, monitoring the response to the treatment. However, quantifying fast cardiac events remains a challenge when using the current achievable frame rate, especially in applications such as stress-echocardiography. Moreover, this limitation becomes more pronounced in 3D conventional focused imaging due to the time needed to insonify and acquire a full volume. The fact that only ~20 volumes per second can currently be achieved is one of the reasons restricting its common usage in clinical practice. Improvements in this field would allow exploiting the important potential of 3D imaging in providing a full quantification of cardiac deformation.

In this context, the aim of this thesis was to develop high frame rate methods and to test their performance in realistic conditions, aiming decision making regarding an eventual clinical translation. To achieve this objective, both *in vitro* and *in vivo* experiments were conducted using 2D and 3D imaging.

Our first contribution was a 2D comparison between two high frame rate modalities in terms of image quality and motion estimation performance. Motivated by our 2D results but especially by the challenge of implementing MLT in practice, we extended this approach to 3D. We studied the feasibility of 3D MLT in both static and dynamic conditions. Finally, since testing novel approaches in physiological complex flows conditions is a step forward towards clinical translation, our third contribution was to evaluate the potential of a ring vortex phantom in providing a realistic test object to validate 2D and 3D high frame rate imaging modes.

Résumé

L'échocardiographie est la modalité d'imagerie la plus utilisée pour évaluer la morphologie et la fonction cardiaque. Il s'agit d'un outil non invasif pour le diagnostic et l'évaluation des maladies cardiaques et il permet en outre de surveiller l'efficacité d'un traitement. Cependant, la quantification des événements cardiaques rapides demeure un défi avec la cadence d'imagerie actuellement réalisable, en particulier dans des applications telles que l'échocardiographie d'effort. De plus, cette limitation devient plus prononcée en imagerie 3D conventionnelle focalisée en raison du temps nécessaire pour insonifier et acquérir un volume complet. Le fait que l'on puisse actuellement atteindre au mieux ~20 volumes par seconde est l'une des raisons qui limitent son utilisation courante dans la pratique clinique. Des améliorations dans ce domaine permettraient d'exploiter l'important potentiel de l'imagerie 3D pour la quantification complète de la déformation cardiaque.

Dans ce contexte, l'objectif de cette thèse était de développer des méthodes à haute cadence d'images et de tester leur performance dans des conditions réalistes afin de se rapprocher au mieux des conditions de la pratique clinique. Pour atteindre cet objectif, des expériences *in vitro* et *in vivo* ont été menées en utilisant l'imagerie 2D et 3D.

Notre première contribution a été une comparaison 2D entre deux modalités à haute cadence d'images en termes de qualité d'image et de performance d'estimation de mouvement. Motivés par nos résultats 2D mais surtout par le défi d'implémenter le MLT dans la pratique, nous avons étendu cette approche en 3D. Nous avons étudié la faisabilité du MLT 3D dans des conditions statiques et dynamiques. Enfin, comme l'évaluation de nouvelles approches dans des conditions physiologiques de flux complexes constitue un pas en avant vers la transition clinique, notre troisième contribution a consisté à évaluer le potentiel d'un fantôme de vortex à devenir un objet de test et de calibration pour les modes d'imagerie 2D et 3D à haute cadence d'imagerie.

Contents

General introduction 9
1 Chapter 1. Fundamental principles of ultrasound 12
1.1. Introduction 13
1.2. Basic ultrasound principles 13
1.2.1. Pulse-echo phenomenon 13
1.2.2. Ultrasound probes 14
1.2.3. Sound-tissue interactions 17
1.3. Conventional ultrasound system 20
1.3.1. Beamforming in transmission 21
1.3.2. Received signals 22
1.3.3. RF processor 23
1.3.4. TGC and ADC 24
1.3.5. Beamforming in reception 25
1.3.6. Imaging modes 26
1.4. Current limitations of conventional clinical echocardiography and the potential of possible improvements 31
1.5. Conclusion 32
2 Chapter 2. High frame rate echocardiography: from image formation to velocity estimation and validation 33
2.1. Introduction 34
2.2. High frame rate modalities 34
2.2.1. ECG (retrospective) gating 35
2.2.2. Multi-line acquisition 35
2.2.3. Synthetic Aperture Approaches 35
2.2.4. Multi line-transmit 38
2.3. Velocity estimation methods 42
2.3.1. Cross-beam Doppler velocity estimation 42
2.3.2. Speckle tracking 43
2.4. 3D high-frame rate imaging 46
2.5. Validation of high frame rate modalities 48
2.6. Conclusion 49

3 Chapter 3. Comparison between Multi Line Transmission and Diverging Wave Imaging: Motion artefacts and their effect on motion estimation 51
3.1. Introduction 52
3.2. Methods 53
3.2.1. Acquisition set-up 53
3.2.2. Acquisition settings for image quality assessment and speckle tracking motion estimator 54
3.2.3. Acquisition settings for Tissue Doppler Imaging 57
3.2.4. *In vitro* models 58
3.2.5. *In vivo* Models 59
3.2.6. Motion estimation methods 61
3.3. Results 61
3.3.1. Image quality assessment on static phantoms 61
3.3.2. Image quality assessment on the rotating disk phantom 63
3.3.3. Motion estimation accuracy 64
3.3.4. Qualitative B-mode and TDI *in vivo* assessment 69
3.4. Discussion 70
3.5. Conclusion 72
4 Chapter 4. Experimental 3D Multi Line Transmission: Feasibility, Improvements and preformance in static and dinamic conditions 74
4.1. Introduction 75
4.2. Methods 76
4.2.1. 3D acquisition system 76
4.2.2. Practical implementation of MLT in 3D 77
4.2.3. Acquisition settings 79
4.2.4. *In vitro* models 82
4.3. Results 83
4.3.1. Feasibility study 83
4.3.2. Improvements aiming at cross-talk reduction 85
4.4. Discussion 90
4.5. Conclusion 92
5 Chapter 5. Validation of high-frame rate velocty estimation approaches on a vortex ring phantom 93
5.1. Introduction 94
5.2. Methods 95
5.2.1. Vortex ring 95

5.2.2. *In vitro*-model 95
5.2.3. 2D Acquisition set-up 96
5.2.4. 3D Acquisition set-up 97
5.2.5. Vector flow velocity estimation 97
5.3. Results 98
5.3.1. 2D results 98
5.3.2. 3D preliminary results 99
5.4. Discussion 100
5.5. Conclusion 100
General conclusion 103
General limitations and perspectives 105
Summary in French/ Résumé en français 116

General introduction

Echocardiography has encountered an enormous progress since its emergence in the 50s: from the first 1D time–motion (M-Mode) techniques to novel and improved imaging modes allowing the assessment of full cardiac images or even volumes. Today 2D echocardiography is the most used imaging modality in the clinical practice. This can be explained by its important benefits over other medical imaging modalities: being non-invasive, low cost, transportable and requiring a relatively short time for an examination. Despite all these advantages and despite the fact that echocardiography is generally sufficient for anatomic and functional evaluation of the heart, fast cardiac events could be better assessed by using a higher frame rate. Stress-echocardiography, fetal echocardiography, and cardiac deformation imaging are just a few examples of applications that could benefit from an increased frame rate. The need for a higher temporal resolution becomes even more significant in 3D where the number of transmission events has to be increased for acquiring a full volume.

Several high-frame rate approaches have been proposed in the literature to cope with the current clinical limitations such as plane/diverging wave (PW/DW) imaging and multi-line transmit (MLT). However, they still lack a rigorous validation that could pave the way to clinical translation.

In this context, the overall objective of this thesis is to develop, implement and validate high frame rate approaches in 2D and 3D and to reveal their advantages and limitations that could lead (or not) to clinical translation.

This dissertation is organized as follows:

In Chapter 1, we start by introducing the pulse-echo principle which is fundamental for ultrasound imaging and it is strongly related to the frame rate. For explaining how an ultrasound image is obtained starting from the pulse-echo principle, we also provide a basic description of the phenomena appearing as the sound propagates through the medium and interacts with the tissue. Additionally, we present the overall pipeline from transmission to reception in order to explain how a conventional ultrasound image is formed and which are the factors limiting the frame rate. The last part of our first chapter presents the specificities of clinical cardiac imaging, highlighting the current limitations and the aspects that could be improved by increasing the temporal resolution and by using 3D high-frame rate imaging.

In Chapter 2, we present various high-frame rate approaches that have been proposed in the literature to cope with the current clinical limitations. As the interest of using such approaches is strongly linked to cardiac dynamics, this chapter also contains a description of the most common motion estimation methods used in echocardiography. Due to the benefits provided by high frame rate methods in 2D and to their potential in 3D imaging, many of them have been already extended to 3D as discussed further in this chapter. However, each method comes with its own advantages and limitations and rigorous validation is required before clinical translation. Thus, in the last part of this chapter, we present the main approaches and tools usually employed as a part of the validation process.

In Chapter 3, we present our first contribution: a comparison between the two promising high-frame rate approaches (MLT and DW) in order to assess if one method is more suitable than the other for cardiac applications. For this purpose, both *in vitro* and *in vivo* experiments were conducted and the performance of the two methods was evaluated in terms of both image quality and impact on two commonly used motion estimation methods: speckle tracking and tissue Doppler imaging.

In Chapter 4, we present our second contribution aiming to exploit the potential of the common clinical usage of 3D imaging. Several authors mentioned the difficulty of implementing 3D MLT in practice which motivated us to test its feasibility. First, the performance of this method was evaluated in both static and dynamic conditions. Second, a different transmission scheme was tested, aiming cross-talk reduction.

In Chapter 5, we present our third contribution, which was the validation of high-frame rate approaches on a ring vortex phantom. The first advantage of using such a phantom is that it is supposed to be stable, reproducible and controllable which is very important in testing novel methods. On the other hand, it is able to reproduce complex physiological flows occurring on the left ventricle which offers very close conditions to the *in vivo* ones, which is an important step towards clinical translation. Both 2D and 3D experiments were conducted for this study in order to reveal the potential of the novel approaches and their possible limitations.

CHAPTER 1:

FUNDAMENTAL PRINCIPLES OF ULTRASOUND

1.1. INTRODUCTION

The objective of this chapter is to present, starting from the very basic ultrasound principles, the factors limiting the frame rate in conventional ultrasound imaging and the possible clinical advantages of a higher frame rate.

First, we describe the pulse-echo principle since the number of pulse-echo events is strongly linked to the frame rate. Then, we discuss different transmitters/receivers that can be used for generating/receiving the pulse-echo ensemble. Additionally, we describe different phenomena appearing during the pulse-echo events, as the sound interacts with the tissue.

Second, we present how these basic principles are used in an ultrasound system and which are the other components required to get from a simple transmission to different ultrasound modes usually used in clinical ultrasound. As a part of this process, we provide the relationship giving the frame rate and the factors limiting it.

Finally, we present the potential clinical applications that could benefit from an increased frame rate in 2D and especially in 3D cardiac imaging. The promising advancements that could be achieved by employing 3D imaging in mainstream echocardiography are also described.

1.2. BASIC ULTRASOUND PRINCIPLES

1.2.1. Pulse-echo phenomenon

The principle of ultrasound imaging is based on a pulse-echo phenomenon firstly exploited during the First World War for detecting submarines. Similar to the sonar, in medical ultrasound imaging a sound wave is sent through the medium and after a certain time, an echo is reflected back. Based on the time needed for the pulse to be transmitted and reflected back and knowing the sound propagation velocity in a certain medium, we can calculate the distance to the reflecting media (1.1).

$$d = \frac{c \cdot t}{2} \tag{1.1}$$

where d is the one-way distance traveled by the wave, t is the time needed for a round trip and c is the propagation velocity of the sound.

An overall illustration of the Pulse-Echo principle is represented in Fig. 1.

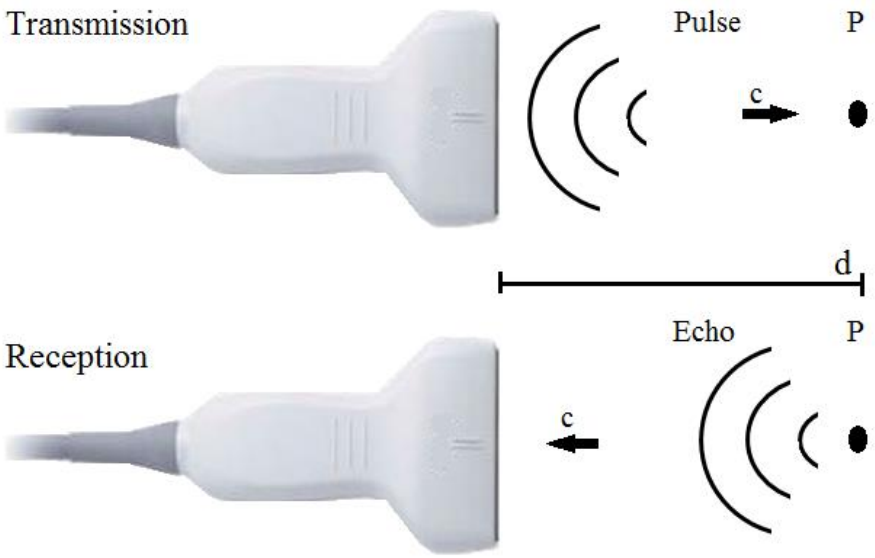

Fig. 1. Pulse-Echo Principle: The probe transmits an ultrasound wave, which travels a distance d with velocity c, to the media point P. Once the beam interacts with the media point, an echo is reflected back to the probe.

The sound waves used in clinical ultrasound have a frequency above the audible range (typically between 1 Mhz and 20 Mhz (Chan & Perlas 2011)) and propagate through the human body as mechanical waves. The velocity varies depending on the density and compressibility of the imaged tissue. However, the average propagation velocity in soft tissue (c) is assumed to be 1540 m/s and it is related to the wavelength (λ) and frequency (f) as shown in (1.2).

$$c = \lambda \cdot f \tag{1.2}$$

1.2.2. Ultrasound probes

Generating the transmitted pulse and receiving the echo is possible thanks to an ultrasound probe that acts as both transmitter and receiver. In this section, we describe how the probe is used for transmitting/ receiving the pulse/echo and how the choice of the probe affects the image, making certain probes more suitable than others for cardiac applications.

The ultrasound probe can contain one or more piezo-electric elements. In transmission, the property of such elements is to convert the electrical energy applied to the probe into sound waves (inverse piezo-electric effect). Conversely, in reception, the reflected sound waves are converted into electrical signals that can be afterward acquired and processed to form the image (direct piezo-electric effect). In order to ensure an effective conversion of the electrical signal to sound and vice versa, the frequency of the electrical signal has to have a frequency within the bandwidth of the transducer. First, a high duration signal has a narrower bandwidth than a low duration signal, assuming that their frequency is invariant in time. Second, the

bandwidth is inversely proportional to the axial resolution as shown in equation (1.3). Therefore, a better resolution will be associated with a broader bandwidth and therefore, in most cases, to a low duration signal.

$$r_z = \frac{c}{2 \cdot BW} \tag{1.3}$$

where r_z is the axial resolution and BW is the bandwidth of the transmitted signal

Thus, if we consider two signals at different frequencies having the same number of cycles, the high-frequency signal will have a lower duration so a better resolution (Vray et al. 2014). The impact of the frequency on the ability to distinguish between two targets placed in the direction of the beam is shown in Fig. 2.

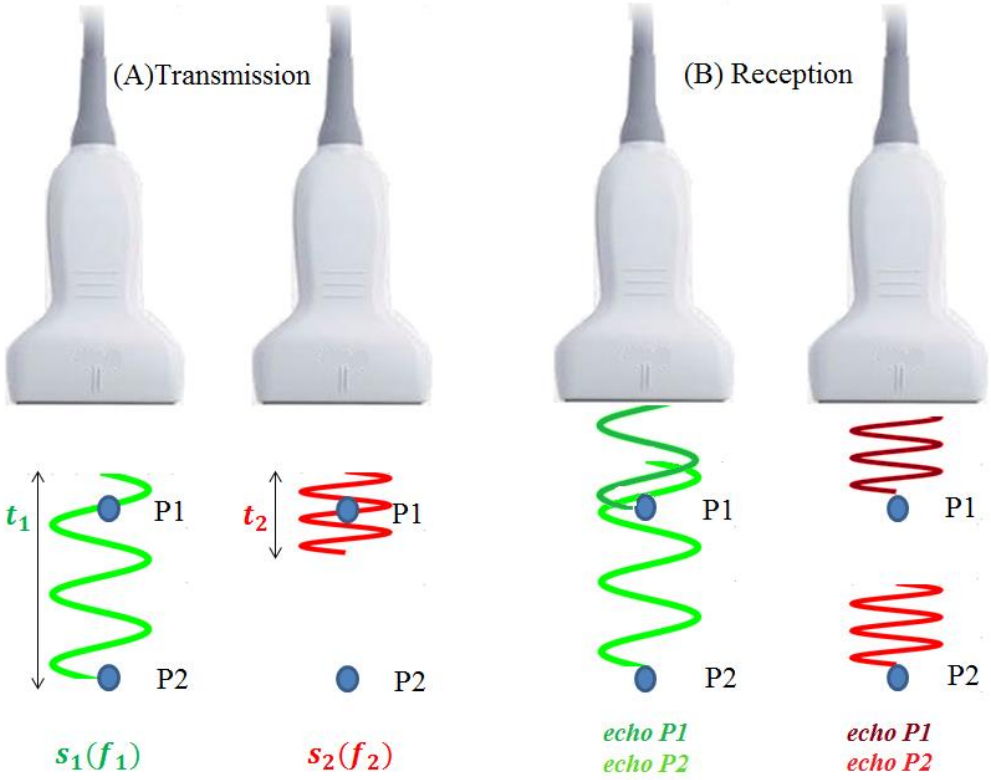

Fig. 2. The impact of the frequency of the transmitted signals on the axial resolution: (A) Two signals (s_1 and s_2) having the same number of cycles and different frequencies (f_1, f_2) are transmitted through the medium. As they interact with two points of the medium (P1 and P2), the echoes are reflected back (B). The echoes corresponding with the low frequency transmission signal (s_1) overlap, meaning that the system will not be able to distinguish between the two echoes and therefore the two targets placed on the direction of the beam; on the other hand, the echoes corresponding with the high frequency transmission signal (s_2) do not overlap, meaning that such a frequency is high enough to ensure a good enough resolution for separating the two scatterers.

But, higher frequencies are more attenuated than lower ones at higher depths. This is an important aspect to be considered when choosing a probe (from the existing types) for 2D cardiac imaging. This aspect is linked to the heart anatomy. An adult heart measures approximatively 12 cm in length and 6 cm

width (Betts et al. 2013), meaning that the probe should not only provide a high penetration depth, but also a large sector width. Finally, being located behind the sternum and rib cartilages, cardiac imaging requires an ultrasound probe with a small footprint in order to avoid including the ribs in the field of view. We will now describe the existing types of ultrasound probes in order to highlight the presence of the desired features for the ultrasound probes used in this thesis.

One of the existing types of probes is the *convex array*. Operating at 2-5 MHz, this kind of probe provides a good penetration depth and a wide field of view that could be useful for cardiac applications. However, its curved and wide footprint makes it more adapted for abdominal applications.

Another type of probe is the *linear array* which operates at frequency ranges between (5-13 Hz (Carmody 2011)). A first characteristic of such probes (as a consequence of its operating frequency range) is that they provide a good resolution with the compromise of a relatively low penetration depth. Another characteristic of these probes is the flat alignment of the elements in a wide head providing a rectangular field of view. Although this type of probe has been already used for pediatric cardiac applications (Fadnes et al. 2014), its low penetration depth and its relatively big footprint is not the best choice for adult echocardiography.

Phased array probes, on the other hand, operate at around 3 MHz, providing good penetration. Even if their resolution is compromised compared to linear arrays, their footprint is small and their field of view is wide at higher depths, being the most adapted for evaluating cardiac structures.

Conventionally, for obtaining 3D imaging, the 1D probes such as the ones presented above, used to be mechanically rotated, tilted or translated. A more efficient alternative is to use *2D arrays*, containing elements disposed in a square matrix.

An overview of different probes and their corresponding field of view is provided in Fig. 3. Due to the aspects discussed above concerning the desired features for cardiac imaging, later in this thesis, we will use the types of probes shown in (B), (C) and (D).

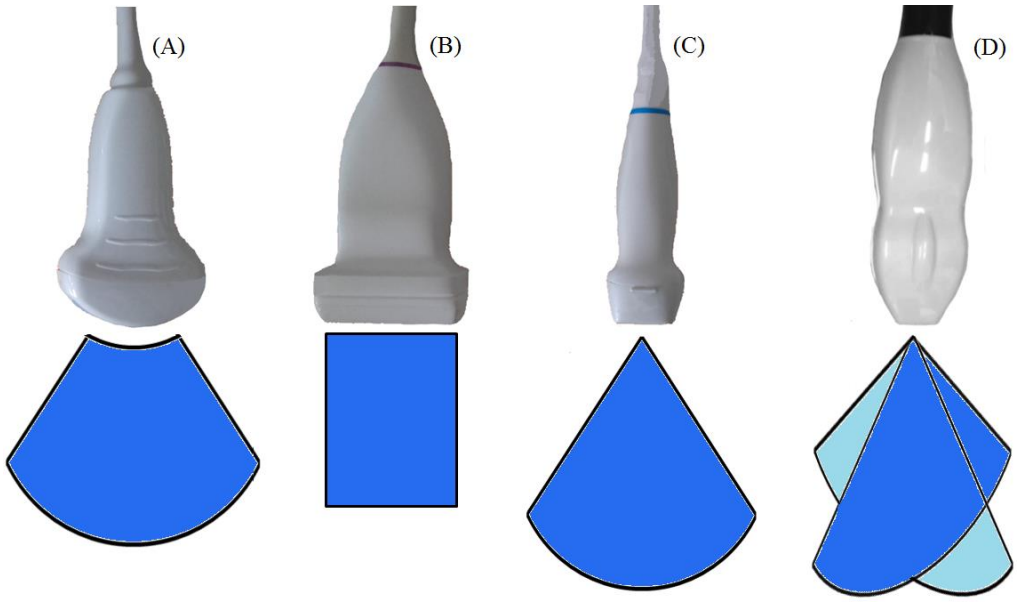

Fig. 3. Different arrays and their corresponding fields of view: (A) 1D Convex, (A) 1D Linear, (B) 1D Phased, (D) 2D Phased.

1.2.3. Sound-tissue interactions

Once the sound is transmitted through the tissue using one of the probes presented in the previous section, it interacts with the media and several phenomena can take place. In this subchapter, we present such phenomena (specular reflection, attenuation, scattering, absorption) and the properties of the tissue influencing their appearance in the ultrasound images.

We will start by defining the acoustic impedance as an important property of the tissue showing its resistance to the sound propagation. For a homogenous and isotropic medium, the acoustic impedance (Z) can be written as the product between the density (ρ) and the propagation velocity (c) as shown in (1.4).

$$Z = \rho \cdot c \tag{1.4}$$

Since the human body is not a homogeneous medium, the ultrasound wave is not reflected in the same proportion from all the tissues. As the sound propagates through the body and it meets a flat, large (compared to one wavelength) and smooth boundary between two tissues, a part of its incident energy (I_i) is reflected (I_r) while the rest is transmitted (I_t). Such a phenomenon, illustrated in Fig. 4, having as a result the echo reflected in a single direction is called *specular reflection***.**

The reflectivity between two tissues having different acoustic impedances (Z_1, Z_2) can be measured using the reflection coefficient (R):

$$R = \frac{I_r}{I_i} = \frac{Z_2 \cos\theta_i - Z_1 \cos\theta_t}{Z_2 \cos\theta_i + Z_1 \cos\theta_t} \tag{1.5}$$

where θ_t is the angle of transmission and θ_i is the angle of incidence.

On the other hand, the transmission coefficient indicates the fraction of transmitted energy and it can be written as:

$$T = \frac{I_t}{I_i} = 1 - R = \frac{2Z_1 \cos\theta_i}{Z_2 \cos\theta_i + Z_1 \cos\theta_t} \tag{1.6}$$

However, as shown in Fig. 4, if the incident beam arrives at the boundary between the two tissues under an angle θ_i, the echo will be reflected under an angle $\theta_r = \theta_i$ (law of reflection) away from the direction of the receiver (ultrasound probe). For this reason, imaging flat surfaces not perpendicular to the beam is more challenging than imaging at $\theta_i = 0°$. Another phenomenon which appears when the sound beam strikes the interface between two media on an oblique angle is refraction. The degree of refraction increases with the difference between the speeds of the sound between the two media. Since the modification of the beam direction as a result of refraction is not taken into consideration for image formation, it can produce artefacts due to the erroneous localization of the structures.

For the case of normal incidence ($\theta_i = \theta_t = 0$), equation (1.5) can be rewritten as:

$$R = \frac{I_r}{I_i} = \frac{Z_2 - Z_1}{Z_2 + Z_1} \tag{1.7}$$

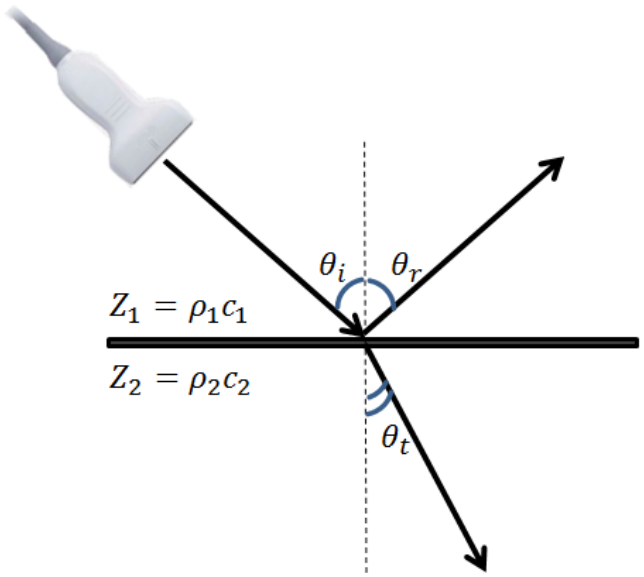

Fig. 4. Reflection and transmission: as the incident beam is transmitted through tissue 1 under the angle θ_i, it interacts with the flat interface between tissues 1 and 2 having different acoustic impedances (Z_1, Z_2). As a result, a part of the beam is reflected under the angle θ_r and the rest is transmitted through the next tissue under the angle θ_t.

As shown in equation (1.7), the greater the difference in acoustic impedance between the tissues, the more energy is reflected back to the transducer. The property of the tissues to reflect a different amount of energy is called echogenicity. Different degrees of echogenicity are described by the terms hyperechoic (strong echo) and hypoechoic (weak echo). For instance, bone is a hyperechoic medium because it has an acoustic impedance which is over 4 times higher than the one of the soft tissue. On the other hand, most fluids can be characterized as being a hypoechoic medium. An example showing different degrees of echogenicity is the image of a 20 weeks fetus, presented in Fig. 5. The skull appears to be hyperechoic compared to the amniotic fluid, which appears to be hypoechoic. The difference in echogenicity will be used later in this thesis for contrast evaluation.

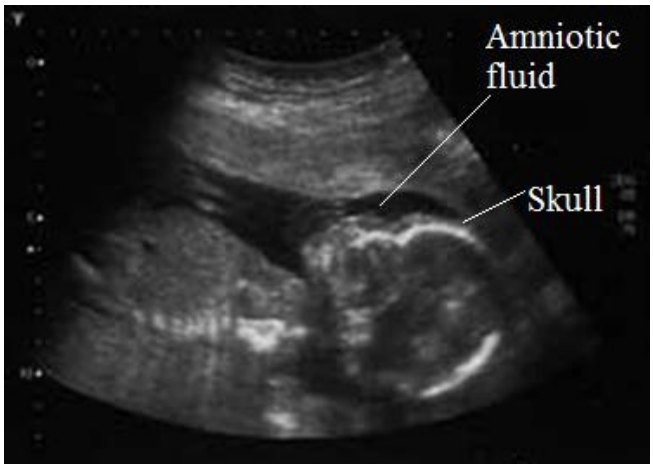

Fig. 5. Different degrees of echogenicity observed on the image of a 20 weeks fetus: The skull appears to be hyperechoic compared to the amniotic fluid which is hypoechoic [Courtesy to Hervé Liebgott].

So far, we discussed phenomena occurring at a smooth and relatively large interface between two media. When the sound beam encounters a small interface/target, whose size is smaller than the wavelength of the ultrasound wave, the echoes will be reflected in many directions. Such a phenomenon, called *Scattering* is shown in Fig. 6 A. Scattering can also occur when the interface between two media is rough and irregular (Fig. 6 B). As a result of the diffuse reflection, a weak echo reaches the ultrasound probe.

Since scattering diminishes the amount of energy that is reflected back to the transducer it contributes to another phenomenon that appears as a result of the sound-tissue interaction which is *attenuation*. Attenuation can also appear due to *absorption*. As explained in (Kuttruff 1991), the *absorption* occurs as the mechanical energy of the sound wave is converted into heat and it causes an exponential decrease in intensity with the distance traveled. According to (Amin 1989), this decrease in acoustic intensity I can be expressed as:

$$I = I_0 \cdot e^{-2\alpha z} \tag{1.8}$$

where I_0 is the initial intensity for a traveled distance z=0 and α is the attenuation coefficient.

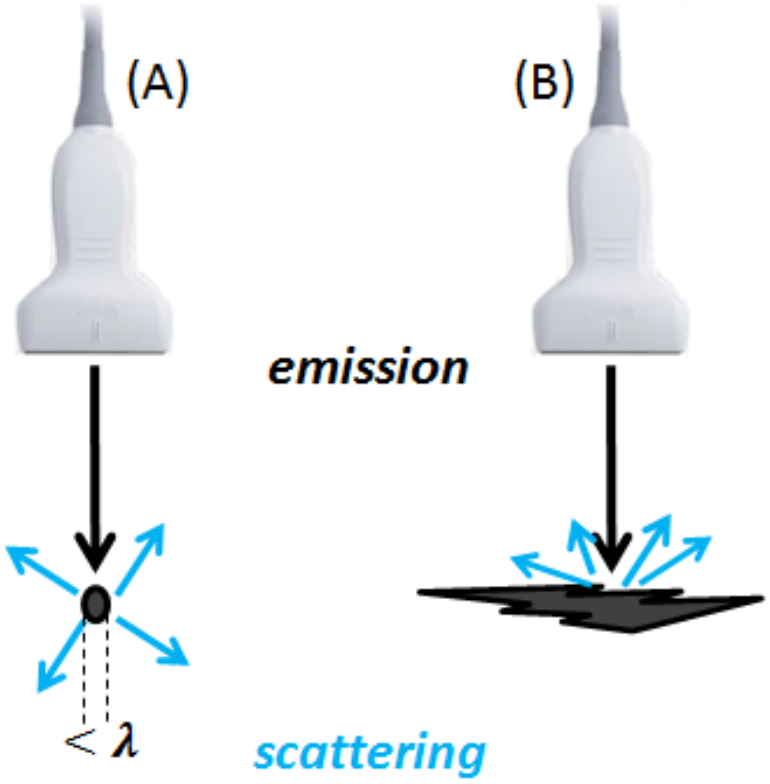

Fig. 6. Scattering: (A) when the sound beam encounters a target, whose size is smaller than the wavelength of the ultrasound wave and (B) when the sound beam encounters a rough and irregular interface between two media.

1.3. CONVENTIONAL ULTRASOUND SYSTEM

In this section, we will describe how the previously presented basic principles can be used in a conventional ultrasound system (together with other components) to obtain different imaging modes used in clinical ultrasound for diagnosis.

The ultrasound system consists of several processing steps that need to be followed in order to get from the electrical signals applied in transmission to the data assisting in diagnosis. An example of an overall block diagram of an ultrasound system is shown in Fig. 7. This section describes each processing step illustrated in the block diagram.

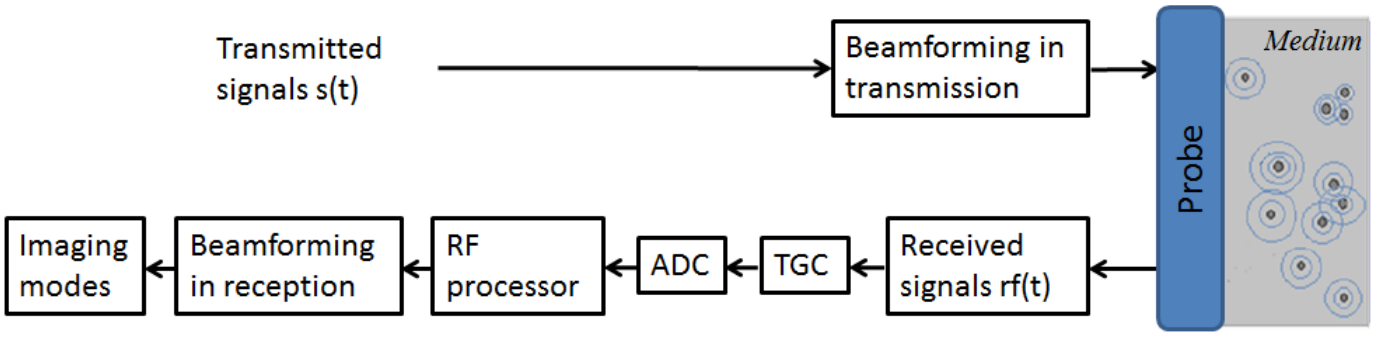

Fig. 7. Block diagram of an ultrasound system: Once the electrical transmitted signals are set and beamformed, they are applied to the probe and converted into sound waves. As they propagate through the medium, they interact with the point targets and the generated echoes are reflected back to the probe. The received sound waves are converted into electrical signals whose gain is adjusted to compensate for the spreading signal attenuation at high depths (TGC). Then, the signals are converted from analog to digital (ADC) and the RF digitized data is obtained. The RF processor may contain a complex demodulator that provides IQ data. After beamforming these data, several imaging modes can be used, depending on the medical investigation purpose.

1.3.1. Beamforming in transmission

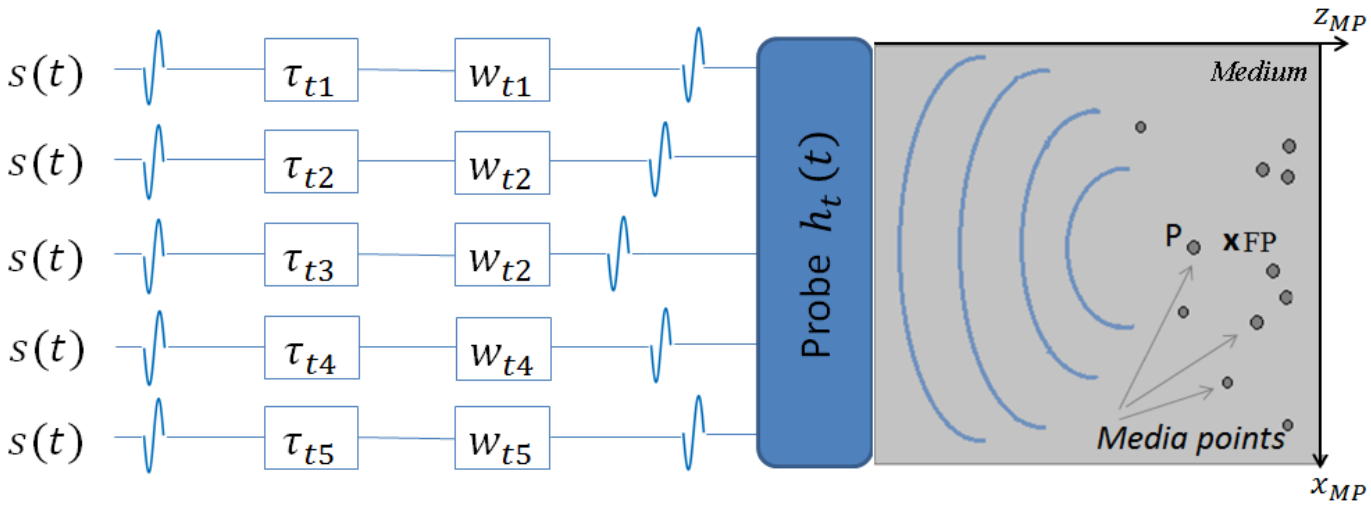

Fig. 8. Conventional transmission for a probe having N=5 elements: a signal s(t) is applied to each element i of the array; the beam is focused in FP (focal point) by delaying with τ_{ti} the signal corresponding to each element; if desired, an apodization (windowing) function (w_{ti}) can be used once each signal i was delayed; when the ensemble of electrical signals is ready to be transmitted, it is applied to the transducer, converted into sound and propagate through the medium which contains several media points as P.

As shown in Fig. 8, a classical transmission process in conventional ultrasound imaging starts by transmitting a signal $s(t)$ to each element i of the transducer. Then, each signal has to be delayed for allowing the waves to meet simultaneously in the same point called focal point (FP). Thus, the values of the delays have to be chosen to compensate for the propagation distance between each element of the probe and the focal point. This can be performed by first finding the maximum distance between each element and the focal point as shown in equation (1.9).

$$d_{max} = \max_{i\in[1N]} \sqrt{(x_i - x_{FP})^2 + (z_i - z_{FP})^2} \tag{1.9}$$

where d_{max} is the maximum distance between each element i located at (x_i, z_i) and the focal point (FP) and x_{FP}, z_{FP} are the lateral and axial coordinates of the focal point, assuming that both the focal point and the elements of the probe are located in the plane y=0.

Then, from the maximum distance, we can subtract each individual distance, corresponding to each element. By converting the resulting compensatory distance into time, the delays used in transmission (τ_{ti}) are obtained (1.10). As it can be deduced from equations (1.9) and (1.10), the transmission delays τ_{ti} are higher for the elements placed closer to the focal point and vice versa.

$$\tau_{ti} = \frac{d_{max} - \sqrt{(x_i - x_{FP})^2 + (z_i - z_{FP})^2}}{c} \tag{1.10}$$

where τ_i is the delay applied to the signal transmitted for the element i, x_{FP}, z_{FP} are the lateral and axial coordinates of the focal point and max is the maximum value.

If desired, an apodization (windowing) function (w) can be used once all the signals are delayed. Under the Fraunhofer approximation, the sidelobe level is dependent on the apodizaton through a Fourier relation (Goodman 2005). In general, the purpose of using the apodization is to reduce the side lobes (Thomenius 1996).

The resulted mathematical expression of the transmitted waveform $s_i(t)$, for a specific element i after delaying and weighting the initial signal, can be found in equation (1.11).

$$s_i(t) = s(t) * \delta(t - \tau_{ti}) \cdot w_{ti} = s(t - \tau_{ti}) \cdot w_{ti} \tag{1.11}$$

where * is used as a notation for temporal convolution.

Once the ensemble of electrical signals ($s_i(t), i \in [1..N]$) is ready to be transmitted, it is applied to the transducer elements and converted into acoustic waves which propagate through the medium. When the transmitted waves arrive at a medium point (P) it has the following expression:

$$tp(t) = \sum_{i=1}^{N} s_i(t) * h_t(t) * m_{ip}(t) \tag{1.12}$$

where $tp(t)$ is the transmitted signal that arrives at a point P of the medium, $h_t(t)$ is the acousto-electrical impulse response of the transducer in emission, $m_{ip}(t)$ is the spatial impulse response of the element i at the point *P* of the medium in far field conditions (Jensen & Svendsen 1992), (Bujoreanu et al. 2017) and it can be written as:

$$m_{ip}(t) = \frac{\delta(t - d_{iP}/c)}{2\pi d_{iP}} \tag{1.13}$$

where d_{iP} is the distance from the element i to the point P.

1.3.2. Received signals

The echoes are reflected back to the transducer and converted into electrical signals. In reception, one element *j* of the transducer receives echoes from all the points in the medium as shown in equation (1.14):

$$\begin{aligned} rf_j(t) &= \sum_{p=1}^{N_{MP}} tp(t) * m_{pj}(t) * h_r(t) + n_j(t) = \\ &= \sum_{p=1}^{N_{MP}} \sum_{i=1}^{N} s_i(t) * h_t(t) * m_{ip}(t) * m_{pj}(t) * h_r(t) + n_j(t) \end{aligned} \tag{1.14}$$

where $rf_j(t)$ is the signal received by the element j of the probe, N_{MP} is the total number of scatterers in the medium, $m_{pj}(t)$ is the spatial impulse response of the element j when the echo is emitted by the point P of the medium, $h_r(t)$ is the acousto-electrical impulse response of the transducer in reception and $n_j(t)$ represents the additive acquisition noise. As suggested by (Jensen & Svendsen 1992), if we assume that the elements of the transducer are completely reversible and of the same shape and size, we can affirm that $m_{pj} = m_{ip}$ (for j = i). In other terms, the spatial impulse response in emission for a given element can be considered the same as the impulse response in reception of the same element. Additionally, in general we assume $h_r(t) = h_{t,}(t), \forall(j,i)$.

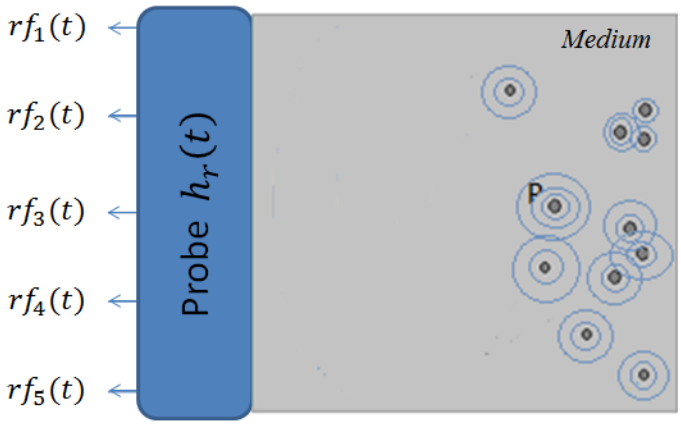

Fig. 9. Reception for a transducer having 5 elements: Each element j of the probe receives echoes from all the points of the medium.

Depending on the position of the medium point P, the echoes arrive at different elements j of the probe with different delays $(d_{jP} + d_{iP})/c$. However, as it will be shown in section 1.3.4, these delays will be compensated in reconstruction.

1.3.3. RF processor

The received digitized signals contain frequencies which lie in the radio communication spectrum (from 20kHz to 300 GHz). Therefore, for the same reason as in telecommunications, these signals are called radio frequency (RF) signals.

The sampling rate of the final RF data is usually reduced compared to the one of the ADC data to facilitate the data transfer rate. According to Shannon theorem, the sampling frequency could be reduced to twice the maximal frequency component of the signal without loss of information. A simple decimation of the digitized data could do this task. However, an optimal modality for achieving the sampling rate reduction without loss of information can be obtained by quadrature demodulation. This operation is performed by multiplying the received signal with $cos(2\pi f_c n)$ on one hand and with $sin(2\pi f_c n)$ on the other hand. The two obtained signals will be then low-pass filtered and summed to recover the baseband signal $I(n) + jQ(n)$ (Fig. 10). The IQ representation of the signal contains both the amplitude and the phase information which is very convenient for Doppler applications.

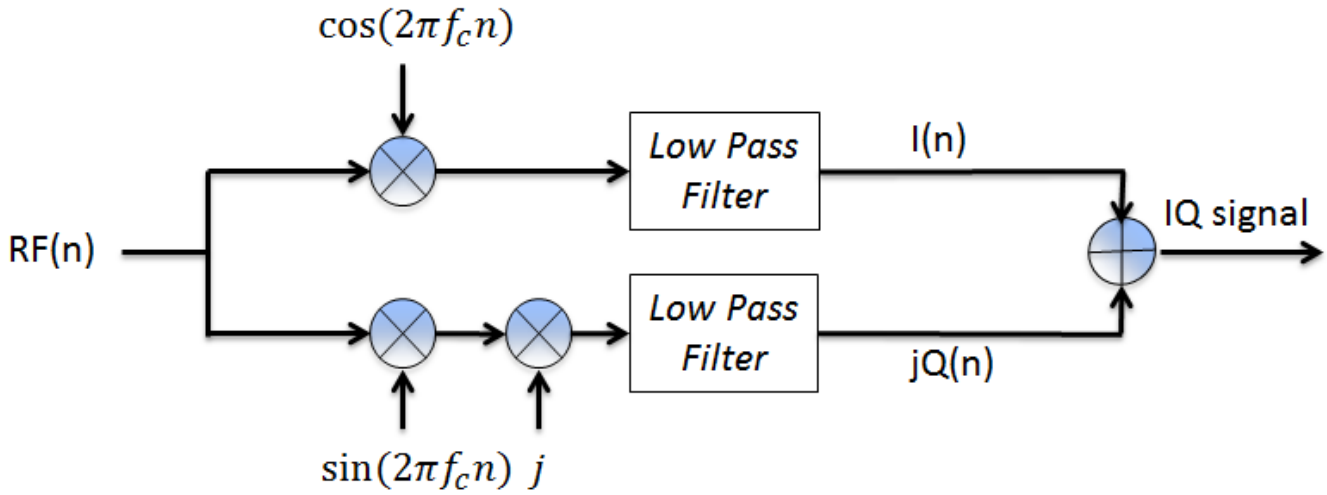

Fig. 10. IQ demodulator: The received RF signal is multiplied with $cos(2\pi f_c n)$ and $jsin(2\pi f_c n)$. The two obtained signals will be then low-pass filtered and summed to obtain the baseband signal $(n) + jQ(n)$.

1.3.4. TGC and ADC

As it can be observed in equation (1.13), each wave emitted by an element i (and by analogy each echo generated by a scatterer placed in P) loses a part of its amplitude during the propagation through the term $1/2\pi d_{iP}$. This effect can be called total round trip spreading attenuation. In order to compensate for this, the received signals are amplified proportionally to the time required for the signal to return to the transducer (i.e. $(d_{jP} + d_{iP})/c$). This processing step is called Time to Gain Compensation (TGC). As shown in Fig. 11 (A), the image obtained when applying a constant gain (C) to the received signals is more attenuated at higher depths than the image (B) obtained using a gain that compensates for the attenuation (D).

Once the signals from the transducer are received and amplified according to the TGC curve, they are digitized using an Analog to Digital Converter (ADC). The sampling frequency of the ADC has to be conservatively high and its value depends on the system used.

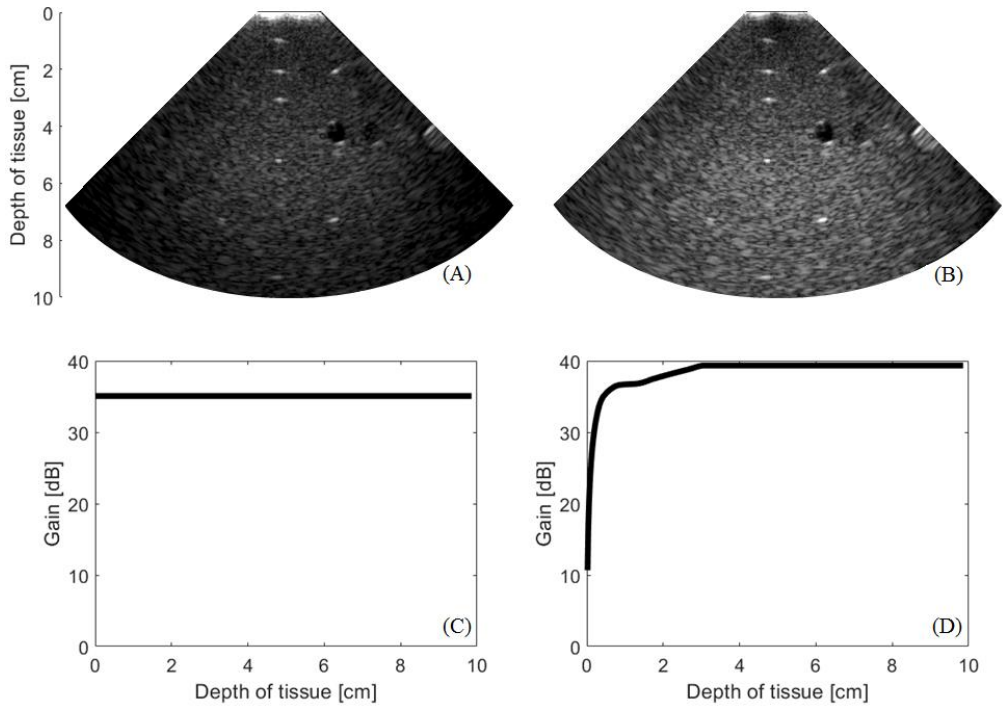

Fig. 11. The impact of TGC curves on B-Mode images: (A) the image obtained when applying a constant gain (C) to the received signals is more attenuated at higher depths than the image (B) obtained using a gain that compensates for the total round trip spreading attenuation (D).

1.3.5. Beamforming in reception

Similar to emission, a delay will need to be applied to the RF/IQ digitized data received by each element to compensate for time differences within the signals. For instance, if we want to reconstruct the specific line of the image that contains the point P (Fig. 12), we will need to apply a delay to each received and digitized RF signal. In addition, if the beamforming is done on IQ signals, a phase shift should be applied to the delayed signals.

Each RF signal shown in Fig. 12 contains echoes coming from all depths z_{MP}, for the fixed lateral position x_{MP_0} where the point P is placed. Once the signals are aligned to the same start point, the apodization can be used to obtain an optimal beampattern (Jensen & Svendsen 1992),(Guenther & Walker 2007). The final beamformed RF line can be written as:

$$BF\left(x_{MP_0}, z_{MP}\right) = \sum_{j=1}^{N} RF_j\left(n - \tau_{rj}\left(x_{MP_0}, z_{MP}\right)\right) \cdot w_{rj} \tag{1.15}$$

where $\tau_{rj} = (d_{jP} + d_{iP})/c$ and w_{rj} are the delay and the apodization used in reception for element j.

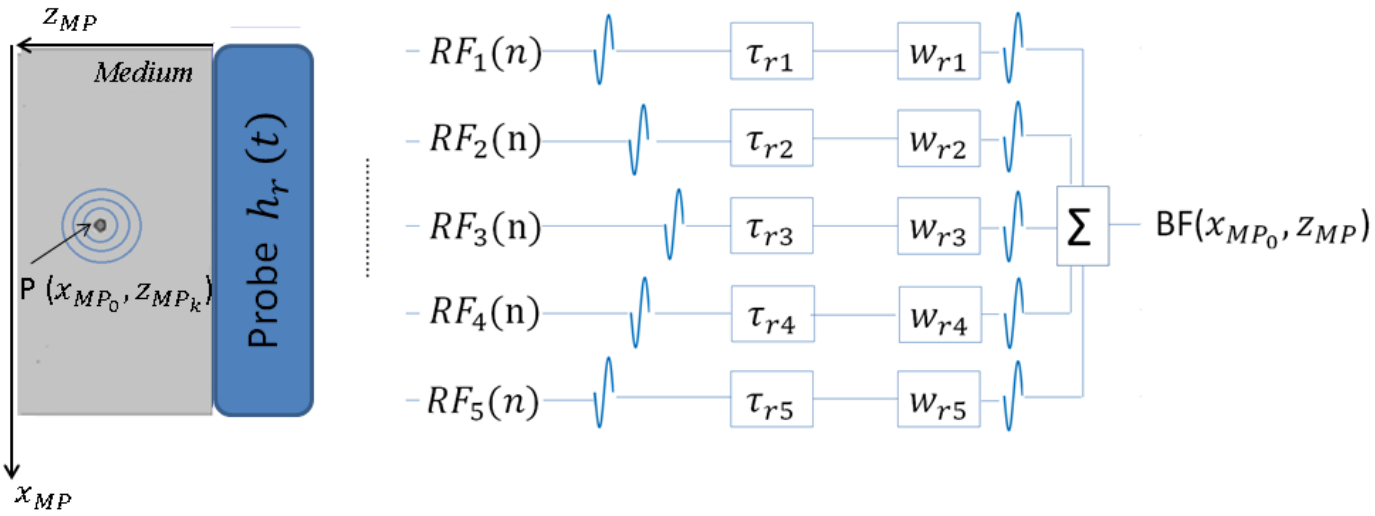

Fig. 12. DAS Beamforming (Reception): For reconstructing the image line corresponding with the lateral position (x_{MP_0}) of the point P, the received RF signals are delayed by τ_{rj} to compensate for time differences within the echoes generated in the same point P but received by different elements j. Similar to emission an apodization function (w_{rj}) can be used for obtaining an optimal beam pattern. The resulting signals are then summed to obtain one beamformed line of the image

1.3.6. Imaging modes

The beamformed data can be further processed for data visualization and diagnostic assessment. Typically, the clinicians are interested in observing, measuring and analyzing the anatomical structures, but also in quantifying the motion which can be an indicator for certain pathologies. Several imaging modes have been developed to assist clinicians in diagnosis. A brief description of different scanning modalities is provided in this section.

1.3.6.1. B-Mode

The B-Mode (Brightness Mode) is the most frequently used imaging modality, allowing real-time gray scale visualization of the imaged body structures.

In order to obtain one column of a B-Mode image, the beamformed RF signal (Fig. 13, A), corresponding to a single transmission event, has to be post-processed as follows: first, the envelope of the RF signal (Fig. 13, B) is extracted in order to highlight the amplitude of the signal. Second, the dynamic range of the signal is reduced by log-compressing the normalized envelope of the signal (Fig. 13, C). In this way, one column of a B-Mode image is created (Fig. 13, D). For obtaining a full B-Mode image containing N_{TX} columns, the same procedure needs to be followed for N_{TX} RF beamformed signals. Since each RF signal is obtained from one transmission event, N_{TX} transmission events are needed to create one B-Mode image.

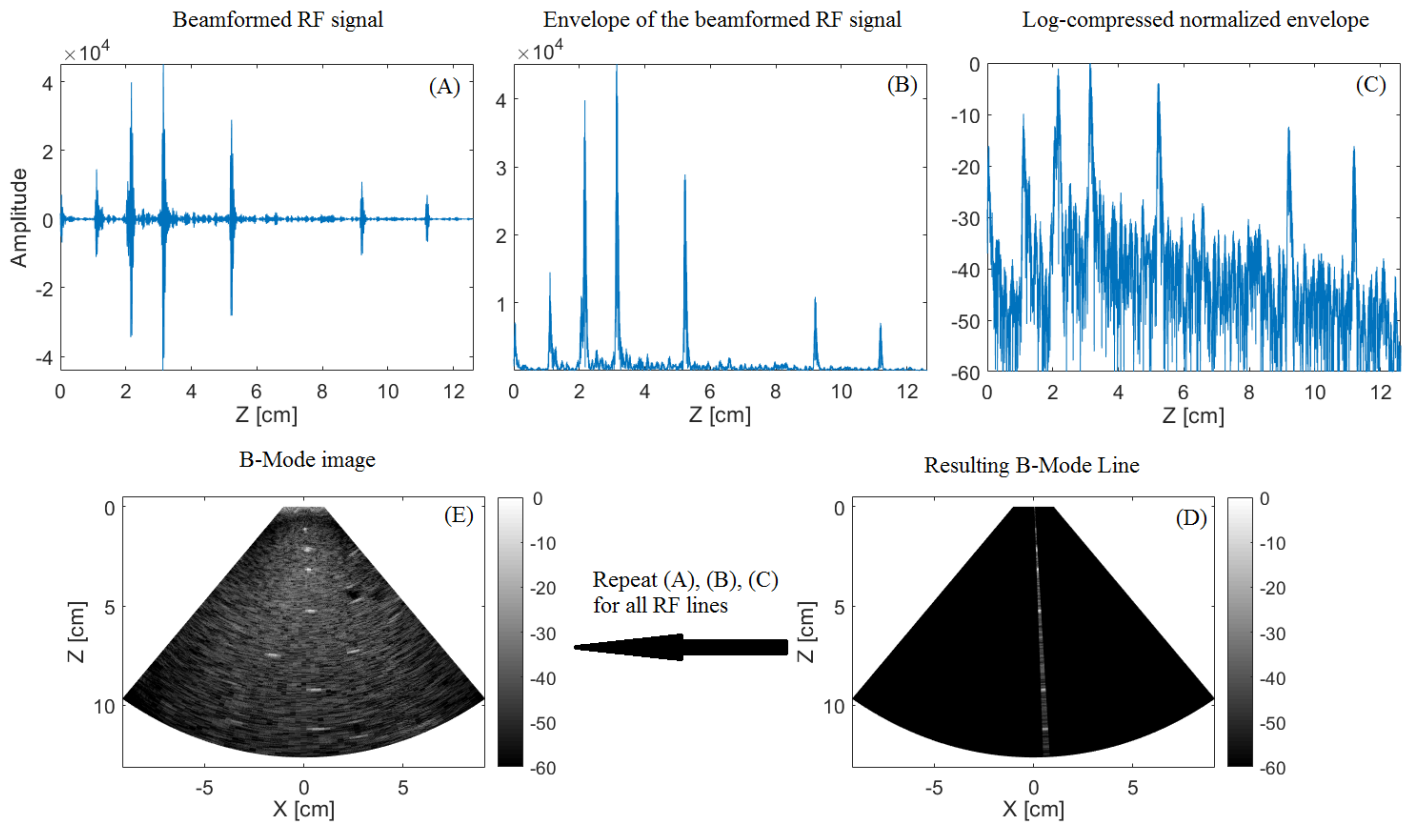

Fig. 13. Obtaining a B-Mode image: The RF signals resulting from one transmission event are beamformed (A). Then, the envelope of the beamformed RF signal is extracted (B) and log-compressed (C). In this way, one column of a B-Mode image is created (D). The steps presented in (A), (B), (C) are repeated till a full B-Mode image is obtained.

The frequency of the transmissions referred as Pulse Repetition Frequency (PRF) is limited by the depth of the imaged media and by the speed of the sound. Since the speed of the sound is constant, the only way of adjusting the PRF is by limiting the penetration depth. As shown in equation (1.16), the interest of adapting the PRF is to obtain a higher frame rate, which could improve the visualization and motion analysis of fast-moving organs.

$$FR = \frac{PRF}{N_{TX}} \tag{1.16}$$

where FR is the frame rate and N_{TX} gives the number of transmissions.

1.3.6.2. M-Mode

The M-Mode (Motion Mode) is used to observe how a line from a B-mode image changes in time. The echo data from the selected line is displayed in an M-Mode image whose main axes are depth and time. Compared to conventional B-Mode, this imaging modality provides a better temporal resolution being used for the evaluation of rapid movements of the heart.

An example of M-Mode image is provided in Fig. 14. The selected B-Mode Line (Fig. 14, B) is illustrated over time (Fig. 14, A) for evaluating if the aortic valve is opening and closing properly.

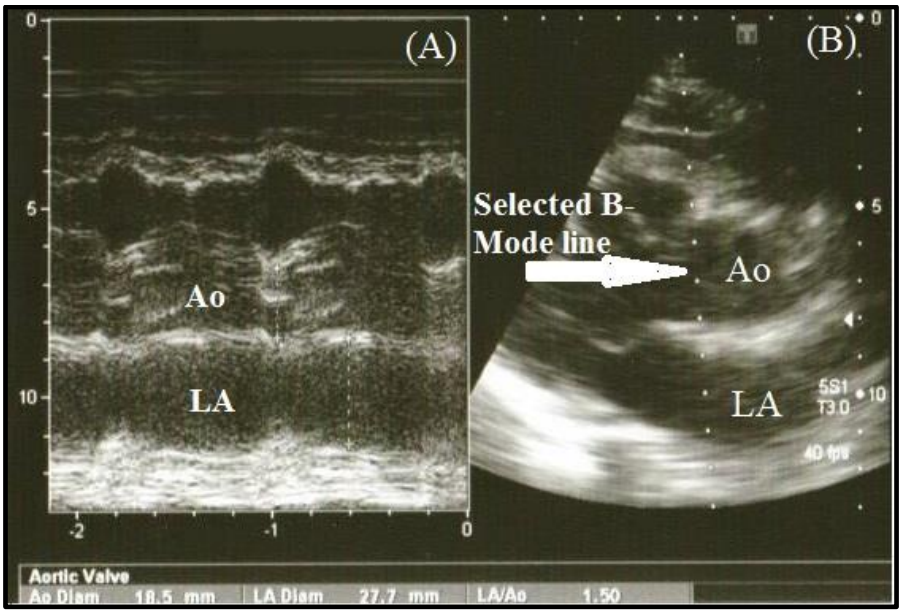

Fig. 14. Example of M-Mode image (A) of a selected B-Mode line (B) crossing the aortic valve (Ao) and the left atrium (LA) [Courtesy to Sorina Kreppenhofer].

1.3.6.3. Doppler modes

Several Doppler modes have been developed to assess the flow presence and the flow velocity. Starting from the basic principle of the Doppler effect, we will briefly describe the advantages and limitation of different Doppler modes. In addition, we will provide more details about the Doppler mode used later in this thesis which is Color Doppler.

Firstly described in 1842 by Christian Doppler, the Doppler effect is the relative change in frequency of a wave generated by a moving source experienced by a stationary observer. As the source is moving away from the observer, the frequency of the wave is observed as being lower than the original frequency of the wave. Conversely, the frequency of the wave appears to be higher when the source moves away from the observer. The Doppler shift can be written as:

$$f_d = \frac{2 f_c V}{c} \cdot \cos\theta \tag{1.17}$$

where f_d is the Doppler frequency shift, f_c is the central frequency of the transducer, V is the velocity of the moving source and θ is the angle between the ultrasound beam and the moving blood.

Already applied in many fields such as astronomy, radar, and sonar, this principle was successfully extended to medical ultrasound imaging. The observer, in this case, is the transducer and the source is the moving reflector. As shown in Fig. 15, it is important to place the probe in a position that minimizes the

angle θ between the ultrasound beam and the moving reflector. In this way, the measured Doppler velocity which is the projection of the real velocity on the beam axis will be closer to the real value.

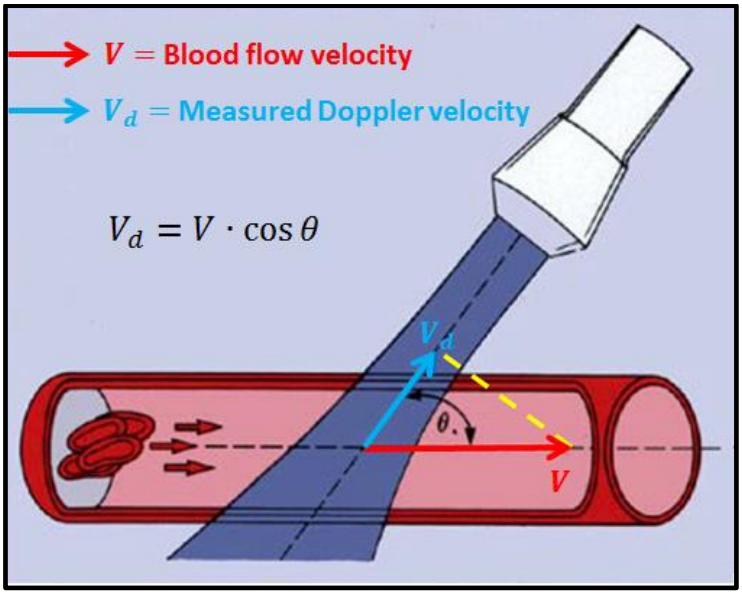

Fig. 15. The dependency of the measured Doppler velocity on the angle between the ultrasound beam and the real velocity vector. Retrieved from (Kisslo & Adams 2001)

In Doppler imaging, there are two types of transmissions that can be used: continuous and pulsed which are illustrated in Fig. 16.

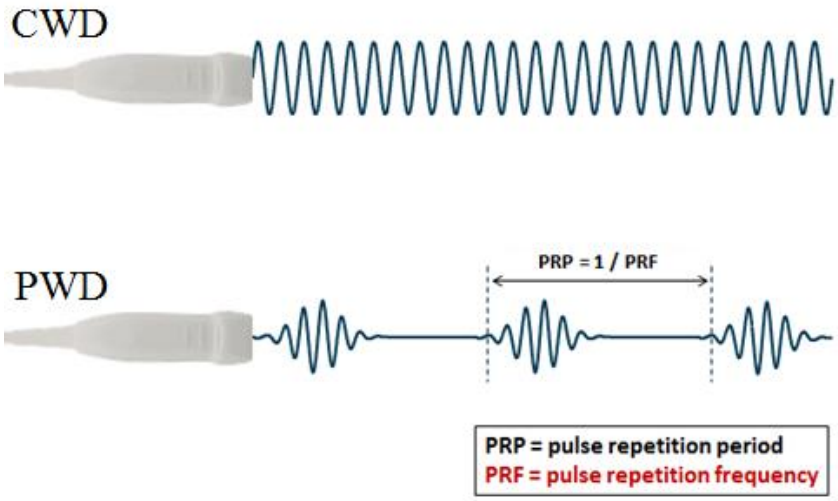

Fig. 16. Continuous and Pulsed wave Doppler [Courtesy to Damien Garcia].

The ***Continuous Wave Doppler (CWD)*** uses a continuous transmission and reception. As the frequency of the wave used in transmission is known, it can be subtracted from the received signal in order to find the Doppler shift. Even if this imaging modality allows the detection of blood flow it cannot be used for localizing the velocities, since the velocity is estimated along the entire length of the beam. This mode is used for detecting high velocities in the aortic valve or tricuspid valve.

The ***Pulsed Wave Doppler (PWD)*** overcomes the limitation of the CWD mode, by providing the specific location of the moving reflector. The Doppler gate is selected at the depth of interest and the velocity is estimated just on the selected area. PWD mode can be used to analyze the mitral valve (MV) for detecting diastolic dysfunction and for calculating the cardiac debit.

Spectral Doppler can be obtained either from a pulsed or from a continuous transmission. Usually, the quadrature demodulated IQ signal is clutter (high-pass) filtered for suppressing high amplitude low-frequency signals coming from stationary echoes (such as walls). In order to provide an accurate velocity resolution, FFT (Fast Fourier Transform) is computed over a large number of samples taken for the same location over time. The collection of samples will be referred as ensemble.

Color Doppler (CD)/ Color Flow Imaging (CFI)/ Color Velocity imaging is a PWD transmission-based mode that provides a 2D color-coded map of the velocity flows. The colors are coded in blue and red nuances, depending if the reflector is moving away or towards the transducer (Jensen, 1996).

This mode is based on the Kasai autocorrelator that measures the velocity projected on the transmitted beam direction by estimating the phase shift for a given depth location along the slow-time axis (Kasai et al. 1985). The estimated Doppler velocity is given by:

$$V_d = \frac{c \cdot PRF}{4\pi f_c} \tan^{-1}\left(\frac{\sum_{n=1}^{N_{TX}} Q(n)I(n+1) - I(n)Q(n+1)}{\sum_{n=1}^{N_{TX}} I(n)I(n+1) - Q(n)Q(n+1)}\right) \tag{1.18}$$

where PRF is the Pulse Repetition Frequency, n shows the transmission number and I, Q are the demodulated in-phase and quadrature signals.

As shown in equation (1.18), the velocity measurement is dependent on the PRF: the higher the PRF, the higher the maximum velocity that can be measured. On the other hand, the maximum PRF is limited by the maximum depth to be imaged. Therefore, an important limitation of the estimator is its inability to measure velocities higher than Nyquist velocity (V_N), given in (1.19). When this limit is exceeded, this mode leads to aliasing.

$$V_N = \frac{c \cdot PRF}{4f_c} \tag{1.19}$$

The variance of this estimator σ^2 is inverse proportional to the duration of the excitation signal T_s and proportional to the Doppler velocity as shown in (Jensen, 1996):

$$\sigma^2 = \frac{c \cdot PRF}{4\pi^2 {f_c}^2 T_s} |V_d| \tag{1.20}$$

For this reason, in practice, we transmit longer excitation signals although this compromises the axial resolution.

Although compared to spectral Doppler, Color Doppler has the advantage of providing 2D maps of the velocities, the current temporal resolution of the ultrasound system does not allow Color Doppler flow quantification.

Power Doppler is an alternative method to color Doppler for a 2D visualization of flow. Therefore, this mode is used for detecting the presence of the blood flow and does not provide any information about its speed and direction. Power Doppler provides the advantage of having a decreased dependence on the angle formed with the moving reflector, compared to Color Doppler. That makes it suitable for detecting low velocities. A limitation of power Doppler is the sensitivity to noise. The speckle noise could be reduced by averaging the estimated values over a packet ensemble with the compromise of the temporal resolution (Kargel et al. 2004).

1.4. CURRENT LIMITATIONS OF CONVENTIONAL CLINICAL ECHOCARDIOGRAPHY AND THE POTENTIAL OF POSSIBLE IMPROVEMENTS

As discussed in section 1.3.6, conventional echocardiography offers many imaging modes providing important information for diagnosis, being established as the most widely used clinical modality for the quantitative and qualitative evaluation of the cardiac function (Otto 2012).

Despite its advantages, conventional cardiac ultrasound imaging still presents some limitations such as the current achievable frame rate (~40-80 Hz). Although this is sufficient for a standard diagnosis, a higher frame rate would be required for some applications characterized by a higher heart rate. Some examples are stress echocardiography (120-140 beats/minute) and fetal echocardiography (120-170 beats/minute). Additionally, a higher frame rate would also allow a better quantification of the heart dynamics at a finer scale and it would provide more sensitive Doppler estimates, enabling a more reliable hemodynamic assessment. The increased sensitivity could also improve the current visualization of low flow rates present for example in coronary arteries. Furthermore, strain and strain rate could also be improved by a higher temporal resolution. Also, the high frame rate could allow assessing the myocardial motion of different ventricular segments within the same heartbeat that could lead to a better understanding of the heart activation/contraction sequence (Cikes et al. 2014).

The limitation concerning the temporal resolution of the current ultrasound systems becomes even more important in 3D imaging. This is because a full volume needs to be insonified for obtaining 3D data and that for each transmission one line of the volume can be formed. Therefore, a full-volume requires increasing the number of transmissions compared to 2D imaging and the frame rate is significantly reduced (equation (1.16)). This is one of the reasons 3D echocardiography is rarely employed during medical examinations, which leads to another limitation of the conventional echocardiography: in spite of the 3D nature of the heart, the diagnosis is based on 2D images and measurements.

For example, during a standard echocardiographic examination, several 2D images are acquired for obtaining complementary anatomic views, while a single 3D volume could provide a complete assessment of the heart anatomy.

A second example is the common way of investigating the left ventricular (LV) chamber dimension and the left ventricular ejection fraction (LVEF), both based on 2D measurements. The current techniques

for calculating LVEF require a precise identification of the end-diastole and end-systole phases, which is inter and intra operator–dependent. Moreover, the detection of the real-time instants of the desired cardiac phases may be challenging at insufficient frame rates. Additionally, the LVEF is calculated based on 2D data using geometric modeling and chamber shape assumptions. The usage of 3D imaging would not just avoid relying on operator dependent measurements but it would also suppress the need of using assumptions for geometric modeling. This is even more important for assessing the right ventricular (RV) volume and function since modeling its geometry is much more challenging than for the left ventricle.

A common usage of three-dimensional echocardiography could also be a benefit for cardiac interventions. For instance, 3D echocardiography proved to be more accurate than the conventional 2D approach for the quantification of aortic regurgitation after transcatheter aortic valve implantation (Altiok et al. 2014). In addition, other studies showed that quantifying the improvement in mitral regurgitation after mitral valve repair is more reliable using 3D than 2D color flow imaging (Gruner et al. 2015).

Therefore, 3D echocardiography presents several advantages over the conventional 2D imaging and coping with the current limitations could be considered as a step ahead to its common usage in clinical practice. Increasing its usage would indeed add clinical value to current diagnosis and enable new advancements in cardiac imaging.

1.5. CONCLUSION

In this chapter, we first presented the basic principles of ultrasound. Second, the pipeline of an ultrasound acquisition process was described step by step, from transmission to reception. We then presented the processing applied to the received data in order to obtain the different imaging modes that assist clinicians in gathering valuable information for diagnosis. However, the current capabilities of the system present several limitations, such as the frame rate. If in 2D, the maximum achievable temporal resolution is limited for capturing fast events, such as the ones occurring during stress-echocardiography, in 3D, this problem becomes even more important since a full volume needs to be insonified.

Thus, there is a need for increasing the frame rate for improving the current clinical analysis in 2D, but a high temporal resolution could be particularly interesting in 3D. Several current assumptions done on the heart geometry for volumetric measurements (eg. LVEF) could be removed leading to an increased accuracy. The response of the research ultrasound community to this limitation will be discussed in the next chapter, where we will also present the conventional motion estimation techniques used together with the proposed approaches.

CHAPTER 2:

HIGH FRAME RATE ECHOCARDIOGRAPHY: FROM IMAGE FORMATION TO VELOCITY ESTIMATION AND VALIDATION

2.1. INTRODUCTION

In response to the current capabilities and limitations of a conventional ultrasound system (section 1.4), several high-frame rate methods have been developed in research ultrasound. In this chapter, we will start by presenting these methods. Since the interest of high-frame rate echocardiography is strongly linked to motion quantification, we will then describe the most used motion estimation approaches. Additionally, we will discuss the advantages of extending high frame-rate methods to 3D. As testing novel methods is an important step before introducing them in clinical practice, several validation approaches of vector flow high frame-rate methods will be then compared. Finally, we will talk about the improvements brought by research echocardiography and the current limitations that will lead to the objectives of this thesis.

2.2. HIGH FRAME RATE MODALITIES

Although the frame rate achievable in standard echocardiography (generally from 40 to 80 Hz) is sufficient for a standard examination, heart dynamics contains short events that cannot be captured with the conventional frame rate. Higher temporal resolution might be essential in rapid cardiac events observed in a number of cases such as stress echocardiography, fetal echocardiography, multi-chamber motion/strain imaging or intracavitary blood flow dynamics (Cikes et al. 2014). In response to the need for higher frame rates, several methods have been proposed in ultrasound imaging.

Conventionally, by fixing a certain depth, the frame rate can be improved either by reducing the line density or by reducing the field of view. Reducing the field of view limits the area of the investigation while decreasing the number of lines of the image will result in limiting the spatial resolution. Therefore there is a compromise between the frame rate, the lateral resolution and the field of view that has to be taken into account when increasing the frame rate in standard echocardiography.

Fewer compromises are accepted when methods such as ECG (electrocardiogram) gating, Multi Line Acquisition, synthetic aperture approaches, and Multi-Line Transmission are employed. It is worth mentioning that for all these methods, the reasoning presented in the first chapter, concerning the emission signals $s_i(t)$, the reception signal $rf_j(t)$ and the beamformed signal, generally holds as shown in equation (2.1). The exceptions will be mentioned when presenting each method.

$$\begin{aligned} s_i(t) &= s(t-\tau_{ti})\cdot w_{ti} \\ rf_j(t) &= \sum_{p=1}^{N_{MP}} tp(t) * m_{pj} * h_r(t) + n_j(t) \\ BF\left(x_{MP_0}, z_{MP}\right) &= \sum_{j=1}^{N} RF_j\left(n-\tau_{rj}\left(x_{MP_0}, z_{MP}\right)\right)\cdot w_{rj} \end{aligned} \tag{2.1}$$

2.2.1. ECG (retrospective) gating

ECG (electrocardiogram) gating allows improving the temporal resolution without limiting the field of view or the spatial resolution. This can be achieved by synchronizing the acquisition moment with the cardiac cycle. At each heartbeat, a small sector of the full field of view is acquired at a high frame rate. For each acquisition, the angle of the sector is changed. After several sectors are acquired, they can be combined in order to form the full image (Fig. 17). Despite the promising frame rate of over 400 Hz obtained in (Shougang Wang et al. 2008) for 2D cardiac images, this method is not well adapted for patients presenting an irregular heartbeat. Moreover, ECG gating requires a prolonged acquisition time and it is sensitive to any additional motion that could occur during the acquisitions.

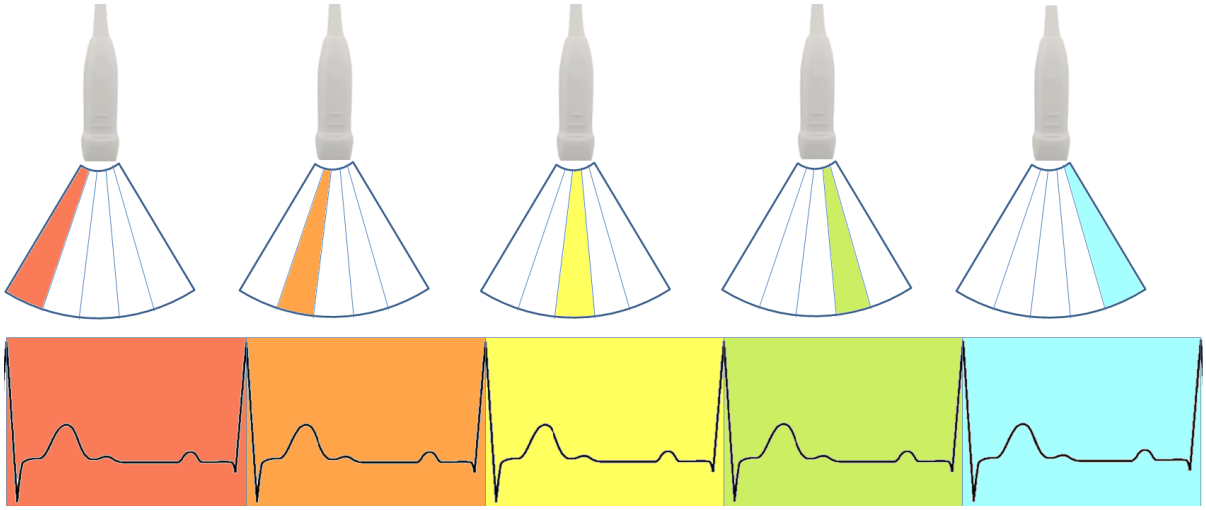

Fig. 17. ECG gating: At each heartbeat, a small sector of the full field of view is acquired at a high frame rate. By changing the angle of the sector for each acquisition, all the resulting high-frame rate sectors can be combined to form a full image.

2.2.2. Multi-line acquisition

An alternative method for increasing the frame rate is Multi Line Acquisition (MLA). Known also as Parallel Receive Beamforming (PRB), this method has been proposed by (Shattuck et al. 1984) and it is implemented in most current clinical scanners. The gain in temporal resolution is achieved by reconstructing multiple image lines from one single transmission. Reconstructing several lines requires a weakly focused beam. Such a beam can be obtained either by limiting the size of the aperture either by using unfocused beams. However, both possibilities come with their compromises. Limiting the aperture will affect the lateral resolution and will result in a lower SNR. Using wide beams allows transmitting with all elements which will improve the SNR. Nevertheless, the lateral resolution is still compromised.

2.2.3. Synthetic Aperture Approaches

Originally proposed for radar in the early 50s, Synthetic Aperture (SA) started to be investigated two decades later in ultrasound imaging (Burckhardt et al. 1974),(Johnson et al. 1975). A basic implementation of this method involves the transmission of a spherical wave using a single element of the transducer. The

echoes are then received using all the elements of the transducer. The data corresponding to one transmission-reception event is processed to form one low resolution image. By repeating this process each time for a different element in emission, and summing the resulting low resolution images, a high resolution image can be obtained (Fig. 18). This method produces a dynamic focusing in transmission and reception. As a consequence, high resolution and contrast are obtained everywhere in the B-Mode image (Jensen et al. 2006).

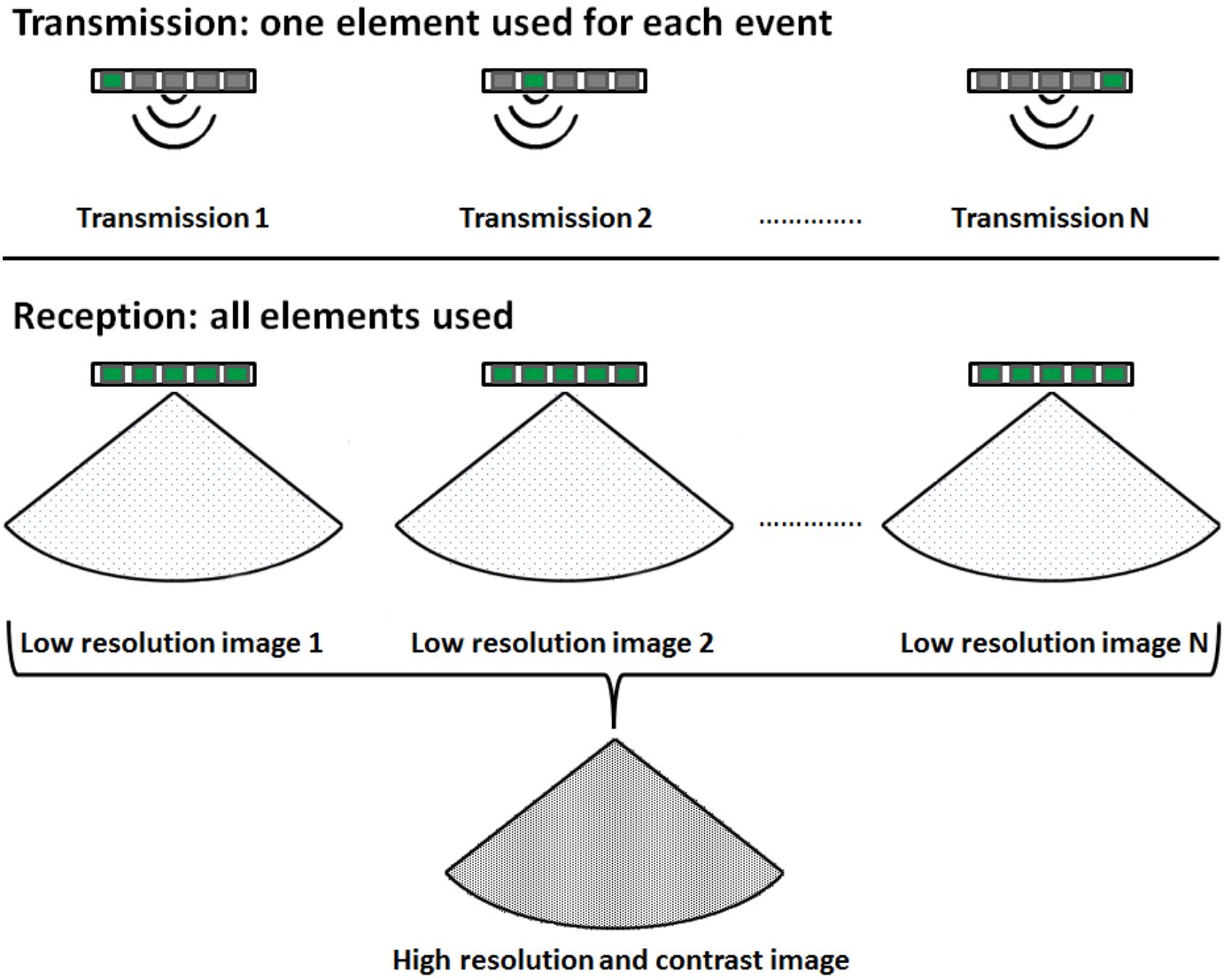

Fig. 18. Basic implementation of synthetic aperture imaging: At each transmission event, a spherical wave is emitted using a single element of the probe. For each reception event, the echoes are received using all the elements of the probe. The data corresponding to one transmission-reception event is processed to form one low resolution image. By summing all the resulting low resolution images, a high resolution and contrast image can be obtained.

Even if the SA frame rate is improved compared to the one obtained in conventional ultrasound when using dynamic focusing in transmission, the gain in temporal resolution is not enough for some cardiac applications such as stress test. Moreover, since the beam is transmitted by single elements, this method

provides a low SNR. As suggested by (Lockwood et al. 1998), this limitation can be reduced by considering sub-apertures made by several elements. In this way, the origins of the beams, called virtual sources are placed behind the transducer instead of superimposing them into the elements of the transducer. An additional improvement of this approach was using sparse SA, meaning that the single transmit elements were sparsely distributed. As shown by Andresen et al, the sparse SA method based on the virtual source transmission, lead to promising *in vivo* cardiac results (Jensen et al. 2006). By reducing the number of transmissions, the frame rate was increased to about 500 Hz for a PRF of 4500. Compared to the frame rate achievable in focus imaging of 70 Hz (for the same PRF and by reconstructing 64 image lines), the temporal resolution was increased 7 times.

The principle of sparse SA have also been exploited by other teams which referred to this method as plane wave (PW) (Sandrin et al. 1999), (Sandrin et al. 2002)/diverging wave (DW) imaging (Hasegawa & Kanai 2011). As in sparse SA, in DW/PW imaging virtual sources located behind the transducer are used to emit defocused waves. The impact of using unfocused beams on the transmitted field, in comparison to the impact of using focused beams (conventional echocardiography) is shown in Fig. 19. As it can be observed, a wider sector can be insonified by PW/DW approaches, compared to focus imaging. Therefore, since fewer transmissions are required to insonify a full sector, the frame rate is increased.

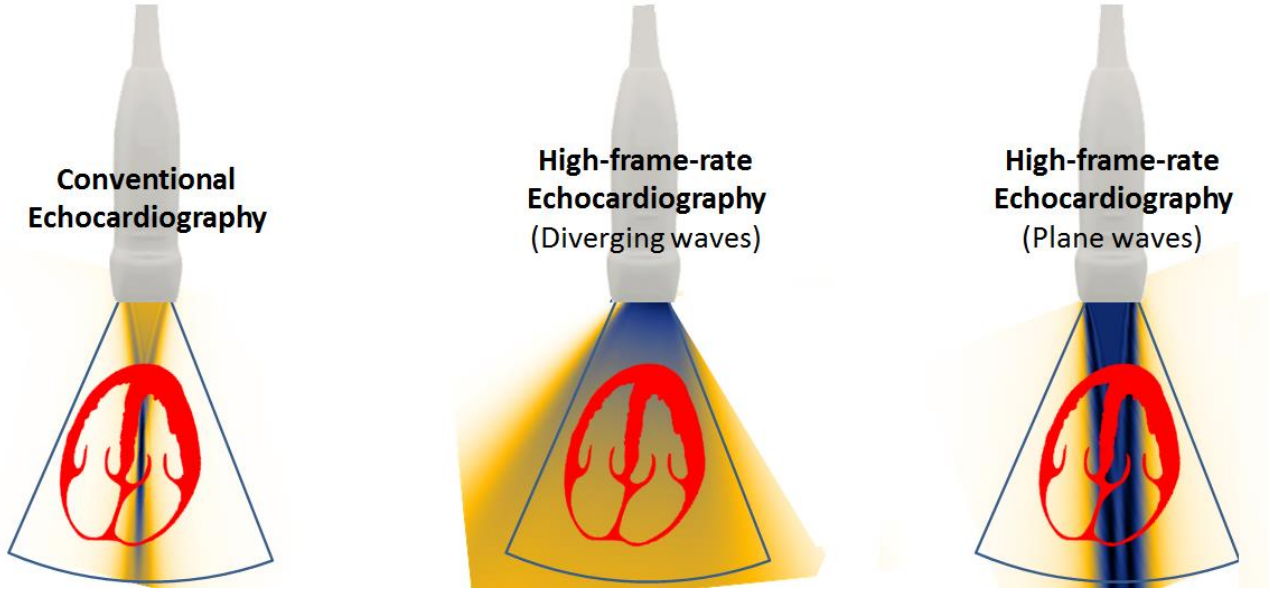

Fig. 19. Transmission in conventional, DW and PW echocardiography [*Courtesy to Damien Garcia].*

However, in order to generate a PW/DW wavefront, the delays in transmission (τ_{ti}) need to be changed compared to conventional imaging. Therefore, the following equation can be used:

$$\tau_{ti} = \frac{\sqrt{(x_i - x_v)^2 + (z_i - z_v)^2} - \min_{i\in[1..N]}\left(\sqrt{(x_i - x_v)^2 + (z_i - z_v)^2}\right)}{c} \quad (2.2)$$

where (x_i, z_i) are the lateral and axial coordinates of the element i of the probe and $(x_v, z_{v)}$ are the lateral and axial coordinates of the virtual sources placed behind the transducer.

From equation (2.2), we can observe that the distance $\sqrt{(x_i - x_v)^2 + (z_i - z_v)^2}$ is comparable with $\min_{i\in[1..N]}\left(\sqrt{(x_i - x_v)^2 + (z_i - z_v)^2}\right)$, if the virtual sources are placed closely to the transducer elements. Thus, τ_{ti} becomes a circular arc (Fig. 20 B), having the radius $\min_{i\in[1..N]}\left(\sqrt{(x_i - x_v)^2 + (z_i - z_v)^2}\right)/c$. Compared to the concave-shaped ensemble waveforms (Fig. 20 A), obtained for the delays calculated in a focused transmission (1.10), the ensemble waveforms in a DW transmission are convex-shaped. Moreover, this shape becomes flat if the virtual source is placed far-enough ($x_i \ll x_v$ or $z_i \ll z_v$). In this case, the difference between the two terms at the numerator in (2.5) becomes 0 and thus the emission delays become null $\tau_{ti} = 0$. Such a delay configuration allows a PW transmission (Fig. 20 C).

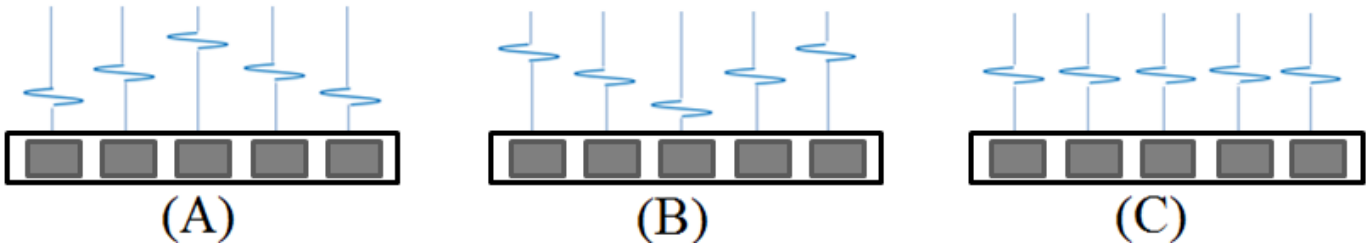

Fig. 20. Delays used for conventional (A), DW (B) and PW (C) imaging.

First applied in elastography (Sandrin et al. 1999), PW imaging demonstrated its potential in providing very high frame rate which motivated its extension to other applications (Salles, Chee, et al. 2015). Even if plane wave using linear arrays has already been applied in open-chest cardiac applications (Couade et al. 2011), (Bouchard et al. 2009), transthoracic echocardiography requires phased array probes having small apertures. As shown in Fig. 19 (right), a plane wave generated with such a transducer will not cover the entire heart. Moreover, sending a single wide beam will compromise the image quality in terms of resolution, contrast, and SNR. Similar to SA, the images obtained from different emission-reception events can be summed to improve the image quality. In DW/PW this process is known as coherent compounding (Montaldo et al. 2009).

DW was proposed as a solution for cardiac imaging and compounding was successfully applied for this method to improve the image quality (Hasegawa & Kanai 2011), (Papadacci et al. 2014b), (Provost et al. 2011). However, there is a trade-off between the image quality and the frame rate that has to be taken into account when choosing the number of steering beams.

2.2.4. Multi line-transmit

An alternative to the unfocused high-frame methods is multi-line transmission (MLT). Similar to Space Division Multiple Access (SDMA) used in telecommunications, this method is based on focusing narrow beams in different directions separated in space

A comparison between conventional focused and MLT imaging is provided in Fig. 21.

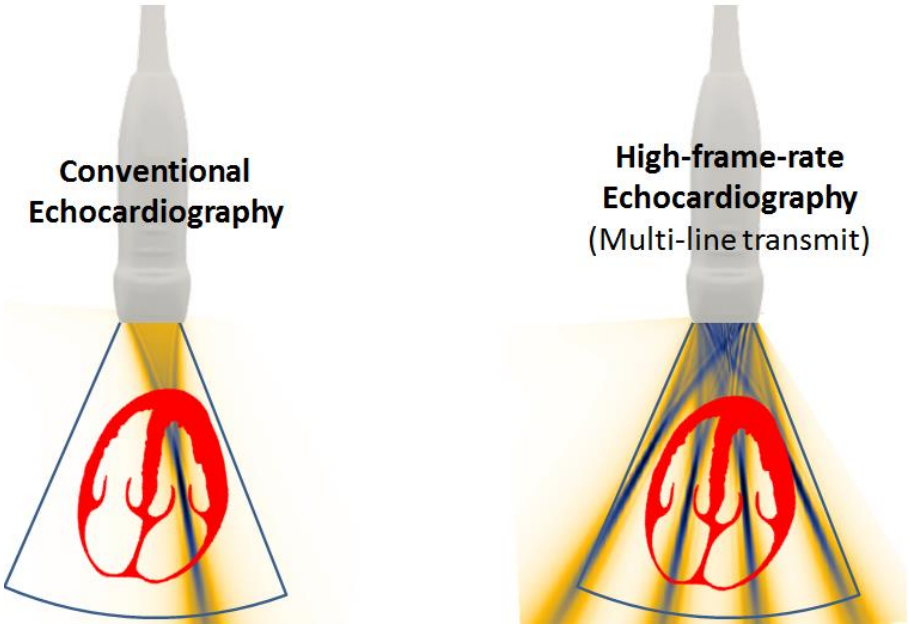

Fig. 21. Comparison between conventional focused imaging and MLT [*Courtesy to Damien Garcia]*

The emitted signal applied to each element ($s_i(t)$) used for such a multi-line transmission is achieved by linearly superposing the excitation signals that we would use in order to emit each focused beam successively. The resulting emitted signal can be written as:

$$s_i(t) = w_{ti} \sum_{k=1}^{N_{MLT}} s\left(t - \tau_{ti}^{k}\right) \tag{2.3}$$

where N_{MLT} stands for the number of beams sent simultaneously and the emission delays τ_{ti}^{k} for each beam k are computed using (1.10). Since N_{MLT} beams are emitted in parallel, it takes N_{MLT} times less emission events in order to reconstruct as many image lines as in conventional focused imaging. Therefore, the frame rate is increased by a factor of N_{MLT} compared to conventional imaging.

An example of combining 3 such focused transmissions for obtaining 3 MLT is shown in Fig. 22. As it can be observed on the right side, the waveform applied to each element in MLT is not just a delayed version of an original signal as it is the case for the other ultrafast methods. Superposing several transmit waveform may result in an irregular complicated signal. For this reason, the implementation of this method in practice requires a certain complexity.

Despite the complexity required by MLT in practice, Tong et al. showed in simulations the potential of this method in increasing the frame rate while preserving an image quality competitive with conventional focused imaging (Tong, Gao, et al. 2013). The practical implementation was later possible thanks to the Arbitrary Waveform Generator (AWG) provided by the ultrasound research system ULA-OP (Ricci et al. 2007).

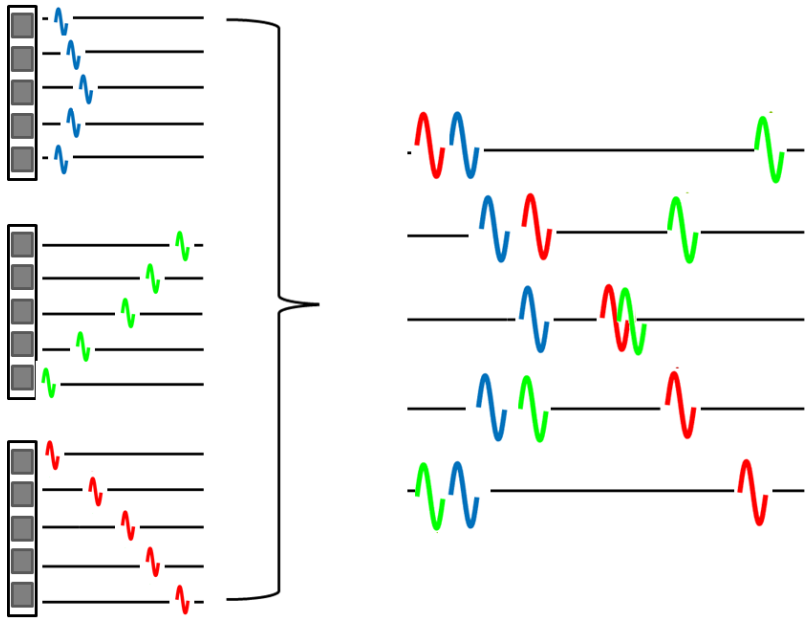

Fig. 22. The waveforms applied normally to focus in 3 different directions in conventional imaging (left) are superposed in one single transmission in MLT (right)

Although the experimental validation of this method in 2D cardiac imaging showed promising results (Tong et al. 2014), the main limitation of this technique is the presence of cross-talk artefacts. The transmit cross-talk appears when the energy of the side lobes of the transmit beam is picked up by the main lobe of the received beam corresponding to a different direction (Fig. 23 A). On the other hand, the receive cross-talk is created when the energy of the main lobe belonging to the transmit beam is picked up by the side lobes of the received beam corresponding to a different direction (Fig. 23 B). The two-way cross-talk appears when the energy from the side lobes belonging to the transmit beam is picked up by the side lobes belonging to the received beam corresponding to a different direction (Fig. 23 C).

The influence of the cross-talk can also be observed by analytically writing the signal received by the element j of the transducer as:

$$\begin{aligned} rf_j(t) = \sum_{k=1}^{N_{MLT}} \sum_{p=1}^{N_{MP}} \sum_{i=1}^{N} s\left(t - \tau_{ti}^{k}\right) * h_t(t) * m_{ip}(t) * m_{pj}(t) * h_r(t) + n_j(t) \; = \\ = \sum_{p=1}^{N_{MP}} \sum_{i=1}^{N} s(t - \tau_{ti}^{crt}) * h_t(t) * m_{ip}(t) * m_{pj}(t) * h_r(t) + n_j(t) \\ + \sum_{k=1, k\neq crt}^{N_{MLT}} \sum_{p=1}^{N_{MP}} \sum_{i=1}^{N} s\left(t - \tau_{ti}^{k}\right) * h_t(t) * m_{ip}(t) * m_{pj}(t) * h_r(t) + n_j(t) \end{aligned} \quad (2.4)$$

Compared to (1.14), the received signal showed in equation (2.4) contains a combination of N_{MLT} signals, received separately in conventional ultrasound. Thus, if we try to use $rf_j(t)$ to reconstruct a single line corresponding to a specific focused beam, the influence from the other $(N_{MLT} - 1)$ simultaneously unwanted focused beams will be taken into account, which will lead to cross-talk artefacts.

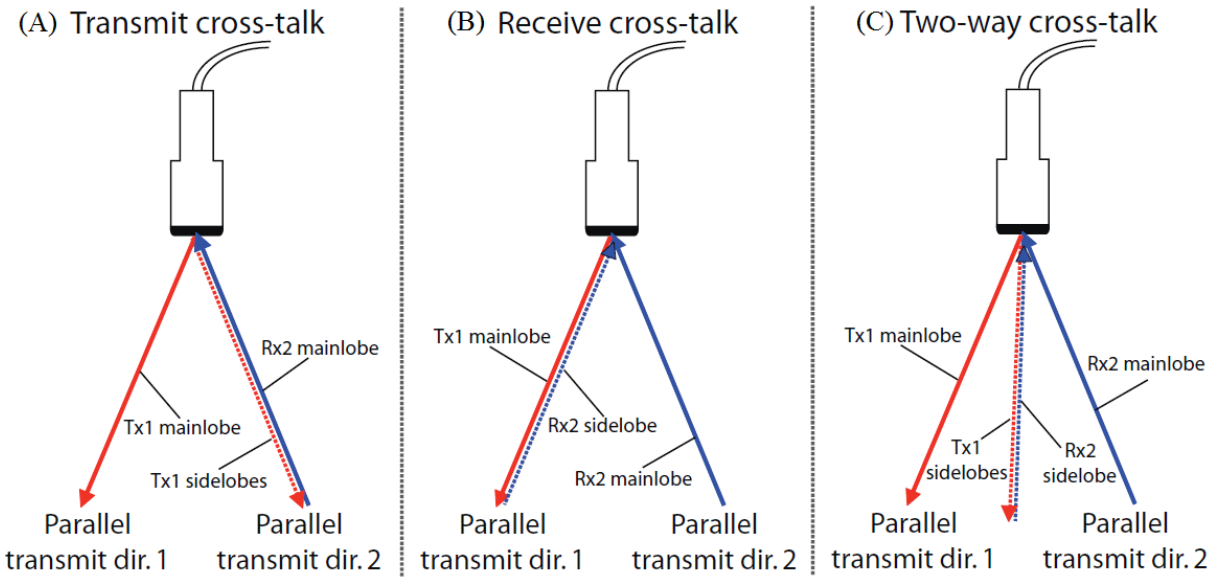

Fig. 23. MLT cross-talk: The transmit cross-talk appears when the energy of the side lobes of the transmit beam is picked up by the main lobe of the received beam corresponding to a different direction (Fig. 23 A). On the other hand, the receive cross-talk is created when the energy of the main lobe belonging to the transmit beam is picked up by the side lobes of the received beam corresponding to a different direction (Fig. 23 B). The two-way cross-talk appears when the energy from the side lobes belonging to the transmit beam is picked up by the side lobes belonging to the received beam corresponding to a different direction (Fig. 23 C). [Retrieved from (Dénarié 2014)**]**

Several methods have been proposed to reduce these artefacts. One possibility would be to divide the bandwidth of the transducer into multiple sub-bands that correspond with different simultaneous transmissions (Demi et al. 2013). Each of the parallels transmits pulses are generated in a different bandwidth**.** However, the main limitation of this technique is the degradation of the axial resolution as a result of the bandwidth division. Cross-talk reduction with less impact on axial resolution can be achieved by using a Tukey apodization in both transmit and receive as proposed in (Tong, Gao, et al. 2013). When compared to the Minimum Variance (MV) Beamforming introduced by (Rabinovich et al. 2015), the Tukey apodization provides a better contrast to noise ratio (CNR) and cross-talk reduction. However, the limitation of this method is the degradation of the lateral resolution. Filtered-Delay Multiply and Sum Beamforming (F-DMAS) has been proposed for improving the lateral resolution while providing a better suppression of the cross-talk (Matrone et al. 2017). A drawback of this method is the reduced CNR when compared with non-apodized DAS. Another strategy that allows obtaining an improved lateral resolution compared to Tukey apodization proposes using a predefined set of apodizations based on low complexity adaptive beamforming (LCA) (Zurakhov et al. 2018).

When cross-talk reduction methods are employed, the minimum number of simultaneous focused beams that allow obtaining an acceptable image quality is reduced compared to conventional MLT imaging. While some authors found that 6 parallel transmissions could offer a good image quality (Tong et al. 2014), (Zurakhov et al. 2018), others investigated further increases in frame rate, proving that up to 8 transmissions could provide good *in vivo* cardiac results (Matrone et al. 2017).

However, forming a full image with just one MLT transmission would not be possible without significant artefacts as it would be the case for PW/DW imaging. On the other hand, transmitting a single unfocused beam would definitely affect the image quality. Although among the methods discussed in this subchapter, MLT and DW/PW imaging offer a very promising gain in frame rate, each one comes with its own compromise between temporal resolution and image quality. A question that one could be posing is which method offers the best compromise for cardiac imaging? Since an important aspect in echocardiography is heart dynamics, the answer should be discussed depending on the particularities of the employed velocity estimation methods.

2.3. VELOCITY ESTIMATION METHODS

Quantitative analysis of heart motion is highly important in diagnosis. Besides the Doppler modes presented in Chapter 1, several methods have been developed for improving cardiac function assessment. For example, cross-beam Doppler methods allow estimating the lateral component of the velocity in addition to the axial component obtained through standard Doppler modes. But as all Doppler methods, this approach is angle dependent. As an alternative, speckle tracking does not just eliminate the angle dependency, but it also offers many advantages over Doppler methods: less sensitive to noise and better temporal resolution (Garcia et al. 2018). The particularities of each method are described in this section.

2.3.1. Cross-beam Doppler velocity estimation

As mentioned in Chapter 1, conventional Doppler methods rely on the Doppler shift and allow motion estimation just on the direction of the ultrasound beam. If we reformulate the equation (1.17) by taking into account both the angle in transmission θ_{T1} and the angle in reception θ_{R1}, the Doppler shift can be written as (Dunmire et al. 2000):

$$f_{d1} = \frac{|V|\cos(\theta_{T1} - \alpha) + |V|\cos(\theta_{R1} - \alpha)}{c} \cdot f_c \tag{2.5}$$

where α represents the moving angle of the blood scatterer.

As indicated in (Jensen et al. 2016a), using the trigonometric relation, $\cos(A - B) = \cos A \cos B + \sin A \sin B$, the equation (2.5) can be reformulated as:

$$\begin{aligned} f_{d1} &= \frac{|V|cos\theta_{T1}cos\alpha + |V|\sin\theta_{T1}\sin\alpha + |V|cos\theta_{R1}cos\alpha + |V|\sin\theta_{R1}\sin\alpha}{c} \cdot f_c \\ &= \frac{|V|cos\alpha(cos\theta_{T1} + cos\theta_{R1}) + |V|\sin\alpha(\sin\theta_{T1} + \sin\theta_{R1})}{c} \cdot f_c \\ &= \frac{V_z(cos\theta_{T1} + cos\theta_{R1}) + V_x(\sin\theta_{T1} + \sin\theta_{R1})}{c} \cdot f_c \end{aligned} \tag{2.6}$$

If we consider just equation (2.6) to solve for V_x and V_z , we have to deal with an undetermined system. By using a different angle in receive (θ_{R2}), we can introduce another equation (2.7) and the two unknowns can be calculated.

$$f_{d2} = \frac{V_z(cos\theta_{T1} + cos\theta_{R2}) + V_x(\sin\theta_{T1} + \sin\theta_{R2})}{c} \cdot f_c \quad (2.7)$$

Thus, the Cross-beam Doppler method allows estimating the lateral component of the velocity, in addition to the axial one (R. Steel & Fish 2002).

Still, this method is very sensitive to the accuracy of the two velocity measurements. In order to cope with this limitation, an overdetermined system can be employed by using multiple transmit-receive angle pairs (Fox 1978),(Overbeck et al. 1992).

2.3.2. Speckle tracking

The term "speckle" is used for describing the random granular pattern of an image. Speckles result from the interaction of the transmit beam with scatterers having a smaller wavelength than the transmit waveform. The interference of multiple beam–scatterer interactions provides the speckle pattern in the B-Mode ultrasound image, whose brightness is given by the echogenicity of the scatterers.

The speckles can be tracked from one frame to another to determine the motion. When the motion is tracked from speckles emerging naturally from blood, this technique is called *speckle tracking*, while when contrast agents are used for increasing the intensity of the speckles, this technique can be called *echographic particle image velocimetry (echo PIV)* (Jensen et al. 2016a). Inspired by optical techniques, speckle tracking was firstly introduced in ultrasound by Trahey et al. in the late 80s (Trahey et al. 1987). More than one decade later, echo PIV was validated for estimating blood velocity fields (Kim et al. 2004). Speckle tracking can be applied either on RF data, either on B-mode images.

Over the last years, many approaches have been proposed to estimate the motion of speckles. They can mainly be classified as block matching approaches and differential optical flow methods.

2.3.2.1. Block matching approaches

The general principle of block matching is to divide two adjacent frames into blocks (also referred as windows) and to define a search area into the previous frame. A specific block of the current frame is compared with other blocks within the search area of the previous frame (Fig. 24).

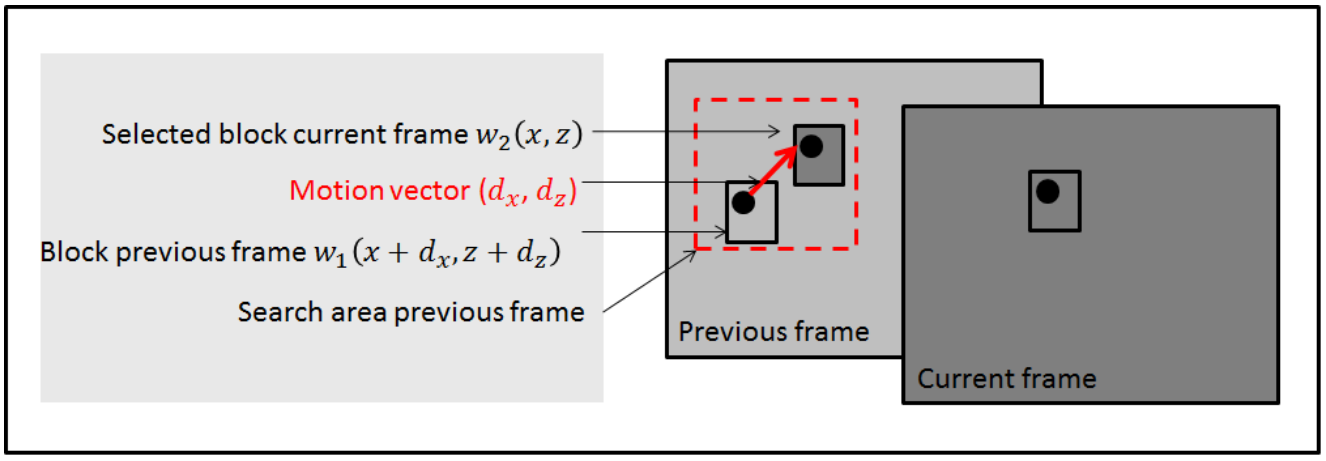

Fig. 24. General principle block matching: A specific block from the current frame is compared with other blocks within the search area of the previous frame. The best match gives the motion vector.

The best match indicates the motion of the selected block between the two frames. For finding the best match, several comparison criteria have been proposed such as mean absolute differences (MAD), mean square differences (MSD) and normalized cross-correlation. Cross-correlation is one of the most used criteria in ultrasound and it can be calculated both in spatial and in frequency domain. As shown in equation (2.8) the spatial cross-correlation is calculated directly using the spatial windows (w_1, w_2) belonging to successive frames (F_1, F_2):

$$r(d_x, d_z) = \frac{\sum_x \sum_z [w_1(x+d_x, z+d_z) - \overline{w_1}] \cdot [w_2(x,z) - \overline{w_2}]}{\sqrt{\sum_x \sum_z [w_1(x+d_x, z+d_z) - \overline{w_1}]^2 \cdot \sum_x \sum_z [w_2(x,z) - \overline{w_2}]^2}} \quad (2.8)$$

where (x, z) are the pixel coordinates of the selected windows and (d_x, d_z) is the motion vector.

On the other hand, the frequency cross-correlation requires the Fourier transformation (F) of the selected blocks. If $W_1 = F(w_1)$ and $W_2 = F(w_2)$, the cross-power spectrum (R) can be calculated as shown in (2.9). The normalized cross-correlation is obtained by taking the inverse Fourier transform (F^{-1}) of the cross-power spectrum (2.10). The displacement is given by the location of the cross-correlation peak.

$$R = \frac{W_1 W_2^*}{|W_1 W_2^*|} \quad (2.9)$$

where * stands from the complex conjugate.

$$r = F^{-1}\left(\frac{W_1 W_2^*}{|W_1 W_2^*|}\right) \quad (2.10)$$

Being a block matching technique, phase correlation does not allow estimating a motion inferior to the pixel size. A subpixel precision can be obtained by fitting the maximum peak of the normalized cross-correlation function to a paraboloid or Gaussian function (Céspedes et al. 1995). An illustration of the overall process of the phase correlation for two B-Mode frames is provided in Fig. 25.

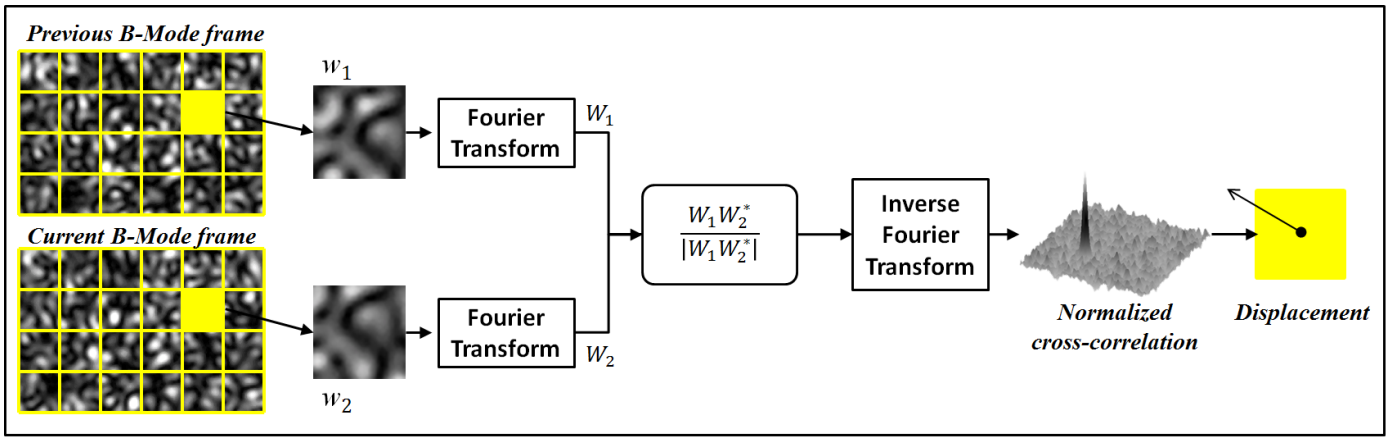

Fig. 25. Phase correlation: the windows belonging to subsequent frames are Fourier transformed for calculating the cross-power spectrum. Then, the inverse Fourier transform of the result is computed for obtaining the normalized cross-correlation, whose peak position gives the displacement [Retrieved from (Garcia et al. 2018)**].**

2.3.2.2. Differential optical flow approaches

While block matching is normally better adapted for tracking large motion, differential optical flow methods provide the advantage of motion estimation at subpixel accuracy. These methods rely on the assumption that the brightness from one frame to another does not change in time, as expressed in (2.11) (Barron et al. 1994):

$$I(x,z,t) = I(x+d_x, z+d_z, t+d_t) \tag{2.11}$$

where $I(x,z,t)$ is the intensity of a region of interest (ROI) centered in (x,z) at the time instance t and $I(x+d_x, z+d_z, t+d_t)$ is the intensity of a ROI centered in $(x+d_x, z+d_z)$ at the time instance $t+d_t$.

Under the assumption of small motion between two subsequent frames, the right side term of (2.11) can be approximated using Taylor series:

$$I(x+d_x, z+d_z, t+d_t) = I(x,z,t) + \frac{\partial I}{\partial x}d_x + \frac{\partial I}{\partial z}d_z + \frac{\partial I}{\partial t}d_t \tag{2.12}$$

where the higher order terms of the series were neglected.

From (2.11) and (2.12), we can write the optical flow equation:

$$\frac{\partial I}{\partial x}d_x + \frac{\partial I}{\partial z}d_z + \frac{\partial I}{\partial t}d_t = 0 \tag{2.13}$$

If we now divide (2.13) by d_t and we consider the velocity components in the lateral (x) and the axial direction (z) as $V_x = d_x/d_t$, and $V_z = d_x/d_t$, equation (2.13) becomes:

$$\frac{\partial I}{\partial x}V_x + \frac{\partial I}{\partial z}V_z + \frac{\partial I}{\partial t} = 0 \quad (2.14)$$

In order to solve this equation with two unknowns, an additional constraint needs to be introduced. A first approach was proposed by (Horn & Schunck 1981) and it imposes smoothness constraint on velocity changes over all image. It can be therefore classified as a global method. The disadvantage of this approach is that is sensitive to noise and it may lead to over-smoothing. To overcome these limitations, (Lucas & Kanade 1981) introduced a local method, based on the assumption of constant velocity over a region of interest. Such an approach was used by (Sühling et al. 2005) for the analysis of the ventricular wall motion from dynamic B-Mode images. However, optical flow methods are sensitive to intensity variations that may occur for large displacements between the frames (likely to occur especially in conventional ultrasound). On the other hand, tissue Doppler imaging is less sensitive to intensity variations, but it allows velocity estimation just along the axial direction. For this reason, several approaches combining the two modalities have been proposed in echocardiography (Tavakoli et al. 2014), (Poree et al. 2018).

2.4. 3D HIGH-FRAME RATE IMAGING

The emergence of high-frame rate ultrasound is particularly promising in 3D imaging where the conventional temporal resolution is highly limited. For instance, the time needed for a two-way beam trajectory considering a volume depth of 15 cm is 194 μs. If we want to reconstruct a 32 by 32 lines volume, the number of transmissions have to be increased 1024 times which results in a total time of approximatively 0.2 s. This gives a frame rate of just 5 Hz. However, reconstructing just 32 lines /plane is considerably less than the number of lines used normally in conventional 2D echocardiography. Using the same settings per plane as in 2D would significantly reduce the frame rate to less than 1 frame/s, which is unacceptable in cardiac imaging.

The temporal resolution gain achieved by decreasing the line density and field of view would definitely not be an optimal solution since the frame rate would still be insufficient for a fine quantification of the rapid cardiac phases. As a natural consequence, the high-frame rate methods described in section 2.2 were extended in the past years to 3D imaging. For instance, MLA was successfully applied to 3D and a frame rate of 8 Hz at 15 cm depth was possible using almost 5000 scan lines and an eight to one parallel processing (von Ramm et al. 1991). This method is implemented on most commercial scanners whose 3D frame rate can attain up to 10-20 Hz if additional parallel processing is employed. But more parallel processing involves wider transmit beams which affect the lateral resolution. Alternative methods have been proposed to overcome this limitation. One of these approaches was 3D sparse SA and it was introduced by Lockwood et al. almost one decade later. Using this method volumetric images were obtained by mechanically rocking a phased array (Lockwood et al. 1998). Important contributions in 3D SA approaches based on 1D array were also made by Jensen's team. For instance, (Nikolov & Jensen 2000) proposed combining the sparse SA with an approach based on treating focal points as virtual sources for increasing the resolution. The same group demonstrated the feasibility of SA when applied to 2D arrays (Nikolov & Jensen 2003). SA proved to offer better contrast, resolution, and SNR than MLA in a phased–array study based on both simulations and phantom measurements (Rasmussen & Jensen 2014). However,

in this paper, the frame rate was fixed to 20 Hz which is the usual frame rates obtained in MLA for achieving a fair comparison. Increasing the frame rate would require reducing the number of virtual sources placed behind the aperture of the transducer. Reducing the number of virtual sources would indeed reduce the resolution, contrast, and SNR.

Sparse synthetic aperture approaches at much higher temporal resolution (up to 3000 volumes/s) were investigated by other groups. (Provost et al. 2014) proposed the 3D implementation of PW/DW imaging emitted from virtual sources placed behind the transducer. Compounding was applied to B-Mode 3D images in order to find the optimal compromise between good quality and frame rate depending on the application. Additionally, this study showed the potential of 3D ultrafast DW imaging for the assessment of heart anatomy, ejection fraction, quantification of blood flow and cardiac displacements. Since compounding was not used for motion analysis, a limitation of this study is the poor energy transmitted through tissue especially for applications when a large field of view and high penetration depth is required.

Multi-line transmit could cope with this inconvenient, since multiple beams can be focalized at deep tissue structures. In a simulation study, (Tong, Ortega, et al. 2013) showed the feasibility of extending this method in 3D. The 2D findings regarding the efficiency of using a Tukey apodization (α=0.5) for cross-talk suppression were also confirmed in 3D. Additionally, using a 2D array allowed testing different transmission patterns for finding a better separation of the beams that could result in less interference. This study was continued by (Ortega et al. 2016), who investigated the optimal MLT-MLA set-up in both simulations and phantom experiments. However, in order to avoid the complexity of approximating superposed waveforms with a tristate pulser, the phantom acquisitions were performed by generating synthetically MLT images. That was done by transmitting independently single focused beams as in conventional ultrasound and summing them up prior to beamforming. The same difficulty was faced by other 3D MLT studies focused on cross-talk suppression. The Minimum Variance (MV) beamforming proposed by (Rabinovich et al. 2015), was also validated only in simulations and synthetic implementations. The 2MLT scans used to image a healthy heart were obtained by averaging data from each two transmit lines. Although a promising gain was achieved when 2MLT was combined with 4MLA, the cross-talk reduction was less efficient compared with Tukey apodization method. Also, MV showed higher variance and lower contrast but higher lateral resolution compared to the tapered apodization results. A competitive cross-talk suppression method proposed by (Denarie et al. 2013) suggested aligning the simultaneous beams along the transverse diagonal of the transducer. Even if a realistic analysis was made by measuring the pressure field of a transducer in water, the MLT investigation was limited to synthetic data.

The current 3D MLT studies showed the potential of this method in preserving a good image quality even for high depths and large field of views. In the same time, up to 16 fold gain in temporal resolution was obtained. Based on these findings one could affirm that this technique is a good candidate for cardiac applications. But to date, 3D MLT was investigated just in simulations and synthetic implementations. Synthetic implementations would not just lower the electronic noise compared to a real implementation but they would also not allow dynamic investigations, which is highly important for cardiac applications. Motion estimation methods have not been yet applied to experimental MLT 3D images. A real time implementation of this method together with the velocity assessment based on realistic images could confirm (or not) the potential of this method in 3D echocardiography.

2.5. VALIDATION OF HIGH FRAME RATE MODALITIES

In the past years, remarkable progress has been done in developing high frame rate ultrasound techniques and velocity estimation methods. Testing novel methods before introducing them in clinical practice is highly important for guarantying their efficiency. The validation of these new contributions is commonly done in simulations (in silico), on test objects (*in vitro*) or on humans/animals (*in vivo*).

Most of the studies evaluate their preliminary results based on simulations which offer significant advantages for both static and dynamic acquisitions.

First, using simulations allows minimizing the factors that could affect the performance of the method and provides a better understanding of its intrinsic limitations. For example, generating very few scatterers would facilitate the assessment of cross-talk artefacts in MLT since the image quality degradation as a result of other factors is minimized.

Second, this validation method offers a great flexibility in defining a specific medium and a specific motion pattern. Depending on the interest of the application, both a simple and complex medium and motion could be generated

Third, even for a very complex motion pattern, it is possible to have a reference which is highly important for evaluating the performances of velocity estimators.

Using simulations is therefore a very useful tool on the early step of the validation process, but this modality has some limitations. It may be time and resource consuming if a very complex medium has to be generated. Although multithreading solutions were proposed to deal with this constraint (Jensen 2014), another limitation is that it reproduces ideal conditions. For example, the most widely used ultrasound simulation software, Field II, estimates the received acoustic fields as a collection of point scattering centers by assuming linear propagation (Jensen 1996). Thus, artefacts that may appear in practice such as reverberations (Bertrand et al. 2016) and signal dropout (Perrino & Reeves 2008) are neglected. Although important progress has been made to achieve realistic cardiac synthetic sequences (Alessandrini et al. 2015), (Zhou et al. 2018), some problems that may appear in practice could not be easily predicted. Thus, simulations can be considered as a necessary but not sufficient step in the validation process.

Test objects can be used in order to overcome the limited realistic conditions provided by simulations. Constructed to mimic tissue properties, they offer the possibility of testing the performances of a technique using real-time acquisitions. The advantage of *in vitro* validation is allowing identifying the limitations of the method in realistic conditions and revealing the issues that may appear in an experimental set-up. Several test objects have been created in ultrasound for this purpose. The image quality assessment is usually performed on commercial phantoms (CIRS, Gammex) but customized phantoms can also be used. For example, the B-Mode contrast evaluation for the 3D DW implementation was performed on a heart-mimicking phantom (067, CIRS,VA) and the resolution on a customized gelatin phantom containing 25 metallic beads at different depths (Provost et al. 2014). Dynamic phantoms are highly important for testing the performance of ultrasound based flow estimation methods. Straight tubular phantoms with close acoustic properties to soft tissue, arterial wall and blood have already been proposed in the literature for Doppler ultrasound measurements (Zhou et al. 2017). Carotid artery bifurcation phantoms for both normal and stenosed lumen geometry have been developed for spectral Doppler investigations (Poepping et al. 2002). Recently, a spiral flow phantom has been constructed for assessment of multi directional flow(Yiu & Yu 2017).

The limitation of most of the current dynamics phantoms is that there are too simple for reproducing complex flows such as the ones in the left ventricle. Some velocity estimation methods could be promising when tested on simple phantoms but their performance could be drastically reduced if the complexity of the model is increased.

Evaluating a technique under complex conditions can be done by imaging humans or animals. The advantage of *in vivo* experiments is providing an ultimate tool to show the feasibility of an approach. It can lead to the translation from bench-to-bedside and it can bring significant contributions in diagnosis. But the direct translation from a simplistic *in vitro* model to animal or human experiments raises ethical questions. Moreover, acquiring *in vivo* data is not a straight-forward process. There is a complex legislative procedure that has to be followed and approved before passing to experiments. Thus, the process is time consuming and expensive.

Increasing the complexity of *in vitro* models could reveal certain limitations of a method before undergoing *in vivo* experiments. Testing the performances of high-frame rate techniques on such a model could optimize the validation process by preventing issues that may appear when imaging humans or animals. Additionally, it could assist in the decision of continuing or not a study with *in vivo* experiments. This could minimize the amount of unjustified translations from *in vitro* to *in vivo*.

2.6. CONCLUSION

In the first two sections of this chapter, we presented the most common high-frame rate techniques together with motion estimation methods used in 2D echocardiography. As described in section 2.2, each high frame rate method comes with its own compromise between the image quality and frame rate. While ECG gating can offer an improvement in temporal resolution, it is very sensitive to patients presenting heart rate variability, since one full image is formed during several heartbeats. MLA allows forming a high frame rate image during a single heartbeat, but the temporal resolution is increased in the detriment of the lateral resolution. Multi-Line- Transmission allows preserving a good lateral resolution, but it is prone to cross-talk artefacts. On the other hand, these artefacts do not appear when PW/DW imaging is used. Moreover, the temporal resolution is very high since one image can be obtained from a single transmission. However, using a single transmission may lead to unsatisfactory image quality. Coherent compounding can to be used to increase the contrast, resolution and SNR but with the degradation of the frame rate. Even if that may cause artefacts when imaging a dynamic medium, motion compensation (MoCo) can deal with this issue.

Among the methods presented above, promising results in phased array configurations at hundreds of frames/s were obtained using both MLT and DW compounded imaging. The image quality can be improved for both cases by compromising the frame rate. But ***for a given frame rate, how accepting a compromise or another would affect the image quality and the motion estimation methods? Is there an approach that is more appropriate than another for cardiac applications?*** Answering these questions is our ***first objective*** and it will be treated in Chapter 3.

As a result of the potential of high-frame rate methods in enabling new insights in cardiac function, but also as an answer to the current limitation of quantifying 3D structures using 2D methods, high frame rate

modalities have been extended to 3D. Using a wide beam in 3D echocardiography would result in spreading the energy even more than in 2D since an entire volume has to be insonified. MLT has the potential to offer good contrast, SNR and resolution at high volume depths by focusing the beam at the region of interest. Additionally, making use of the 2D geometry of the probe allows a better separation of the beams and a better suppression of cross-talk artefacts. The promising potential of this method has been shown by several authors, but all the investigations were limited to simulations or synthetic approaches due to the complexity required by a practical implementation. Moreover, the velocity estimation performance has not been yet evaluated on MLT 3D images. The attenuation, the noise, the heating issues, and the motion artefacts are just a few of many problems that could be revealed by a real time implementation. This leads to a set of questions that will formulate our ***second objective***: ***Would MLT still be a modality of choice in 3D echocardiography despite the possible problems that may appear in practice? Which are the limits in both static and dynamic acquisitions?*** These questions will be treated in Chapter 4.

Testing the potential and limitations of the 2D and 3D high-frame rate methods is a very important step for evaluating if they could be translated into clinical echocardiography. Even if preliminary analysis should be done in simulations, there is an important step between good results in silico and good results *in vivo*. *In vitro* analysis is often employed as an intermediate phase. The difficulty to extrapolate a technique from *in vitro* to *in vivo* is determined by the lack of complex phantoms. Currently, blood flow quantification methods are usually tested on simple tubular or bifurcation phantoms for assessing their performances on applications like carotid artery disease. But recent studies showed that analyzing complex flows such as the vortices formed in left ventricle can provide new insights for cardiac diagnosis (Pedrizzetti et al. 2014). The validation of high frame rate methods on a complex flow phantom could facilitate the translation from *in vitro* to *in vivo* studies. ***But could a vortex phantom be a good candidate for quantifying complex flows using ultrasound high frame rate methods?*** Answering this question will be our ***third objective*** which will be treated in Chapter 5 of this thesis.

CHAPTER 3:

COMPARISON BETWEEN MULTI LINE TRANSMISSION AND DIVERGING WAVE IMAGING: MOTION ARTEFACTS AND THEIR EFFECT ON MOTION ESTIMATION

*Parts of this work was submitted to revision to: Emilia Badescu, Damien Garcia, Philippe Joos, Adeline Bernard, Lionel Augeul, René Ferrera, Magalie Viallon, Lorena Petrusca, Denis Friboulet, Hervé Liebgott, "Comparison between Multi Line Transmission and Diverging Wave Imaging: motion artefacts and their effect on motion estimation", *IEEE Trans. Ultrason. Ferroelectr. Freq.Control*, 2018

3.1. INTRODUCTION

The emergence of high frame rate ultrasound led to innovative quantitative tools in echocardiography, such as the assessment of the electromechanical properties of the heart (Provost et al. 2010), solving the incompatibility between imaging and quantification for blood flow characterization (Nikolov & Jensen 2003a), (Papadacci et al. 2014b) or the evaluation of 2D vector flow dynamics within the same cardiac cycle (Faurie et al. 2017) .

As discussed in Chapter 2, among the high-frame rate techniques, an important gain in temporal resolution became possible with the advent of unfocused and multiple focused beams approaches. The unfocused beams approaches use a subaperture to simulate a virtual point located behind the probe. While the first investigations of this approach were referred to as synthetic aperture multi-element techniques (Karaman et al. 1995), later contributions are known as plane (PW) (Sandrin et al. 1999) or diverging (DW) (Hasegawa & Kanai 2011) waves techniques. The alternative focused high-frame rate method is multi-line transmission (MLT). Initially proposed by (Mallart & Fink 1992), this method has been further investigated by KU Leuven group.

This latter group showed through several studies, based on both simulations (Tong, Gao, et al. 2013) and *in vivo* acquisitions (Tong et al. 2014), the potential of MLT in achieving high frame rates while mostly preserving image quality. Additionally, it has been shown that MLT can be efficiently combined with MLA to further improve the temporal resolution. Although the increase in temporal resolution does not compromise to a great extend the contrast, resolution, and SNR (signal-to-noise ratio) compared to SLT, it does compromise the amount of image artefacts as a result of simultaneous transmissions. Due to its predisposition to cross-talk artefacts, this beamforming method has not received yet as much attention as DW especially in motion estimation. For instance, tissue Doppler imaging (TDI) has been just recently applied to MLT images (Tong et al. 2016).

Alternative ultrafast methods using plane or diverging waves allow one to obtain an entire image with just a single transmission. Since the time needed for insonifying a full medium by using plane/diverging wave imaging corresponds to the time needed for insonifying *n* lines of the image with MLT and one single line with SLT, the frame rate is considerably increased. Image quality, however, is significantly compromised in terms of both resolution and contrast (Sandrin et al. 1999). Coherent compounding has thus been proposed to cope with this limitation (Karaman et al. 1995), (Montaldo et al. 2009), (Papadacci et al. 2014a). By coherently summing multiple images obtained at different PW/DW obliquities, image quality can be improved substantially. Since this approach may fail if the medium is characterized by a strong motion from one transmission to another, motion compensation (MoCo) must be used in the presence of high-velocity tissues to ensure adequate coherent compounding. MoCo was first introduced in synthetic aperture imaging for axial motion compensation (Trahey & Nock 1992) and later extended to 2D motion compensation approaches (Denarie et al. 2013). The potential of MoCo has been shown *in vivo* for abdominal imaging using synthetic aperture approaches (Gammelmark & Jensen 2014) and for cardiac imaging using DW approaches (Poree et al. 2016).

In this study, we proposed a comparison between two promising ultrafast methods (DW imaging with

MoCo and MLT imaging) in terms of image quality, motion artefacts and their effects on motion estimation using speckle tracking and TDI.

3.2. METHODS

3.2.1. Acquisition set-up

The data were acquired with a Vantage 256 research scanner (Verasonics Inc., Redmond, WA) driving a P4-2 phased array probe having 64 elements and a central frequency of 2.5 MHz. The pulse repetition frequency (PRF) was set to 4500, the sector size to 90º and the maximum range to 13 cm.

As a general principle, the transmission waveform was adapted in order to obtain the same total emitted power for both MLT and DW. For MLT, we used an excitation signal which was on during 1/5 of the half cycle and off for the rest of the time. We computed the transmission matrix by overlapping the excitation signals corresponding to all elements and to all simultaneous transmissions. Then, we compared the resulting signals with a threshold in order to obtain a tristate pulse (-1/ 0/ +1) as required by the Vantage system. The transmitted signal and consequently the transmitted power for MLT were different for each transmission and for each element. However, the total transmitted power calculated over all elements and over all transmissions did not change considerably when the frame rate was varied. That was because, for a low frame rate, the low power resulting from a reduced superposition of waveforms in a single transmit-event was compensated by summing the power over many transmissions. On the other hand, for a high frame rate, the high power resulting from a high superposition of waveforms in a single transmit-event was compensated by summing the power over fewer transmissions. But for DW, the total transmitted power increased with the number of transmissions, since the power in a single event transmission was constant. Therefore, the total transmitted power with MLT did not vary as much with the decrease of the frame rate as it did for DW. We compensated for that by modifying the transmit waveforms when using a reduced number of steering angles for DW. Details about how the excitation signals were changed for DW and about how the power was balanced for static/ speckle tracking (ST) acquisitions on one hand and for Doppler acquisitions, on the other hand are provided in sections 3.2.2 and 3.2.3.

The simulated acoustic pressure field obtained with the two methods for one transmission is represented in Fig. 26.

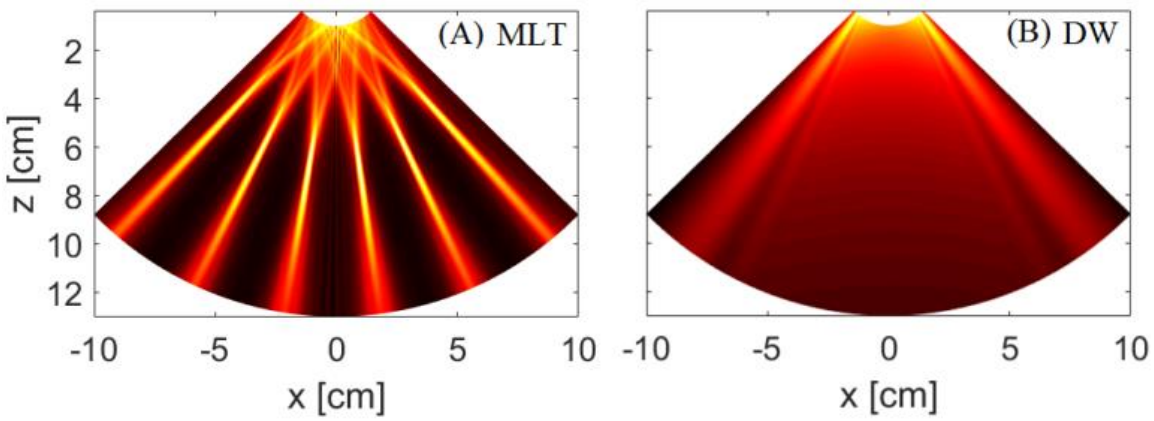

Fig. 26. Normalized Root Mean Square (RMS) pressure fields obtained for one transmission with 6 MLT (A) and with DW (B). Results obtained using an in-house simulation tool

3.2.2. Acquisition settings for image quality assessment and speckle tracking motion estimator

The same frame rates were used for static conditions and speckle tracking. More specifically, the tested frame rates were set to 225, 450 and 900 by reducing the number of transmission events per reconstructed image from 20 to 10 and 5. An overview of the transmission settings applied to DW and MLT allowing to obtain the same frame rates is presented in Table I.

The total power of the two high frame-rate methods was balanced using equation (3.1).

$$P_{MLT/DW}^{B/ST} = \sum_{t=1}^{N_{tx}} \sum_{e=1}^{N_e} \frac{1}{N_s} \sum_{s=1}^{N_s} |wf_{set}|^2 \tag{3.1}$$

where wf_{set} represents one sample s of the waveform wf applied to the element e of the transducer for the transmission t; N_s is the number of samples of the waveform wf, N_e is the number of elements of the transducer and N_{tx} is the total number of transmissions needed to form an image (MLT) or a compound image (DW). This equation holds for both B-mode and ST acquisitions (notation: B/ST).

Once the power was calculated for each frame rate in MLT, the duty cycle (given by the ratio between the pulse active time and the total period of the pulse) of the transmitted DW waveform was modified to match the same total power for each of the 3 settings. Thus, the duration of the transmitted signals did not change from DW to MLT, the only parameter changing being the duty cycle. More specifically, this duration corresponded to a half cycle of the transmitted square waveform centered at 2.5 Mhz. Given that the excitation signal was generated by a clock of 250 MHz, half a cycle at 2.5 MHz corresponded to 50 cycles.

3.2.2.1. Description of diverging waves sequence and motion compensation technique

The diverging waves were generated using virtual sources placed behind the transducer as shown in Fig. 27 A. The coordinates of the virtual sources (x_v, z_v) can be written depending on the tilt angles (θ), the angular width (β) and the aperture of the transducer (a) (Poree et al. 2016):

$$\tan\left(\theta \pm \frac{\beta}{2}\right) = \frac{\pm\frac{a}{2} + x_v}{-z_v} \tag{3.2}$$

The maximum tilt angle (θ_{max}) was varied with the number of transmissions. Therefore for the lowest frame rate of 225, we used the range of [-8.6º, 8.6º], for the frame rate of 450, we used the range of [-4.3º, 4.3º], and for the highest frame rate of 900, the maximum tilt angle was ±2.15º. The resulting lateral (x) positions ranges of the virtual sources obtained using these tilt angle were: [-2.98, 2.98] mm for 20 DW, [-1.51, 1.51] mm for 10 DW and [-0.75, 0.75] mm for 5 DW (Fig. 27 B). Since small maximum tilt angles were employed for all 3 settings, the axial (z) position of the virtual sources slightly changed from -10.08 mm (tilt angles up to +/- 4.3º) to -9.6 mm (tilt angle +/- 8.6º). Fixing the maximum value of the angular range to a higher value would have resulted in a higher angular pitch and therefore in a better lateral resolution. However, using a constant angular pitch ensures avoiding transmit grating lobes.

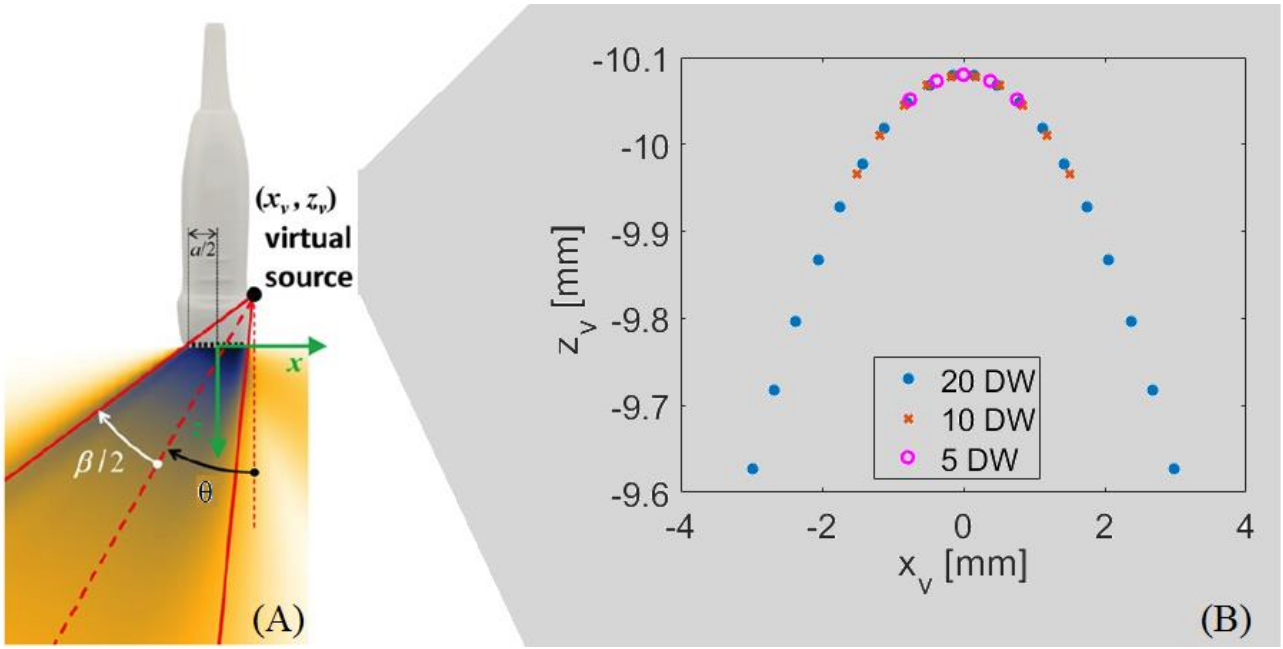

Fig. 27. (A) The origin of the DW having the angular width β and the tilt angle θ is the virtual source(x_v, z_v) in the coordinate system (x, z). Retrieved from (Poree et al. 2016)**. (B) Position of the virtual sources for different number of transmissions**

As previously mentioned in chapter 2, the images obtained using different tilt angles can be coherently compounded for image quality enhancement. However, the result can be significantly affected if the

scatterers move between the acquisitions at different angles. The resulting artefacts become more visible as the velocity of the scatterers increases (Wang Jing & Lu Jian-yu 2007) (Denarie et al. 2013). This is the case for the velocities in the myocardium which can reach up to 20 cm/s. In this study we used a motion compensation method proposed by (Poree et al. 2016) to ensure proper synthetic focusing. Since in phased arrays, the angular resolution is much poorer compared to the radial resolution, motion artefacts are less affected by the inadequate angular misalignment of the compounded images. Thus, this method only compensates for the radial motion. The motion between successive transmits (assumed to be time-invariant) was detected by autocorrelating the N_{TX} slow time received IQ signals. But the autocorrelation was not applied directly on the data obtained from successive transmits resulted from linearly spaced tilt angles. That was because as the angles are linearly increasing, the position of the side lobes rotates clockwise. Even in static conditions, MoCo detects the modification of the side lobes position as a movement. When the tilt angles are linearly increasing, the autocorrelation rephases the side lobes to the same position. To avoid the coherent summation of the side lobes, the order of tilt angles could be changed. One approach, proposed by (Denarie et al. 2013), would be arranging the angles using the alternate sequence (1, N_{TX}, 2, N_{TX}-1…..). Although this method allows the incoherent summation of the side lobes, it reduces the correlation between the IQ signals, due to the difference in transmit diffraction patterns. Therefore this technique increases the variance of the estimator. An alternative approach that allows not only reducing the side lobes but also a smaller variance of the motion estimator is arranging the tilt angles in a triangular sequence: (1, 3, .., $N_{TX}/2$ -1, $N_{TX}/2$, .., 4, 2) (Poree et al. 2016). Two one-lag-autocorrelations (R_1, R_2) along the slow time axis are then computed: one for the IQ signals corresponding with the ascending part and the other for the IQ signals corresponding to the descending part of the triangular sequence. The expressions of the two discrete autocorrelations are provided in the following equation:

$$R_1(\theta,r) = \sum_{n=1}^{\frac{N_{TX}}{2}-1} \frac{IQ_n \cdot \overline{IQ_{n+1}}}{|IQ_n \cdot \overline{IQ_{n+1}}|} \text{ and } R_2(\theta,r) = \sum_{n=\frac{N_{TX}}{2}}^{N_{TX}} \frac{IQ_n \cdot \overline{IQ_{n+1}}}{|IQ_n \cdot \overline{IQ_{n+1}}|} \quad (3.3)$$

where N_{TX} is an even number of tilt angles/ transmissions and IQ_n is the n^{th} IQ signal (out of N_{TX}) determined at the polar coordinates (θ, r).

The phase angle (ϕ_{MoCo}), giving the phase delays due to the motion was calculated using the product of the two autocorrelations (R_1, R_2). As shown in equation (3.4), a ½ factor is needed to recover the phase angle, which decreases the maximum detectable velocity by a factor 2, compared to the Nyquist velocity.

$$\phi_{MoCo}(\theta,r) = \frac{1}{2} arg\{R_1 R_2\} \quad (3.4)$$

where (θ, r) are the polar coordinates and arg represents the argument of the complex R_1R_2.

The triangular sequence together with the autocorrelation product helped in reducing the side lobes

effect.

The image quality and motion estimation were evaluated on compounded MoCo B-Mode images using the triangular sequence.

3.2.2.2. Multi-Line Transmit

For achieving equivalent temporal resolution, we progressively increased the number of simultaneous transmissions from 3 to 6 and 12. The focal point was set to 7 cm. No apodization was used in transmit or receive. Image reconstruction was performed using 5 MLA, meaning that 5 image lines centered in the focal point of the transmitted beam were reconstructed in parallel.

TABLE I. TRANSMISSION SETTINGS MLT VS DW

Frame Rate	Number of transmit events	MLT: number of simultaneous transmissions	DW: number of tilt angles
225	20	3	20
450	10	6	10
900	5	12	5

3.2.3. Acquisition settings for Tissue Doppler Imaging

We fixed constant the two parameters having a high impact on the estimator for both MLT and DW: the PRF and the packet size. Since for DW, the compounding was computed in parallel with the Doppler estimator, the packet size corresponds to the number of tilt angles. Given the PRF of 4500 and a packet size of 8, the resulting Doppler frame rate is 562 Hz. To study the effect of cross-talk in MLT, we kept the same simultaneous focused transmissions configurations as for speckle tracking: 12 MLT, 6 MLT, and 3 MLT. However, since we needed to steer 8 times in the same place for each transmission, the Doppler frame rate was drastically decreased compared to DW from 112 to 56 and 28 Hz. An overview of these parameters is presented in Table II.

TABLE II. DTI TRANSMISSION SETTINGS MLT VS DW

Packet size	MLT		DW	
	Number of simultaneous transmissions	Frame Rate	Number of tilt angles	Frame Rate
8	3	28	8	562
8	6	56	8	562
8	12	112	8	562

For Doppler acquisitions, the total power was calculated and balanced using equation (3.5) for MLT and equation (3.6) for DW:

$$P_{MLT}^{TDI} = PS \cdot \sum_{t=1}^{N_{tx}} \sum_{e=1}^{N_e} \frac{1}{N_s} \sum_{s=1}^{N_s} |wf_{set}|^2 \tag{3.5}$$

$$P_{DW}^{TDI} = PS \cdot \sum_{e=1}^{N_e} \frac{1}{N_s} \sum_{s=1}^{N_s} |wf_{set}|^2 \tag{3.6}$$

where PS is the packet size. We found necessary to use the number of transmissions needed to form a full MLT image since a 2D autocorrelation was used for Doppler estimation. Therefore, the total power obtained with MLT was much higher than that obtained with DW using half-cycle waveforms. Adapting just the duty cycle was not enough to balance the two total powers. Thus, we needed to use longer waveforms for DW: between 1 and 1.5 cycles for TDI acquisitions, depending on the number of transmissions.

3.2.4. *In vitro* models

3.2.4.1. Image quality assessment on static phantoms

The image quality was first evaluated on a Gammex phantom using contrast and resolution metrics as proposed in (Liebgott et al. 2016). Therefore, we used as a metric the Contrast to Noise Ratio (CNR) defined as:

$$CNR = 20 \log_{10} \left(\frac{|\mu_{bck} - \mu_{cyst}|}{\sqrt{\sigma_{bck}^2 + \sigma_{cyst}^2}} \right) \tag{3.7}$$

where μ_{bck}, μ_{cyst} are the means and σ^2_{bck}, σ^2_{cyst} are the corresponding variances of the background and the cyst regions calculated for a B-Mode image.

We evaluated the contrast at 4 cm and 11 cm respectively for the 3 settings mentioned in Table I. Our dynamic range was 60 dB.

For the same acquisition settings, the resolution was evaluated at four different image depths (from 5 cm to 11 cm with a step of 2 cm) using full width at half maximum (FWHM).

3.2.4.2. Image quality assessment on dynamic phantoms

The image quality assessment in dynamic conditions was performed on a tissue mimicking rotating disk phantom made from agar (4%), silica (1%) and water. The disk was created to contain four inclusions for facilitating the contrast assessment (Fig. 32A). The CNR was computed using the mean of the four inclusions for each frame. The velocity of the disk was controlled by a step motor and adjusted to 9 different values from 50 º/s to 450 º/s, using a step of 50º.

For each velocity, the mean CNR for the 4 inclusions was averaged over 10 frames.

3.2.5. *In vivo* Models

First, we acquired our sequences on an open-chest pig. Transthoracic acquisitions were also attempted, but obtaining satisfying data was very challenging. The reason for that was the high attenuation as a result of the thick layer of the skin. Another challenge, which appeared due to cut section, was obtaining 4 chamber open-chest acquisitions. The cut section was not adequate to allow a good contact of the probe with the apex. For obtaining better transthoracic 4 chamber images, we used our sequences on a human subject. Therefore, our *in vivo* models were both animals and humans, depending on the desired view.

The acquisition sequences and settings were similar to those used for the *in vitro* data. The DW and MLT acquisition sequences were concatenated and the buffers of the Vantage 256 system were adapted to receive alternatively sets of DW and MLT frames. Thus, the comparison could be assessed at close cardiac phases within the same cardiac cycle. For B-mode images, an intermediate frame rate of 450 Hz was chosen for both DW and MLT (Table I, third row). Similarly, the intermediate settings provided in Table II (fourth row) were used for *in vivo* TDI acquisitions.

3.2.5.1. Animal subjects

The animal experiments were approved by the Animal Ethical Committee with agreement number A693830501. The only difference in the acquisition settings compared to *in vitro* data was the focal point for MLT which was placed at 4 cm, due to the available view.

The probe was placed as indicated in Fig. 28 for obtaining parasternal short axis views, examined for both B-mode images and tissue Doppler.

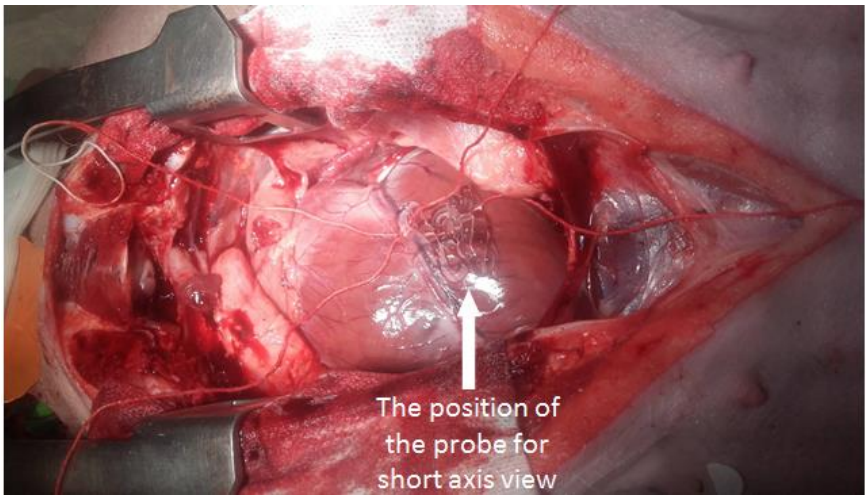

Fig. 28. Open-chest *in vivo* acquisitions: The probe was placed in the area indicated by the arrow for acquiring parasternal short axis views.

3.2.5.2. Human subjects

The probe was placed as shown in Fig. 29, for obtaining an apical 4 chamber view. The acquisition sequences and settings were similar to those used for the *in vitro* data, including the focal point which was kept at 7 cm. The image depth was set to 16 cm.

Fig. 29. Transthoracic *in vivo* acquisitions: The position of the probe for acquiring apical four chambers views

3.2.6. Motion estimation methods

The influence of the two ultrafast imaging strategies on motion estimation was tested using speckle tracking and tissue Doppler (TDI).

A block matching method was used based on the normalized cross-correlation in the Fourier domain (Hein & O'Brien 1993). The B-Mode images were divided into 32×32 windows. The speckle patterns were tracked with a window overlap of 50%. The pixel size was 0.28 mm in the radial direction and 0.3º in the cross-range direction. For achieving a subpixel precision parabolic peak fitting was applied for finding the maximum of the cross-correlation function. Since we used high frame rate imaging, it seemed legitimate to assume constant motion between successive frames. Therefore, to improve the robustness of the method we used an ensemble correlation over 15 frames. The frame lag was increased from 1 to 2 and 4 for the frame rates of 225, 450 and 900 since it is known that block matching is better adapted to extract displacements greater than one pixel. The speckle tracking parameters (window size, frame lag) were chosen to obtain good estimates when applied to DW images. Then, the same parameters were used for MLT images. Since the two high temporal resolution imaging methods (MLT and DW) were compared at the same frame rates and on images having the same pixel size and number of pixels, choosing the same parameters (frame lag and window size) should provide equivalent conditions for the two methods.

Doppler velocity was estimated using a 2D auto-correlator applied on the IQ data as proposed in (Kasai et al. 1985),(Loupas et al. 1995). By using this method, the phase shift was used to estimate the displacement. In order to preserve a high Doppler frame rate, TDI was applied to uncompounded DW images. With a PRF of 4500, the maximum velocity that we could detect with no aliasing was 69 cm/s with MLT and 35 cm/s for DW MoCO (equation (3.4)).

The accuracy of the estimates in a selected direction d was evaluated using the Normalized Root Square Error (NRSE) for each pixel i, given by:

$$NRSE_{di} = \frac{\left|V_{ref_{di}} - V_{estim_{di}}\right|}{\left|V_{ref_d}\right|_{max}} \tag{3.8}$$

where $V_{ref_{di}}$, $V_{estim_{di}}$ are the reference and the estimated velocity for a given pixel i and selected direction d (d=x for lateral; d=z for axial); $\left|V_{ref_d}\right|_{max}$ is the maximum of the absolute reference velocities over the entire image.

3.3. RESULTS

3.3.1. Image quality assessment on static phantoms

Fig. 30 shows the B-Mode images of the Gammex phantom obtained at different frame rates. The left column illustrates the results of using an MLT transmission whereas the right column corresponds to the images resulting from compounded DW. For facilitating the comparison, each row of Fig. 30, displays images acquired at different frame rates.

The contrast values (CNR) for a hypoechoic cyst at 4 cm is reported in Table III and for a cyst at 11 cm in Table IV.

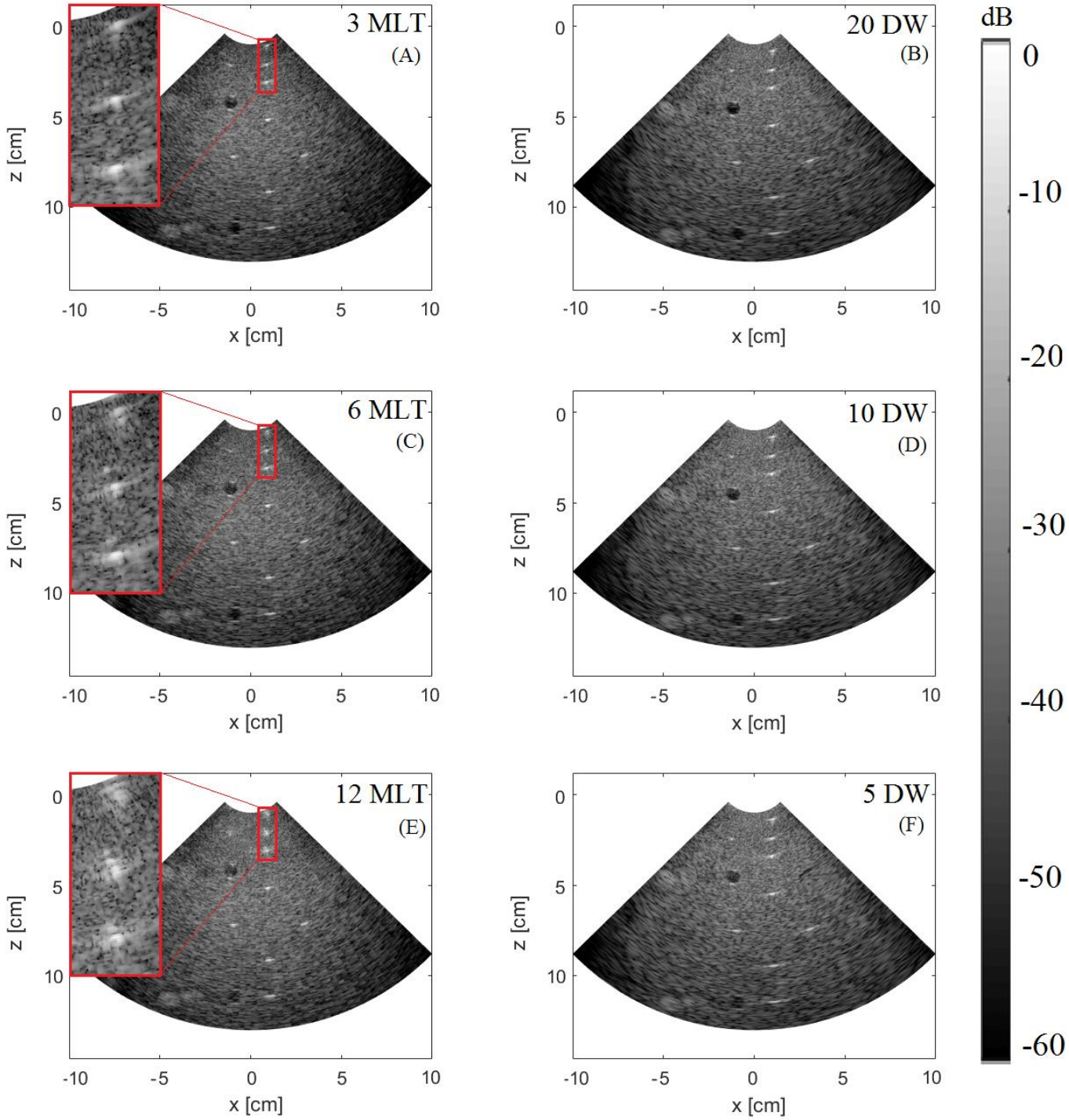

Fig. 30. Image quality for MLT (left column) and DW (right column) by using a frame rate of 225 Hz (A), (B), 450 Hz (C), (D), and 900 Hz (E), (F). A zoomed region (x=[0.4cm:1.4cm]; z=[0.8cm:3.5cm]) is provided in the red box for MLT (A, C, E) for a better visualization of artefacts next to the surface of the probe.

TABLE III. CNR VALUES FOR A CYST AT 4 CM

Frame rate/ Transmission Type	225	450	900
MLT	6.38 dB	5.66 dB	3.75 dB
DW	8.82 dB	7.54 dB	5.36 dB

TABLE IV. CNR VALUES FOR A CYST AT 11 CM

Frame rate/ Transmission Type	225	450	900
MLT	5.35 dB	4.46 dB	1.51 dB
DW	4.84 dB	3.53 dB	0.12 dB

The lateral resolution (FWHM) at 4 different image depths (5 cm, 7 cm, 9 cm, 11 cm) is illustrated in Fig. 31. Since the resolution did not change significantly from 5 to 10 or 20 DWs, we chose to show just one case for providing the resolution values. The same trend of lateral resolution saturation starting with a limited number of DWs was also reported in other studies (Zhang et al. 2016).

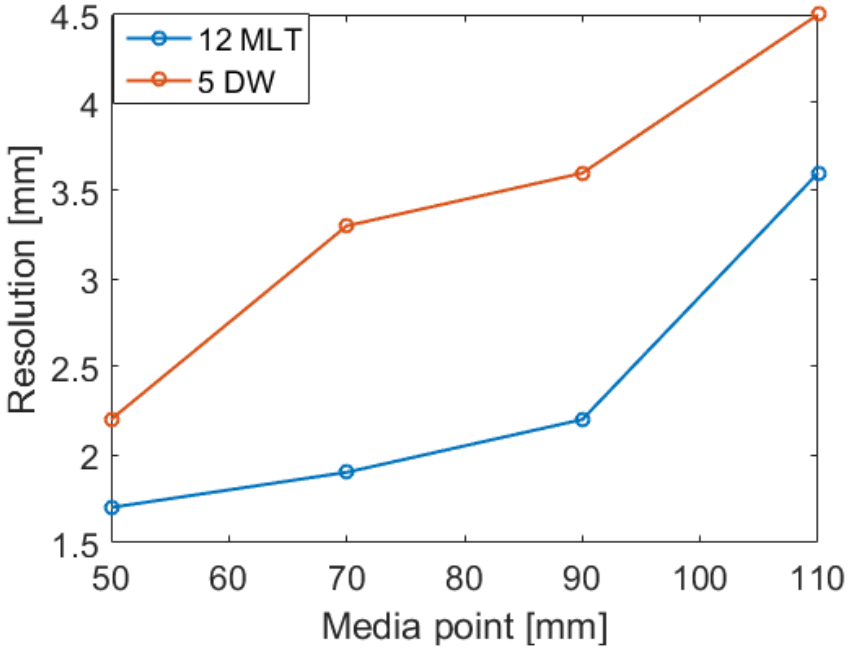

Fig. 31. Lateral resolution at different image depths for a frame rate of 900 Hz

3.3.2. Image quality assessment on the rotating disk phantom

In order to observe how the contrast is affected when the imaged medium is undergoing motion, we calculated the CNR for 9 different velocities of the disk. The results are illustrated in Fig. 32. For each velocity, we plotted the mean contrast over 10 frames and the corresponding standard deviation.

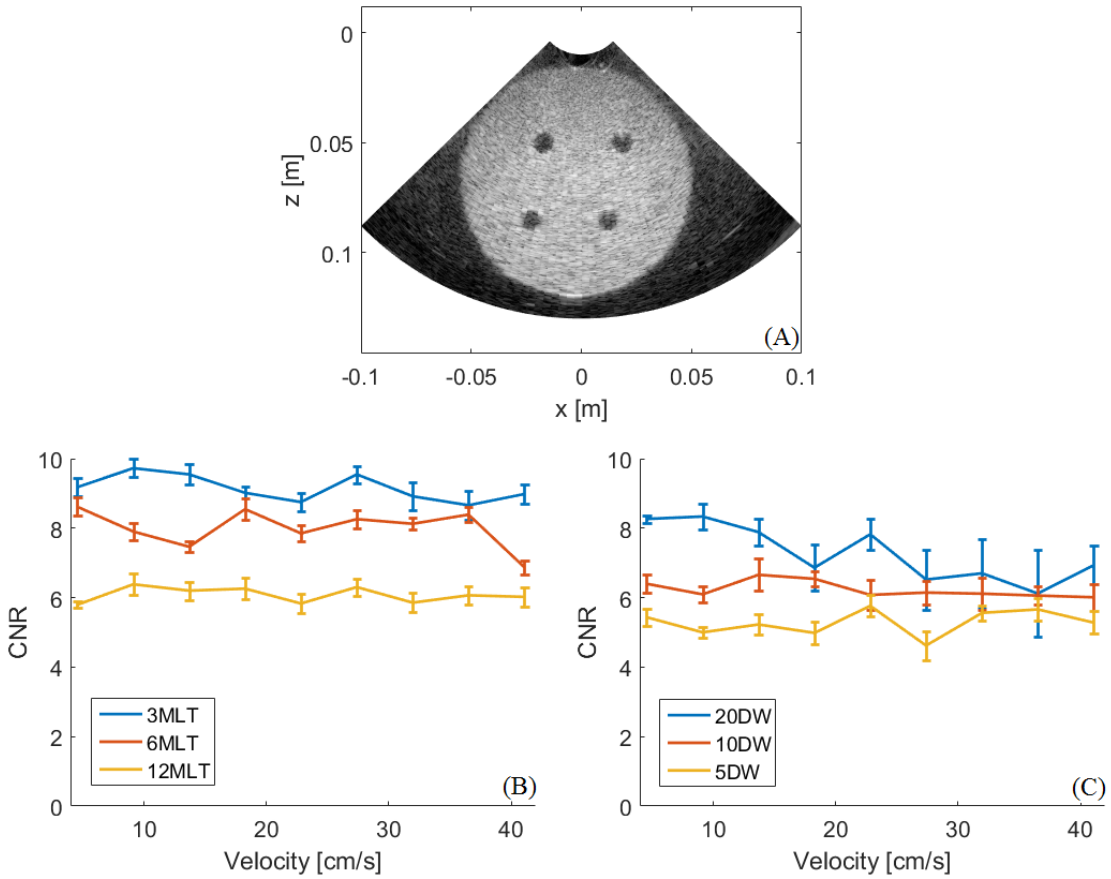

Fig. 32. CNR at different velocities of the disk calculated on the phantom showed in (A). Results for MLT (B) and DW (C) at a frame rate of 225 (blue), 450 (red) and 900 (yellow) Hz

3.3.3. Motion estimation accuracy

For analyzing the pixelwise ST errors we provide the color-coded results for the intermediate velocity of 250°/s and frame rate of 450 HZ, for both DW (Fig. 33) and MLT (Fig. 34). The reference velocity maps (A, D) are shown together with the estimated velocity maps (B, E) and with the NRSE errors (C, F). The results for all frame rates are represented using boxplots, containing the median of the NRSE: Fig. 35 shows the axial (in-range) error distribution while Fig. 36 shows the lateral (cross-range) error distribution. The median of the NRSE is represented in red while the lower and the upper box limits are the first and the third quartiles of the error. The results obtained with MLT (left) and DW (right) at different frame rates are illustrated: 225 Hz (A), (B), 450 Hz (C), (D), 900 Hz (E), (F). Below each set of boxplots, we show the differences in median (*Med*) and interquartile range (*IQR*) between MLT and DW. The IQR was calculated by subtracting the 25th percentile from the 75th percentile of the NRSE. In order to study if these differences are significant, we used a one-sample t-test to get the p-value for each difference.

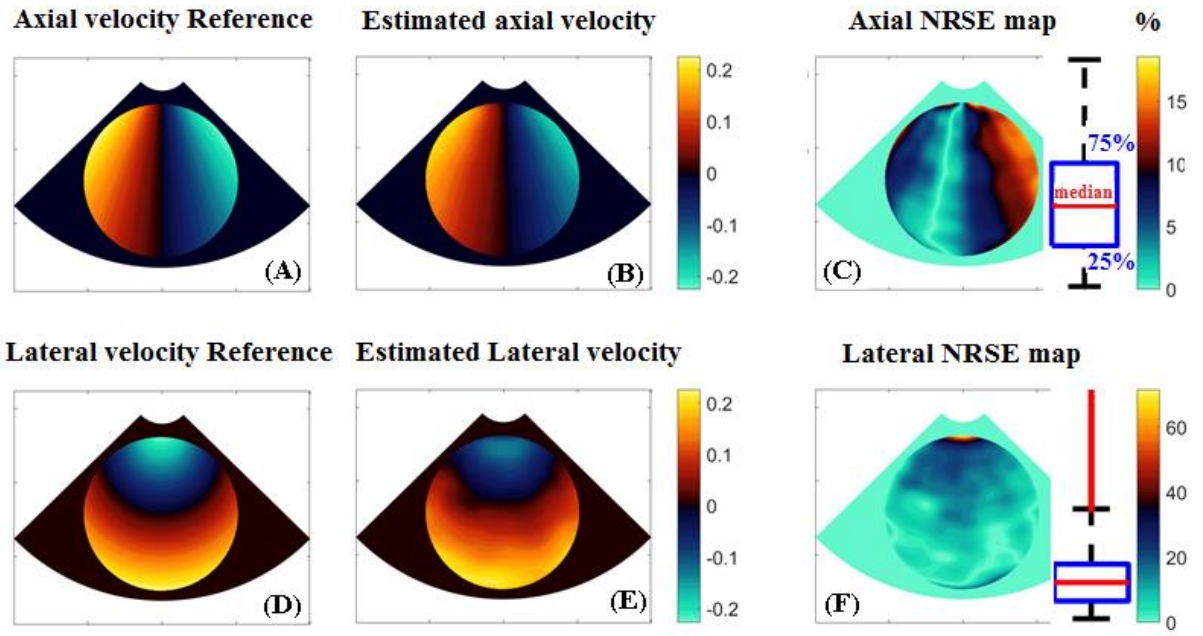

Fig. 33. From left to right: Axial and lateral reference velocity (A, D), estimated velocity (B, E) and NRSE (C, F) for 10 DW and a velocity of 250°/s

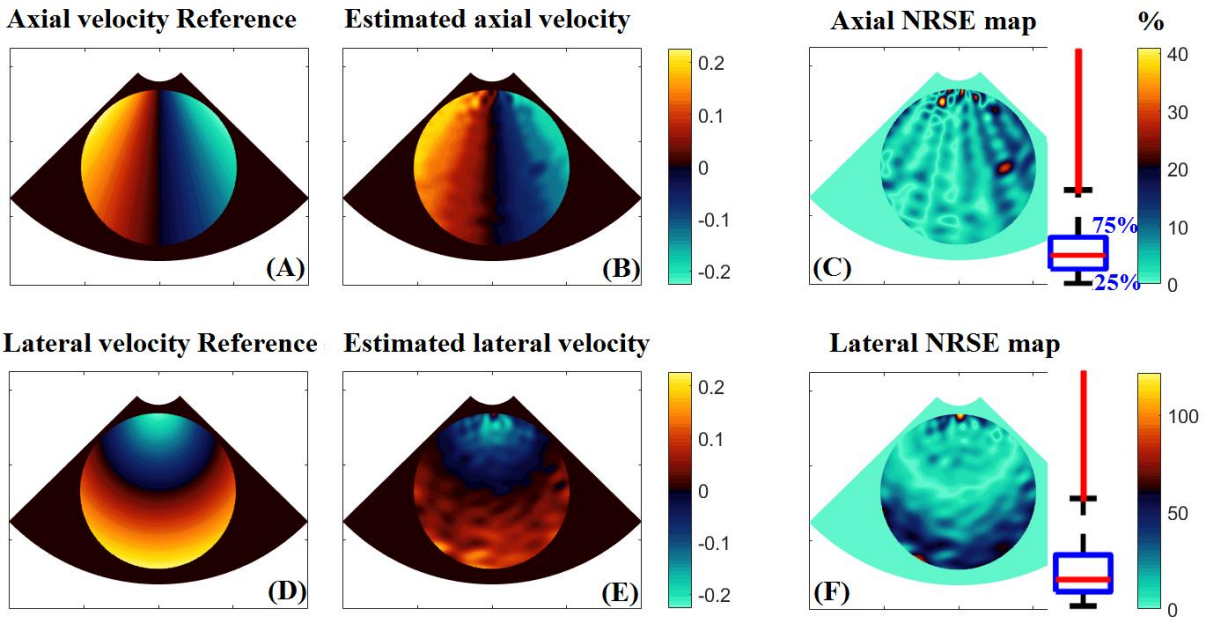

Fig. 34. From left to right: Axial and lateral reference velocity (A, D), estimated velocity (B, E) and NRSE (C, F) for 6 MLT and a velocity of 250°/s

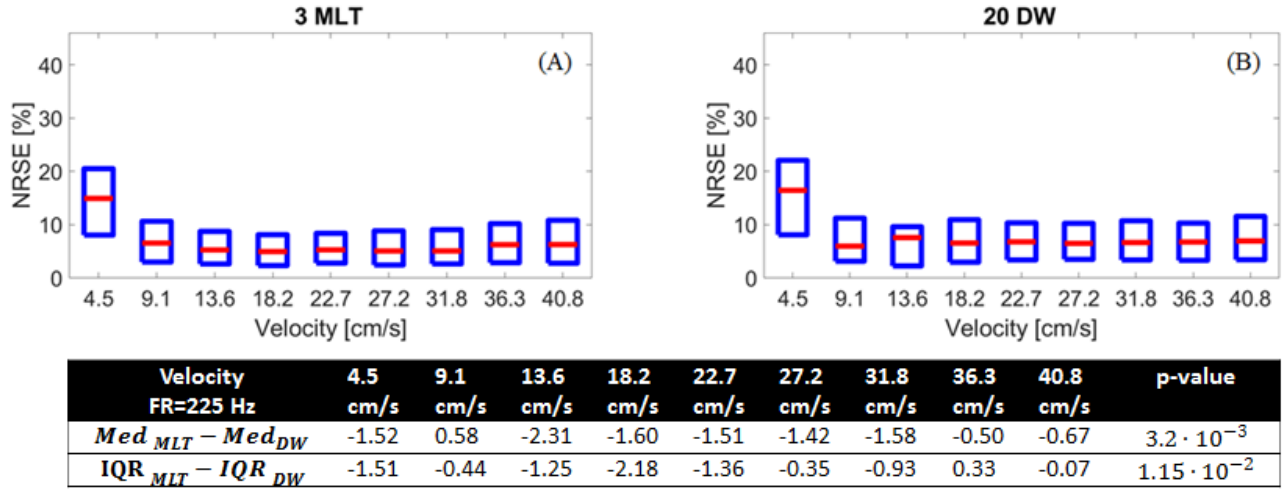

Velocity FR=225 Hz	4.5 cm/s	9.1 cm/s	13.6 cm/s	18.2 cm/s	22.7 cm/s	27.2 cm/s	31.8 cm/s	36.3 cm/s	40.8 cm/s	p-value
$Med_{MLT} - Med_{DW}$	-1.52	0.58	-2.31	-1.60	-1.51	-1.42	-1.58	-0.50	-0.67	$3.2 \cdot 10^{-3}$
$IQR_{MLT} - IQR_{DW}$	-1.51	-0.44	-1.25	-2.18	-1.36	-0.35	-0.93	0.33	-0.07	$1.15 \cdot 10^{-2}$

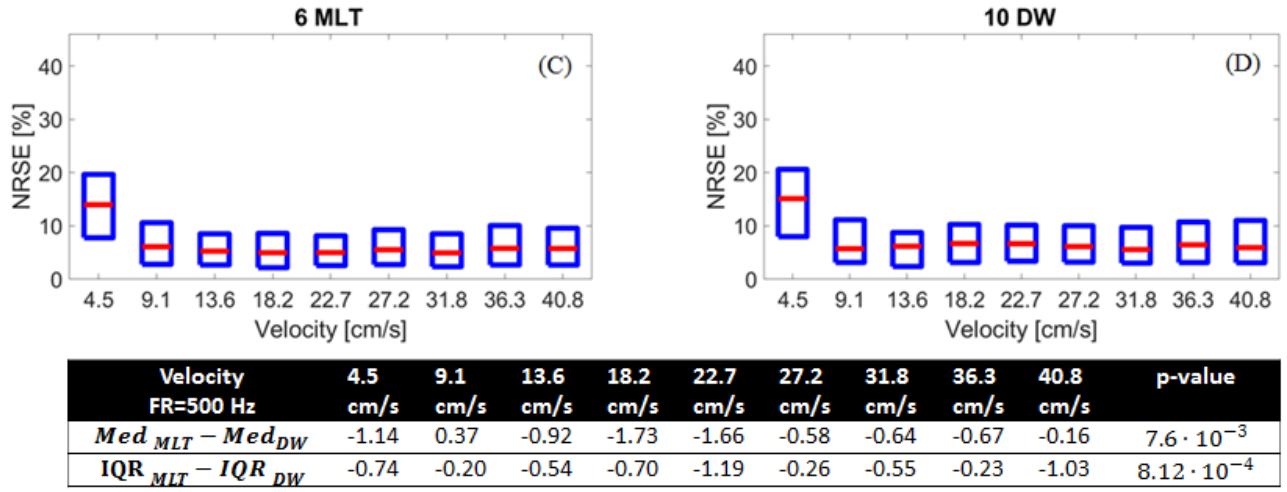

Velocity FR=500 Hz	4.5 cm/s	9.1 cm/s	13.6 cm/s	18.2 cm/s	22.7 cm/s	27.2 cm/s	31.8 cm/s	36.3 cm/s	40.8 cm/s	p-value
$Med_{MLT} - Med_{DW}$	-1.14	0.37	-0.92	-1.73	-1.66	-0.58	-0.64	-0.67	-0.16	$7.6 \cdot 10^{-3}$
$IQR_{MLT} - IQR_{DW}$	-0.74	-0.20	-0.54	-0.70	-1.19	-0.26	-0.55	-0.23	-1.03	$8.12 \cdot 10^{-4}$

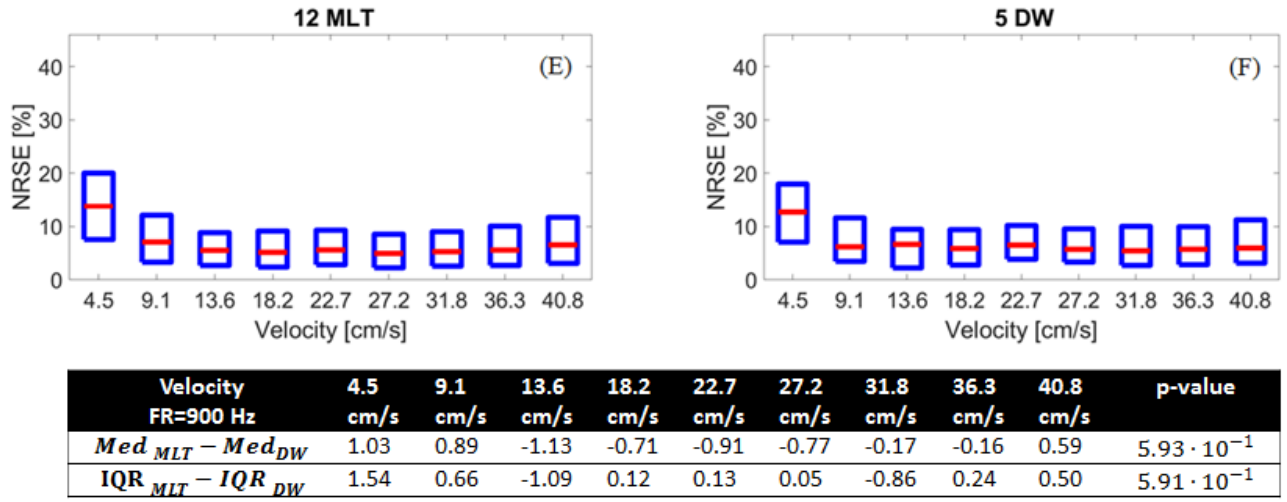

Velocity FR=900 Hz	4.5 cm/s	9.1 cm/s	13.6 cm/s	18.2 cm/s	22.7 cm/s	27.2 cm/s	31.8 cm/s	36.3 cm/s	40.8 cm/s	p-value
$Med_{MLT} - Med_{DW}$	1.03	0.89	-1.13	-0.71	-0.91	-0.77	-0.17	-0.16	0.59	$5.93 \cdot 10^{-1}$
$IQR_{MLT} - IQR_{DW}$	1.54	0.66	-1.09	0.12	0.13	0.05	-0.86	0.24	0.50	$5.91 \cdot 10^{-1}$

Fig. 35. Axial NRSE at different velocities of the disk at different frame rates (Speckle Tracking): 225 (A), (B); 450 (C), (D) and 900 (E), (F). Below each set of boxplots, we show the differences in median (Med) and interquartile range (IQR) between MLT and DW. Additionally, we provide the associated p-values.

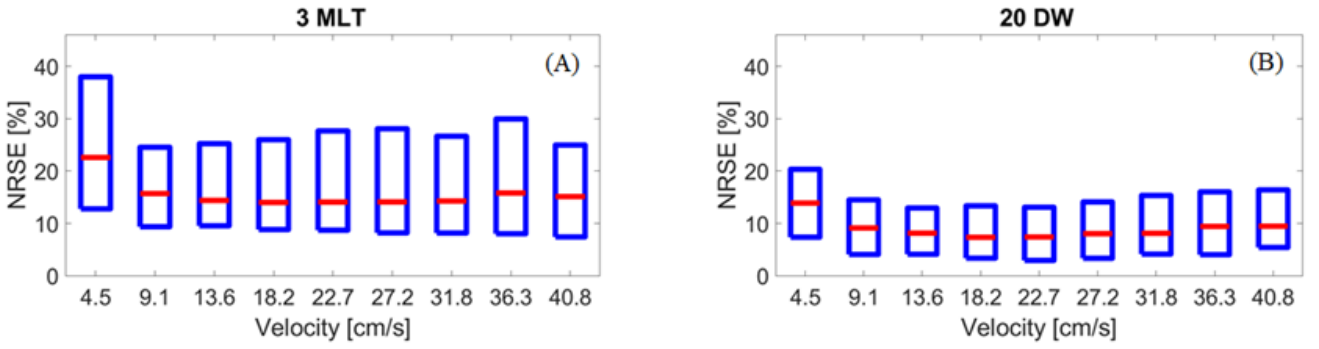

Velocity FR=225 Hz	4.5 cm/s	9.1 cm/s	13.6 cm/s	18.2 cm/s	22.7 cm/s	27.2 cm/s	31.8 cm/s	36.3 cm/s	40.8 cm/s	p-value
$Med_{MLT} - Med_{DW}$	8.69	6.57	6.23	6.62	6.66	6.04	6.15	6.36	5.63	$1.5 \cdot 10^{-8}$
$IQR_{MLT} - IQR_{DW}$	12.23	4.73	6.84	7.15	8.79	9.12	7.27	9.91	6.54	$4.17 \cdot 10^{-6}$

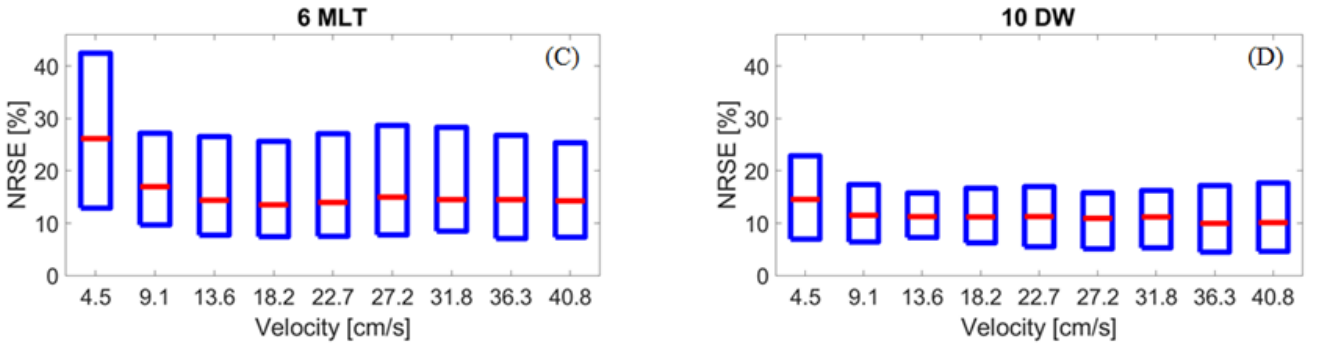

Velocity FR=450 Hz	4.5 cm/s	9.1 cm/s	13.6 cm/s	18.2 cm/s	22.7 cm/s	27.2 cm/s	31.8 cm/s	36.3 cm/s	40.8 cm/s	p-value
$Med_{MLT} - Med_{DW}$	11.58	5.45	3.13	2.32	2.69	4.04	3.29	4.51	4.15	$1.2 \cdot 10^{-3}$
$IQR_{MLT} - IQR_{DW}$	13.65	6.55	10.32	7.77	8.08	10.21	8.86	6.97	4.94	$7.91 \cdot 10^{-6}$

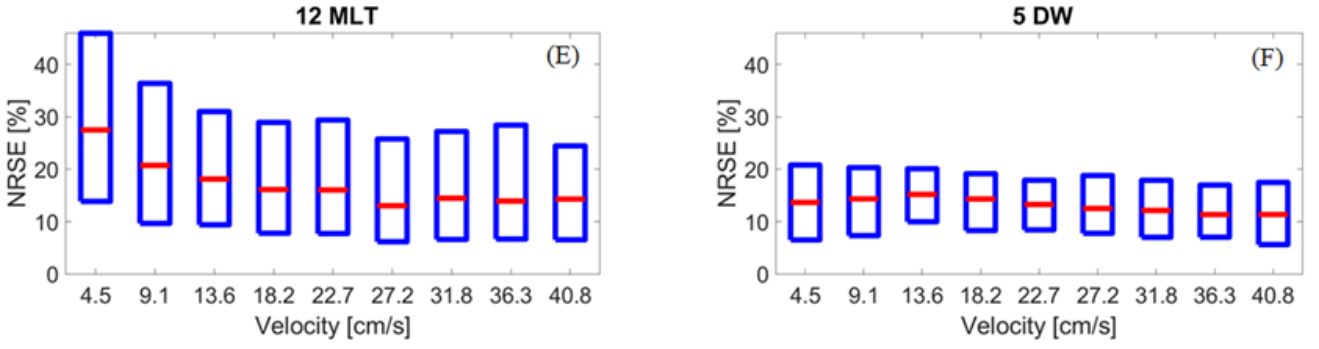

Velocity FR=900 Hz	4.5 cm/s	9.1 cm/s	13.6 cm/s	18.2 cm/s	22.7 cm/s	27.2 cm/s	31.8 cm/s	36.3 cm/s	40.8 cm/s	p-value
$Med_{MLT} - Med_{DW}$	13.82	6.38	2.92	1.8	2.76	0.52	2.33	2.57	2.94	$1.68 \cdot 10^{-2}$
$IQR_{MLT} - IQR_{DW}$	17.78	13.72	11.48	10.30	12.18	8.56	9.72	11.78	6.05	$7.1 \cdot 10^{-6}$

Fig. 36. Lateral NRSE at different velocities of the disk at different frame rates (Speckle Tracking): 225 (A), (B); 450 (C), (D) and 900 (E), (F). Below each set of boxplots, we show the differences in median (*Med*) and interquartile range (*IQR*) between MLT and DW. Additionally, we provide the associated p-values.

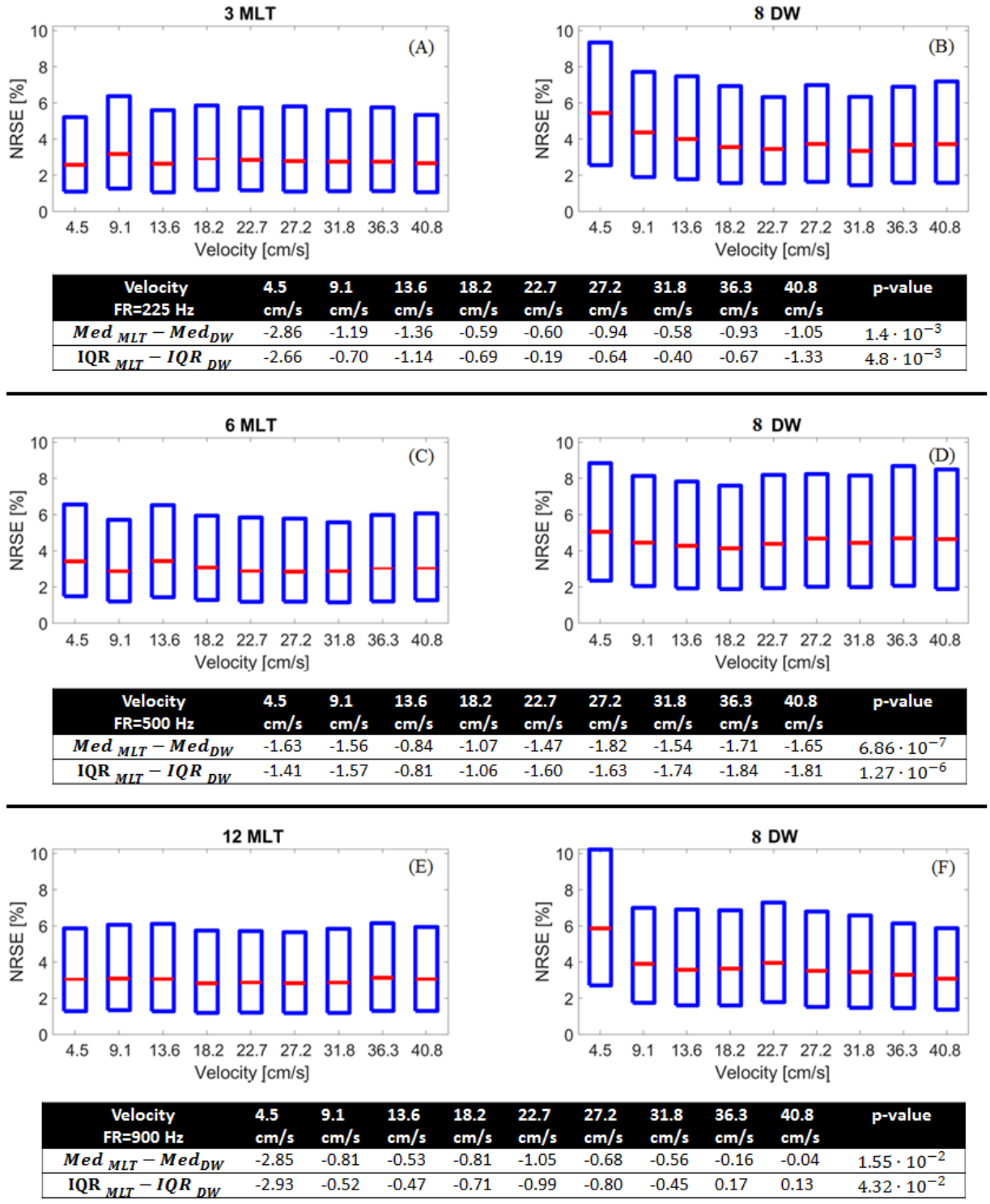

Velocity FR=225 Hz	4.5 cm/s	9.1 cm/s	13.6 cm/s	18.2 cm/s	22.7 cm/s	27.2 cm/s	31.8 cm/s	36.3 cm/s	40.8 cm/s	p-value
$Med_{MLT} - Med_{DW}$	-2.86	-1.19	-1.36	-0.59	-0.60	-0.94	-0.58	-0.93	-1.05	$1.4 \cdot 10^{-3}$
$IQR_{MLT} - IQR_{DW}$	-2.66	-0.70	-1.14	-0.69	-0.19	-0.64	-0.40	-0.67	-1.33	$4.8 \cdot 10^{-3}$

Velocity FR=500 Hz	4.5 cm/s	9.1 cm/s	13.6 cm/s	18.2 cm/s	22.7 cm/s	27.2 cm/s	31.8 cm/s	36.3 cm/s	40.8 cm/s	p-value
$Med_{MLT} - Med_{DW}$	-1.63	-1.56	-0.84	-1.07	-1.47	-1.82	-1.54	-1.71	-1.65	$6.86 \cdot 10^{-7}$
$IQR_{MLT} - IQR_{DW}$	-1.41	-1.57	-0.81	-1.06	-1.60	-1.63	-1.74	-1.84	-1.81	$1.27 \cdot 10^{-6}$

Velocity FR=900 Hz	4.5 cm/s	9.1 cm/s	13.6 cm/s	18.2 cm/s	22.7 cm/s	27.2 cm/s	31.8 cm/s	36.3 cm/s	40.8 cm/s	p-value
$Med_{MLT} - Med_{DW}$	-2.85	-0.81	-0.53	-0.81	-1.05	-0.68	-0.56	-0.16	-0.04	$1.55 \cdot 10^{-2}$
$IQR_{MLT} - IQR_{DW}$	-2.93	-0.52	-0.47	-0.71	-0.99	-0.80	-0.45	0.17	0.13	$4.32 \cdot 10^{-2}$

Fig. 37. Axial NRSE at different velocities of the disk (Doppler) by fixing the packet size to 8. The transmitted power was adjusted for DW to compare (A) with (B), (C) with (D) and (E) with (F). Below each set of boxplots, we show the differences in median (Med) and interquartile range (IQR) between MLT and DW. Additionally, we provide the associated p-values.

3.3.4. Qualitative B-mode and TDI *in vivo* assessment

In Fig. 38, we show B-mode images acquired on an open-chest pig obtained at the intermediate frame rate of 450 Hz for both MLT (A) and DW (B). Additionally, we show in Fig. 39 the tissue Doppler images for the two high frame rate methods. Two pairs of TDI images are shown at two different phases of the cardiac cycles. MLT and DW TDI results are firstly shown during ventricular filling when the mitral valve is fully opened (A, B) and secondly the same images are shown when the mitral valve starts to close (C, D).

Similarly, Fig. 40 shows B-mode transthoracic acquisitions on a human subject obtained at the intermediate frame rate of 450 Hz for both MLT (A) and DW (B). Tissue Doppler images for the two high frame rate methods are shown in Fig. 41.

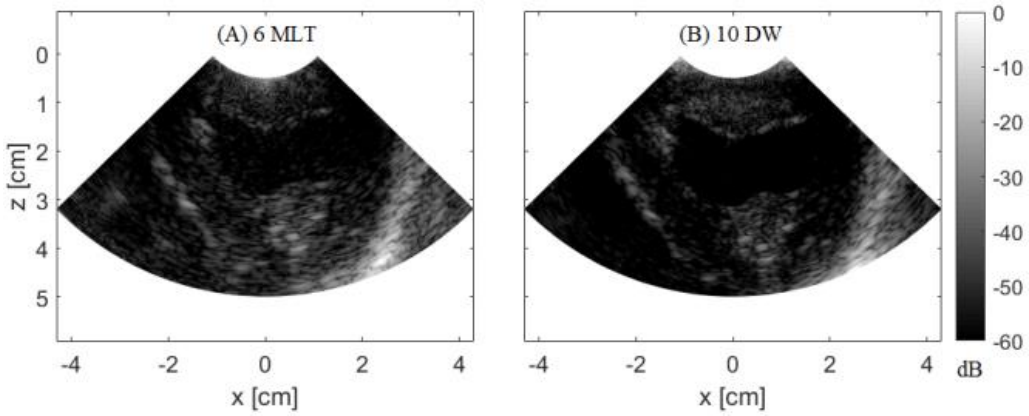

Fig. 38. B-mode *in vivo* images for MLT (A) and DW (B) at a frame rate of 450 Hz for the same phase of the cardiac cycle

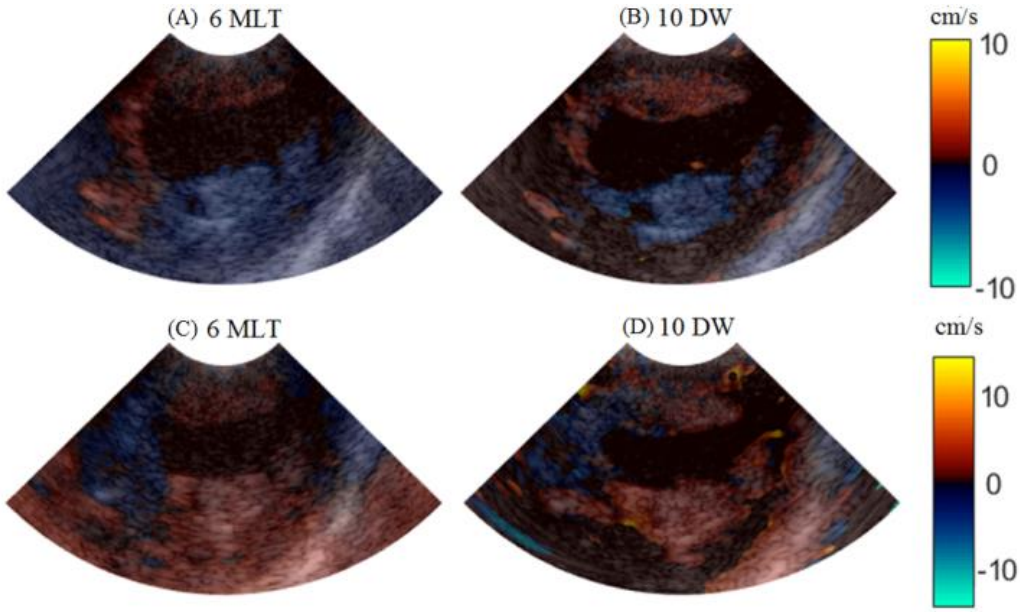

Fig. 39. TDI *in vivo* images for MLT (A, C) and DW (B, D) during two phases of the cardiac cycle: when the mitral valve is fully opened (A, B) and when the mitral valve starts to close (C, D).

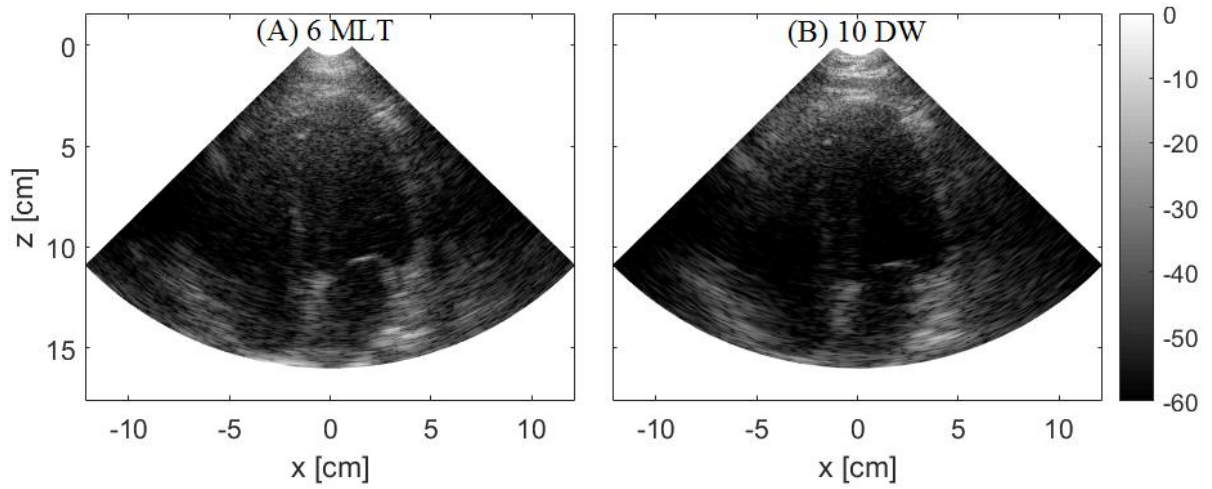

Fig. 40. B-mode *in vivo* 4 chamber view (human subject) for MLT (A) and DW (B) at a frame rate of 450 Hz

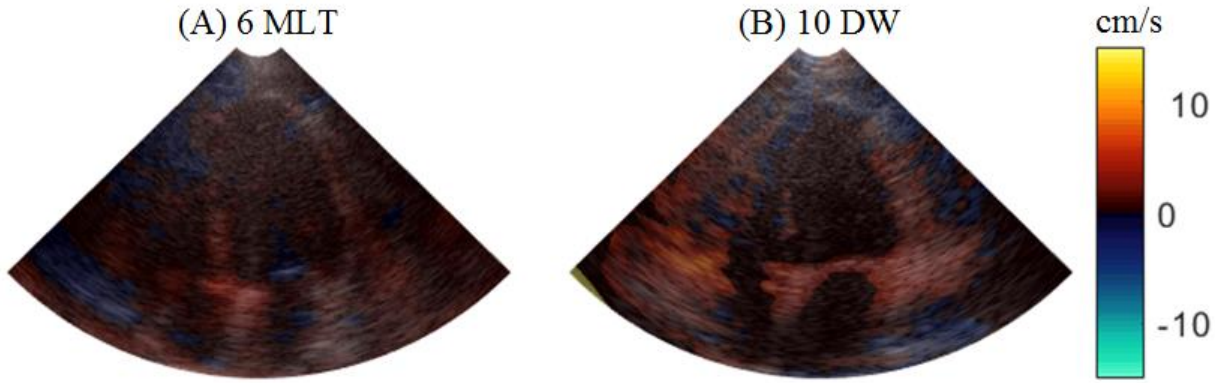

Fig. 41. TDI *in vivo* 4 chamber view (human subject) for MLT (A) and DW (B)

3.4. DISCUSSION

Fig. 30 shows the image quality degradation with the decrease in the number of transmissions and therefore the increase in frame rate. Even if the degradation was present for both MLT and DW its nature was different for the two methods. For instance, for MLT, the amount of cross-talk artefacts at a depth up to 4 cm was considerably increased as seen in magnified regions marked by the red boxes of Fig. 30 (A), Fig. 30 (C) and Fig. 30 (E). On the other hand, using DW led to a good image quality up to 4 cm. In addition to the absence of cross-talk, the CNR of the cyst placed at 4 cm was higher for the DW wide beam transmission as compared to the focused beam transmission (Table III). However, DW showed a higher attenuation of the signal at higher depths compared to MLT for all frame rates (although the transmitted energy was equivalent for the two methods). This explains the CNR values for the cyst at 11 cm that were reduced when the unfocused DW transmission was used compared to MLT (Table IV). This phenomenon

appears even though the position of the cyst at 11 cm is 4 cm away from the focal point. The DW attenuation and therefore the CNR degradation at high depths and high frame rates would have been increased if the same duty cycle of transmit waveform had been used for all frame rates.

We evaluated the lateral resolution starting from 5 cm to 11 cm with a step of 2 cm. Since it has been shown that the lateral resolution stabilizes starting with 3 diverging waves (Zhang et al. 2016) and since we used a number of diverging waves superior to this value for all the settings considered in this study, we chose to show the lateral resolution just for one case. This case corresponds to 5 DW which gives a frame rate of 900 Hz. As it can be observed in Fig. 31, a better resolution was achieved by using MLT than by using DW and the resolution degraded with depth for both methods. However, the lateral resolution with DW could be improved further by using a higher angular pitch.

The contrast evaluation on the rotating disk phantom showed a degradation of the contrast with the increase of the frame rate for all the velocities applied to the motor (Fig. 32 B and C). Note that the higher CNR values obtained in the rotating disk phantom compared with the Gammex phantom came from the difference in echogenicity between the two phantoms. The CNR was approximatively constant with the variation of the velocity, which is consistent with the results presented in (Poree et al. 2016). However, the curves present slight deviations which appeared as a consequence of calculating the average CNR at different positions of the inclusions at different velocities. Despite this limitation, the trend of a better MLT contrast compared to DW MoCo can still be observed for all velocities and for all frame rates. This can be explained by the fact that the cysts were placed from 4.5 cm to 9.5 cm in a region of interest where we showed that MLT is likely to provide a better image quality. Evaluating the CNR in dynamic conditions at lower depths may lead to opposite results-since the MLT cross-talk level is enhanced at low depths.

When speckle tracking was applied to MLT images and compounded motion-compensated DW images, strong outliers in the error distribution were found next to the surface of the probe, for both axial and lateral direction (Fig. 33 and Fig. 34). Since those outliers were biasing our mean errors, we decided to perform our analysis based on medians and IQR values of the NRSE. Overall, similar medians and IQR values were obtained in both cases in the axial direction for each frame rate and velocity value (Fig. 35). For all the acquisitions, the difference in median and IQR was inferior to 2%. The predominant negative values of the differences between the median NRSE obtained with MLT and DW, for the frame rates of 225 Hz and 450 Hz, show the trend of MLT to perform slightly better than DW, which can be associated with the impact of focusing on the B-Mode image quality. On the other hand, this trend is less general for the frame rate of 900 Hz where the presence of transmit artefacts in MLT is more significant. However, the p-values superior to 10^{-4} indicate a marginal difference in results between the two methods. The difference in results became more significant in the lateral direction especially in terms of the interquartile range where the p-value was reduced to an order of 10^{-6} (Fig. 36). This may be related to the presence of receive cross-talk artefacts that could be reduced using apodization as suggested in (Tong et al. 2014). For both directions and all frame rates considered, we can observe the trend of the block matching to provide less accurate estimates at the lowest velocity (reduced movement between the frames). Since we compensated for a higher temporal resolution by incrementing the lag between the frames, the estimator is not significantly affected by the frame rate variation.

When TDI was investigated for the two high-frame rate methods, the predominant negative difference in medians and IQR indicates slightly better estimates for MLT (Fig. 37). However, the improvement was inferior to 3% for all the cases. On the other hand, DW allows performing compounding and MoCo for B-Mode visualization based on the same packet size used for motion estimation. Thus the temporal resolution is diminished just by a single parameter: the packet size. On the opposite, for estimating the Doppler velocities on MLT images while preserving a high PRF, successive transmissions have to be performed

several times for the same image location. Therefore, the time required between the formation of the first and the last line of the image is increased not just with the packet size but also with the number of transmissions needed to achieve a full B-Mode image. In consequence, the Doppler frame rate is significantly limited as compared to a DW transmission. As shown in Table II, this leads to frame rates of 28, 56 and 112, depending on the amount of cross-talk we would be ready to accept, as compared to a frame rate of 562 with DW. Using a higher number of steering angles in DW may improve the Doppler estimates while providing a high enough frame rate, but increasing the packet size in MLT would reduce drastically the Doppler temporal resolution. For instance, using 32 steering angles for the first will result in a Doppler frame rate of 140 Hz whereas using a 32 packet size for 3 MLT will result in a Doppler frame rate of 7 Hz. Additionally, an overlap of 50 % can be used for the DW transmissions as suggested in (Poree et al. 2016), which would allow frame rates twice higher. If the two methods had been compared at the same Doppler frame rates, it is very likely that DW would have performed better than MLT. Using a higher number of transmissions for MoCo would have resulted in a better synthetic focusing. However, it would have been difficult to assess if the performance of the DW Doppler estimator had come from decreased variance (as a result of the packet size increase) or from the inherent features of the data obtained with the two imaging modalities (MLT and DW).

B-mode *in vivo* acquisitions showed that the two methods are competitive in providing good image quality at high frame rates for both open-chest parasternal short axis views (Fig. 38) and apical four chambers views (Fig. 40). However, the presence of cross-talk next to the surface of the probe in MLT makes DW a better candidate for the visualization of low depth structures (Fig. 38). On the other hand, for in-depth regions, MLT led to a better delimitation of the heart walls compared to the surrounding heart structures. This is particularly true if the focal point is placed around the in-depth region of interest. For example, the septum in Fig. 40 (A) is more visible than in (B). However, it would be worthwhile mentioning that just 10 DW were used for these B-Mode images, which is not optimal for DW MoCo (Poree et al. 2016). When TDI was applied to the *in vivo* images obtained with the two high frame rate methods, the obtained velocity maps were competitive (Fig. 39 and Fig. 41). Overall, the obtained results show that the choice of using one ultrafast method over the other depends on the application. Even if for the B-Mode visualization of organs placed at a lower depth, DW is more adapted than MLT, the energy dissipates faster with the penetration depth compared to MLT. Although cardiac images are characterized by rapid movements, the CNR seems to be better preserved with MLT. Competitive speckle tracking estimates were found for the two methods, considering that the MLT setting could be further improved. In terms of Doppler velocity estimator, MLT provides slightly lower errors than DW, but much higher Doppler frame rates can be obtained with DW. Even if MLT may be enough for TDI, higher frame rate may be desirable for blood velocity estimation, case in which DW would be more adapted. Since the MLT Doppler temporal resolution is considerably affected if a full image needs to be reconstructed, estimating the velocity just over a few lines of interest in the image would definitely eliminate this limitation.

3.5. CONCLUSION

In this study, we compared two ultrafast methods in static and dynamic conditions for *in vitro* and *in vivo* experiments. Since both methods can provide competitive frame rates compared to conventional imaging, our aim was to evaluate their performance at different frame rates, superior to the ones specific for

SLT. We were particularly interested in analyzing the image quality and in assessing the influence of each ultrafast method on two motion estimation techniques commonly used in echocardiography: speckle tracking and tissue Doppler imaging.

The performance of the two ultrafast competitive methods was investigated for different frame rates and different velocities. DW imaging provides better image quality at limited depths whereas MLT imaging allows a better concentration of the energy around a focal point that could be placed at higher depths. Similar speckle tracking axial errors were obtained for the two methods, but DW with MoCo provides better lateral estimates than MLT. Slightly lower TDI errors were obtained for MLT but much higher Doppler frame rates can be obtained with DW.

The two methods showed to be competitive in both image quality and motion estimation and the choice for a certain method is dependent on the application.

CHAPTER 4:

EXPERIMENTAL 3D MULTI LINE TRANSMISSION: FEASIBILITY, IMPROVEMENTS, AND PERFORMANCE IN STATIC AND DYNAMIC CONDITIONS

*Parts of this work were presented as:

1. Emilia Badescu, Denis Bujoreanu, Lorena Petrusca, Denis Friboulet, Hervé Liebgott, "Multi-Line Transmission For 3D ultrasound imaging: An experimental study*", IEEE International Ultrasonics symposium, Washington, D.C., USA, September 2017*

2. Emilia Badescu, Lorena Petrusca, Damien Garcia, Denis Friboulet, Hervé Liebgott, "Doppler Velocity estimation in 3D cardiac ultrafast ultrasound imaging: an *in vitro* study", *IEEE International Ultrasonics symposium, Washington, D.C., USA, September 2017*

3. Emilia Badescu , Lorena Petrusca , Denis Friboulet , Hervé Liebgott, "Experimental cross-talk reduction for 3D Multi-line transmission"*, IEEE International Ultrasonics symposium, Kobe, Japan, October 2018*

4.1. INTRODUCTION

Two-dimensional (2D) echocardiography is the modality of choice in current clinical practice due to its wide accessibility, noninvasive nature, low cost and high potential in clinical diagnosis. Clinicians now agree that 3D echocardiography can be complementary to 2D echocardiography. This imaging modality, however, is still rarely used at patient bedside since it is not possible to perform volumetric sequences at adequate temporal and spatial resolutions in a single heartbeat. The alternative multi-plane 2D imaging for reconstructing volumetric measurements and motion may lead to unreliable physiological parameters due to missing out-of-plane components.

Achieving high-frame-rate 3D echocardiography is highly relevant for clinical diagnosis. For example, improving temporal resolution of 3D echo would allow capturing rapid phases of the whole left ventricle for a better assessment of cardiac function. Furthermore, pediatric echocardiography (Fadnes et al. 2017), blood flow quantification (Faurie et al. 2017), assessment of the electromechanical properties (Provost et al. 2010) could also benefit from 3D ultrafast echocardiography.

As discussed in Chapter 2, conventional methods for increasing the temporal resolution such as sector angle reduction, decrease in line density, multi-line-acquisition (MLA) (von Ramm et al. 1991) have been already extended to 3D imaging. Other approaches based on plane/diverging waves were also introduced to 3D for further increasing the frame rate (Papadacci et al. 2014b). However, the main disadvantage of the wide-beam methods is the trade-off with image quality. An alternative technique to reach high frame rates with a minimum impact on the spatial resolution is multi-line transmit (MLT). Several studies demonstrated the potential of this method in 2D (Mallart & Fink 1992), (Tong et al. 2014). Even if MLT may lead to cross-talk artefacts, it has been proved to be very competitive with the conventional single-line transmission, especially if: an adequate apodization is used (Tong, Gao, et al. 2013), different frequency bands for the transmitted beams are employed (Demi et al. 2012), if a minimum variance beamforming is used (Rabinovich et al. 2015) or if the beams are properly positioned (Denarie et al. 2013).

Despite the promising potential of this method in 2D, few studies focused on analyzing its performances in 3D. Moreover, previous 3D MLT investigations were limited to simulations and could not be used in dynamic conditions due to their retrospective synthetic implementations. More specifically, the channel data corresponding to different SLT (single line transmit) sequences was synthetically summed before beamforming (Ortega et al. 2016).

In this section, we present the first implementation of the real-time 3D MLT on a research ultrasound system. First, we concentrated on proving its feasibility. To do so, we used a simple linear MLT transmission scheme. We investigated the performance of the data resulting from such transmission scheme on both static and dynamic *in vitro* models. The static model was used to study the image quality of MLT imaging compared with conventional focused imaging. The tests of experimental 3D MLT on *in vitro* dynamic phantoms were performed to investigate the potential of the method for tissue Doppler applications.

Following our preliminary feasibility study, we targeted the improvement of the acquisition settings. Therefore, we changed the excitation signals and the transmission scheme aiming image quality improvement and cross-talk reduction. Besides investigating the effects of these changes on *in vitro* static models, we additionally studied their impact on a dynamic phantom.

4.2. METHODS

4.2.1. 3D acquisition system

The 3D images were acquired by synchronizing four Vantage 256 scanners (Verasonics, Kirkland, WA, USA) through a Multi-System Synchronization Module. This module allows distributing the 250 MHz clock of the Master to the other 3 systems, which are the Slaves. Each of the systems controls 256 elements of a 1024 ultrasound transducer (Petrusca et al. 2018). An overview of the 3D acquisition system is provided in Fig. 42 :

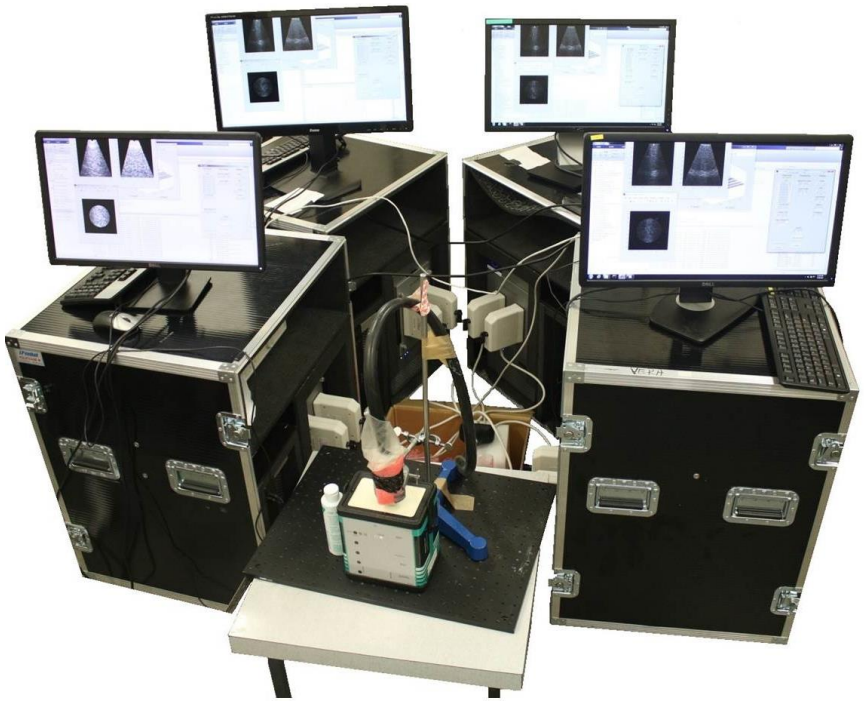

Fig. 42. Overview of the 3D acquisition system: Four Vantage 256 research scanners were synchronized to control each of the 256 elements of a 1024 Vermon ultrasound transducer

This project has received funding from the European Union's Horizon 2020 research and innovation programme under the Marie Skłodowska-Curie grant agreement No 642612, VPH-CaSE (www.vph-case.eu). This work was performed within the framework of the LABEX PRIMES (ANR-11-LABX-0063) of Université de Lyon, within the program "Investissements d'Avenir" (ANR-11-IDEX-0007) operated by the French National Research Agency (ANR).

We would like to thank LabTAU for their contribution in the development of the 32x32 probe prototype compatible with a driving 1 to 4 Verasonics Vantage256 as well as for providing us the probe and two Vantage 256 systems. The Verasonics system was cofounded by the FEDER program, Saint-EtienneMetropole (SME) and Conseil General de la Loire (CG42) within the framework of the SonoCardioProtection Project leaded by Dr Pierre Croisille.

The 1024 elements of the 2D Vermon probe (Vermon, Tours, France) are distributed in a 32x35 matrix array (3 lines of the matrix are not connected) The central frequency of the probe is 3MHz with a 70.9% bandwidth at -6 dB. The size of the square elements of the probe is 249 µm and the pitch 300 µm. An overview of the matrix array distribution is provided in Fig. 43.

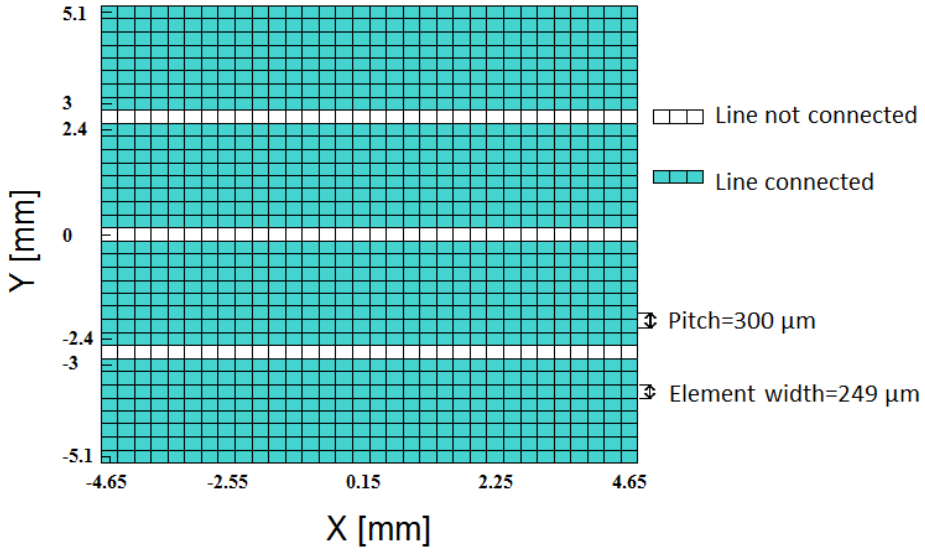

Fig. 43. Matrix array of the 2D probe: 1024 elements are distributed in a 32 (X) by 35 (Y) array configuration, containing 3 lines on Y direction which are not connected.

4.2.2. Practical implementation of MLT in 3D

The flexibility allowed by the high channel density platform is crucial for the practical implementation of MLT which requires a certain complexity. Unlike other US transmission methods (Focused, DW/PW), the signal applied to each element in MLT is not just a delayed version of an initial waveform. Therefore, defining the basic transmission waveform and the delays applied to each element is not sufficient for experimental MLT acquisitions. Multiple waveforms need to be superposed for a single transmission which requires a system capable of emitting non-identical excitation pulses to all elements. This is possible if the system is equipped with an Arbitrary Waveform Generator (AWG) or with a tristate pulser. The implementation of MLT using the first option has been successfully demonstrated in 2D by (Tong et al. 2014). The advantage of an AWG is that it allows the user to apply directly the desired signals in transmission. Unlike AWG, a system equipped with a tristate pulser requires in addition coding the complex superposition of waveforms using 3 states (+V, 0, -V).

Since our Vantage system is equipped with such a pulser, the implementation of MLT presented in this study was done by taking into consideration the tristate pulser requirements and other specifications of the system. The overall transmission pipeline is illustrated in Fig. 44 for an initial one-cycle-sine excitation signal (A). For simplicity, the excitation matrix is shown just for one 4 MLT transmission event (B). Each superposed signal $tw_i(t)$ of the matrix, corresponding to one element i of the probe, is compared with a threshold. If the absolute value of the signal is inferior to the threshold thr, the tristate signal $tri_i(t)$ is set to 0. If not, the tristate is set to -/+V, depending on the polarity of the superposed signal as shown in equation (4.1) and Fig. 44 C.

$$tri_i(t) = \begin{cases} 0, & if\ |tw_i(t)| < thr \\ V \cdot sign\big(tw_i(t)\big), & if\ |tw_i(t)| \geq thr \end{cases} \quad (4.1)$$

Once the tristate signal is obtained, the Vantage research scanner requires coding the tristate sequence further for obtaining a sequence compatible with the pulse code specification. Therefore the vector containing tristate values have to be converted into a matrix, where each line has the following form: [Z1, P1, Z2, P2, R]. Z1 and Z2 are the number of zeros contained between different polarities given by the sign of P1 and P2. The absolute values of P1 and P2 provide the number of samples of a given polarity while R indicates the number of times the line is repeated (Fig. 44 D).

Note that the steps B, C and D in Fig. 44 had to be followed independently for each Vantage system controlling 256 elements of the probe.

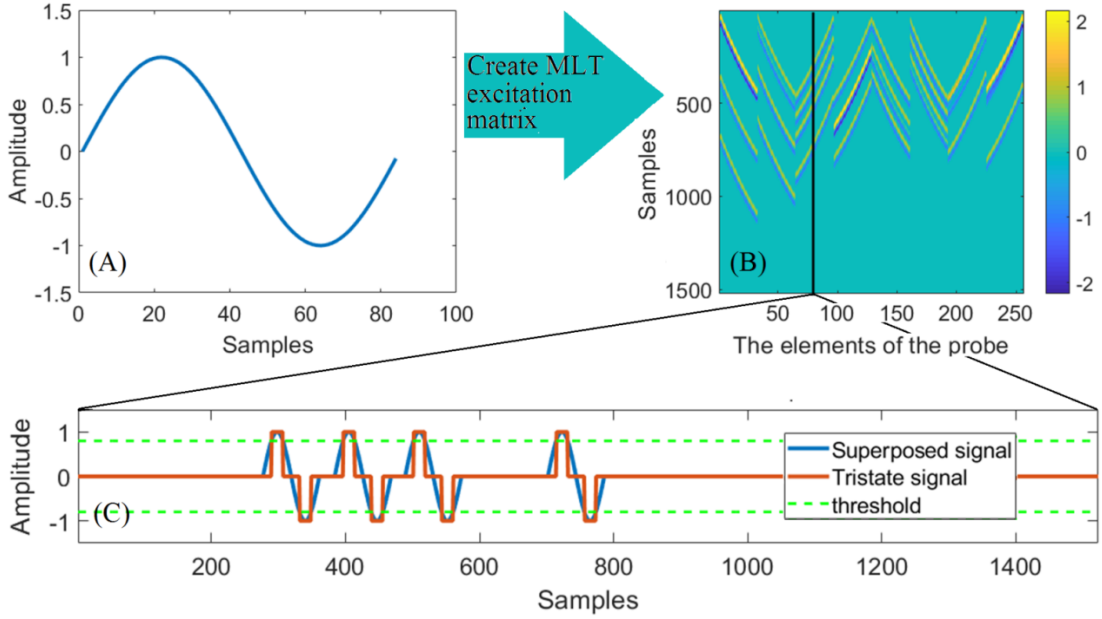

		Z1	P1	Z2	P2	R
(D)	Pulse Code	289	17	25	-17	1
		48	17	25	-17	1
		46	17	25	-17	1
		154	17	25	-17	1
		750	0	0	0	1

Fig. 44. Overall, the implementation of MLT consisted of several steps, done independently for each Vantage system controlling 256 elements of the probe: (A) We defined the initial excitation waveform; (B) Based on this excitation waveform, we created an excitation matrix containing the superposition of waveforms for all elements and for all transmission events; for simplicity, we show the excitation matrix obtained from a single 4 MLT transmission event; (C)We then converted each signal of the excitation matrix into a tristate excitation signal, (D) Finally, we converted each tristate signal into a pulse code

4.2.3. Acquisition settings

4.2.3.1. Feasibility study

To study the feasibility of experimental 3D MLT, a scan volume was created by disposing 32 sectors (each of angular width = 60^o) along the azimuthal direction. For each triangular sector, $32/nMLT$ transmission events were used to insonify a full sector by sending simultaneously nMLT equidistant focused beams. Thus, the total number of transmissions was $32x32/nMLT$, corresponding to 32 (elevational → y) × 32 (azimuthal → x) focal beams.

In order to investigate the compromise between the frame rate and image quality in static conditions, nMLT was varied from 4 to 8 and 16. Therefore, the number of transmissions per azimuthal sector was changed from 8 (Fig. 45) to 4 (Fig. 46) and 2 (Fig. 47), leading to a total number of transmissions per volume of 256, 128 and 64. The performance of MLT 3D in dynamic conditions was studied using the intermediate value of 8 MLT.

The focal point was set to 4 cm for static acquisitions and to 6.7 cm for dynamic acquisitions. No apodization was used either in emission or reception. The received signals were sampled at four times the central frequency of the transducer.

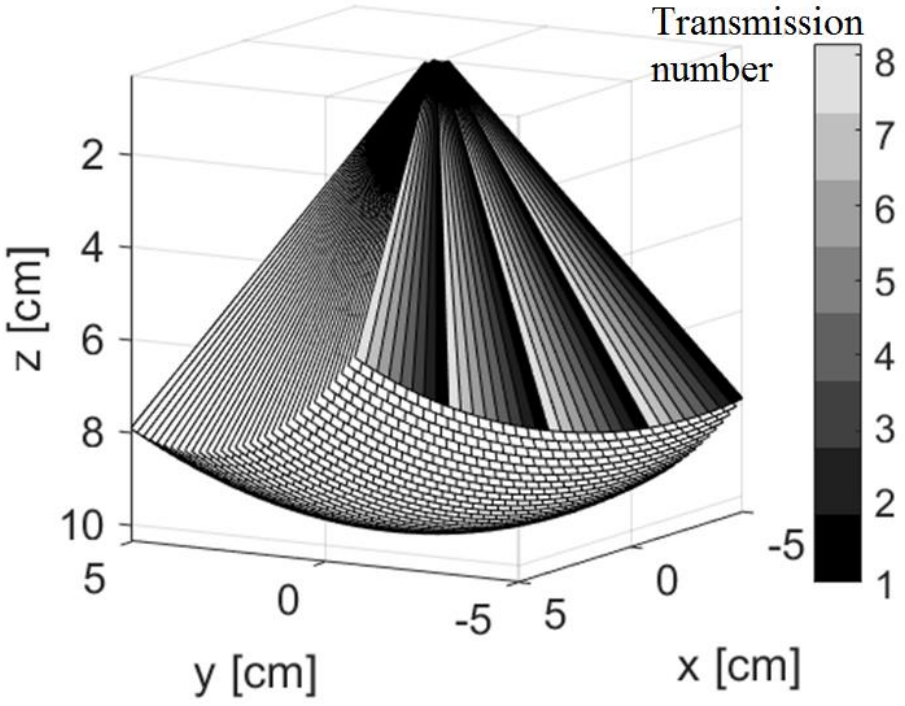

Fig. 45. Transmission scheme for 4 MLT: For each azimuthal sector (x direction), 8 transmission events were used to insonify a full sector by sending simultaneously 4 equidistant focused beams. The total number of transmissions per volume was 256

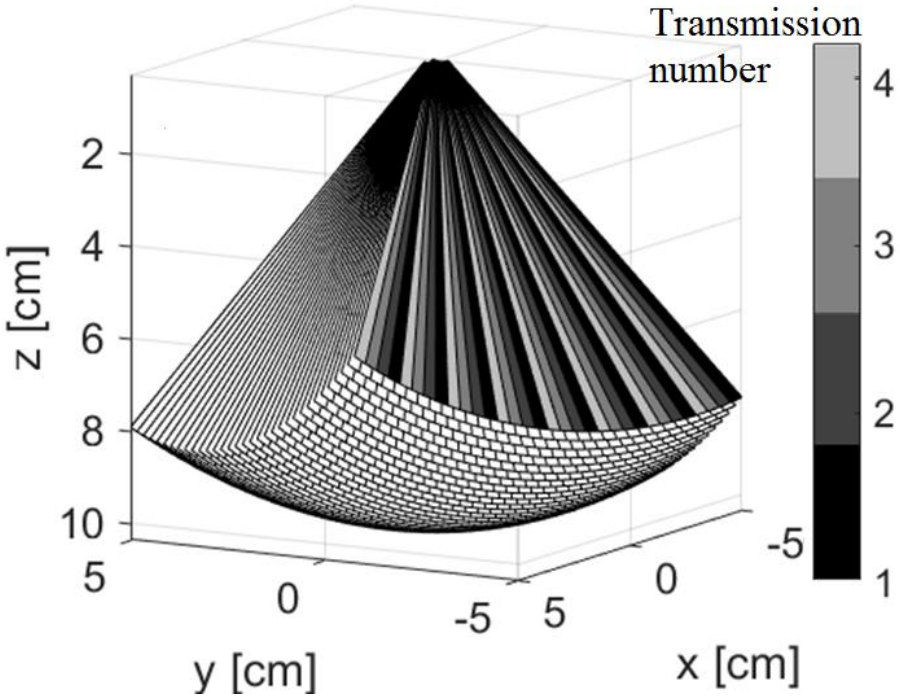

Fig. 46. Transmission scheme for 8 MLT: For each azimuthal sector (x direction), 4 transmission events were used to insonify a full sector by sending simultaneously 8 equidistant focused beams. The total number of transmissions per volume was 128

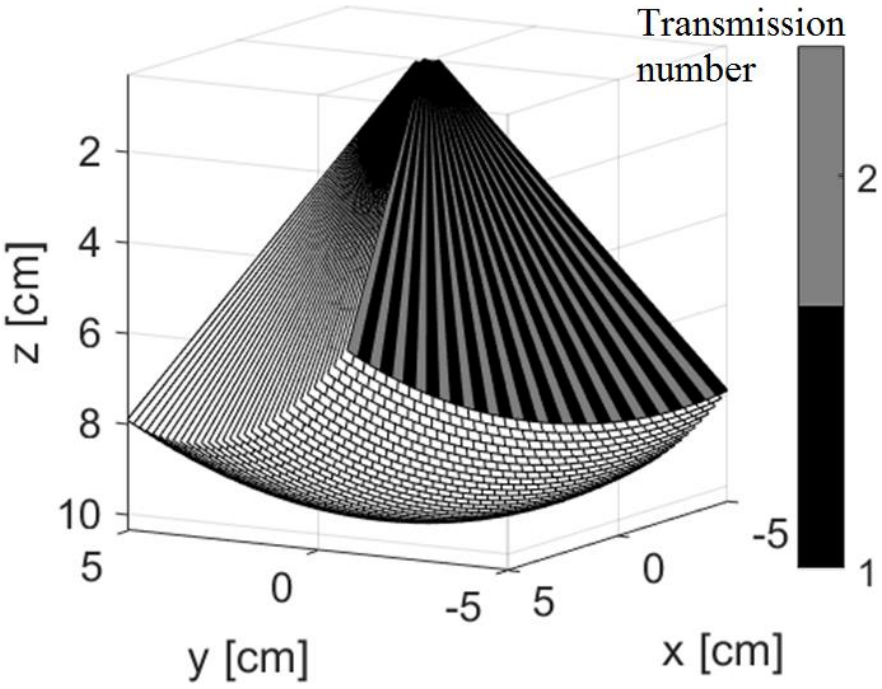

Fig. 47. Transmission scheme for 16 MLT: For each azimuthal sector (x direction), 2 transmission events were used to insonify a full sector by sending simultaneously 16 equidistant focused beams. The total number of transmissions per volume was 64

4.2.3.2. Improvements aiming at cross-talk reduction

As explained in section 2.2.4, the principal cause of cross-talk artefacts is the interference between the main lobe and the side lobes of parallel transmissions. This interaction becomes even more important if the inter-space beam is reduced as it happens for a linear transmission scheme (Fig. 45 - Fig. 47) when the number of transmissions increases. A simple approach for extending the inter-beam space without compromising the frame rate is distributing the transmissions along the entire scan volume, instead of limiting it to single planes. For choosing an appropriate distribution, we got inspired by the study conducted by (Denarie et al. 2013). Based on the observation that the pressure field of a rectangular transducer will have the shape of a sinc function in the focal plane (Fraunhofer approximation), the authors assumed that the 2D pressure field will have a cross shape. Under the hypothesis of linear propagation, this results from a 2D convolution between the sinc profiles along the azimuthal and the elevational planes. They confirmed the theoretical cross-pattern of the pressure field by simulations and hydrophone measurements. Given its shape, the maximum energy of the cross-like pressure field is oriented along the azimuthal and elevational planes. Therefore, by distributing the beams along the main directions of the transducer (elevational/azimuthal) the interferences between simultaneous transmissions is maximized. On the other hand, a diagonal distribution could minimize these interferences.

Motivated by these findings, we replaced the typical alignment of the transmissions presented in the feasibility study, by an alignment along the transverse diagonal of the transducer (Fig. 48).

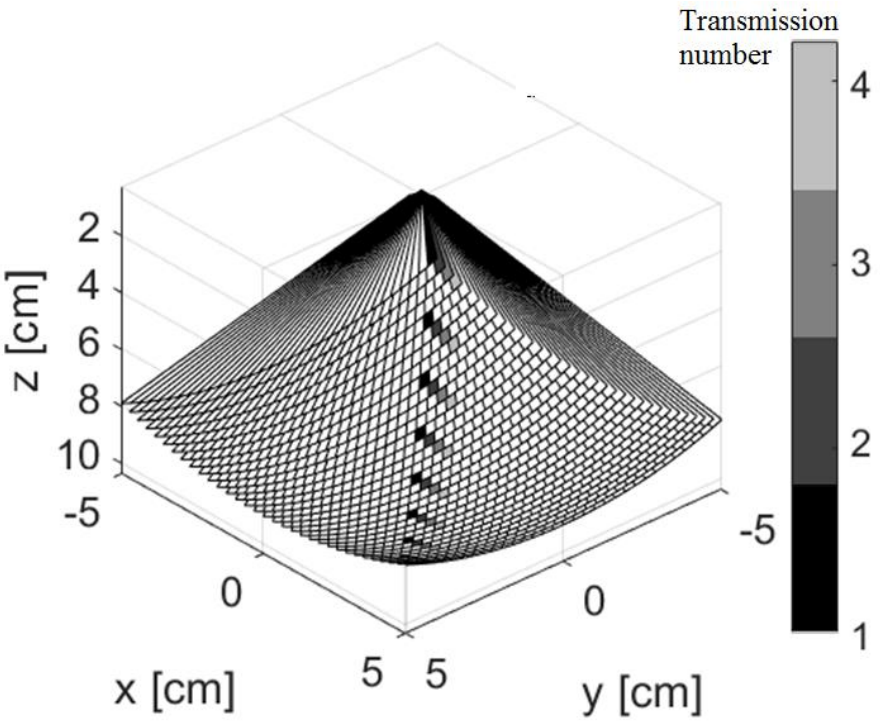

Fig. 48. Transmission scheme for 8 MLT along the transverse diagonal of the transducer

For this analysis, the intermediate value of 8MLT was selected. To get a higher penetration depth and contrast, the initial excitation signal was set on during a longer time than for the first part of this study.

More specifically, it was set to a 2 cycles sine before any superposition. The threshold was fixed to 0.8, to compute the corresponding tristate signal. The focal point was set to correspond to the resolution and the contrast phantom targets respectively. Thus, it was set to 5 cm for resolution measurements and 4 cm for CNR measurements. The received signals were sampled at four times the central frequency of the transducer.

4.2.4. *In vitro* models

4.2.4.1. Feasibility study

We evaluated the performance of 3D MLT using both static and dynamic *in vitro* models.

As static models, we used a CIRS ultrasound phantom (Model 054GS) for image quality assessment. We calculated the CNR (3.7) and the resolution which was computed using full width at –6 dB.

Our dynamic phantom was a tissue mimicking spinning disc with a diameter of 10 cm whose speed could be controlled by a step motor. The disk was placed at 1.6 cm away from the transducer and the image depth was ~10.5 cm. The dynamic experimental set-up is illustrated in Fig. 49.

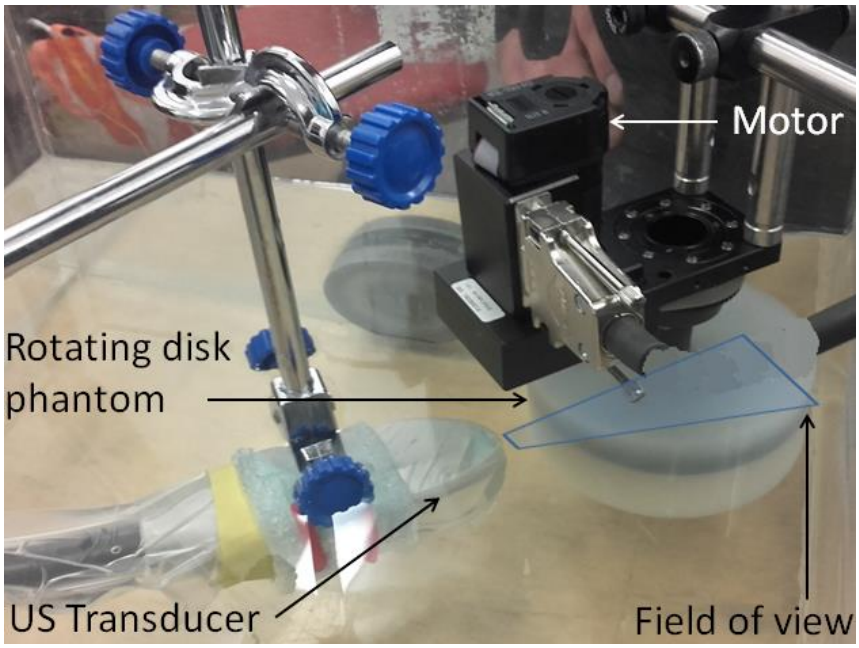

Fig. 49. Experimental set-up for dynamic acquisitions: The transducer insonifies a 10 cm diameter rotating disk. The velocity of the disk is controlled by the step motor, being set to 17 cm/s.

The phantom was rotated at an angular velocity of 200 degrees/s. This set-up gave a maximum tangential velocity at the edge of the disk of 17.4 cm/s, which corresponds to myocardial peak velocities reported in (Nagueh et al. 1997). The PRF was set to 2250 Hz (Nyquist velocity = 29 cm/s). In-plane axial Doppler velocities were then estimated by IQ-demodulating offline the beamformed RF data and then applying on it a 2D auto-correlator using a packet length of 7 (Loupas et al. 1995).

4.2.4.2. Improvements aiming at cross-talk reduction

The effects of a diagonal transmission scheme on the image quality were evaluated using a Gammex (Sono410 SCG) phantom for resolution measurements and CNR on a hypoechoic cyst. Additionally, we used a CIRS (054GS) phantom for assessing the CNR on a hyperechoic cyst.

The consequence of this transmission scheme on the motion was evaluated on the same phantom as the one used for the feasibility study (Fig. 49). The velocity of the motor and the method used for estimating it remained unchanged from section 4.2.4.1.

4.3. RESULTS

4.3.1. Feasibility study

The acquisitions on the CIRS phantom successfully allowed reconstructing 3 sections of a 3D volume, as shown in Fig. 50. The XZ plane (A) shows the contrast and the resolution inclusions obtained for 8 MLT, whereas the YZ plane (B) shows the perpendicular plane which passes through the cyst. Additionally, we present in (C) the cross-section of the cyst.

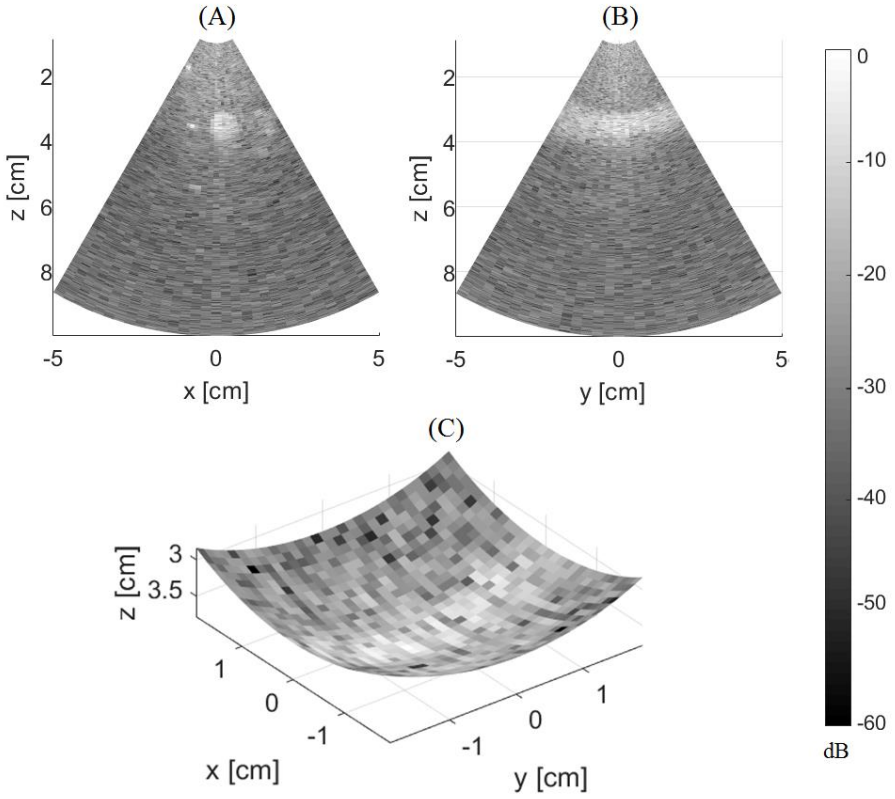

Fig. 50. 3D results for 8 MLT: (A) XZ and (B) YZ reconstructed planes and (c) a surface at a constant depth (Z=3.8 cm)

As shown in Fig. 51, the image quality changes with the number of simultaneous transmissions. The contrast was investigated for a hyperechoic cylinder, whilst the resolution was measured for a media point, both placed on the focal point (4 cm). The contrast and the axial resolution values for focus imaging, 4 MLT, 8 MLT, and 16 MLT are reported in Table V.

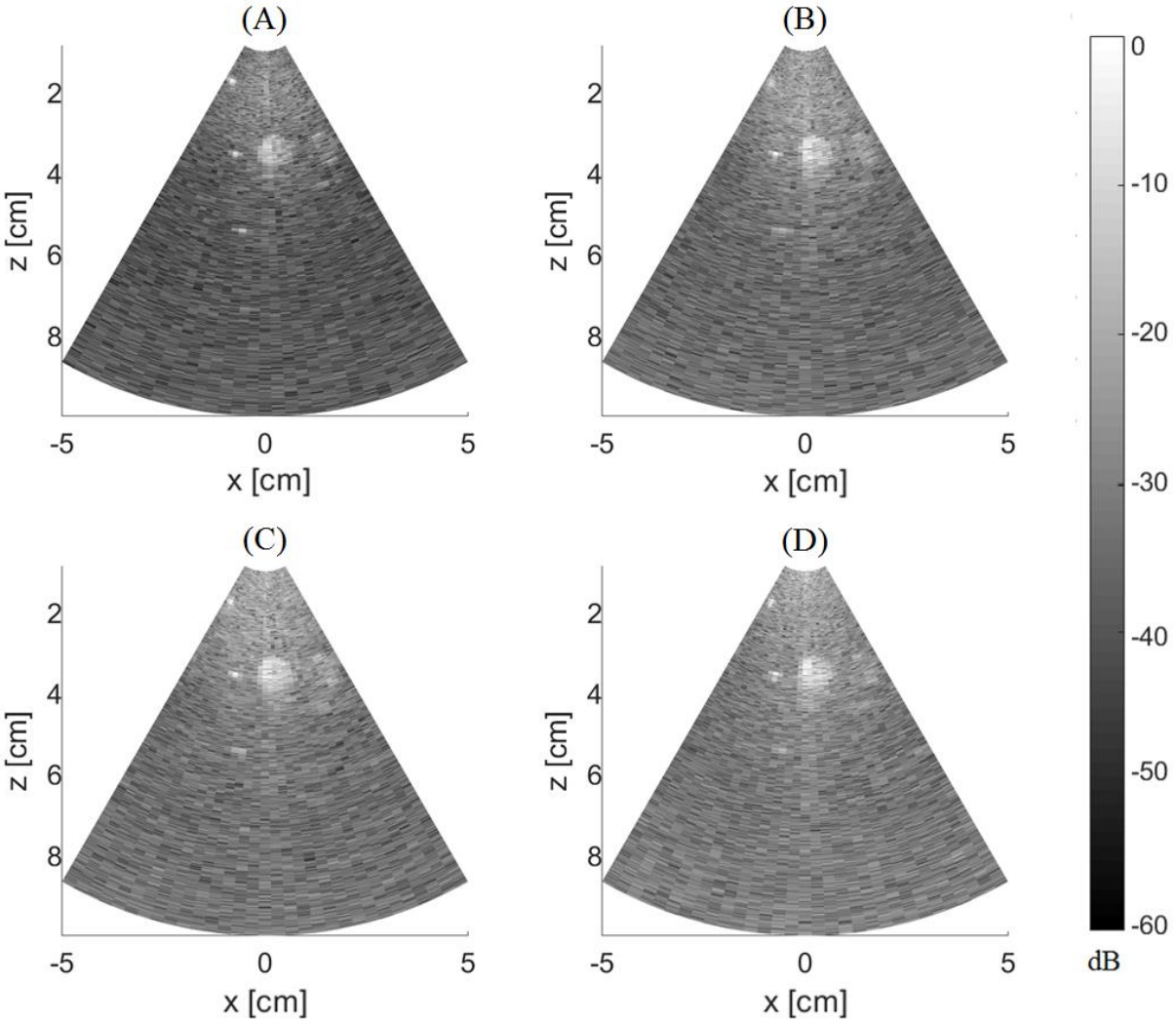

Fig. 51. : Comparison XZ planes for focus (A), 4 MLT (B), 8 MLT (C) and 16 MLT (D)

TABLE V: AXIAL RESOLUTION AND CONTRAST VALUES

Sequence/ Image quality	Focus	4MLT	8MLT	16MLT
Axial Resolution	0.33 mm	0.54 mm	0.57 mm	0.61 mm
Contrast	3.60 dB	3.02 dB	2.83 dB	2.61 dB

The multi-plane Doppler velocity volume is presented in Fig. 52. The estimated velocity values (B) were in agreement with the expected velocities (A). The mean relative error was 4.1 %.

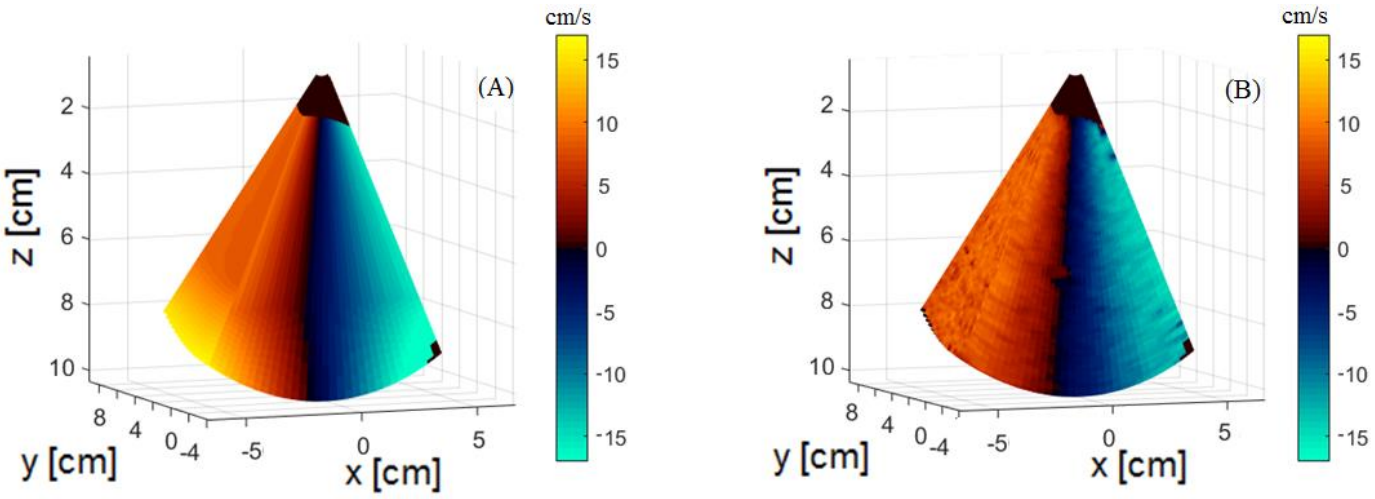

Fig. 52. Multiple plane velocity map: (A) Reference velocity map; (B) Estimated velocity map

4.3.2. Improvements aiming at cross-talk reduction

We first evaluated the impact of using different transmission schemes on the Gammex phantom. Hence, we show in Fig. 53 the comparison between the results using the linear transmission scheme (left) and the diagonal transmission scheme (right) for both XZ (A, B) and YZ planes (C, D). The axial resolution values measured at the focal point (5 cm) are provided in Table VI. In order to highlight the difference between the main and side lobes obtained with the two transmission schemes, we show in Fig. 54 the axial profiles at the center of XZ (A) and YZ (C) planes. The regions of interest around the focal point, marked by the black rectangle, were normalized around [0, -60 dB] for a quantitative evaluation of these differences. The measured values are provided in the zoomed regions presented in B and D. By using the same phantom and by changing the imaged region of the volume and the focal point (compared to Fig. 53), the CNR on a hypoechoic cyst was evaluated. A qualitative comparison between the results for the linear transmission scheme (left) and the diagonal transmission scheme (right) is provided in Fig. 55. Both XZ (A, B) and YZ planes (C, D) planes are shown. For a quantitative analysis, the CNR values for the hypoechoic cyst placed at the focal point (4 cm) are provided in Table VII.

For evaluating the image quality on a hyperechoic cyst, we used the CIRS phantom. In Fig. 56, we show the qualitative comparison between images obtained using the linear transmission scheme (left) and the diagonal transmission scheme (right) for both XZ (A, B) and YZ planes (C, D). Additionally, we provide in Table VIII the CNR for the hyperechoic cyst placed in the focal point (4 cm).

The effect of using the two transmission schemes on the rotating disk is shown in Fig. 57. The middle XZ planes can be compared for the linear transmission scheme (A) and for the diagonal one (B).

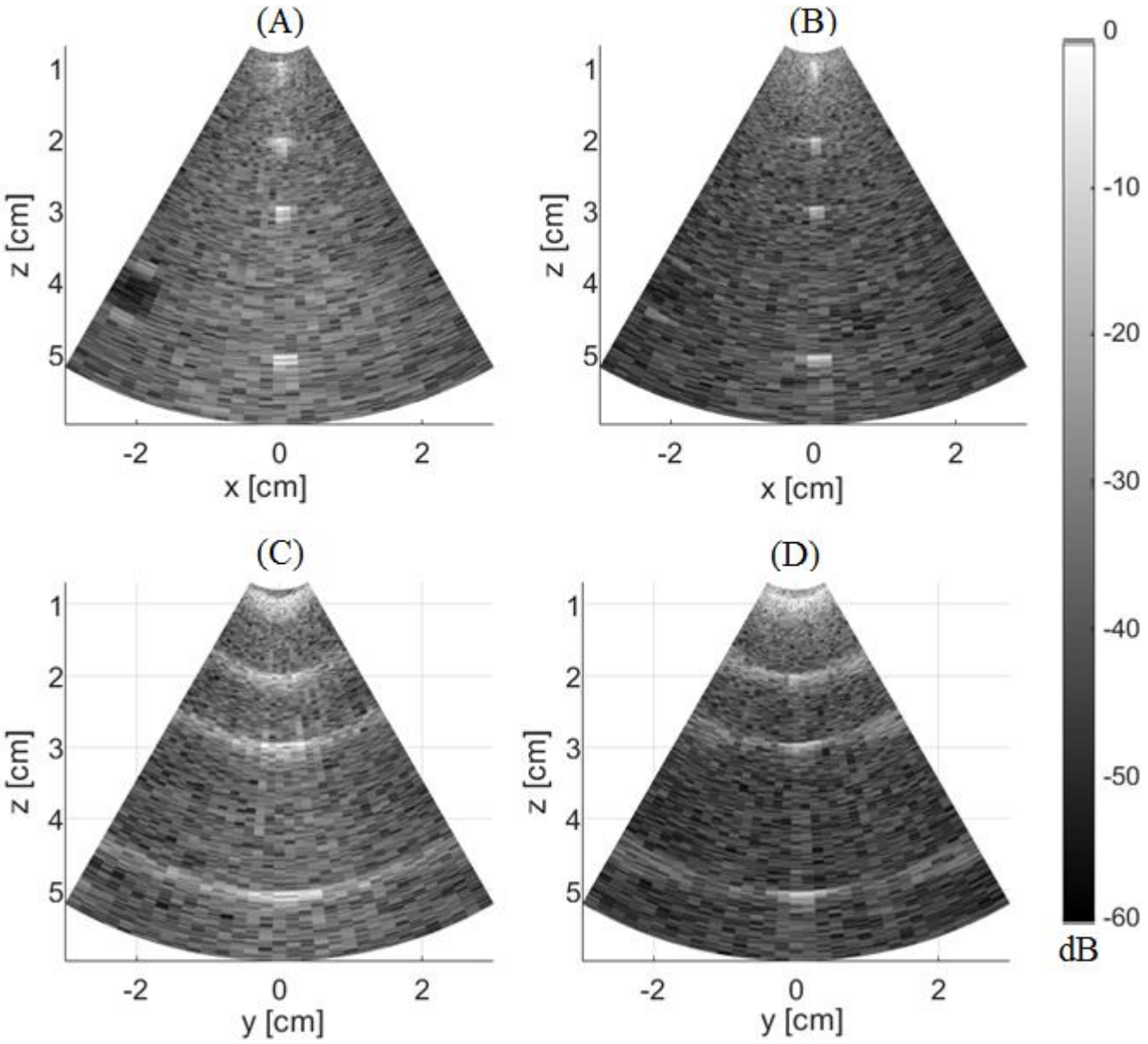

Fig. 53. Comparison between the 8 MLT Gammex phantom results using the linear transmission scheme (left) and the diagonal transmission scheme (right) for both XZ (A, B) and YZ planes (C, D).

TABLE VI: AXIAL RESOLUTION FOR DIFFERENT TRANSMISSION SCHEMES

Sequence/ Image quality	8 MLT Linear Transmission	8 MLT Diagonal Transmission
Axial Resolution at focal point (5 cm)	1.14 mm	0.45 mm

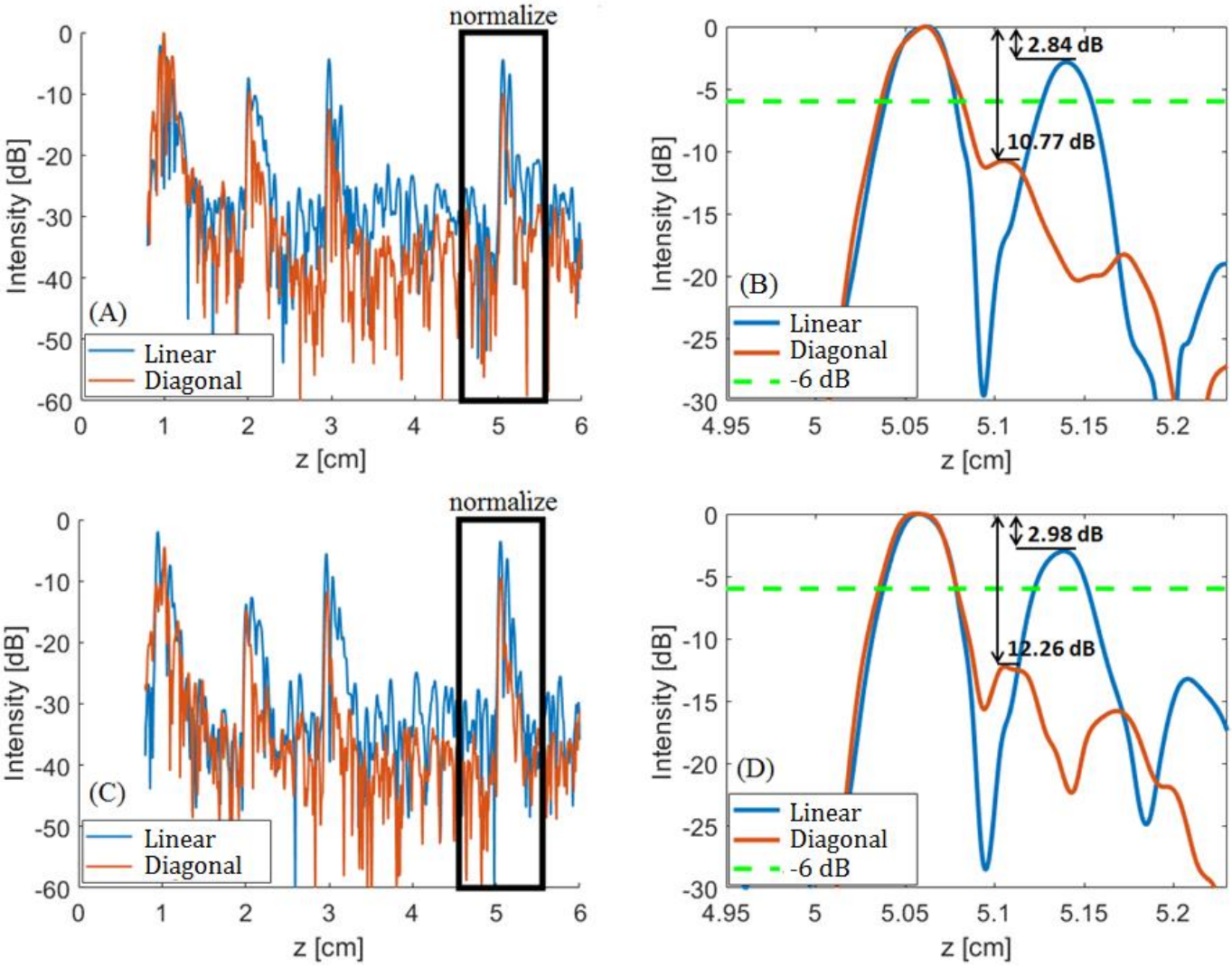

Fig. 54. Axial profiles at the center of the XZ (A) and YZ (C) planes, and their corresponding zoomed regions (B, D), after normalizing the region of interest (black rectangle) between [-60, 0] dB. The difference between the main and the side lobe is shown for each case.

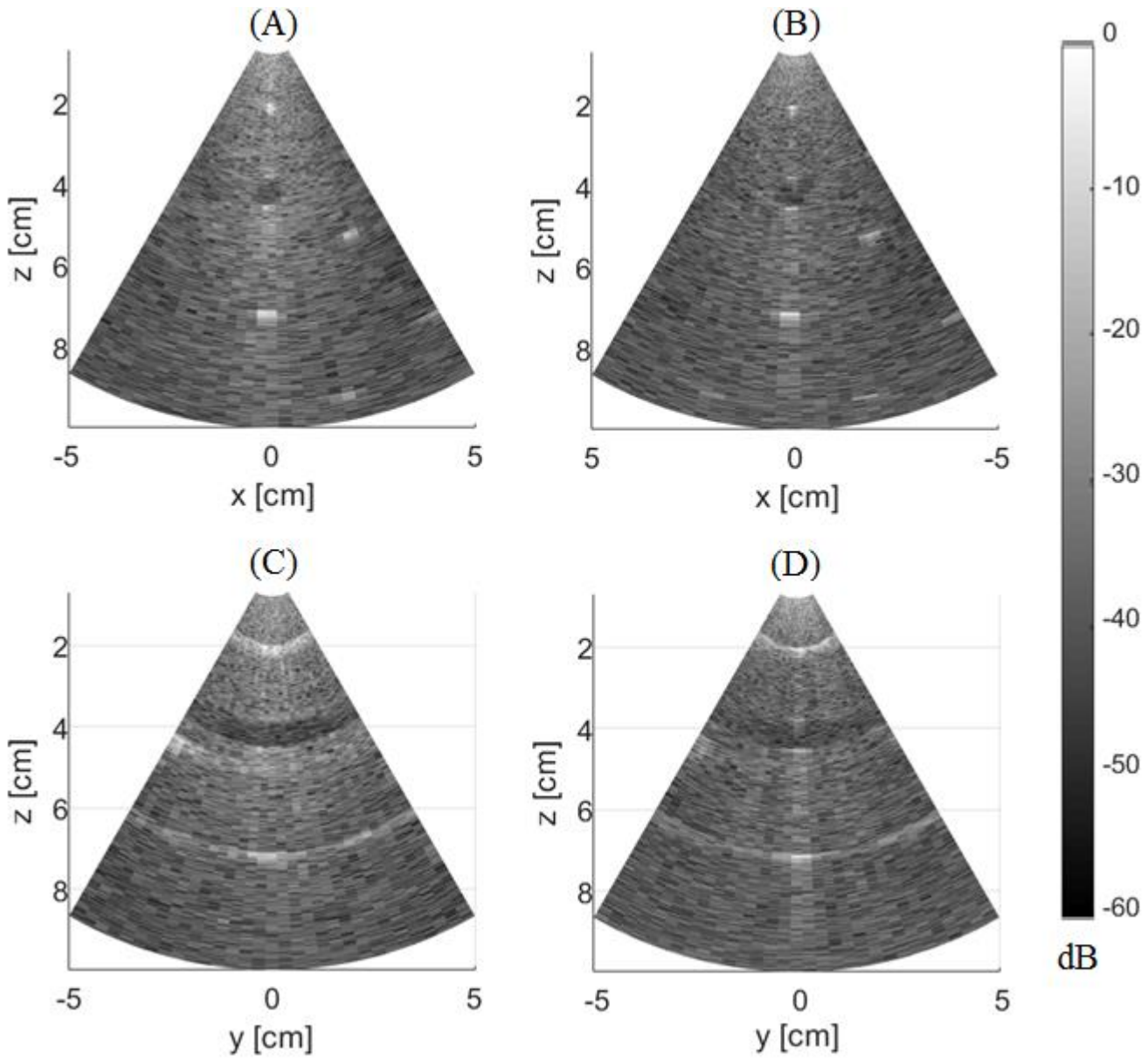

Fig. 55. Comparison between the 8 MLT Gammex phantom results using the linear transmission scheme (left) and the diagonal transmission scheme (right) for both XZ (A, B) and YZ planes (C, D).

TABLE VII. : CONTRAST ON A HYPOECHOIC CYST FOR DIFFERENT TRANSMISSION SCHEMES

Sequence/ Image quality	8 MLT Linear Transmission	8 MLT Diagonal Transmission
CNR at focal point (4 cm)	0.91 dB	-2.17 dB

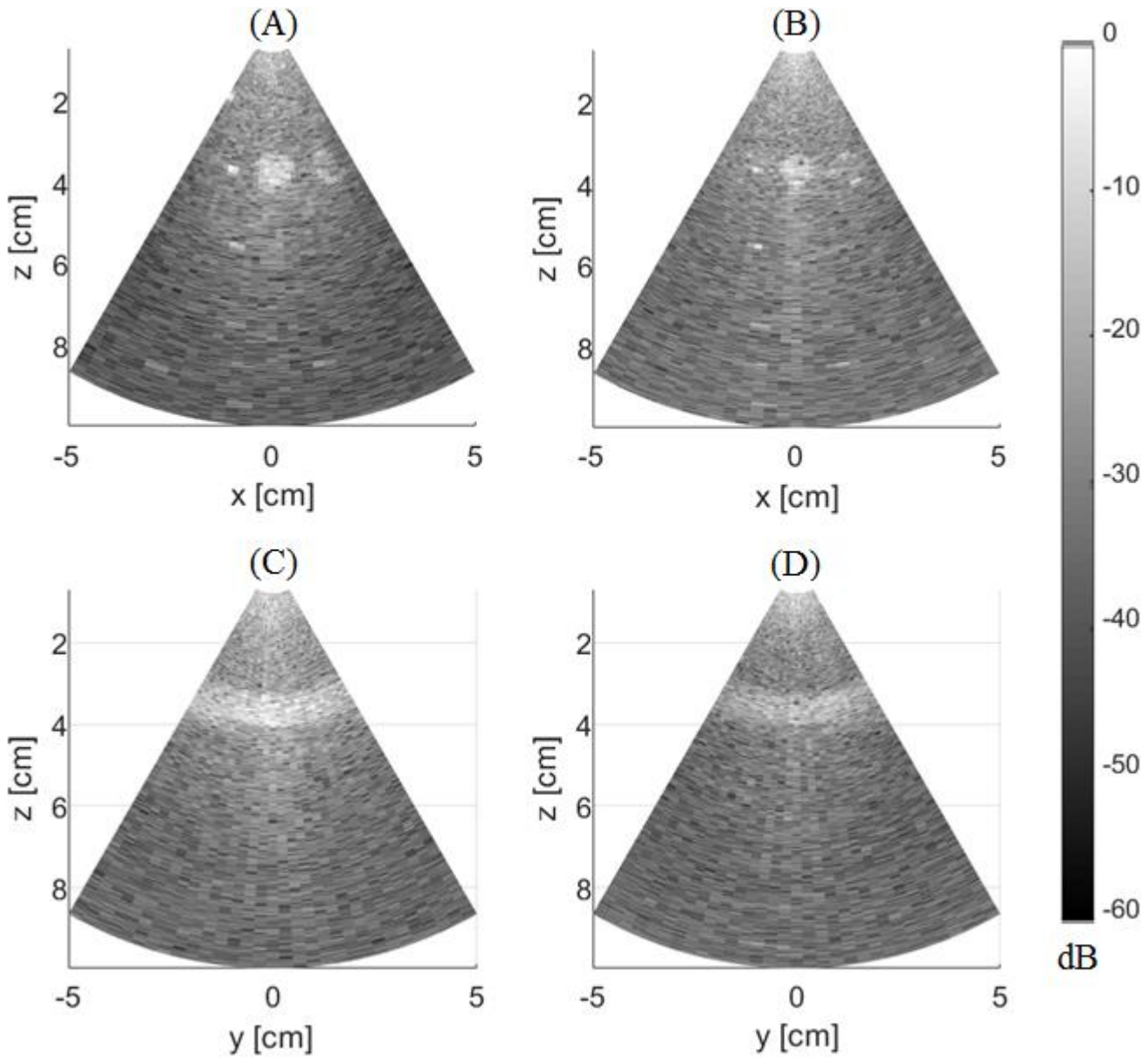

Fig. 56. Comparison between the 8 MLT CIRS phantom results using the linear transmission scheme (left) and the diagonal transmission scheme (right) for both XZ (A, B) and YZ planes (C, D).

TABLE VIII: CONTRAST ON A HYPERECHOIC CYST FOR DIFFERENT TRANSMISSION SCHEMES

Sequence/ Image quality	8 MLT Linear Transmission	8 MLT Diagonal Transmission
CNR at focal point (4 cm)	5.97 dB	2.03 dB

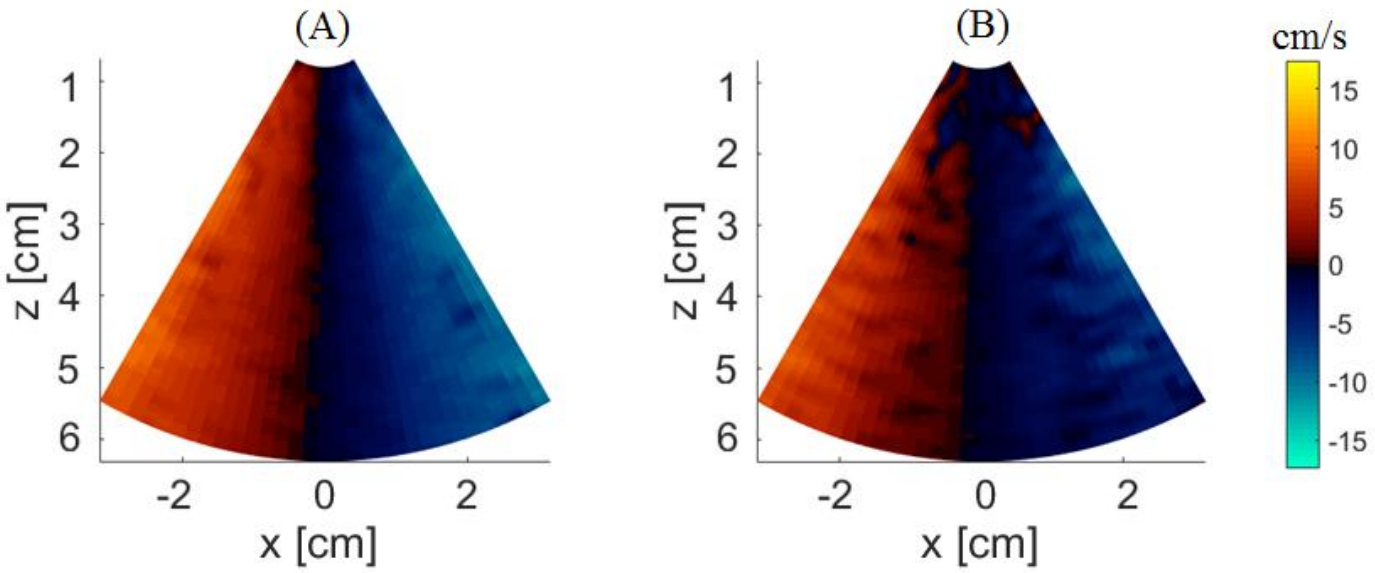

Fig. 57. Velocity maps obtained with the linear transmission scheme (A) and with the diagonal transmission scheme (B) for the middle XZ plane

4.4. DISCUSSION

For the first part of this study, we concentrated on proving the feasibility of experimental MLT 3D in both static and dynamic conditions.

The feasibility in static conditions was presented in Fig. 50, where we showed that orthogonal sections of a 3D volume could successfully be reconstructed from experimental MLT data. As shown in Fig. 51, the image quality degraded with the number of simultaneous transmissions. While the contrast had a value of 3.60 dB for the linear transmission it was reduced by 15 % for 4 MLT (3.02 dB) and up to 27% (2.61 dB) for the highest number of transmissions considered in this study (16 MLT). In the same time, the axial resolution degraded from 0.33 mm to 0.61 mm with a 16-fold increase in frame rate.

Once the image quality was evaluated in static conditions, we extended our study to dynamic conditions. The feasibility of tissue Doppler velocity estimation for 3D MLT ultrasound imaging has also been demonstrated as shown in Fig. 52. The results proved that accurate estimators can be obtained despite the eight-fold increase in frame rate.

In spite of proving the experimental feasibility of MLT in 3D and in spite of the potential demonstrated in both static and dynamic conditions, a limitation of the first part of this study was that it was restricted to a basic implementation. The transmission settings were not further improved, therefore the results showed the worst case scenario for 3D MLT, especially in terms of image quality. For example, the transmission scheme was a linear one, along the columns of the transducer. Given the 2D geometry of the probe, the simultaneous transmissions could have been better separated for cross-talk reduction. Moreover, the initial excitation signal was on for a very short time, limiting the penetration depth.

To cope with these limitations, the second part of this study was focused on improving the transmission parameters. As shown in Fig. 48, by aligning the transmissions along the transverse diagonal

of the transducer, the spacing between the simultaneous transmissions was increased. Therefore the interference between the beams was reduced which impacted the image quality as shown in Fig. 53. Qualitatively, for both XZ and YZ planes, the axial resolution targets seemed to be thinner for the images obtained using the diagonal transmission scheme compared those obtained using the linear one. The axial resolution values measured at the focal point confirmed this observation (Table VI). Moreover, the axial profiles provided in Fig. 54 showed that there was indeed a non-negligible difference between the main and the side lobes when the two transmission schemes were used. While the difference was just 2.84 dB for the linear transmission, it increased to 10.77 dB when the diagonal transmission was used for the XZ plane (B). Similarly, for the YZ plane, the difference was 2.98 dB for the first case and 12.26 dB for the second one (D). Overall, the main lobe was up to 5% higher than the side lobe for the linear transmission and up to 25 % higher for the diagonal one. As the cross-talk appears as a result of the main and side lobes interactions, a higher difference can be associated with a lower cross-talk level.

Despite the negative impact of the linear transmission on the resolution, the higher superposition of the beams provided higher main lobes intensity (Fig. 54 A, C) for depths higher than 1 cm, compared to the diagonal transmission. This can explain the brighter intensity appearance of Fig. 55 A (obtained for a linear transmission) compared to Fig. 55 B (obtained for a diagonal transmission), especially for the background region surrounding the hypoechoic cyst which was used for computing the CNR. According to equation (3.7) used for CNR calculation, we expect higher absolute difference between the background and the cyst ($|\mu_{bck} - \mu_{cyst}|$), which depending on the differences in variance between the images resulted from the two transmission schemes, may lead to a better CNR for the linear transmission. The values presented in Table VII, confirmed the qualitative evaluation, showing a CNR which was 3 times higher for the linear transmission. Similarly, although the hyperechoic cyst in Fig. 56 (B) was better defined than the one in (A) due to the better resolution, the contrast seemed higher for the linear transmission (A, C). The calculated values in Table VIII showed indeed a CNR ratio of 3 between the two. Note that the contrast value presented in Table VIII for the linear transmission is higher than the one shown in Table V (forth column, third row) for the same phantom and transmission scheme. This can be explained by the different excitation signals used for the two cases. The longer duty cycle of the excitation signal also improved the penetration depth (Fig. 51 C compared to Fig. 56 A).

When tested in dynamic conditions, the diagonal transmission gave a noisier velocity map than the linear one (Fig. 57). That can be explained by the fact that the velocity was estimated in planes different from the transmissions ones, while for the linear scheme the planes were the same. Analyzing further different MLT configurations would allow obtaining the optimal compromise between high volume rate and quality color Doppler.

A first limitation of this study was that the 1-D Doppler velocities were estimated from 3D volumes. The extension of the velocity estimator in 3D would enable a complete quantification of the heart velocities. An interesting approach for estimating 3D velocity vectors, based on Transverse Oscillations, was proposed in (Pihl & Jensen 2014), (Salles, et al. 2015). Although applying such a method for cardiac applications had been shown to be challenging (Joos 2017), this technique proved promising results when tested on a flow-rig system with steady flow (Pihl et al. 2013), in simulations and on a gelatin phantom (Salles, et al. 2015).

A second limitation of this study comes from the method used for dealing with the beams superposition. Since the conversion from the superposed signal to the tristate signal was done through a

threshold, we did not compensate for a high amplitude superposition by a higher duty cycle. Therefore, our method is an approximation of the real superposition. Using Pulse Width Modulation (PWM) approach could lead to a more precise approximation. However, for a high number of transmissions, PWM would allocate a high duty cycle for a maximum superposition of the signals compared to the duty cycle allocated for a low superposition. Depending on the pattern of the overlapping signals, low amplitude signals could be coded as tristate pulses fixed on a polarity less than 3 samples. Our in hand system needs at least 3 samples to commute from one polarity to another. Therefore, PWM could also lead to important approximations. Adapting the classical PWM according to the capabilities of the hardware would be worthwhile for increasing the precision of the current MLT implementation.

Despite these limitations, this study successfully showed, for the first time, the experimental feasibility of MLT 3D in both static and dynamic conditions. Although we improved the resolution obtained using a linear transmission scheme by distributing the beams in diagonal, the contrast and the tissue Doppler estimates were affected. The compromise between cross-talk reduction and other image quality metrics were also reported by other authors. For instance, (Tong et al. 2014) showed that a Tukey apodization can reduce significantly the cross-talk, but with the compromise of the lateral resolution. Other studies proposed using filtered delay multiply and sum (FDMAS) beamforming for limiting the cross-talk but this was achieved at the cost of a CNR degradation compared to conventional DAS (Matrone et al. 2017).

4.5. CONCLUSION

The results presented in the first part of this chapter indicate the experimental feasibility of MLT in 3D and its potential for achieving high contrast and resolution while increasing the frame acquisition rate, even for a simple transmission scheme and when no apodization is used. When tested on dynamic acquisitions, the MLT volume rate was increased 8 times while the image quality was preserved to allow accurate velocity estimators. Using 3D MLT could allow new advancements in ultrafast color Doppler.

The results presented in the second part of this chapter showed that the MLT cross-talk artefacts could be reduced by aligning the simultaneous transmissions in diagonal. However, the contrast and the Doppler velocity maps were affected compared to the linear transmission.

CHAPTER 5:

VALIDATION OF HIGH-FRAME RATE VELOCITY ESTIMATION APPROACHES ON A VORTEX RING PHANTOM

*Parts of this work were presented as:

1. Emilia Badescu, Denis Friboulet, Hervé Liebgott, Damien Garcia, "Time resolved imaging of vortex rings with ultrafast ultrasound: an *in vitro* study", *Frontiers of Simulation and Experimentation for Personalized Cardiovascular Management and Treatment, London, UK, July, 2018*

2. Emilia Badescu , Simone Ambrogio , John Fenner , Hervé Liebgott , Denis Friboulet , Damien Garcia, "Vortex ring phantom for investigation of ultrasound vector flow ", *IEEE International Ultrasonics symposium, Kobe, Japan, October 2018*

5.1. INTRODUCTION

The emergence of high-frame-rate ultrasound imaging has enabled important progress in blood flow quantification, as it makes it possible to acquire wide-field of view data at fine temporal steps. Before considering bench-to-bedside translation, there is a need in evaluating the multi-component time-resolved velocity fields provided by the new imaging methods. As discussed in section 2.5, *in vitro* test objects can be used to perform such an evaluation, since they provide realistic experimental conditions.

Several such test devices have been proposed over time. A simple example is given by the flow tubular phantoms through which a blood mimicking fluid is usually pumped (Law et al. 1987), (Hoskins et al. 1989). Although the first attempts used c-flex rubber for constructing the walls of the vessels, this material caused the distortion of the ultrasound wave (Robin Steel & Fish 2002), which motivated the use of the vessel mimicking materials (King et al. 2011), (Zhou et al. 2017). Even if these phantoms provide a good experimental model, having close acoustic properties to soft tissue, arterial wall, and blood, they do not take into account important anatomical features such as arterial branching. In order to cope with this limitation, carotid bifurcation test objects have been proposed, which increase the complexity with respect of both anatomy and blood perfusion (Poepping et al. 2002), (Meagher et al. 2007). Other authors focused on developing rotating disk phantoms (Kripfgans et al. 2006), that could better describe the features of *in vivo* flow, by producing a wide range of velocities. Additionally, assessing multi-directional flow has become possible thanks to the rotating spiral flow *in vitro* model proposed by (Yiu & Yu 2017).

Although significant progress has been made over the years for increasing the complexity of the test objects and providing realistic physiological flows, the above-mentioned phantoms are still insufficient for characterizing a distinguishing feature of the intraventricular flow: the formation of vortices. Studying the vortex dynamics has been shown to reveal unstable physiological conditions that could allow early identification of cardiac abnormalities (Pedrizzetti et al. 2014). A realistic test object that allows simulating the left heart circulation and the vortex formation has been proposed in (Tanné et al. 2010). Although the validation of this phantom using vector flow mapping in conventional ultrasound successfully revealed the vortex dynamics (Garcia et al. 2010), this model presented the limitation of not being easily controllable and transportable. The ring vortex phantom proposed in (Ferrari et al. 2018) overcomes these limitations by offering a stable, reproducible and controllable model. Moreover, it allows the possibility to generate vortices at different sizes and velocities. Thus, it provides many features that are particularly interesting for the validation of high frame rate ultrasound vector flow methods.

In this context, the objective of this preliminary study was to evaluate if the vortex phantom is a good candidate for quantifying complex flows using ultrasound high frame rate methods. Both 2D and 3D acquisitions were conducted for attaining the mentioned purpose.

5.2. METHODS

5.2.1. Vortex ring

A vortex ring is a toroidal volume of fluid moving along the axis perpendicular to the torus plane (x axis). The velocity along this axis (V_{trans}), represented in red in Fig. 58, is called translational. The toroidal vortex ring moves together with a flattened ellipsoidal volume which embraces it, called vortex atmosphere. Inside the vortex atmosphere, the fluid circulates along the closed streamlines surrounding the toroidal core (Akhmetov 2009). The toroidal core is constituted by concentric circles rotating at the angular velocity ω. The angular velocity together with the radius of the concentric circles give the rotational velocity, V_{rot} , as represented in green in Fig. 58.

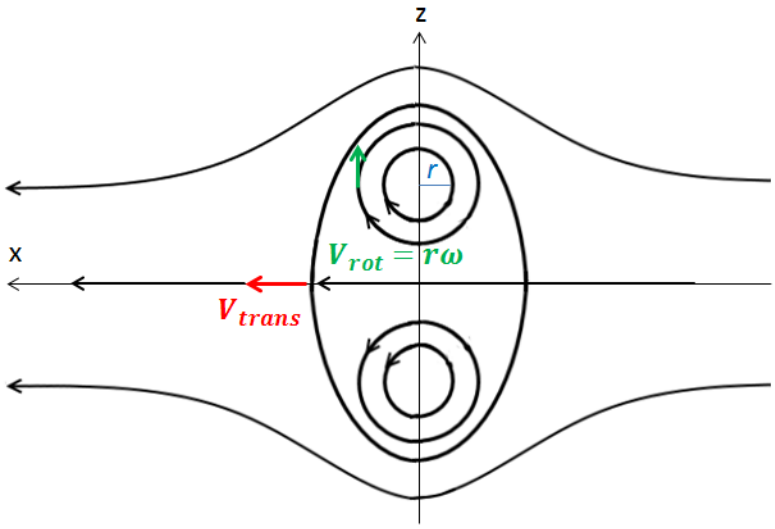

Fig. 58. Streamline pattern of the vortex ring: The most exterior flattened ellipsoidal volume represents the vortex atmosphere. Inside, the fluid circulates along the closed streamlines that surround the vortex core.

For generating such a vortex ring model in practice, a cylinder-piston mechanism that ejects the fluid through a circular orifice can be used. Such a system will be described in the next section.

5.2.2. *In vitro*-model

Our *in vitro*-model was a more recent prototype of the liquid-based vortex phantom proposed in (Ferrari et al. 2018), developed by the same authors and built in the framework of the VPH-CaSE Marie Curie European project. The main components of this system are shown in Fig. 59. The laptop/PC containing the Arduino software is connected to the Arduino Uno microcontroller (ATmega328) included in the electronic components box. Thus, several parameters can be changed in the software for controlling the pins responsible for the generated pulse. These pins serve as input control signals for the DM542 digital stepper driver (OMC Corporation Limited, Nanjing, China). The stepper driver is supplied with a

power of 150 W (OMC Corporation Limited, Nanjing, China) to achieve good driving performances of the stepper motor (Nema 23 OMC Corporation Limited, Nanjing, China). The motor drives the threaded screw of length 150 mm which is connected to the plunger thanks to the nut embedded at one of its ends. On the other end, the piston head of the plunger has a crucial role in pushing the fluid: first along the cylinder and then, through the orifice. As a result, the fluid rolls up (Fig. 59, left bottom rectangle) and the generated vortices travel further along the tank, having the dimensions 15 cm (W) x 35 cm (L) x 16.5 cm (H). The phantom allows changing the diameters of the orifice.

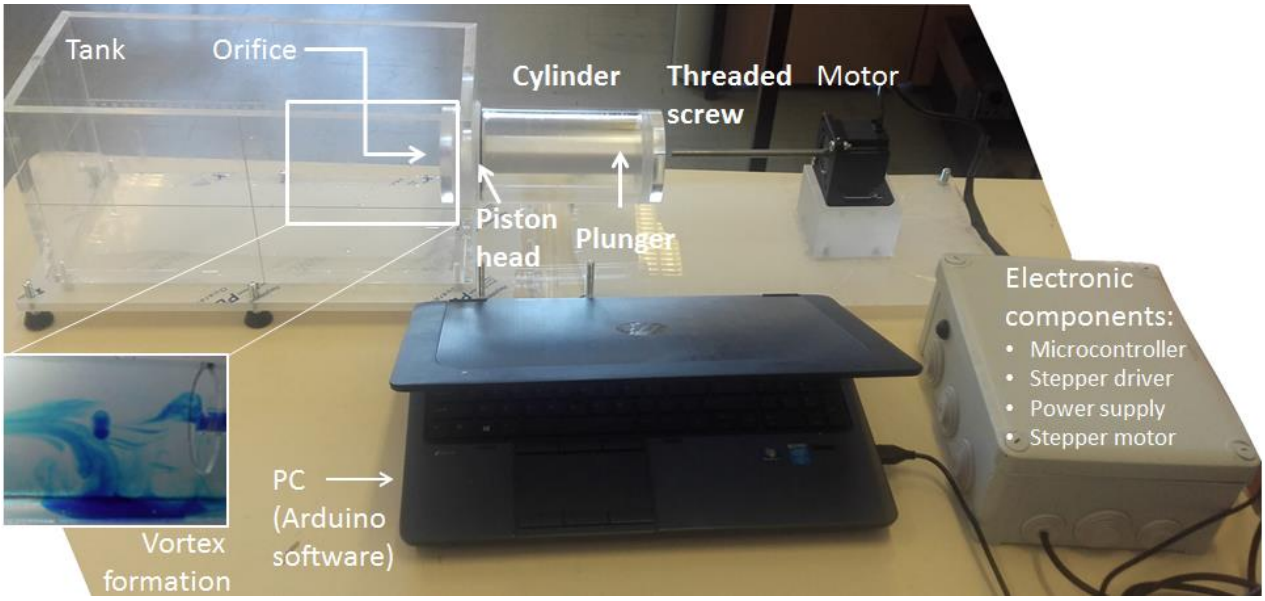

Fig. 59. *In vitro* vortex system: The PC (Arduino software) allows controlling the pins responsible for the generated pulse, belonging to the microcontroller. These pins serve as input control signals for the digital stepper driver which is supplied with a power of 150 W to achieve good driving performances of the stepper motor. The motor drives the threaded screw which is connected to the plunger thanks to the nut embedded at one of its ends. On the other end, the piston head of the plunger has a crucial role in pushing the fluid: first along the cylinder and then, through the orifice. As a result, the fluid rolls up and the generated vortices travel further along the tank. Such a vortex formation for a water-ink experiment is illustrated in the left bottom rectangle.

The fluid contained in the tank was a mix of water and glass hollow spheres (110P8, LaVision GmbH, Germany) having an average diameter within the range of [9 13] μm. The concentration of the glass hollow spheres was adjusted to increase the backscattered signal and consequently to improve the velocity estimates.

5.2.3. 2D Acquisition set-up

Ultrasound 2-D images were acquired using a Vantage 256 research scanner (Verasonics Inc., Redmond, WA) controlling a 5-MHz linear transducer (ATL L7-4, 128 elements). We placed the probe at approximatively 10 cm away from the orifice as shown in Fig. 60 A. Series of unsteered plane waves were

then transmitted through the seeded fluid and sets of vortex images were acquired in the plane shown in Fig. 60 B.

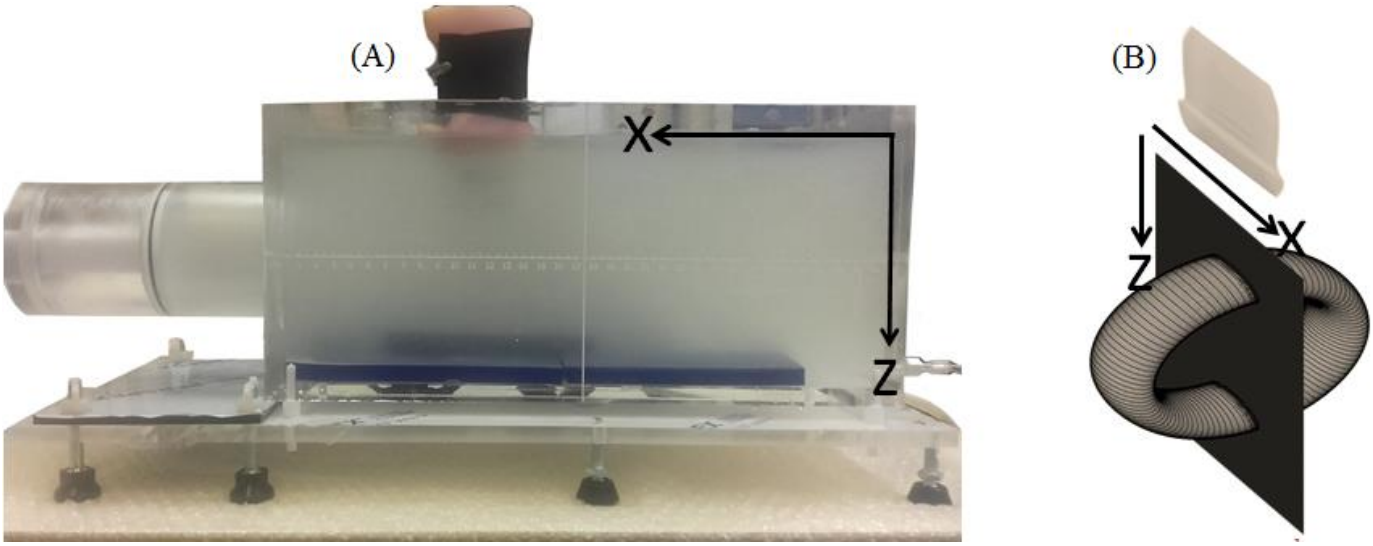

Fig. 60. The position of the probe was placed at approximatively 10 cm away from the orifice (A), which allowed imaging vortex planes as showed in (B)

5.2.4. 3D Acquisition set-up

Ultrasound volumes were acquired using four Vantage 256 scanners (Verasonics, Kirkland, WA, USA) synchronized to control a 3-MHz 2D transducer (Vermon, Tours, France), as briefly described in section 4.2.1. For more details about the 3D system, the reader can refer to (Petrusca et al. 2018).

5.2.5. Vector flow velocity estimation

First, for 2D acquisitions, we estimated the vortex velocity fields using 1) echo-PIV by tracking the real-envelope speckle patterns using phase correlation (section 2.3.2.1); and 2) vector Doppler by using a receive dual-beam approach, as described in (Jensen et al. 2016b) and section 2.3.1. For vector Doppler, the signals were beamformed at two receive angles (± 15º).

Second, since we did not have a reference at the time of the acquisitions, we acquired multiple sets of acquisitions for investigating a potential link between different components of the velocity. We retrieved the maximum rotational component from the Doppler velocity estimates as shown in green in Fig. 61. Multiple Doppler maps estimated at different instants of the time were used for retrieving the translational component. For a better illustration of this process, we show in Fig. 61 the Doppler maps over a longer time than the one used for the estimation (1s compared to tens of ms). For estimating the translational component, we used a phase correlation method. Various diameters and velocities (2 and 2.5 cm, 1-7 cm/s) of the vortex phantom were used for this analysis. Totally, we acquired 21 datasets consisting of 49 frames each. For each dataset, we estimated 15 pairs of rotational-translational velocity components.

Third, for 3D acquisitions, we estimated Doppler velocity fields using a 2D autocorrelator applied on the IQ data as described in (Kasai et al. 1985), (Loupas et al. 1995).

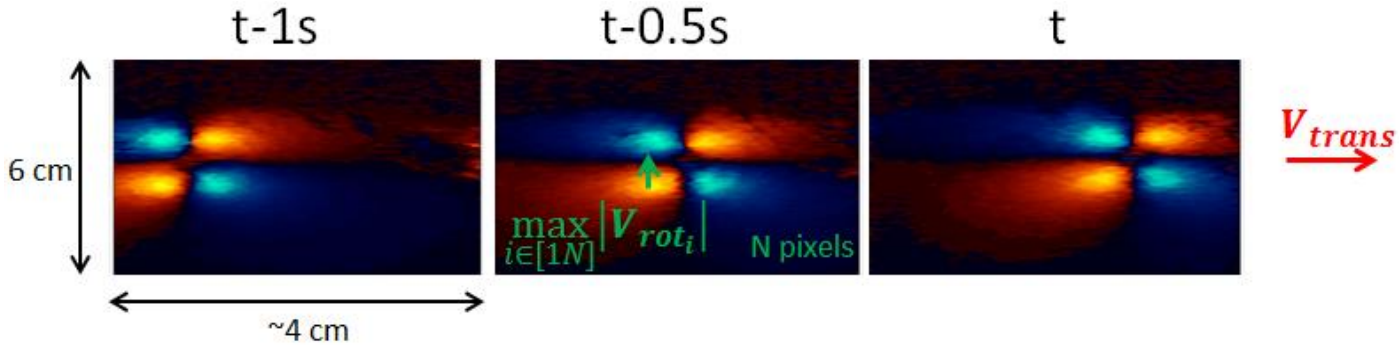

Fig. 61. Multiple Doppler maps estimated at different time instances were used for determining the translational component of the velocity using phase correlation.

5.3. RESULTS

5.3.1. 2D results

The velocity maps are shown in Fig. 62 for both Echo-PIV (A) and Vector Doppler (B).

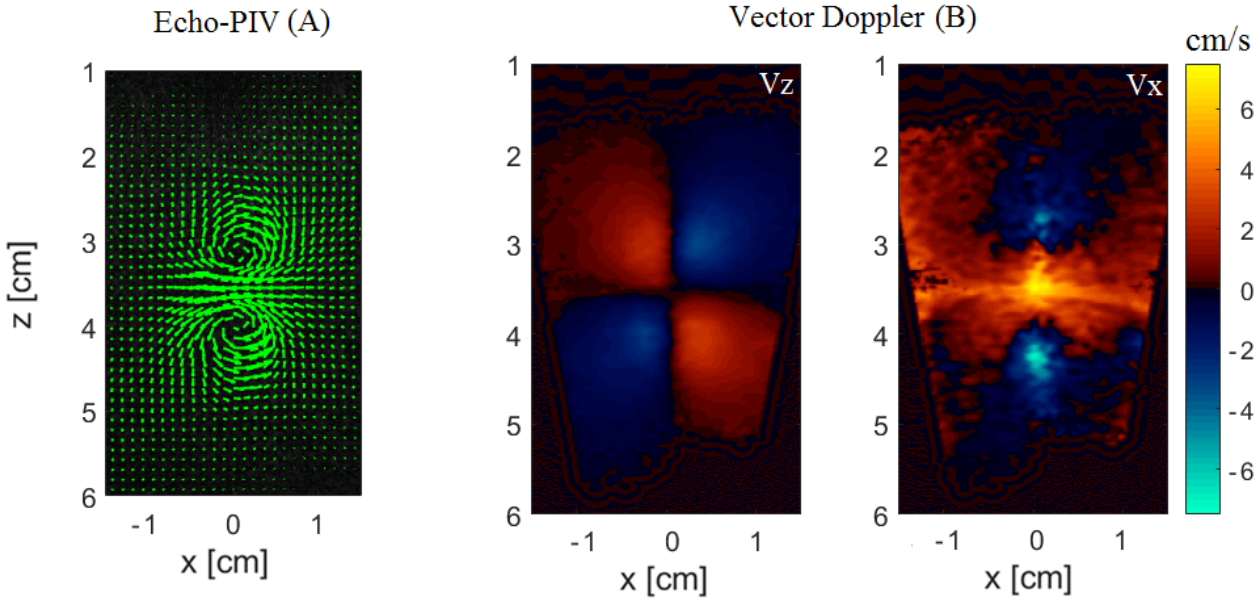

Fig. 62. Velocity estimation using Echo-PIV (A) and Vector Doppler (B) for z (left) and x (right) directions

The link between the rotational and translational velocity is shown in Fig. 63, where each set of points corresponds with a different set of acquisitions, acquired for a different translational velocity (between 1-7 cm/s) and for one of the two diameters: 2.5 cm (blue) and 2 cm (black). For each set of acquisitions, we show the median over 15 estimates and their deviation from the median (calculated as the absolute

difference between the median and the min/max estimated value over the 15 pairs). The regression curve between the two velocity components is shown in red.

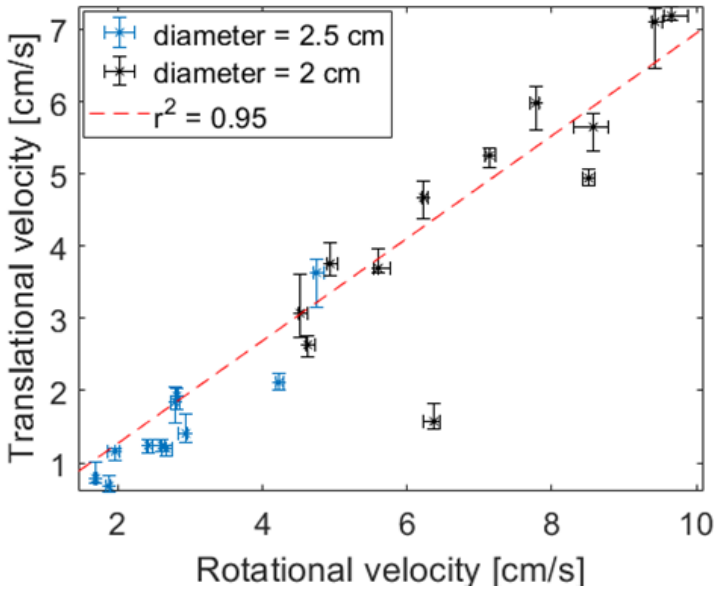

Fig. 63. Linear relationship between the rotational and the translational velocities for 2 orifice diameters (2.5 cm and 2 cm)

5.3.2. 3D preliminary results

Fig. 64 shows the Doppler maps obtained from a volumetric insonification of the vortex ring. Both xz and yz velocity maps are provided.

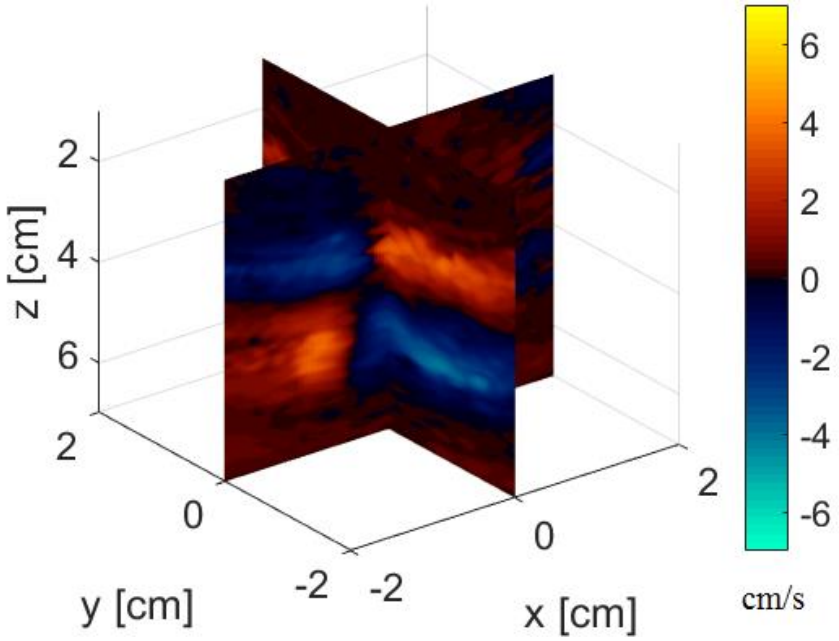

Fig. 64. 1D Doppler velocity components for xz and yz planes

5.4. DISCUSSION

Our preliminary results showed a good concordance with the geometry and kinematics of the toroidal vortices, which demonstrates that high-speed echo-PIV and vector Doppler by ultrafast ultrasound can be successfully used to evaluate the dynamics of cardiac-type vortices (Fig. 62). When the link between the rotational and translational speeds was investigated, the two velocity components were highly correlated ($r2 = 0.95$, Fig. 63), in accordance with theory (Tinaikar et al. 2018). Although this shows a stable phantom behavior at a given position of the vortex propagation, a limitation of this study is that we did not compare our results with a reference. When developing new imaging-based diagnostic tools, it is extremely important to evaluate their accuracy and reproducibility. Indeed, this can have a great impact on the clinical decision and it can affect the diagnosis of the patient. For example, if the system overestimates the peak systolic velocity, a patient could be misclassified as having severe stenosis, which would drastically change its treatment from medication to surgery (Hoskins 1996). This is the reason why a precise knowledge of the ground truth of the phantom velocities is necessary; otherwise, it is impossible to evaluate quantitatively the performance of a given imaging method. Therefore, an important perspective of this study would be comparing the ultrasound results with the analytical model or with computational fluid dynamics simulations. Another interesting solution could be comparing the echo PIV with optical PIV as done in conventional ultrasound (Kheradvar et al. 2010). Furthermore, an MRI compatible prototype of the phantom would allow comparing the ultrasound velocity vectors against the alternative imaging modality as done for vorticity in (Faurie et al. 2017).

In spite of the current difficulty in providing a quantitative measure of accuracy, our promising 2D results in revealing the vortex kinematics, motivated us to extend our study to 3D. As observed in Fig. 64, in addition to the axial Doppler velocity component available, when using a 1D array (Fig. 62 B, Vz), 2D array acquisitions also allowed computing the sagittal Doppler component. Extending further the Doppler and the echo PIV approaches to 3D could offer a complete three-dimensional vector field.

The 2D and 3D results presented in this study are very preliminary. Nevertheless, we showed the compatibility of the vortex ring generator with the ultrasound system.

5.5. CONCLUSION

High frame rate ultrasound can successfully be used to estimate complex vector flows such as the ones characterizing the ring vortices. 2D echo PIV and vector Doppler appear to be capable to recover the vortex velocity maps. Preliminary 3D Doppler results showed that the Doppler velocities along both xz and yz planes can be recovered from series of volumetric insonifications.

Overall, this study showed that the vortex ring phantom represents a good candidate for optimizing and validating ultrasound flow imaging methods in controllable, non-stationary, three-dimensional complex flows.

General conclusion

Cardiac motion has been actively studied over the past decades thanks to its potential to evaluate the contractility properties of the myocardium. Despite the enormous progress done over the past years in cardiac ultrasound imaging allowing its current clinical capabilities (Chapter 1), several aspects could still be improved, as the frame rate and the common usage of 3D imaging. As a response, high frame rate methods have been proposed and extended to 3D by the ultrasound research community as explained in Chapter 2. The objective of this thesis was to evaluate those new approaches in realistic conditions, as close as possible to those of a future clinical translation. Among these methods, an important gain in frame rate at good image quality has been achieved with Multi-Line Transmission (MLT) and Diverging/Plane Wave (DW/PW) imaging. This motivated us to focus on these two approaches in this thesis.

In this context, our first objective was to compare MLT and DW in phased arrays configurations in order to determine if one method is more appropriate than the other for cardiac 2D imaging (Chapter 3). Based on our results, it can be affirmed that DW provides a better image quality at relatively low depths, where the low inter-beam spacing of MLT causes cross-talk artefacts. However, MLT allows a better image quality close to the focal point that can be placed at higher depths. Regarding the influence of the two high frame rate approaches on speckle tracking and tissue Doppler imaging, close Normalized Root Square Errors (NRSE) were obtained for the two cases: DW MoCo performed slightly better than MLT for the speckle tracking lateral estimates while MLT performed slightly better than DW MoCo for tissue Doppler estimates. However, for a higher packet size, DW would perform better and the Doppler frame rate would be significantly higher as the one achievable with MLT. In consequence, the two methods proved to be very competitive, each one having its advantages and limitations. Thus, no clear-cut conclusion can be deduced from our results and the choice of using one method to the other has to be adapted depending on the application.

Motivated by our promising 2D results but also by the potential of 3D imaging in allowing new advancements in diagnosis, our second objective was to extend one of the high-frame rate methods presented in Chapter 3 in 3D. Once we proved the MLT 3D feasibility in static conditions, we showed using the rotating disk phantom that accurate Doppler maps can be obtained from MLT 3D data. However, all the results obtained for the feasibility study were produced using a transmission along the planes of the volume. A better separation of the transmitted beams was achieved in the second part of this study by distributing the simultaneously focused beams along the entire volume. Although that resulted in a thinner appearance of the resolution inclusions, the CNR was affected and the Doppler maps were noisier. Investigating the impact of both transmission schemes on a more complex *in vitro* model could provide an additional outcome that could eventually lead to clinical translation of the method giving the most suitable compromise.

In this context, the last objective of this thesis was to evaluate the potential of a new complex *in vitro* model for validating high frame rate motion estimation methods. More specifically, our model was a vortex ring generator. For simplicity, we started our evaluation in 2D, using echo PIV and dual cross beam Doppler approaches. The vortex kinematics was successfully revealed by using the two approaches. Additionally, by acquiring multiple acquisitions at various velocities and diameters, we observed a linear

regression between the rotational and translational velocity components, as expected from the theory. Then, we extended our study to 3D acquisitions. However, our 3D results are still preliminary and further work is required for a complete 3D analysis.

Overall, in this thesis we developed, implemented and tested high frame rate approaches for 2D and 3D cardiac imaging in order to reveal their advantages, test their limits and assist in decision making towards clinical translation.

General limitations and perspectives

The first contribution presented in this thesis was a comparison between two high-frame rate methods: MLT and DW, performed in both static and dynamic conditions. However, an important limitation of this study is that the acquisition settings were not optimized for each method individually in order to perform a comparison in the best case scenario for each technique. This can be explained by the hardware constraints that restricted us to use a short excitation signal for MLT. To compare the two methods in equivalent conditions, we balanced the total transmitted power by adapting the excitation signal for DW accordingly. Using relatively longer excitation signals for both methods would have allowed a better penetration depth, contrast, and signal to noise ratio. Moreover, the MLT sequence could have been further optimized for aiming at cross-talk reduction. The flexibility in choosing the desired signal would have allowed us to investigate if a coded excitation (based on chirps, Golay codes) could be a good candidate for this purpose. Alternative approaches to cope with the limitation of a basic implementation of MLT where no cross-talk reduction was considered could be: using a proper apodization (Tong, Gao, et al. 2013), the Filtered-Delay Multiply and Sum beamforming (Matrone et al. 2017), the Minimum Variance beamforming (Rabinovich et al. 2015) or dividing the bandwidth of the transducer into sub-bands used for simultaneous transmissions (Demi et al. 2013)

Another limitation is that we calculated the average contrast over 4 inclusions of the rotating disk phantom without resetting the position of the phantom before each acquisition. Although we could observe the trend of MLT to provide a better CNR than DW MoCo for all the velocities and frame rates, the curves presented slight deviations due to the different positions of inclusions taken into account. Another limitation comes from the choice of the packet size value used for Doppler estimates. In order to keep an acceptable Doppler frame rate for MLT imaging, we used a packet size of 8. However, using just 8 diverging waves for MoCo is not optimal to minimize the compound sidelobes (Poree et al. 2016). An alternative choice would have been to compare the two methods at the same Doppler frame rate instead of the same packet size.

The second contribution of this thesis was the experimental implementation of MLT in 3D. Although we showed its feasibility, the method used for generating the codes corresponding to the excitation matrix could be further improved. More specifically, we compared the superposed signal to a threshold for generating the tristate pulse, which reduces the sensitivity of the method to the amplitude variations. An improvement could be achieved by compensating for the high-amplitude signals by longer duration signals as usually done in Pulse Width Modulation (PWM).

A second aspect related to our second contribution that could be further investigated is the minimum number of transmissions that could be used at an acceptable image quality. Although in this work, the total number of transmissions was reduced down to 64, compared to 1024 used for obtaining a full 32 by 32 volume in SLT, this number is still considerably higher than the one that could be used in DW imaging. For example, (Provost et al. 2014) showed that the resolution remains high even for a single DW transmission, the contrast stabilizes starting with 36 virtual sources and one single transmission is enough for blood flow

quantification. However, increasing the number of simultaneous focused beams to achieve DW-equivalent volume rates would increase the amount of cross-talk artefacts. Even if we showed that arranging these beams along the transverse diagonal of the transducer could reduce the cross-talk level, this method presented the limitation of reducing the contrast. Investigating the optimal arrangement of the beams for achieving the best compromise between cross-talk suppression and image quality by simulations can also be considered as a perspective. Once this is realized, the performance of MLT at volume rates comparable to the ones achievable in DW imaging could assist in the choice of the method to be considered for clinical translation.

A third limitation and therefore perspective of our second contribution is that the velocity estimator used on 3D MLT data was not extended to provide 3D vector fields. Moreover, our *in vitro* model was the tissue mimicking disk undergoing a relatively simple motion. Since the full volume is not insonified at once when using MLT, the precision of some motion estimators such as speckle tracking may be affected for models undergoing a high and a complex motion.

Our third contribution focused on validating high frame rate methods on such a complex phantom. Although the kinematics of the ring vortex was successfully recovered with two commonly used motion estimation methods, we could not provide the accuracy of these methods, since we did not have a reference. A perspective of this study is comparing the ultrasound vector fields with those obtained analytically, from computational fluid dynamics simulations or from optical approaches. Having a reference would also allow testing the high frame rate methods investigated in our previous contributions in more complex conditions. Additionally, similarly to our 3D MLT work, our preliminary 3D study could be extended to provide 3D vector fields.

In conclusion, the long-term perspective of this work would be the 3D velocity field assessment using volumetric high frame rate imaging. Testing this approach on the vortex phantom and comparing the obtained results with a reference would be the first step for accuracy evaluation. Finally, the translation *in vivo* would reveal the clinical advantages of volumetric high frame rate imaging.

Akhmetov, D.G., 2009. Theoretical Models of Vortex Rings. In *Vortex Rings*. Berlin, Heidelberg: Springer Berlin Heidelberg, pp. 5–32.

Alessandrini, M. et al., 2015. A Pipeline for the Generation of Realistic 3D Synthetic Echocardiographic Sequences: Methodology and Open-Access Database. *IEEE Transactions on Medical Imaging*, 34(7), pp.1436–1451.

Altiok, E. et al., 2014. Comparison of Two- and Three-Dimensional Transthoracic Echocardiography to Cardiac Magnetic Resonance Imaging for Assessment of Paravalvular Regurgitation After Transcatheter Aortic Valve Implantation. *The American Journal of Cardiology*, 113(11), pp.1859–1866.

Amin, V.R., 1989. *Ultrasonic attenuation estimation for tissue characterization*. Ames: Iowa State University, Digital Repository.

Barron, J.L., Fleet, D.J. & Beauchemin, S.S., 1994. Performance of optical flow techniques. *International Journal of Computer Vision*, 12(1), pp.43–77.

Bertrand, P.B. et al., 2016. Fact or Artifact in Two-Dimensional Echocardiography: Avoiding Misdiagnosis and Missed Diagnosis. *Journal of the American Society of Echocardiography : official publication of the American Society of Echocardiography*, 29(5), pp.381–91.

Betts, J.G. et al., 2013. *Anatomy and Physiology*, OpenStax.

Bouchard, R.R. et al., 2009. *In Vivo* Cardiac, Acoustic-Radiation-Force-Driven, Shear Wave Velocimetry. *Ultrasonic Imaging*, 31(3), pp.201–213.

Bujoreanu, D., Friboulet, D. & Nicolas, B., 2017. Simultaneous coded plane wave imaging in ultrasound: Problem formulation and constraints. In *2017 IEEE International Conference on Acoustics, Speech and Signal Processing (ICASSP)*. IEEE, pp. 6254–6258.

Burckhardt, C.E., Grandchamp, P.-A. & Hoffmann, H., 1974. An Experimental 2 MHz Synthetic Aperture Sonar System Intended for Medical Use. *IEEE Transactions on Sonics and Ultrasonics*, 21(1), pp.1–6.

Carmody, K., 2011. *Handbook of critical care and emergency ultrasound*, McGraw-Hill.

Céspedes, I. et al., 1995. Methods for Estimation of Subsample Time Delays of Digitized Echo Signals. *Ultrasonic Imaging*, 17(2), pp.142–171.

Chan, V. & Perlas, A., 2011. Basics of Ultrasound Imaging. In *Atlas of Ultrasound-Guided Procedures in Interventional Pain Management*. New York, NY: Springer New York, pp. 13–19.

Cikes, M. et al., 2014. Ultrafast Cardiac Ultrasound Imaging. *JACC: Cardiovascular Imaging*, 7(8), pp.812–823.

Couade, M. et al., 2011. In Vivo Quantitative Mapping of Myocardial Stiffening and Transmural Anisotropy During the Cardiac Cycle. *IEEE Transactions on Medical Imaging*, 30(2), pp.295–305.

Demi, L. et al., 2013. Implementation of parallel transmit beamforming using orthogonal frequency division multiplexing-achievable resolution and interbeam interference. *IEEE Transactions on Ultrasonics, Ferroelectrics, and Frequency Control*, 60(11), pp.2310–2320.

Demi, L., Verweij, M.D. & Van Dongen, K.W.A., 2012. Parallel transmit beamforming using orthogonal frequency division multiplexing applied to harmonic Imaging-A feasibility study. *IEEE Transactions on Ultrasonics, Ferroelectrics and Frequency Control*, 59(11), pp.2439–47.

Denarie, B.., Bjastad, T.. & Torp, H.., 2013. Multi-line transmission in 3-D with reduced crosstalk artifacts: a proof of concept study. *IEEE Transactions on Ultrasonics, Ferroelectrics, and Frequency Control*, 60(8), pp.1708–1718.

Denarie, B. et al., 2013. Coherent Plane Wave Compounding for Very High Frame Rate Ultrasonography of Rapidly Moving Targets. *IEEE Transactions on Medical Imaging*, 32(7), pp.1265–1276.

Dénarié, B.E., 2014. *Real-time 3-D echocardiography:challenges of parallel transmission and acquisition*. Norwegian University of Science and Technology Faculty of medicine.

Dunmire, B. et al., 2000. Cross-beam vector Doppler ultrasound for angle-independent velocity measurements. *Ultrasound in medicine & biology*, 26(8), pp.1213–35.

Fadnes, S. et al., 2017. In vivo intracardiac vector velocity imaging using phased array transducers for pediatric cardiology. *IEEE Transactions on Ultrasonics, Ferroelectrics, and Frequency Control*, pp.1–1.

Fadnes, S. et al., 2014. Shunt flow evaluation in congenital heart disease based on two-dimensional speckle tracking. *Ultrasound in medicine & biology*, 40(10), pp.2379–91.

Faurie, J. et al., 2017. Intracardiac Vortex Dynamics by High-Frame-Rate Doppler Vortography—In Vivo Comparison With Vector Flow Mapping and 4-D Flow MRI. *IEEE Transactions on Ultrasonics, Ferroelectrics, and Frequency Control*, 64(2), pp.424–432.

Ferrari, S. et al., 2018. The Ring Vortex: A Candidate for a Liquid-Based Complex Flow Phantom for Medical Imaging. In Springer, Cham, pp. 893–902.

Fox, M.D., 1978. Multiple crossed-beam ultrasound Doppler velocimetry. *IEEE Transactions on Sonics and Ultrasonics*, 25(5), pp.281–286.

Gammelmark, K.L. & Jensen, J.A., 2014. 2-D tissue motion compensation of synthetic transmit aperture images. *IEEE Transactions on Ultrasonics, Ferroelectrics, and Frequency Control*, 61(4), pp.594–610.

Garcia, D. et al., 2010. Two-Dimensional Intraventricular Flow Mapping by Digital Processing Conventional Color-Doppler Echocardiography Images. *IEEE Transactions on Medical Imaging*, 29(10), pp.1701–1713.

Garcia, D., Lantelme, P. & Saloux, E., 2018. Introduction to speckle tracking in cardiac ultrasound imaging. In *Handbook of Speckle Filtering and Tracking in Cardiovascular Ultrasound Imaging and Video*. Institution of Engineering and Technology, pp. 571–598.

Goodman, J.W., 2005. *Introduction to Fourier optics*, Roberts & Co.

Gruner, C. et al., 2015. Quantification of Mitral Regurgitation by Real Time Three-Dimensional Color Doppler Flow Echocardiography Pre- and Post-Percutaneous Mitral Valve Repair. *Echocardiography*, 32(7), pp.1140–1146.

Guenther, D. & Walker, W., 2007. Optimal apodization design for medical ultrasound using constrained least squares part I: theory. *IEEE Transactions on Ultrasonics, Ferroelectrics and Frequency Control*, 54(2), pp.332–342.

Hasegawa, H. & Kanai, H., 2011. High-frame-rate echocardiography using diverging transmit beams and parallel receive beamforming. *Journal of Medical Ultrasonics*, 38(3), pp.129–140.

Hasegawa, H. & Kanai, H., High-frame-rate echocardiography using diverging transmit beams and parallel receive beamforming.

Hein, I.A. & O'Brien, W.D., 1993. Current time-domain methods for assessing tissue motion by analysis from reflected ultrasound echoes-a review. *IEEE Transactions on Ultrasonics, Ferroelectrics and Frequency Control*, 40(2), pp.84–102.

Horn, B.K.P. & Schunck, B.G., 1981. Determining optical flow. *Artificial Intelligence*, 17(1–3), pp.185–203.

Hoskins, P.R., 1996. Accuracy of maximum velocity estimates made using Doppler ultrasound systems. *The British Journal of Radiology*, 69(818), pp.172–177.

Hoskins, P.R., Anderson, T. & McDicken, W.N., 1989. A computer controlled flow phantom for generation of physiological Doppler waveforms. *Physics in medicine and biology*, 34(11), pp.1709–17.

Jensen, Jørgen, A., 1996. *Estimation of blood velocities using ultrasound : a signal processing approach*, Cambridge University Press.

Jensen, J.A. et al., 2006. 2K-6 Cardiac In-Vivo Measurements Using Synthetic Transmit Aperture Ultrasound. In *2006 IEEE Ultrasonics Symposium*. IEEE, pp. 1115–1118.

Jensen, J.A., 2014. A multi-threaded version of Field II. In *2014 IEEE International Ultrasonics Symposium*.

IEEE, pp. 2229–2232.
Jensen, J.A., 1996. Field: A Program for Simulating Ultrasound Systems. *Paper presented at the 10th Nordic-Baltic Conference on Biomedical Imaging Published in Medical & Biological Engineering & Computing*, 34(sup. 1), pp.351–353.
Jensen, J.A. et al., 2006. Synthetic aperture ultrasound imaging. *Ultrasonics*, 44, pp.e5–e15.
Jensen, J.A. et al., 2016a. Ultrasound Vector Flow Imaging: I: Sequential Systems. *IEEE Transactions on Ultrasonics, Ferroelectrics, and Frequency Control*, 63(11), pp.1–1.
Jensen, J.A. et al., 2016b. Ultrasound Vector Flow Imaging: I: Sequential Systems. *IEEE Transactions on Ultrasonics, Ferroelectrics, and Frequency Control*, pp.1–1.
Jensen, J.A. & Svendsen, N.B., 1992. Calculation of pressure fields from arbitrarily shaped, apodized, and excited ultrasound transducers. *IEEE Transactions on Ultrasonics, Ferroelectrics and Frequency Control*, 39(2), pp.262–267.
Johnson, S.A. et al., 1975. Digital Computer Simulation Study of a Real-Time Collection, Post-Processing Synthetic Focusing Ultrasound Cardiac Camera. In *Acoustical Holography*. Boston, MA: Springer US, pp. 193–211.
Joos, P., 2017. *Imagerie ultrasonore ultra-rapide dédiée à la quantification 3D du mouvement cardiaque*. Université de Lyon.
Karaman, M., Pai-Chi Li & O'Donnell, M., 1995. Synthetic aperture imaging for small scale systems. *IEEE Transactions on Ultrasonics, Ferroelectrics and Frequency Control*, 42(3), pp.429–442.
Kargel, C. et al., 2004. Doppler Ultrasound Systems Designed for Tumor Blood Flow Imaging. *IEEE Transactions on Instrumentation and Measurement*, 53(2), pp.524–536.
Kasai, C. et al., 1985. Real-Time Two-Dimensional Blood Flow Imaging Using an Autocorrelation Technique. *IEEE Transactions on Sonics and Ultrasonics*, 32(3), pp.458–464.
Kheradvar, A. et al., 2010. Echocardiographic Particle Image Velocimetry: A Novel Technique for Quantification of Left Ventricular Blood Vorticity Pattern. *Journal of the American Society of Echocardiography*, 23(1), pp.86–94.
Kim, H.B., Hertzberg, J.R. & Shandas, R., 2004. Development and validation of echo PIV. *Experiments in Fluids*, 36(3), pp.455–462.
King, D.M. et al., 2011. Development of a Vessel-Mimicking Material for use in Anatomically Realistic Doppler Flow Phantoms. *Ultrasound in Medicine & Biology*, 37(5), pp.813–826.
Kisslo, J.A. & Adams, D.B., 2001. Principles of Doppler Echocardiography and the Doppler Examination #1 - Semantic Scholar.
Kripfgans, O.D. et al., 2006. Vector Doppler imaging of a spinning disc ultrasound Doppler phantom. *Ultrasound in Medicine & Biology*, 32(7), pp.1037–1046.
Kuttruff, H., 1991. Absorption of Ultrasound. In *Ultrasonics*. Dordrecht: Springer Netherlands, pp. 207–240.
Law, Y.F. et al., 1987. Computer-controlled pulsatile pump system for physiological flow simulation. *Medical & biological engineering & computing*, 25(5), pp.590–5.
Liebgott, H. et al., 2016. Plane-Wave Imaging Challenge in Medical Ultrasound. In *2016 IEEE International Ultrasonics Symposium (IUS)*. IEEE, pp. 1–4.
Lockwood, G.R., Talman, J.R. & Brunke, S.S., 1998. Real-time 3-D ultrasound imaging using sparse synthetic aperture beamforming. *IEEE Transactions on Ultrasonics, Ferroelectrics and Frequency Control*, 45(4), pp.980–988.
Loupas, T., Powers, J.T. & Gill, R.W., 1995. An axial velocity estimator for ultrasound blood flow imaging, based on a full evaluation of the Doppler equation by means of a two-dimensional autocorrelation approach. *IEEE Transactions on Ultrasonics, Ferroelectrics and Frequency Control*, 42(4), pp.672–688.

Lucas, B.D. & Kanade, T., 1981. An iterative image registration technique with an application to stereo vision. , pp.674–679.

Mallart, R. & Fink, M., 1992. Improved imaging rate through simultaneous transmission of several ultrasound beams. In F. L. Lizzi, ed. pp. 120–130.

Matrone, G. et al., 2017. High Frame-Rate, High Resolution Ultrasound Imaging With Multi-Line Transmission and Filtered-Delay Multiply And Sum Beamforming. *IEEE Transactions on Medical Imaging*, 36(2), pp.478–486.

Meagher, S. et al., 2007. Anatomical flow phantoms of the nonplanar carotid bifurcation, Part II: Experimental validation with Doppler ultrasound. *Ultrasound in Medicine & Biology*, 33(2), pp.303–310.

Montaldo, G. et al., 2009. Coherent plane-wave compounding for very high frame rate ultrasonography and transient elastography. *IEEE transactions on ultrasonics, ferroelectrics, and frequency control*, 56(3), pp.489–506.

Nagueh, S.F. et al., 1997. Doppler Tissue Imaging: A Noninvasive Technique for Evaluation of Left Ventricular Relaxation and Estimation of Filling Pressures. *Journal of the American College of Cardiology*, 30(6), pp.1527–1533.

Nikolov, S.I. & Jensen, J.A., 2000. 3D synthetic aperture imaging using a virtual source element in the elevation plane. In *IEEE Ultrasonics Symposium. Proceedings. An International Symposium (Cat. No.00CH37121)*. IEEE, pp. 1743–1747.

Nikolov, S.I. & Jensen, J.A., 2003a. In-vivo synthetic aperture flow imaging in medical ultrasound. *IEEE Transactions on Ultrasonics, Ferroelectrics and Frequency Control*, 50(7), pp.848–856.

Nikolov, S.I. & Jensen, J.A., 2003b. Investigation of the feasibility of 3D synthetic aperture imaging. In *IEEE Symposium on Ultrasonics*. IEEE, pp. 1903–1906.

Ortega, A. et al., 2016. A Comparison of the Performance of Different Multiline Transmit Setups for Fast Volumetric Cardiac Ultrasound. *IEEE Transactions on Ultrasonics, Ferroelectrics, and Frequency Control*, 63(12), pp.2082–2091.

Otto, C.M., 2012. *The practice of clinical echocardiography*, Elsevier/Saunders.

Overbeck, J.R., Beach, K.W. & Strandness, D.E., 1992. Vector Doppler: accurate measurement of blood velocity in two dimensions. *Ultrasound in medicine & biology*, 18(1), pp.19–31.

Papadacci, C. et al., 2014a. High-contrast ultrafast imaging of the heart. *IEEE transactions on ultrasonics, ferroelectrics, and frequency control*, 61(2), pp.288–301.

Papadacci, C. et al., 2014b. High-contrast ultrafast imaging of the heart. *IEEE Transactions on Ultrasonics, Ferroelectrics, and Frequency Control*, 61(2), pp.288–301.

Pedrizzetti, G. et al., 2014. The vortex—an early predictor of cardiovascular outcome? *Nature Reviews Cardiology*, 11(9), pp.545–553.

Perrino, A.C. & Reeves, S.T., 2008. *A practical approach to transesophageal echocardiography*, Wolters Kluwer Health/Lippincott Williams & Wilkins.

Petrusca, L. et al., 2018. Fast Volumetric Ultrasound B-Mode and Doppler Imaging with a New High-Channels Density Platform for Advanced 4D Cardiac Imaging/Therapy. *Applied Sciences*, 8(2), p.200.

Pihl, M. & Jensen, J., 2014. A transverse oscillation approach for estimation of three-dimensional velocity vectors, Part I: concept and simulation study. *IEEE Transactions on Ultrasonics, Ferroelectrics, and Frequency Control*, 61(10), pp.1599–1607.

Pihl, M.J. et al., 2013. Preliminary examples of 3D vector flow imaging. In J. G. Bosch & M. M. Doyley, eds. International Society for Optics and Photonics, p. 86750H.

Poepping, T.L. et al., 2002. An in vitro system for Doppler ultrasound flow studies in the stenosed carotid

artery bifurcation. *Ultrasound in medicine & biology*, 28(4), pp.495–506.

Poree, J. et al., 2018. A Dual Tissue-Doppler Optical-Flow Method for Speckle Tracking Echocardiography at High Frame Rate. *IEEE Transactions on Medical Imaging*, 37(9), pp.2022–2032.

Poree, J. et al., 2016. High-Frame-Rate Echocardiography Using Coherent Compounding With Doppler-Based Motion-Compensation. *IEEE Transactions on Medical Imaging*, 35(7), pp.1647–1657.

Provost, J. et al., 2014. 3D ultrafast ultrasound imaging *in vivo*. *Physics in Medicine and Biology*, 59(19), pp.L1–L13.

Provost, J. et al., 2011. Electromechanical wave imaging for arrhythmias. *Physics in Medicine and Biology*, 56(22), pp.L1–L11.

Provost, J. et al., 2010. Electromechanical Wave Imaging of Normal and Ischemic Hearts In Vivo. *IEEE Transactions on Medical Imaging*, 29(3), pp.625–635.

Rabinovich, A., Feuer, A. & Friedman, Z., 2015. Multi-line transmission combined with minimum variance beamforming in medical ultrasound imaging. *IEEE Transactions on Ultrasonics, Ferroelectrics, and Frequency Control*, 62(5), pp.814–827.

von Ramm, O.T., Smith, S.W. & Pavy, H.G., 1991. High-speed ultrasound volumetric imaging system. II. Parallel processing and image display. *IEEE Transactions on Ultrasonics, Ferroelectrics and Frequency Control*, 38(2), pp.109–115.

Rasmussen, M. & Jensen, J., 2014. Comparison of 3-D synthetic aperture phased-array ultrasound imaging and parallel beamforming. *IEEE Transactions on Ultrasonics, Ferroelectrics, and Frequency Control*, 61(10), pp.1638–1650.

Ricci, S. et al., 2007. Multichannel FPGA-based arbitrary waveform generator for medical ultrasound. *Electronics Letters*, 43(24), p.1335.

Salles, S., Chee, A.J.Y., et al., 2015. 2-D arterial wall motion imaging using ultrafast ultrasound and transverse oscillations. *IEEE transactions on ultrasonics, ferroelectrics, and frequency control*, 62(6), pp.1047–58.

Salles, S., Liebgott, H., et al., 2015. Full 3-D transverse oscillations: a method for tissue motion estimation. *IEEE transactions on ultrasonics, ferroelectrics, and frequency control*, 62(8), pp.1473–85.

Sandrin, L. et al., 2002. Shear modulus imaging with 2-D transient elastography. *IEEE transactions on ultrasonics, ferroelectrics, and frequency control*, 49(4), pp.426–35.

Sandrin, L. et al., 1999. Time-Resolved Pulsed Elastography with Ultrafast Ultrasonic Imaging. *Ultrasonic Imaging*, 21(4), pp.259–272.

Shattuck, D.P. et al., 1984. Explososcan: A parallel processing technique for high speed ultrasound imaging with linear phased arrays. *The Journal of the Acoustical Society of America*, 75(4), pp.1273–1282.

Shougang Wang et al., 2008. A composite high-frame-rate system for clinical cardiovascular imaging. *IEEE Transactions on Ultrasonics, Ferroelectrics and Frequency Control*, 55(10), pp.2221–2233.

Steel, R. & Fish, P.J., 2002. Lumen pressure within obliquely insonated absorbent solid cylindrical shells with application to Doppler flow phantoms. *IEEE transactions on ultrasonics, ferroelectrics, and frequency control*, 49(2), pp.271–80.

Steel, R. & Fish, P.J., 2002. Velocity bias and fluctuation in the standard dual beam Doppler reconstruction algorithm. *IEEE Transactions on Ultrasonics, Ferroelectrics and Frequency Control*, 49(10), pp.1375–1383.

Sühling, M. et al., 2005. Myocardial motion analysis from B-mode echocardiograms. *IEEE transactions on image processing : a publication of the IEEE Signal Processing Society*, 14(4), pp.525–36.

Tanné, D. et al., 2010. Assessment of left heart and pulmonary circulation flow dynamics by a new pulsed mock circulatory system. *Experiments in Fluids*, 48(5), pp.837–850.

Tavakoli, V. et al., 2014. Tissue Doppler Imaging Optical Flow (TDIOF): A Combined B-Mode and Tissue Doppler Approach for Cardiac Motion Estimation in Echocardiographic Images. *IEEE Transactions on Biomedical Engineering*, 61(8), pp.2264–2277.

Thomenius, K.E., 1996. Evolution of ultrasound beamformers. In *IEEE Ultrasonics Symposium. Proceedings*. IEEE, pp. 1615–1622.

Tinaikar, A., Advaith, S. & Basu, S., 2018. Understanding evolution of vortex rings in viscous fluids. *Journal of Fluid Mechanics*, 836, pp.873–909.

Tong, L. et al., 2012. Comparison of conventional parallel beamforming with plane wave and diverging wave imaging for cardiac applications: a simulation study. *IEEE Transactions on Ultrasonics, Ferroelectrics and Frequency Control*, 59(8), pp.1654–1663.

Tong, L., Ortega, A., et al., 2013. Fast three-dimensional ultrasound cardiac imaging using multi-transmit beam forming: A simulation study. In *2013 IEEE International Ultrasonics Symposium (IUS)*. IEEE, pp. 1456–1459.

Tong, L. et al., 2014. Multi-Transmit Beam Forming for Fast Cardiac Imaging - Experimental Validation and In Vivo Application. *IEEE Transactions on Medical Imaging*, 33(6), pp.1205–1219.

Tong, L. et al., 2016. Wide-Angle Tissue Doppler Imaging at High Frame Rate Using Multi-Line Transmit Beamforming: An Experimental Validation In Vivo. *IEEE Transactions on Medical Imaging*, 35(2), pp.521–528.

Tong, L., Gao, H. & D'hooge, J., 2013. Multi-transmit beam forming for fast cardiac imaging-a simulation study. *IEEE Transactions on Ultrasonics, Ferroelectrics, and Frequency Control*, 60(8), pp.1719–1731.

Trahey, G.E., Allison, J.W. & von Ramm, O.T., 1987. Angle Independent Ultrasonic Detection of Blood Flow. *IEEE Transactions on Biomedical Engineering*, BME-34(12), pp.965–967.

Trahey, G.E. & Nock, L.F., 1992. Synthetic receive aperture imaging with phase correction for motion and for tissue inhomogeneities. II. Effects of and correction for motion. *IEEE Transactions on Ultrasonics, Ferroelectrics and Frequency Control*, 39(4), pp.496–501.

Vray, D. et al., 2014. Ultrasound Medical Imaging. In *Medical Imaging Based on Magnetic Fields and Ultrasounds*. Hoboken, USA: John Wiley & Sons, Inc., pp. 1–72.

Wang Jing & Lu Jian-yu, 2007. Motion Artifacts of Extended High Frame Rate Imaging. *IEEE Transactions on Ultrasonics, Ferroelectrics and Frequency Control*, 54(7), pp.1303–1315.

Yiu, B.Y.S. & Yu, A.C.H., 2017. Spiral Flow Phantom for Ultrasound Flow Imaging Experimentation. *IEEE Transactions on Ultrasonics, Ferroelectrics, and Frequency Control*, 64(12), pp.1840–1848.

Zhang, M. et al., 2016. Extension of Fourier-Based Techniques for Ultrafast Imaging in Ultrasound With Diverging Waves. *IEEE Transactions on Ultrasonics, Ferroelectrics, and Frequency Control*, 63(12), pp.2125–2137.

Zhou, X. et al., 2017. Fabrication of Two Flow Phantoms for Doppler Ultrasound Imaging. *IEEE Transactions on Ultrasonics, Ferroelectrics, and Frequency Control*, 64(1), pp.53–65.

Zhou, Y. et al., 2018. A Framework for the Generation of Realistic Synthetic Cardiac Ultrasound and Magnetic Resonance Imaging Sequences From the Same Virtual Patients. *IEEE Transactions on Medical Imaging*, 37(3), pp.741–754.

Zurakhov, G. et al., 2018. Multiline Transmit Beamforming Combined With Adaptive Apodization. *IEEE Transactions on Ultrasonics, Ferroelectrics, and Frequency Control*, 65(4), pp.535–545.

Publications

Journals

Emilia Badescu, Damien Garcia, Philippe Joos, Adeline Bernard, Lionel Augeul, René Ferrera, Magalie Viallon, Lorena Petrusca, Denis Friboulet, Hervé Liebgott, "Comparison between Multi Line Transmission and Diverging Wave Imaging: motion artefacts and their effect on motion estimation", *IEEE Trans. Ultrason. Ferroelectr. Freq.Control*, 2018, *Revision submitted for publication*

International Conferences

1. **Emilia Badescu**, Sébastien Salles, Denis Friboulet, Hervé Liebgott, "A measure of confidence for phase-based motion estimator applied to 2D US-To images", *IEEE International Ultrasonics symposium, Tours, France, September 2016*
2. **Emilia Badescu**, Denis Bujoreanu, Lorena Petrusca, Denis Friboulet, Hervé Liebgott, "Multi-Line Transmission For 3D ultrasound imaging: An experimental study*", IEEE International Ultrasonics symposium, Washington, D.C., USA, September 2017*
3. **Emilia Badescu**, Lorena Petrusca, Damien Garcia, Denis Friboulet, Hervé Liebgott, "Doppler Velocity estimation in 3D cardiac ultrafast ultrasound imaging: an *in vitro* study", *IEEE International Ultrasonics symposium, Washington, D.C., USA, September 2017*
4. Emmanuel Roux, **E. Badescu**, Lorena Petrusca, François Varray, Alessandro Ramalli, Christian Cachard, Marc Robini, Hervé Liebgott, Piero Tortoli, "Validation of optimal 2D sparse arrays in focused mode: phantom experiments" , *IEEE International Ultrasonics symposium, Washington, D.C., USA, September 2017*
5. **Emilia Badescu**, Denis Friboulet, Hervé Liebgott, Damien Garcia, "Time resolved imaging of vortex rings with ultrafast ultrasound: an *in vitro* study", *Frontiers of Simulation and Experimentation for Personalized Cardiovascular Management and Treatment, London, UK, July, 2018*
6. **Emilia Badescu** , Simone Ambrogio , John Fenner , Hervé Liebgott , Denis Friboulet , Damien Garcia, "Vortex ring phantom for investigation of ultrasound vector flow", *IEEE International Ultrasonics symposium, Kobe, Japan, October 2018*
7. **Emilia Badescu** , Lorena Petrusca , Denis Friboulet , Hervé Liebgott, "Experimental cross-talk reduction for 3D Multi-line transmission", *IEEE International Ultrasonics symposium, Kobe, Japan, October 2018*
8. Paolo Mattesini , Emmanuel Roux , **Emilia Badescu** , Lorena Petrusca , Olivier Basset , Piero Tortoli , Hervé Liebgott, "Optimal virtual sources distribution in 3-D Diverging Wave Ultrasound Imaging: an experimental study" , *IEEE International Ultrasonics symposium, Kobe, Japan, October 2018*
9. Vincent Perrot , Yanis Mehdi Benane , **Emilia Badescu** , Hervé Liebgott , Damien Garcia, "Dual-Frequency Alias-Free Color Doppler using Chirping and Pulse Compression", *IEEE International Ultrasonics symposium, Kobe, Japan, October 2018*
10. Yanis Mehdi Benane and Denis Bujoreanu, **Emilia Badescu**, Barbara Nicolas, Christian Cachard, Hervé Liebgott, Olivier Basset, *IEEE International Ultrasonics symposium, Kobe, Japan, October 2018*

Personal portofolio

Outreach events

Date	Name	Place
April 2016	Festival of Life	Sheffield, UK
October 2017	Fête de la science	Lyon, FR
July 2017	Hearts and how to heal them	London, UK

Secondments

Date	Type	Institution/ Place
April 2016 (5 days)	Industrial	Leeds Test Objects, UK
January 2017 (4 days)	Clinical	Saint Etienne Hospital, FR
April 2017 (5days)	Academic	The University of Sheffield, UK

Trainings

Date	Name	Place	Number of hours
October - December 2015	Course in ultrasound imaging	Lyon, FR	20
October 2015 - May 2017	French courses (A2->C1)	Lyon, FR	129
November 2015	Writing scientific articles	Lyon,FR	21
November 2015	VPH-Case Training Activity 1 (Personal Development, Ethics, Research dissemination)	Sheffield, UK	8
June 2016	VPH-Case Training Activity 2 (Design and development of endovascular medical devices)	Milan, IT	30
June-July 2016	OPUS summer school	Lyon, FR	20
July 2016	Image registration day	Lyon, FR	8
September - October 2016	Making Successful presentations	Lyon, FR	24
September 2016 - December 2017	Seminars doctoral school	Lyon, FR	22
October 2016	VPH-Case Training Activity 3 (Experimental techniques: from acquisitions to data interpretation)	Eindhoven, NL	27
June 2017	VPH-Case Training Activity 4 (Clinical and industrial translation)	Lyon,FR	25
February 2017	CardioFunXion Winter School	Paris,FR	7
September - October 2018	Training outreach presentation	Lyon, FR	12
December 2017	Workshop in cardiovascular applications of medical ultrasound imaging	Lyon,FR	6
February 2018	CardioFunXion Winter School	Lyon,FR	8
July 2018	VPH-Case Training Activity 5 (outreach, research dissemination)	London, UK	18

Résumé en français

CHAPITRE 1

L'échocardiographie est la modalité de choix dans la pratique clinique quotidienne pour l'imagerie cardiaque grâce à ses avantages par rapport à d'autres modalités d'imagerie médicale telles que l'imagerie par résonance magnétique (IRM) ou la tomodensitométrie (TDM). Le fait que cette modalité soit non invasive, peu coûteuse et transportable a motivé des progrès notables dans le traitement du signal ultrasonore, l'électronique et la conception de matériel au cours des dernières années. D'autres améliorations pourraient accroître la précision de l'évaluation structurelle et fonctionnelle du cœur dans les cas normaux et pathologiques.

L'objectif de notre premier chapitre est de décrire le processus conduisant aux images d'échocardiographie conventionnelle afin de mettre en évidence deux limitations que nous visons à étudier et à améliorer dans cette thèse : la cadence d'acquisition des images et l'utilisation peu fréquente de l'imagerie 3D dans la pratique clinique quotidienne. Pour expliquer comment les données ultrasonores sont obtenues, nous présentons d'abord les principes de base de l'échographie. Deuxièmement, le *pipeline* d'un processus d'acquisition par ultrasons est décrit étape par étape, de l'émission à la réception. Nous présentons ensuite la procédure d'obtention de différents modes d'imagerie à partir des données reçues. L'utilisation de ces modes et l'adaptation des différentes caractéristiques du système aux spécificités de l'échographie cardiaque aident les cliniciens à recueillir des informations précieuses pour le diagnostic. Cependant, les systèmes actuels présentent plusieurs limites, telles que la cadence d'images. Si en 2D, la résolution temporelle maximale réalisable est limitée pour capturer des événements rapides, tels que ceux qui se produisent lors de l'échocardiographie de stress, en 3D ce problème devient d'autant plus important car il faut insonifier un volume complet.

Il y a donc une nécessité clinique d'augmenter la cadence d'imagerie pour améliorer l'analyse actuelle en 2D, mais une résolution temporelle élevée pourrait être également particulièrement intéressante en 3D. En effet en 3D plusieurs hypothèses actuellement nécessaires sur la géométrie du cœur pour les mesures volumétriques pourraient être levées, ce qui a permettrait d'obtenir des mesures quantitatives plus précises.

CHAPITRE 2

La réponse de la communauté de la recherche en échographie aux limites présentées dans le premier chapitre a consisté en l'émergence de techniques à haute cadence d'images dédiée à l'estimation du mouvement. D'après la description détaillée de chaque méthode fournie dans la version anglaise de ce document, nous pouvons affirmer que chaque méthode permettant une cadence d'images élevée conduit à un compromis spécifique entre la qualité de l'image et la cadence d'images. Bien que la méthode appelée « ECG (electrocardiogram) gating » puisse améliorer la résolution temporelle, elle est très sensible aux patients présentant une variabilité de la fréquence cardiaque, puisqu'une image complète est formée à partir de données acquises pendant plusieurs battements cardiaques. Le MLA (« Multi Line Acquisition ») permet de former une image à haute cadence lors d'un seul battement de cœur, mais la résolution temporelle est augmentée au détriment de la résolution latérale. Le MLT (« Multi Line Transmit ») permet de conserver une bonne résolution latérale, mais elle est affectée par des artefacts appelés « cross-talk » (qui apparaissent

à cause des interférences entre les ondes émises simultanément). Par contre, ces artefacts n'apparaissent pas lorsque l'imagerie PW/DW est utilisée. De plus, la résolution temporelle est très élevée puisqu'une image peut être obtenue à partir d'une seule transmission. Toutefois, l'utilisation d'une seule transmission peut entraîner une qualité d'image insatisfaisante. La sommation cohérente peut alors être utilisée pour augmenter le contraste, la résolution et le SNR mais conduit dans ce cas à nouveau à une diminution de la cadence d'imagerie. Même si cette sommation peut provoquer des artefacts lors de l'imagerie d'un objet dynamique, ceux-ci peuvent être atténués par une compensation de mouvement (MoCo). Parmi les méthodes présentées ci-dessus, des résultats prometteurs à des centaines d'images/s, avec une sonde cardiaque, ont été obtenus en utilisant le MLT et le DW. La qualité de l'image peut être améliorée dans les deux cas au prix d'une diminution de la cadence d'images. Mais pour une cadence d'images donnée, de quelle façon un compromis donné affecte-t-il la qualité de l'image et les méthodes d'estimation du mouvement ? Existe-t-il une approche plus appropriée qu'une autre pour les applications cardiaques? Répondre à ces questions était notre premier objectif et il a été traité dans le Chapitre 3.

Du fait du potentiel des méthodes à haute cadence d'images permettant de nouvelles découvertes sur la fonction cardiaque, mais aussi en raison de la limitation actuelle de la quantification des structures 3D à l'aide de méthodes 2D, les modalités à haute cadence d'images ont été étendues en 3D. L'utilisation d'un faisceau large en échocardiographie 3D permettrait de répartir l'énergie encore plus qu'en 2D puisqu'un volume entier doit être insonifié. Le MLT a le potentiel d'offrir un bon contraste, un bon rapport signal-bruit et une bonne résolution à des profondeurs de volume élevées en concentrant le faisceau sur la région d'intérêt. De plus, l'utilisation de la géométrie 2D de la sonde permet une meilleure séparation des faisceaux et une meilleure suppression du cross-talk. Le potentiel prometteur de cette méthode a été démontré par plusieurs auteurs, mais toutes les recherches se sont limitées à des simulations ou à des mises en œuvre expérimentales synthétiques en raison de la complexité des séquences mises en jeu. De plus, la performance de l'estimation de la vitesse n'a pas encore été évaluée expérimentalement sur les images MLT 3D. L'atténuation, le bruit, les problèmes d'échauffement et les artefacts de mouvement ne sont que quelques-uns des nombreux problèmes qui pourraient être mis en évidence par une implémentation en temps réel. Cela nous amène à nous poser une série de questions qui formuleront notre deuxième objectif : le MLT représente-il toujours une modalité de choix en échocardiographie 3D malgré les problèmes possibles qui peuvent apparaître dans la pratique ? Quelles sont les limites des acquisitions statiques et dynamiques ? Ces questions ont été traitées dans le Chapitre 4.

Tester le potentiel et les limites des méthodes 2D et 3D à haute cadence d'images est une étape très importante pour évaluer si elles peuvent être appliquées en échocardiographie clinique. Même si une analyse préliminaire doit être faite en simulation, il y a une différence importante entre de bons résultats *in silico* et de bons résultats *in vivo*. L'analyse in vitro est souvent utilisée comme phase intermédiaire. La difficulté d'extrapoler une technique de l'*in vitro* à l'*in vivo* est liée à l'absence de fantômes complexes. Actuellement, les méthodes de quantification du débit sanguin sont généralement testées sur de simples fantômes tubulaires ou de bifurcation pour évaluer leurs performances dans des applications telles que la maladie carotidienne. Mais des études récentes ont montré que l'analyse de flux complexes tels que les vortex formés dans le ventricule gauche peut fournir de nouvelles perspectives pour le diagnostic cardiaque (Pedrizzetti et al. 2014). La validation de méthodes à haute cadence d'image sur un fantôme à flux complexe pourrait faciliter le passage d'études *in vitro* à des études *in vivo*. Mais un fantôme capable de produire de manière répétable des vortex dont on maîtrise les caractéristiques pourrait-il être un bon

candidat pour tester les nouveau modes d'imagerie ultra rapide développés dans la communauté ? La réponse à cette question était notre troisième objectif, qui a été traité dans le Chapitre 5.

CHAPITRE 3 (PREMIERE CONTRIBUTION)

3.1. Introduction

Parmi les techniques d'imagerie ultrarapide présentées dans le Chapitre 2, un gain important en résolution temporelle est devenu possible avec l'avènement des approches à faisceaux focalisés multiples et non focalisés. Les approches par faisceau non focalisé, d'abord introduites sous forme de techniques par synthèse d'ouverture (Karaman et al. 1995) puis appelées techniques en ondes planes (en anglais « plane waves » PW) (Sandrin et al. 1999) ou divergentes (« diverging waves » DW) (Hasegawa & Kanai 2011) présentent l'avantage d'insonifier un milieu complet avec une seule transmission. Cependant, la qualité de l'image est considérablement compromise en termes de résolution et de contraste (Sandrin et al. 1999). La méthode de transmission à haute cadence focalisée alternative, appelée transmission focalisée en parallèle (« multi-line transmit » MLT), introduite par (Mallart & Fink 1992), permet d'atteindre des cadences d'images élevées tout en préservant la qualité d'image, comme le montrent (Tong, Gao, et al. 2013) , (Tong et al. 2014).

D'autre part, la qualité de l'image peut également être améliorée en imagerie PW/DW en utilisant la sommation cohérente (Karaman et al. 1995), (Montaldo et al. 2009), (Papadacci et al. 2014a). Mais cette approche peut échouer si le milieu est caractérisé par un fort mouvement d'une transmission à l'autre. Pour y faire face, une compensation de mouvement (MoCo) a été proposée (Trahey & Nock 1992), (B. Denarie et al. 2013), (Gammelmark & Jensen 2014). Comme le montre (Poree et al. 2016), l'utilisation de DW MoCo permet d'obtenir un bon contraste et des estimateurs Doppler tissulaire (« Tissue Doppler Imaging » TDI) précis en échocardiographie, ce qui rend cette approche très compétitive par rapport au MLT (Tong et al. 2014). Ainsi, le choix d'utiliser l'une ou l'autre méthode n'est pas très évident.

L'objectif de ce chapitre est de comparer les deux méthodes prometteuses d'imagerie ultrarapide (le DW MoCo et le MLT) et de révéler leurs limites qui aideront éventuellement à choisir l'approche la plus appropriée en échocardiographie. La comparaison est faite en termes de qualité d'image et de précision d'estimation du mouvement pour le suivi de speckle (en anglais « speckle tracking » ST) et pour le TDI.

3.2. Méthodes

3.2.1. Mise en place de l'acquisition

Les données ont été acquises à l'aide d'un scanner de recherche Verasonics Vantage 256 (Verasonics Inc., Redmond, WA) pilotant une sonde P4-2 de 64 éléments ayant une fréquence centrale de 2,5 MHz . Le milieu a été insonifié à l'aide d'une fréquence de répétition des impulsions (PRF) de 4500 Hz et d'une taille de secteur de 90º.

L'onde de transmission a été adaptée afin d'obtenir la même puissance totale émise pour le MLT et le DW.

3.2.2. Paramètres d'acquisition pour l'évaluation de la qualité d'image et l'estimateur de mouvement de suivi de speckle

La même cadence d'images de 450 Hz a été utilisée pour les conditions statiques et le suivi de speckle. Ainsi, le nombre de transmissions nécessaire pour construire une image a été fixé à 10, tant pour le DW que pour le MLT.

En DW, l'angle de transmission maximum (θ_{max}) était de 4,3º. Les images obtenues en utilisant différents angles ont été sommées de manière cohérente pour améliorer la qualité de l'image finale. Pour éviter un désalignement angulaire inadéquat des images composées, nous avons utilisé la technique de compensation de mouvement proposée dans (Poree et al. 2016).

Pour obtenir une cadence d'images équivalente avec le MLT, le nombre de transmissions simultanées a été fixé à 6. Aucune apodisation n'a été utilisée en émission ou en réception et le point focal a été fixé à 7 cm. La reconstruction de l'image a été effectuée en utilisant 5 MLA, ce qui signifie que 5 lignes d'image centrées sur le point focal du faisceau transmis ont été reconstruites en parallèle.

3.2.3. Paramètres d'acquisition pour l'imagerie Doppler tissulaire

La taille de la fenêtre a été fixé constante pour le MLT et le DW pour chaque ensemble de 8 acquisitions. Cependant comme pour le MLT nous avons dû transmettre les faisceaux 8 fois au même endroit pour chaque transmission, la fréquence d'image Doppler a été considérablement réduite (56 Hz) par rapport à celle obtenue avec le DW (562 Hz).

3.2.4. Modèles in vitro

3.2.4.1. Evaluation de la qualité d'image sur des fantômes statiques

La qualité de l'image a d'abord été évaluée sur un fantôme Gammex en termes de contraste et de résolution, en utilisant comme paramètres le Rapport Contraste/Bruit (« Contrast to Noise Ratio » CNR) et la largeur à mi-hauteur (« full width at half maximum » FWHM). Nous avons évalué le CNR à 4 cm et 11 cm, en utilisant une gamme dynamique de 60 dB. La résolution a été évaluée à quatre profondeurs d'image différentes (de 5 cm à 11 cm avec un pas de 2 cm).

3.2.4.2. Evaluation de la qualité d'image sur des fantômes dynamiques

L'évaluation de la qualité de l'image dans des conditions dynamiques a été effectuée sur un fantôme de disque tournant. Le disque contient quatre inclusions afin de faciliter l'évaluation du contraste (Fig. 3 A). Le CNR a été calculé en utilisant la moyenne des quatre inclusions pour chaque image. La vitesse du disque a été contrôlée par un moteur pas à pas et ajustée à 9 valeurs différentes de 50 °/s à 450 °/s, en utilisant un pas de 50º. Pour chaque vitesse, la moyenne du CNR pour les 4 inclusions a été calculée sur 10 images.

3.2.5. Modèles in vivo

Nous avons fait des acquisitions thorax ouvert (sur un cochon) pour obtenir des coupes en vue parasternale petit axe. Les séquences d'acquisition et les réglages étaient les mêmes que ceux utilisés pour les données *in vitro*, la seule différence étant que le point focal du MLT était placé à 4 cm.

3.2.6. Méthodes d'estimation du mouvement

L'influence des deux stratégies d'imagerie ultra-rapide sur l'estimation du mouvement a été testée en utilisant le suivi de speckle et le Doppler tissulaire. Pour le suivi de speckle, nous avons utilisé l'approche basée sur la corrélation normalisée dans le domaine de Fourier proposée dans (Hein & O'Brien 1993) tandis que pour le TDI nous avons utilisé l'approche basée sur un auto-corrélateur 2D appliqué sur les données IQ, proposée dans (Kasai et al. 1985),(Loupas et al. 1995).

La précision des estimations dans une direction choisie d a été évaluée à l'aide de l'erreur quadratique normalisée (NRSE) pour chaque pixel i, donnée par :

$$NRSE_{di} = \frac{\left|V_{ref_{di}} - V_{estim_{di}}\right|}{\left|V_{ref_d}\right|_{max}} \quad (3.1)$$

où $V_{ref_{di}}, V_{estim_{di}}$ sont la vitesse de référence et la vitesse estimée pour un pixel i donné et la direction sélectionnée (d=x pour latéral; d=z pour axial); $\left|V_{ref_d}\right|_{max}$ est le maximum des vitesses absolues de référence sur l'image entière.

3.3. Résultats

3.3.1. Evaluation de la qualité d'image sur des fantômes statiques

La Fig. 1 montre les images en mode B du fantôme Gammex obtenues pour le MLT (A) et le DW (B) à une cadence d'images de 450 Hz. La valeur de contraste (CNR) d'un kyste hypoechogène placé à 4 cm était de 5,66 dB pour le MLT et 7,54 dB pour le DW. Pour le kyste placé à 11 cm, le contraste était légèrement plus élevé pour le MLT (4,46 dB) que pour le DW (3,53 dB).

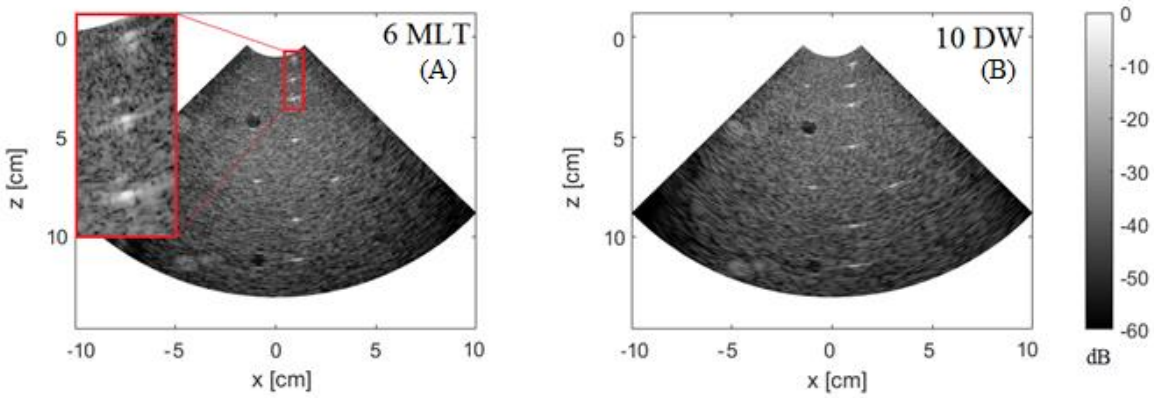

Fig. 1. Qualité d'image pour le MLT (A) et le DW (B) en utilisant une cadence d'images de 450 Hz. Une zone zoomée (x=[0.4cm:1.4cm] ; z=[0.8cm:3.5cm]) correspondant au rectangle rouge pour le MLT (A) est donnée pour une meilleure visualisation des artefacts près de la surface de la sonde.

La résolution latérale à 4 profondeurs d'image différentes (5 cm, 7 cm, 9 cm, 11 cm) est illustrée dans la Fig. 2.

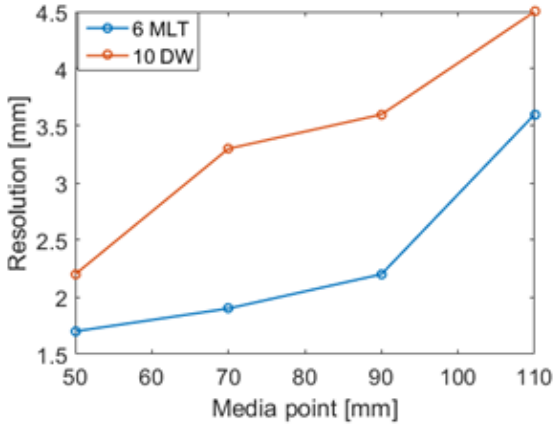

Fig. 2. Résolution latérale à différentes profondeurs d'image pour une cadence d'image de 900 Hz

3.3.2. Evaluation de la qualité d'image sur le fantôme du disque tournant

Afin d'observer comment le contraste est affecté lorsque le milieu imagé est en mouvement, nous avons calculé le CNR pour 9 vitesses différentes du disque. Les résultats sont illustrés dans la Fig. 3. Pour chaque vitesse, nous avons tracé le contraste moyen sur 10 images et l'écart-type correspondant.

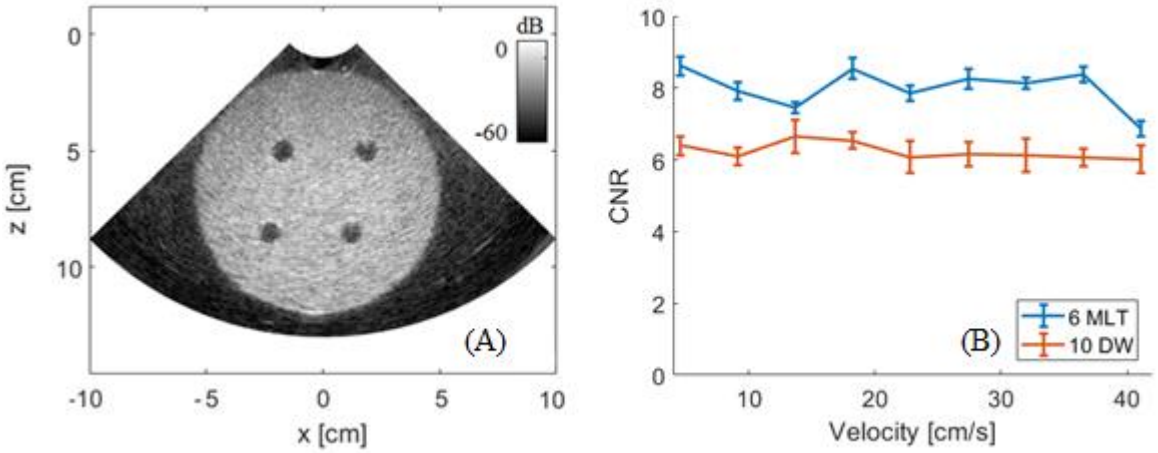

Fig. 3. CNR à différentes vitesses du disque calculées sur le fantôme représenté en (A). Résultats pour le MLT (B) et le DW (C) à une cadence d'images de 450 Hz

3.3.3. Précision de l'estimation du mouvement

Les résultats obtenus avec le MLT (à gauche) et le DW (à droite) sont représentés à l'aide de boxplots, contenant la médiane de la NRSE : la Fig. 4 montre la distribution axiale des erreurs (suivi de speckle), la Fig. 5 la distribution latérale (suivi de speckle) et la Fig. 6 la distribution axiale des erreurs (Doppler). La médiane de la NRSE est représentée en rouge tandis que les limites inférieure et supérieure de la boîte représentent les premier et troisième quartiles de l'erreur. Sous chaque série de boxplots, nous montrons les différences d'écart médian (Med) et interquartile (IQR) entre le MLT et le DW. L'IQR a été calculé en soustrayant le 25ème percentile du 75ème percentile du NRSE. Afin d'étudier si ces différences sont significatives, nous avons utilisé un test de Student pour obtenir la valeur p pour chaque différence.

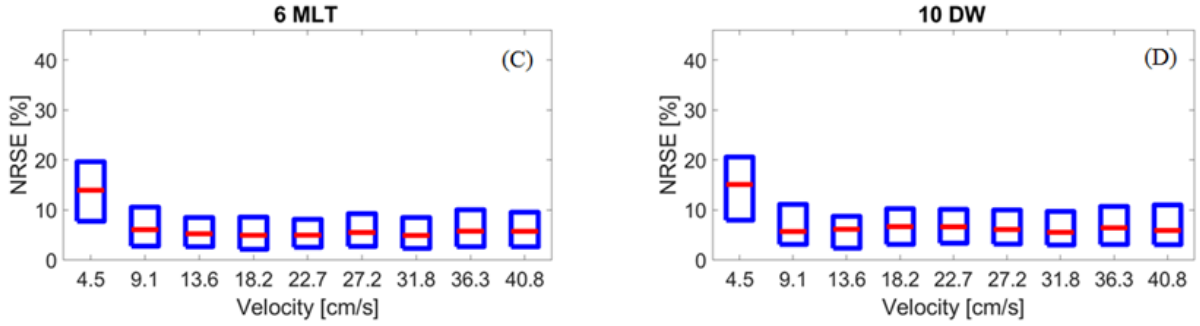

Velocity FR=500 Hz	4.5 cm/s	9.1 cm/s	13.6 cm/s	18.2 cm/s	22.7 cm/s	27.2 cm/s	31.8 cm/s	36.3 cm/s	40.8 cm/s	p-value
$Med_{MLT} - Med_{DW}$	-1.14	0.37	-0.92	-1.73	-1.66	-0.58	-0.64	-0.67	-0.16	$7.6 \cdot 10^{-3}$
$IQR_{MLT} - IQR_{DW}$	-0.74	-0.20	-0.54	-0.70	-1.19	-0.26	-0.55	-0.23	-1.03	$8.12 \cdot 10^{-4}$

Fig. 4. NRSE axial à différentes vitesses du disque pour une cadence d'image de 450 Hz (suivi de spekle). Sous chaque série de boxplots, nous montrons les différences d'écart médian (Med) et interquartile (IQR) entre le MLT et le DW. De plus, nous donnons les valeurs p associées.

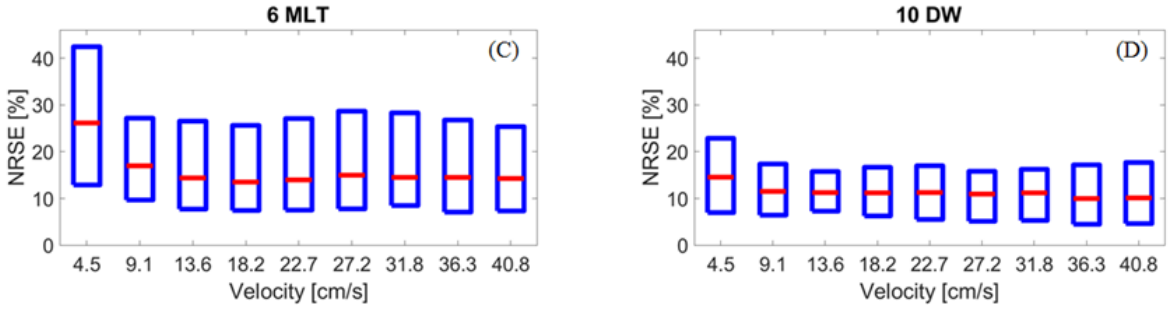

Velocity FR=450 Hz	4.5 cm/s	9.1 cm/s	13.6 cm/s	18.2 cm/s	22.7 cm/s	27.2 cm/s	31.8 cm/s	36.3 cm/s	40.8 cm/s	p-value
$Med_{MLT} - Med_{DW}$	11.58	5.45	3.13	2.32	2.69	4.04	3.29	4.51	4.15	$1.2 \cdot 10^{-3}$
$IQR_{MLT} - IQR_{DW}$	13.65	6.55	10.32	7.77	8.08	10.21	8.86	6.97	4.94	$7.91 \cdot 10^{-6}$

Fig. 5. NRSE latéral à différentes vitesses du disque pour une cadence d'image de 450 Hz (suivi de spekle). Sous chaque série de boxplots, nous montrons les différences d'écart médian (Med) et interquartile (IQR) entre le MLT et le DW. De plus, nous donnons les valeurs p associées.

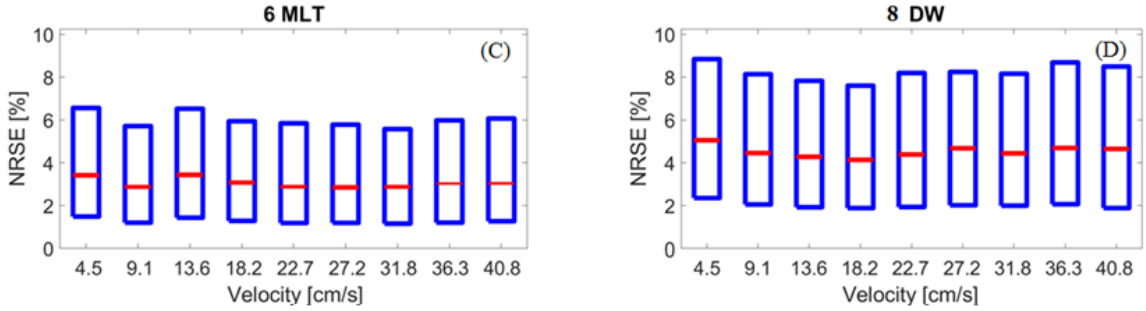

Velocity FR=500 Hz	4.5 cm/s	9.1 cm/s	13.6 cm/s	18.2 cm/s	22.7 cm/s	27.2 cm/s	31.8 cm/s	36.3 cm/s	40.8 cm/s	p-value
$Med_{MLT} - Med_{DW}$	-1.63	-1.56	-0.84	-1.07	-1.47	-1.82	-1.54	-1.71	-1.65	$6.86 \cdot 10^{-7}$
$IQR_{MLT} - IQR_{DW}$	-1.41	-1.57	-0.81	-1.06	-1.60	-1.63	-1.74	-1.84	-1.81	$1.27 \cdot 10^{-6}$

Fig. 6. NRSE axial à différentes vitesses du disque en fixant la taille de la fenêtre d'estimation le long de plusieurs acquisitions à 8 (Doppler). Sous chaque série de boxplots, nous montrons les différences d'écart médian (Med) et interquartile (IQR) entre le MLT et le DW. De plus, nous donnons **les valeurs p associées.**

3.3.4. Évaluation qualitative du mode B et de la TDI in vivo.

Sur la Fig. 7, nous montrons des images en mode B acquises sur un cœur de cochon en thorax ouvert pour le MLT (A) et le DW (B). De plus, nous montrons sur la Fig. 8 les images TDI pour les deux méthodes à haute cadence d'images.

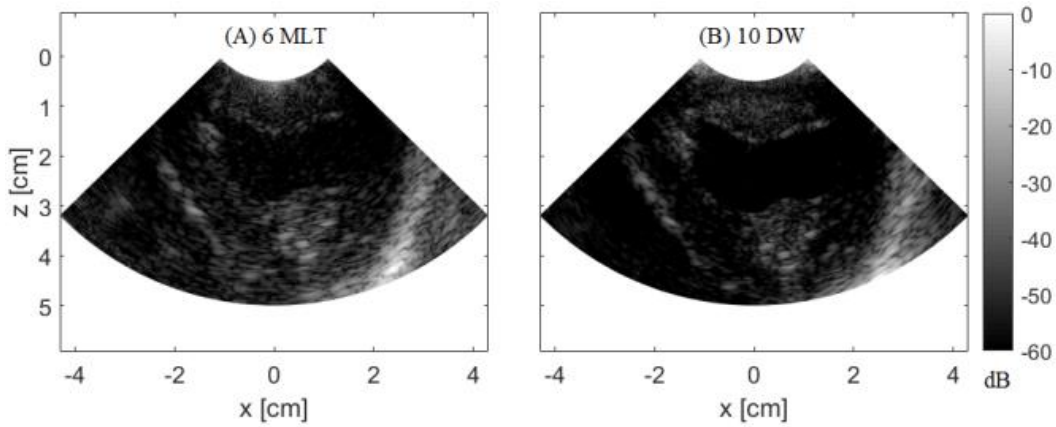

Fig. 7. Images in vivo en mode B pour le MLT (A) et le DW (B) à une cadence d'image de 450 Hz

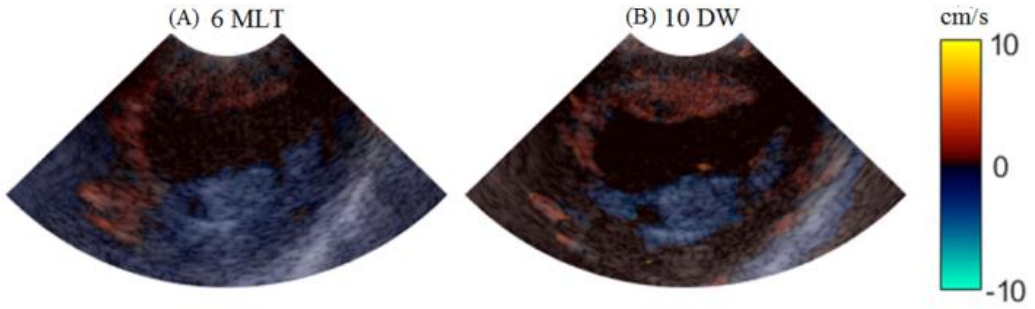

Fig. 8. Images TDI in vivo pour le MLT (A) et le DW (B).

3.4. Discussion

Dans cette étude, nous avons d'abord évalué la qualité de l'image dans des conditions statiques. Comme on peut le voir dans les zones agrandies marquées par les rectangles rouges de la Fig. 1 (A), la qualité de l'image pour le MLT est affectée par le cross-talk (des artefacts qui apparaissent à cause de l'interférence des ondes émises simultanément) alors qu'une bonne qualité d'image a été obtenue pour le DW pour ces mêmes zones. De plus, le CNR du kyste placé à 4 cm était plus élevé pour le DW que pour le MLT. Cependant, le DW a montré une plus grande atténuation du signal à des profondeurs plus élevées que le MLT (bien que l'énergie transmise soit équivalente pour les deux méthodes). Ceci explique les valeurs de CNR pour le kyste à 11 cm qui sont plus basses pour le DW que pour le MLT. Ce phénomène apparaît même si la position du kyste à 11 cm est à 4 cm du point focal. La résolution latérale a été évaluée sur des cibles placées de 5 cm à 11 cm avec un pas de 2 cm. Cette résolution s'est dégradée en profondeur pour les deux méthodes. Même si le MLT donne de meilleurs résultats que le DW (Fig. 2), la résolution latérale avec le DW pourrait être encore améliorée en utilisant un pas (« pitch ») angulaire plus élevé.

Deuxièmement, nous avons évalué la qualité de l'image dans des conditions dynamiques. Le CNR calculé sur le fantôme du disque tournant était approximativement constant avec la variation de la vitesse, ce qui est conforme aux résultats présentés dans (Poree et al. 2016). Cependant, les courbes présentent de légers écarts qui sont apparus à la suite du calcul du CNR moyen à différentes positions des inclusions à différentes vitesses. Malgré cette limitation, la tendance d'un meilleur contraste du MLT par rapport au DW MoCo peut encore être observée pour toutes les vitesses. Cela peut s'expliquer par le fait que les kystes ont été placés de 4,5 cm à 9,5 cm dans une région d'intérêt où nous avons montré que le MLT est susceptible de fournir une meilleure qualité d'image. L'évaluation du CNR dans des conditions dynamiques à de faibles

profondeurs peut mener à des résultats opposés puisque le niveau de cross-talk du MLT est plus élevé à de faibles profondeurs.

Troisièmement, nous avons évalué la précision du suivi de speckle pour les deux méthodes à haute cadence d'image. Nous avons effectué notre analyse sur la base des médianes et des valeurs IQR de la NRSE. Dans l'ensemble, des médianes et des valeurs IQR similaires ont été obtenues dans les deux cas dans la direction axiale pour chaque valeur de vitesse (Fig. 4). Pour l'ensemble des acquisitions, l'écart entre la médiane et l'IQR était inférieur à 2 %. Les valeurs négatives prédominantes des différences entre le NRSE médian obtenu avec le MLT et le DW montrent la tendance du MLT à avoir une performance légèrement meilleure que le DW, ce qui peut être expliqué par l'impact de la focalisation sur la qualité d'image en mode B. La différence entre les résultats est plus importante dans la direction latérale, où le DW a fourni des IQR inférieurs à ceux du MLT et où la valeur p correspondante a été réduite à un ordre de 10^{-6} (Fig. 5). Cela peut être lié à la présence de cross-talk en réception qui pourrait être réduit par apodisation, comme le suggèrent (Tong et al. 2014).

Quatrièmement, nous avons examiné la précision de la TDI pour les deux méthodes à haute cadence d'images. Bien que la différence négative prédominante entre les médianes et l'IQR indique des estimations légèrement meilleures pour le MLT (Fig. 6), l'amélioration est inférieure à 2 % pour tous les cas. D'autre part, le DW permet d'effectuer la sommation cohérente et le MoCo pour la visualisation en mode B sur la base de la même taille de la fenêtre le long de plusieurs acquisitions que celle utilisée pour l'estimation du mouvement. Ainsi, la résolution temporelle est liée à un seul paramètre : la taille de la fenêtre au cours de plusieurs acquisitions. A l'inverse, pour estimer les vitesses Doppler sur des images MLT tout en conservant une PRF élevée, des transmissions successives doivent être effectuées plusieurs fois pour la même région d'image. Par conséquent, le temps nécessaire entre la formation de la première et de la dernière ligne de l'image augmente non seulement avec la taille de la fenêtre au cours de plusieurs acquisitions mais aussi avec le nombre de transmissions nécessaires pour obtenir une image complète en mode B. Par conséquent, la cadence d'image Doppler en MLT est significativement limitée (56 Hz) par rapport à une transmission DW (562 Hz). L'utilisation d'un nombre plus élevé d'émissions en DW peut améliorer les estimations Doppler, tout en fournissant une cadence d'images assez élevée, mais l'augmentation de la taille de la fenêtre au cours de plusieurs acquisitions en MLT réduirait considérablement la résolution temporelle Doppler. Si les deux méthodes avaient été comparées aux mêmes fréquences d'images Doppler, il est très probable que DW aurait eu de meilleurs résultats que le MLT. L'utilisation d'un plus grand nombre de transmissions pour le MoCo aurait permis d'obtenir une meilleure focalisation synthétique. Cependant, il aurait été difficile d'évaluer si la performance de l'estimateur Doppler DW provenait d'une diminution de la variance (en raison de l'augmentation de la taille des fenêtres) ou des caractéristiques inhérentes des données obtenues avec les deux modalités d'imagerie (le MLT et le DW).

Enfin, les acquisitions *in vivo* en mode B ont montré que les deux méthodes sont capables de fournir une bonne qualité d'image à une cadence d'image élevée (Fig. 7). Cependant, la présence de cross-talk près de la surface de la sonde en MLT fait du DW un meilleur candidat pour la visualisation des structures de faible profondeur (Fig. 7). Lorsque la TDI a été appliquée aux images in vivo obtenues avec les deux méthodes à haute cadence, les cartes de vitesse obtenues étaient relativement proches (Fig. 8).

3.5. Conclusion

Dans cette étude, nous avons comparé deux méthodes ultra-rapides en conditions statiques et dynamiques pour des expériences in vitro et in vivo. L'imagerie DW fournit une meilleure qualité d'image à des profondeurs limitées tandis que l'imagerie MLT permet une meilleure concentration de l'énergie autour d'un point focal qui peut être placé à des profondeurs plus élevées. Des erreurs axiales de suivi de speckle similaires ont été obtenues pour les deux méthodes, mais le DW avec MoCo fournit de meilleures estimations latérales que le MLT. Des erreurs TDI légèrement inférieures ont été obtenues pour le MLT, mais des cadences d'images Doppler beaucoup plus élevées peuvent être obtenues avec le DW.

Pour conclure, nous avons démontré que chaque méthode à ses limitations et ses avantages et le choix d'une certaine méthode dépend de l'application.

CHAPITRE 4 (DEUXIEME CONTRIBUTION)

4.1. Introduction

L'échocardiographie 3D à haute cadence d'images est très pertinente pour le diagnostic clinique. Par exemple, l'amélioration de la résolution temporelle de l'écho 3D permettrait de capturer les phases rapides de l'ensemble du ventricule gauche pour une meilleure évaluation de la fonction cardiaque. De plus, l'échocardiographie pédiatrique (Fadnes et al. 2017), la quantification du débit sanguin (Faurie et al. 2017), l'évaluation des propriétés électromécaniques (Provost et al. 2010) pourraient également bénéficier de l'échocardiographie 3D ultra rapide.

Les méthodes conventionnelles d'augmentation de la résolution temporelle telles que la réduction de l'angle de secteur, la diminution de la densité de lignes, l'acquisition multi-ligne (« «multi-line-acquisition » MLA) (von Ramm et al. 1991) ont déjà été appliquées à l'imagerie 3D. D'autres approches basées sur des ondes planes/divergentes ont également été introduites en 3D pour augmenter encore la cadence d'images (Papadacci et al. 2014b). Cependant, le principal inconvénient de ces méthodes est le compromis avec la qualité de l'image. Une autre technique permettant d'atteindre des cadences d'images élevées avec un impact minimal sur la résolution spatiale est la transmission focalisée en parallèle (MLT). Plusieurs études ont démontré le potentiel de cette méthode en 2D (Mallart & Fink 1992), (Tong et al. 2014). Malgré cela, peu d'études se sont concentrées sur l'analyse de ses performances en 3D. De plus, les précédentes études du MLT en 3D se limitaient à des simulations et ne pouvaient pas être utilisées dans des conditions dynamiques en raison de leur mise en œuvre synthétique rétrospective (Ortega et al. 2016).

Dans cette section, nous présentons l'implémentation du MLT en 3D en temps réel sur un échographe de recherche. Nous avons en premier lieu voulu prouver sa faisabilité dans des conditions statiques et dynamiques, puis nous avons cherché à réduire le cross-talk.

4.2. Méthodes

4.2.1. Le système d'acquisition en 3D et la mise en œuvre expérimentale du MLT

Les images 3D ont été acquises en synchronisant quatre ssystèmes Vantage 256 (Verasonics, Kirkland, WA, USA). Chacun des systèmes contrôle 256 éléments d'une sonde en comportant 1024 (Petrusca et al. 2018).

En imagerie MLT, de multiples signaux doivent être superposés pour une seule transmission, ce qui nécessite un système capable d'émettre des impulsions d'excitation non identiques sur tous les éléments. Une telle excitation est possible sur notre échographe de recherche, qui est équipé d'un générateur d'impulsions à 3 états. En utilisant ce générateur d'impulsions, la superposition complexe de signaux doit être codée en utilisant 3 états (+V, 0, -V).

4.2.2. Paramètres d'acquisition

4.2.2.1. Etude de faisabilité

Pour étudier expérimentalement la faisabilité du MLT 3D, un volume d'imagerie complet a été créé en assemblant 32 secteurs triangulaires (chacun de largeur angulaire = 60^o) le long de la direction azimutale. Pour chaque secteur triangulaire, 32/nMLT transmissions ont été utilisés pour insonifier un secteur complet en envoyant simultanément nMLT faisceaux focalisés équidistants. Ainsi, le nombre total de transmissions était de 32x32/nMLT, ce qui correspond à 32 (élévation → y) par 32 (azimut → x) faisceaux focaux..

Afin d'étudier le compromis entre la cadence d'image et la qualité de l'image dans des conditions statiques, les valeurs de nMLT de 4 à 8 et 16 ont été utilisées. Le schéma de transmission pour le 8 MLT est illustré sur la Fig. 9. La performance du MLT en 3D dans des conditions dynamiques a été étudiée en utilisant la valeur intermédiaire de 8 MLT.

La forme d'onde d'excitation initiale (avant toute superposition) a été activée sur 10 échantillons et désactivée sur 300 échantillons à la fréquence d'horloge des Vantage qui est de 250 Mhz. Le point focal a été fixé à 4 cm pour les acquisitions statiques et à 6,7 cm pour les acquisitions dynamiques. Aucune apodisation n'a été utilisée ni en émission ni en réception. Les signaux reçus ont été échantillonnés à quatre fois la fréquence centrale du transducteur.

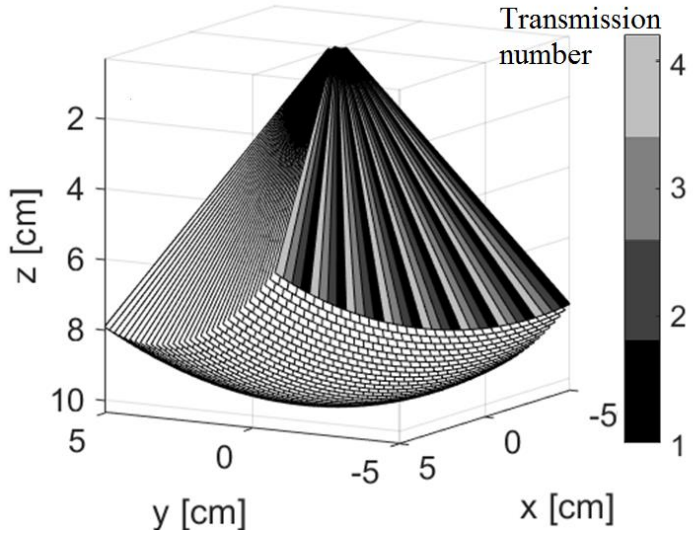

Fig. 9. Schéma de transmission pour 8 MLT : Pour chaque secteur azimutal (direction x), 4 transmissions ont été utilisés pour insonifier un secteur complet en envoyant simultanément 8 faisceaux focalisés équidistants. Le nombre total de transmissions par volume était de 128

4.2.2.2. Améliorations visant à réduire le cross-talk

Une approche simple pour étendre l'espace inter-faisceaux sans compromettre la cadence d'images est de répartir les transmissions sur l'ensemble du volume de balayage, au lieu de le limiter à un seul plan. Pour choisir une distribution appropriée, nous nous sommes inspirés de l'étude proposée par (B. Denarie et al. 2013). Ainsi, nous avons remplacé l'alignement classique des transmissions présentées dans l'étude de faisabilité, par un alignement le long de la diagonale transversale du transducteur (Fig. 10).

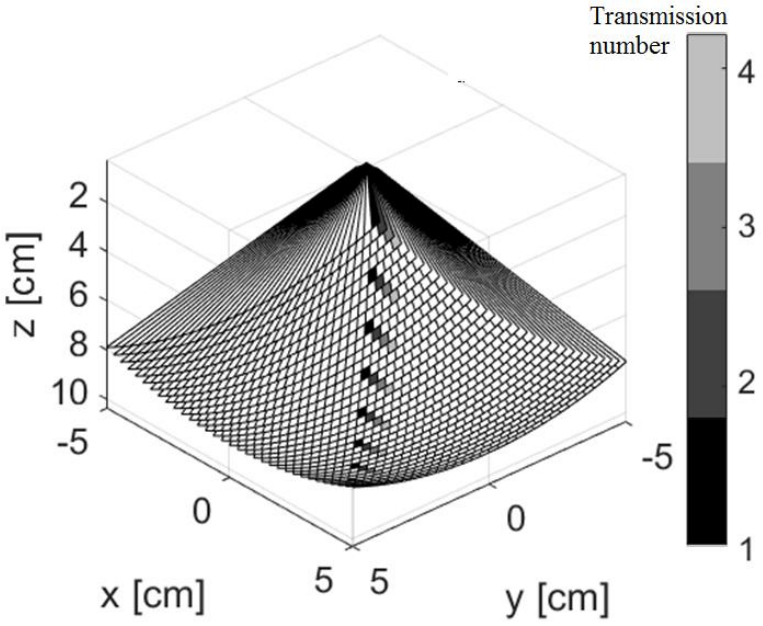

Fig. 10. Schéma de transmission pour 8 MLT le long de la diagonale transversale du transducteur

Pour cette analyse, la valeur intermédiaire de 8 MLT a été choisie. Pour obtenir une profondeur et un contraste plus élevés, le signal d'excitation initial a été activé pendant une durée plus longue (2 cycles sinusoïdaux) que pour la première partie de cette étude. Le point focal a été fixé à 5 cm pour les mesures de résolution et à 4 cm pour les mesures de CNR.

4.2.3. Modèles in vitro

4.2.3.1. Etude de faisabilité

Nous avons évalué la performance du MLT 3D à l'aide de modèles in vitro statiques et dynamiques.

Comme modèle statique, nous avons utilisé un fantôme CIRS (modèle 054GS) pour évaluer la qualité de l'image (en utilisant le CNR et le FWHM).

Notre fantôme dynamique était un disque tournant d'un diamètre de 10 cm dont la vitesse pouvait être contrôlée par un moteur pas à pas. La vitesse angulaire du disque était de 200 degrés/s. Cette configuration a donné une vitesse maximale de 17,4 cm/s, ce qui correspond aux vitesses maximales du myocarde rapportées dans (Nagueh et al. 1997). La PRF a été réglée à 2250 Hz (vitesse de Nyquist = 29 cm/s). Les vitesses Doppler axiales ont ensuite été estimées par démodulation IQ des données RF beamformées, puis par application d'un auto-corrélateur 2D sur ces données, en utilisant unetaille de la fenêtre le long de plusieurs acquisitions de 7 (Loupas et al. 1995).

4.2.3.2. Améliorations visant à réduire le cross-talk

Les effets d'un schéma de transmission diagonal sur la qualité de l'image ont été évalués en utilisant un fantôme Gammex (Sono410 SCG) pour les mesures de résolution et les mesures de CNR sur un kyste hypoechogène. De plus, nous avons utilisé un fantôme CIRS (054GS) pour évaluer le CNR sur un kyste hyperéchogène.

4.3. Résultats

4.3.1. Etude de faisabilité

Les acquisitions sur le fantôme CIRS ont permis de reconstruire avec succès 3 sections d'un volume 3D, comme le montre la Fig. 11. Le plan XZ (A) montre le contraste et les inclusions de résolution obtenus pour 8 MLT, tandis que le plan YZ (B) montre le plan perpendiculaire qui passe par le kyste. De plus, nous présentons en (C) la section transversale du kyste.

Comme le montre la Fig. 12, la qualité de l'image varie en fonction du nombre de transmissions simultanées. Le contraste a été étudié pour un cylindre hyperéchoïque, tandis que la résolution a été mesurée pour un une structure ponctuelle, tous deux placés au point focal (4 cm). Les valeurs de contraste et de résolution axiale pour l'imagerie focalisée, 4 MLT, 8 MLT et 16 MLT sont indiquées dans le Tableau I.

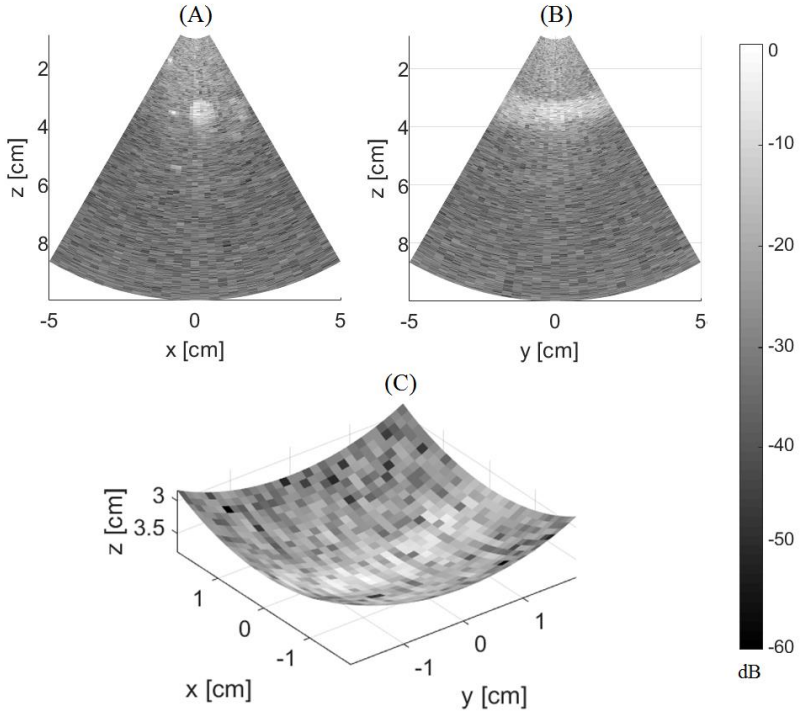

Fig. 11. Résultats 3D pour 8 MLT : (A) XZ et (B) YZ plans reconstruits et (c) surface à une profondeur constante (Z=3,8 cm)

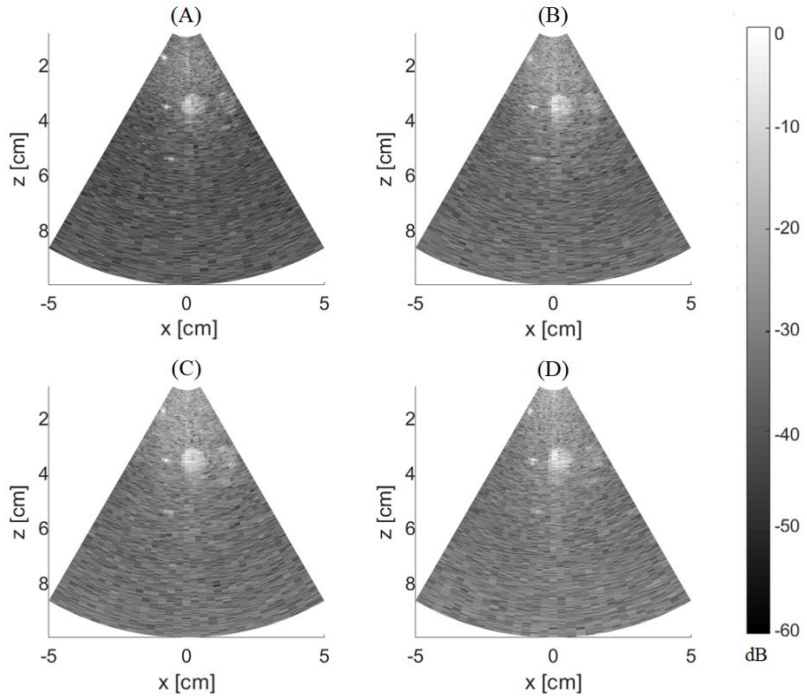

Fig. 12. : Comparaison des plans XZ pour l'imagerie focalisée (A), 4 MLT (B), 8 MLT (C) et 16 MLT (D)

TABLEAU I: RÉSOLUTION AXIALE ET VALEURS DE CONTRASTE

Séquence/ Qualité des images	Focalisée	4MLT	8MLT	16MLT
Résolution axiale	0.33 mm	0.54 mm	0.57 mm	0.61 mm
Contraste	3.60 dB	3.02 dB	2.83 dB	2.61 dB

La vitesse Doppler multi-plans est présentée en Fig. 13. Les valeurs de vitesse estimées (B) correspondent aux vitesses de référence (A). L'erreur relative moyenne est de 4,1 %.

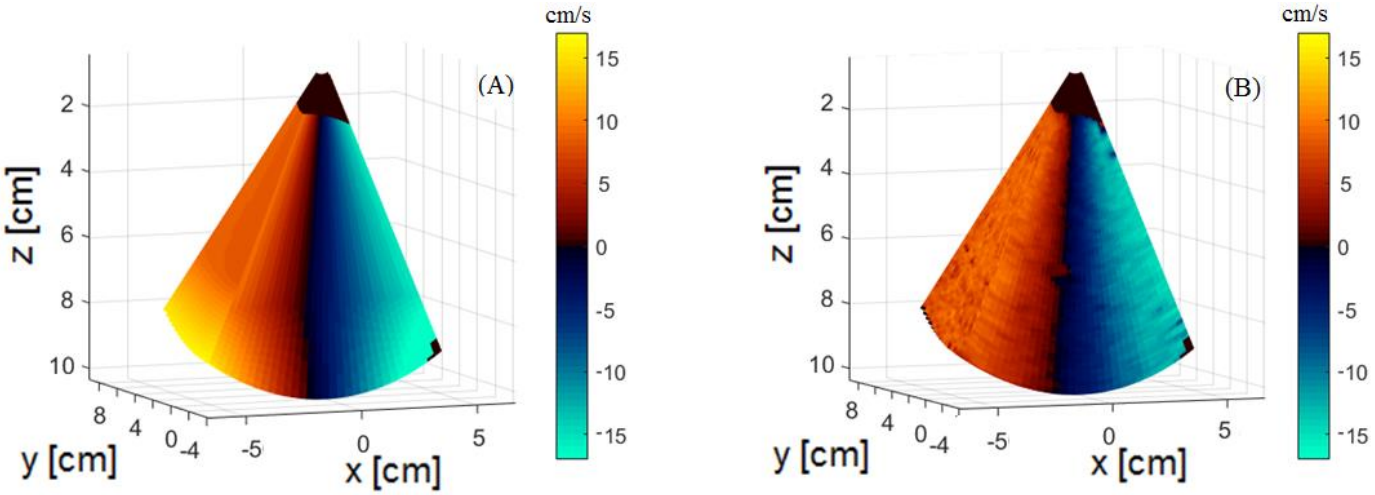

Fig. 13. (A) Carte des vitesses de référence et (B) Carte des vitesses estimées

4.3.2. Améliorations visant à réduire le cross-talk

Nous avons d'abord évalué l'impact de l'utilisation de différents schémas de transmission sur le fantôme Gammex. Par conséquent, nous montrons en Fig. 14 la comparaison entre les résultats obtenus en utilisant le schéma de transmission conventionnel (à gauche) et le schéma de transmission diagonal (à droite) pour les plans XZ (A, B) et YZ (C, D). La résolution axiale mesurée au point focal (5 cm) était de 1,14 mm pour la transmission conventionnelle et de 0,45 mm pour la transmission diagonale. Pour fournir une analyse quantitative, nous avons mesuré la différence entre le lobe principal et le niveau du lobe secondaire au point focal placé à 5cm. Pour le plan XZ, la différence mesurée était de 10,77 dB pour la transmission diagonale alors qu'une différence de seulement 2,84 dB a été trouvée pour la transmission classique. De même, une différence de 12,26 dB par rapport à seulement 2,98 dB a été mesurée dans le plan YZ. En utilisant le même fantôme et en changeant la région imagée du volume et le point focal, le CNR sur un kyste hypoechogène a été évalué, comme le montre la Fig. 15. Les plans XZ sont fournis pour le schéma de transmission conventionnel (A) et pour le schéma de transmission diagonal (B). Les valeurs CNR calculées pour le kyste hypoechogène étaient de 0,91 dB pour la transmission conventionnelle et de -2,17 dB pour la transmission diagonale.

Pour évaluer la qualité de l'image sur un kyste hyperéchogène, nous avons utilisé le fantôme CIRS. En Fig. 16, nous montrons la comparaison qualitative entre les images obtenues en utilisant le schéma de transmission conventionnel (A) et le schéma de transmission diagonal (B) pour le plan XZ. Le CNR calculé pour le kyste hyperéchogène placé dans le point focal (4 cm) était de 5,97 dB pour (A) et 2,03 dB pour (B).

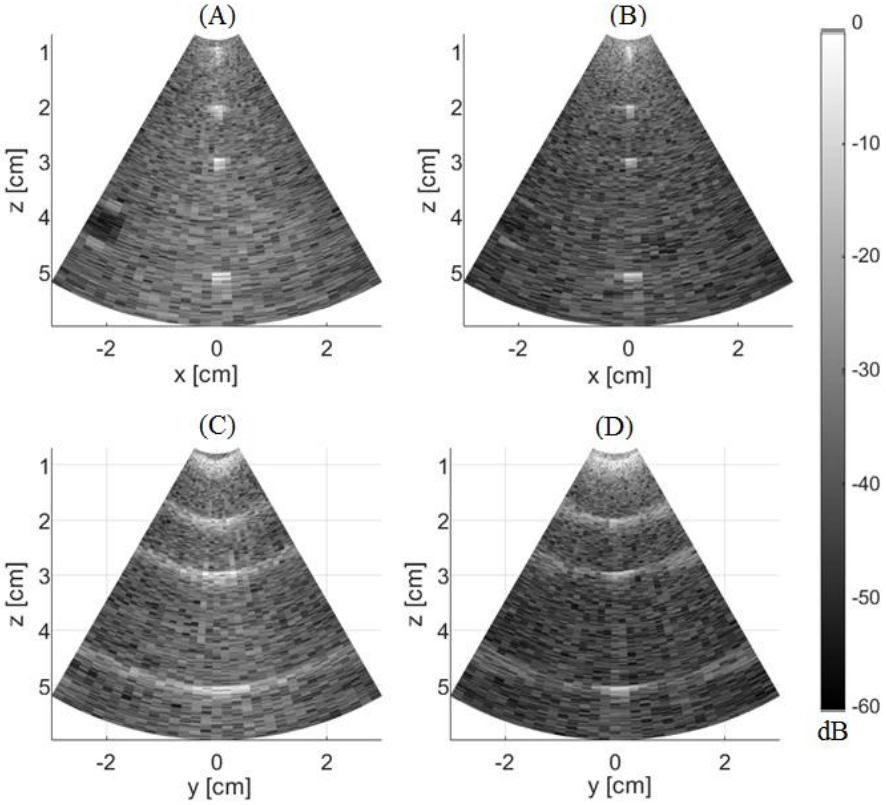

Fig. 14. Comparaison entre les résultats du 8 MLT sur le fantôme Gammex en utilisant le schéma de transmission conventionnel (à gauche) et le schéma de transmission diagonal (à droite) pour les deux plans XZ (A, B) et YZ (C, D).

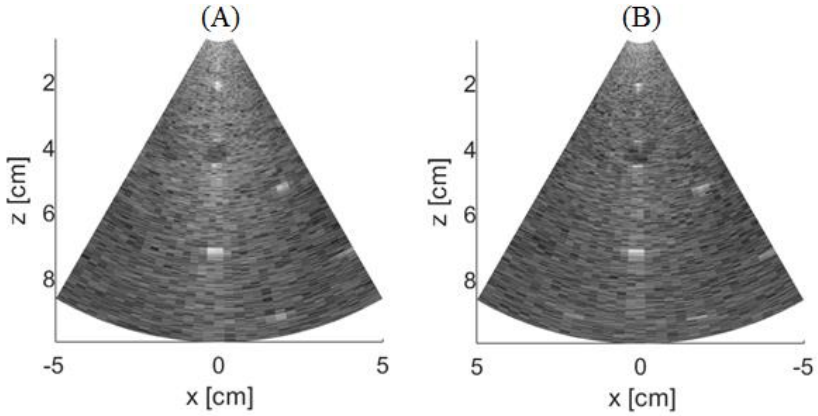

Fig. 15. Comparaison entre les résultats du 8 MLT sur le fantôme Gammex en utilisant le schéma de transmission conventionnel (A) et le schéma de transmission diagonal (B) pour le plan XZ.

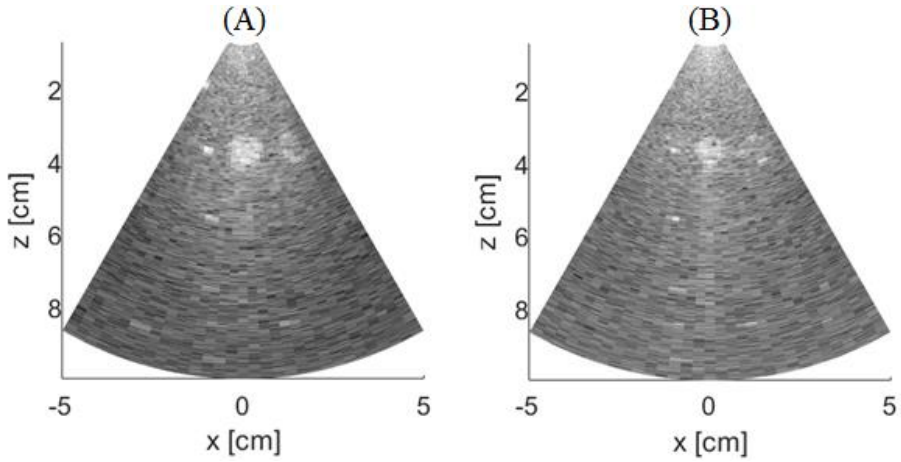

Fig. 16. Comparaison entre les résultats du 8 MLT sur le fantôme Gammex en utilisant le schéma de transmission conventionnel (A) et le schéma de transmission diagonal (B) pour le plan XZ.

4.4. Discussion

Pour la première partie de cette étude, nous nous sommes concentrés sur la démonstration de la faisabilité expérimentale du MLT en 3D dans des conditions statiques et dynamiques.

La faisabilité en conditions statiques a été présentée en Fig. 11, où nous avons montré que des coupes orthogonales d'un volume 3D pouvaient être reconstruites avec succès à partir de données MLT expérimentales. Comme le montre la Fig. 12, la qualité de l'image se dégrade avec le nombre de transmissions simultanées. Alors que le contraste a une valeur de 3,60 dB pour la transmission conventionnelle, il est réduit de 15 % pour le 4 MLT (3,02 dB) et jusqu'à 27 % (2,61 dB) pour le plus grand nombre de transmissions considérées dans cette étude (le 16 MLT). Dans le même temps, la résolution axiale s'est dégradée de 0,33 mm à 0,61 mm avec la cadence d'images 16 fois supérieure.

Une fois la qualité de l'image évaluée en conditions statiques, nous avons étendu notre étude aux conditions dynamiques. La faisabilité de l'estimation de la vitesse Doppler tissulaire pour l'imagerie ultrasonore du MLT en 3D a également été démontrée comme le montre la Fig. 13. Les résultats ont prouvé qu'il est possible d'obtenir des estimateurs précis malgré l'augmentation d’un facteur 8 de la cadence d’images.

Même si la faisabilité expérimentale du MLT en 3D et le potentiel ont été démontrés dans des conditions statiques et dynamiques, une limitation de la première partie de cette étude est qu'elle était restreinte à une implémentation de base. Les réglages de transmission n'ont pas été encore optimisés, ce qui explique que les résultats correspondent au pire scénario pour le MLT 3D, en particulier en termes de qualité d'image. Par exemple, le schéma de transmission était conventionnel, le long des colonnes du transducteur. Compte tenu de la géométrie 2D de la sonde, les transmissions simultanées auraient pu être mieux séparées pour réduire le cross-talk. De plus, le signal d'excitation initial a été activé pendant une très courte période, ce qui a limité la profondeur de pénétration.

Pour faire face à ces limites, la deuxième partie de cette étude s'est concentrée sur l'amélioration des paramètres de transmission. Comme le montre la Fig. 10, en alignant les transmissions le long de la

diagonale transversale du transducteur, l'espacement entre les transmissions simultanées a été augmenté. Par conséquent, l'interférence entre les faisceaux a été réduite, ce qui a eu un impact sur la qualité de l'image, comme le montre la Fig. 14. Qualitativement, pour les plans XZ et YZ, les cibles ponctuelles de résolution axiale semblaient plus fines pour les images obtenues à l'aide du schéma de transmission diagonal que celles obtenues à l'aide du schéma classique. Les valeurs de résolution axiale mesurées au point focal ont confirmé cette observation. De plus, nous avons mesuré la différence entre le lobe principal et le lobe secondaire. Globalement, le lobe principal était jusqu'à 5% plus élevé que le lobe secondaire pour la transmission conventionnelle et jusqu'à 25% plus élevé pour la transmission diagonale. Comme le cross-talk apparaît comme résultat des interactions entre les lobes principaux et secondaires, une différence plus grande peut être associée à un niveau de cross-talk plus bas.

Malgré ces résultats prometteurs, le contraste des images obtenues par transmission diagonale était trois fois inférieur à celui obtenu par transmission conventionnelle, tant pour les kystes hypoéchogènes (Fig. 15) qu'hyperéchogènes (Fig. 16). Toutefois, d'autres auteurs ont également signalé le compromis entre la réduction du cross-talk et d'autres paramètres de qualité d'image. Par exemple, (Tong et al. 2014) ont montré qu'une apodisation de Tukey peut réduire significativement le cross-talk, mais avec le compromis de la résolution latérale. D'autres études ont proposé d'utiliser la formation de voie «filtered delay multiply and sum » (FDMAS) pour limiter le cross-talk, mais cela s'est fait au prix d'une dégradation du CNR par rapport aux DAS classiques (Matrone et al. 2017).

4.5. Conclusion

Les résultats présentés dans la première partie de cet article indiquent la faisabilité expérimentale du MLT en 3D et son potentiel pour obtenir un contraste et une résolution élevés tout en augmentant la cadence d'acquisition d'images, même pour un schéma de transmission simple et quand aucune apodisation n'est utilisée. Lors d'essais sur des acquisitions dynamiques, la cadence d'acquisition volumique du MLT a été augmentée d'un facteur 8 tout en préservant la qualité de l'image, conduisant à des estimateurs de vitesse précis. L'utilisation du MLT en 3D pourrait donc permettre de nouvelles avancées en Doppler couleur ultra-rapide.

Les résultats présentés dans la deuxième partie de ce document ont montré que les artefacts de cross-talk pouvaient être réduits en alignant les transmissions simultanées en diagonale. Cependant, le contraste a été affecté par rapport à la transmission conventionnelle.

CHAPITRE 5 (TROISIEME CONTRIBUTION)

5.1. Introduction

L'émergence de l'imagerie ultrasonore à haute cadence a permis d'importants progrès dans la quantification du débit sanguin, puisqu'elle permet d'acquérir des données à plus large champ de vue avec un pas temporel fin. Avant d'envisager le passage en clinique de ces méthodes il est nécessaire de les

évaluer dans des conditions expérimentales réalistes. Plusieurs fantômes ont été proposés au fil du temps pour effectuer une telle évaluation, comme les fantômes tubulaires (Law et al. 1987), (Hoskins et al. 1989), (King et al. 2011), (Zhou et al. 2017), les fantômes de bifurcation carotidienne (Poepping et al. 2002), (Meagher et al. 2007) de disque tournant (Kripfgans et al. 2006) et de spirale (Yiu & Yu 2017).

Bien que des progrès significatifs aient été réalisés au fil des ans pour accroître la complexité des objets à tester et fournir des flux physiologiques réalistes, les fantômes mentionnés ci-dessus sont encore insuffisants pour reproduire une des caractéristiques spécifiques du flux intraventriculaire : la formation de vortex. Il a été démontré que l'étude de la dynamique des vortex révèle des conditions physiologiques instables qui pourraient permettre l'identification précoce des anomalies cardiaques (Pedrizzetti et al. 2014).

Dans ce contexte, la validation d'approches d'estimation de mouvement à haute cadence d'images sur un fantôme de vortex pourrait fournir un résultat très réaliste et pertinent pour une application in vivo. Ainsi, l'objectif de cette étude préliminaire était d'évaluer si le fantôme vortex est un bon candidat pour quantifier des débits complexes à l'aide de méthodes ultrasonores à haute cadence. Des acquisitions 2D et 3D ont été réalisées pour atteindre l'objectif mentionné.

5.2. Méthodes

5.2.1. Mise en place de l'acquisition 2D

Les images ultrasonores 2D ont été acquises à l'aide d'un système de recherche Vantage 256 (Verasonics Inc., Redmond, WA) qui contrôle un transducteur linéaire de 5 MHz (ATL L7-4, 128 éléments). Notre modèle in vitro était un prototype de fantôme de vortex à base liquide proposé par (Ferrari et al. 2018). Le fluide contenu dans le réservoir était un mélange de particules de verre et d'eau (110P8, LaVision GmbH, Allemagne). Nous avons utilisé des ondes planes non orientées pour imager le milieu.

5.2.2. Configuration de l'acquisition 3D

Les volumes ont été acquis à l'aide de quatre scanners Vantage 256 (Verasonics, Kirkland, WA, USA) synchronisés pour contrôler un transducteur 2D de 3 MHz (Vermon, Tours, France), comme décrit par (Petrusca et al. 2018).

5.2.3. Estimation de la vitesse d'écoulement vectorielle

Premièrement, pour les acquisitions 2D, nous avons estimé les champs de vitesse par 1) Velocimétrie échographique d'image de particule (Echo-PIV) en réalisant un suivi de speckle sur l'enveloppe réelle par corrélation de phase; et 2) Doppler vectoriel en utilisant une approche à double faisceau en réception, comme décrit dans (Jensen et al. 2016).

Deuxièmement, comme nous n'avions pas de référence, nous avons acquis de multiples ensembles d'acquisitions pour étudier un lien potentiel entre différentes composantes de la vitesse. Nous avons extrait la composante rotationnelle maximale des estimations de vitesse Doppler, tandis que la composante

translationnelle a été estimée en appliquant la corrélation de phase aux cartes de vitesse Doppler. Différents diamètres et vitesses (2 et 2,5 cm, 1-7 cm/s) du fantôme vortex ont été utilisés pour cette analyse.

Troisièmement, pour les acquisitions 3D, nous avons estimé les champs de vitesse du vecteur Doppler à l'aide d'un autocorrecteur 2D appliqué sur les données du IQ tel que décrit dans (Kasai et al. 1985), (Loupas et al. 1995).

5.3. Résultats

5.3.1. Résultats en 2D

Les cartes de vitesse sont illustrées dans la Fig. 17 pour Echo-PIV (A) et Doppler vectoriel (B).

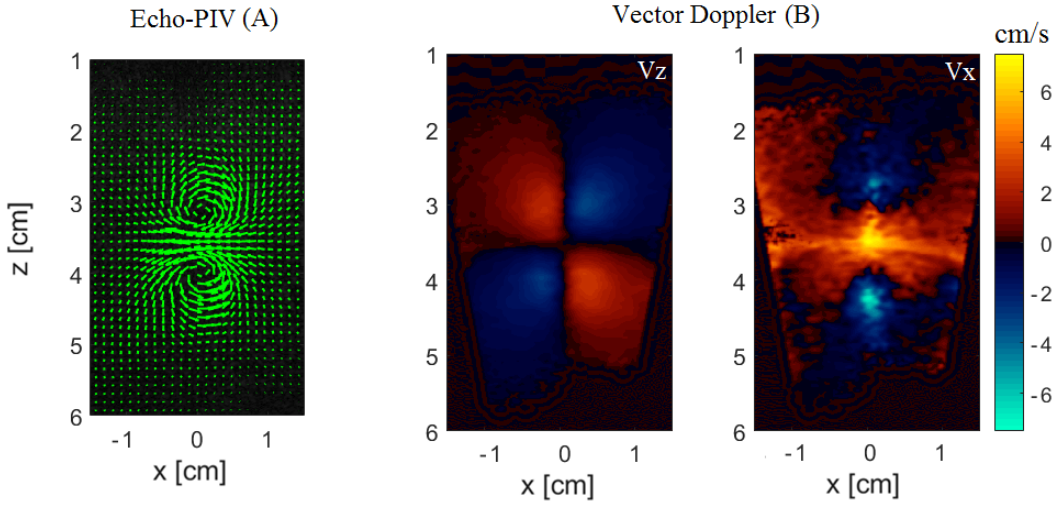

Fig. 17. Estimation de la vitesse avec Echo-PIV (A) et Doppler vectoriel (B) pour les directions z (gauche) et x (droite)

Le lien entre la vitesse de rotation et la vitesse de translation est illustré en Fig. 18, où chaque ensemble de points correspond à un ensemble différent d'acquisitions, réalisées pour une vitesse de translation différente (entre 1-7 cm/s) et pour un des deux diamètres : 2,5 cm (bleu) et 2 cm (noir). Pour chaque série d'acquisitions, nous montrons la médiane sur 15 estimations et leur écart par rapport à la médiane. La courbe de régression entre les deux composantes de vitesse est affichée en rouge.

5.3.2. Résultats préliminaires en 3D

La Fig. 19 montre les cartes Doppler obtenues par insonification volumétrique du vortex. Les cartes de vitesse xz et yz sont fournies.

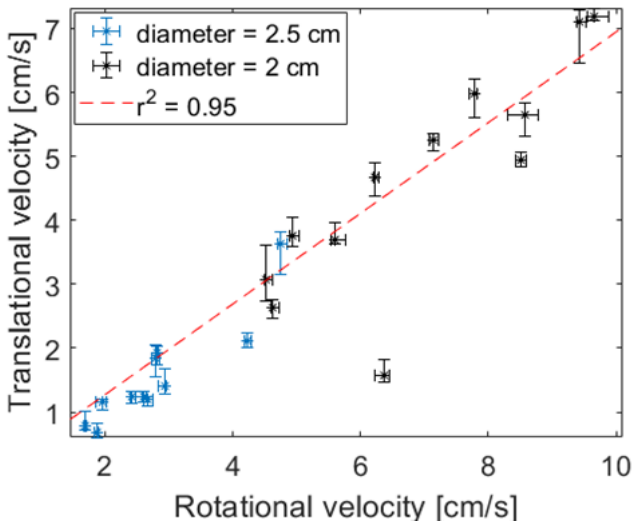

Fig. 18. Rapport linéaire entre les vitesses de rotation et de translation pour 2 diamètres d'orifice (2,5 cm et 2 cm)

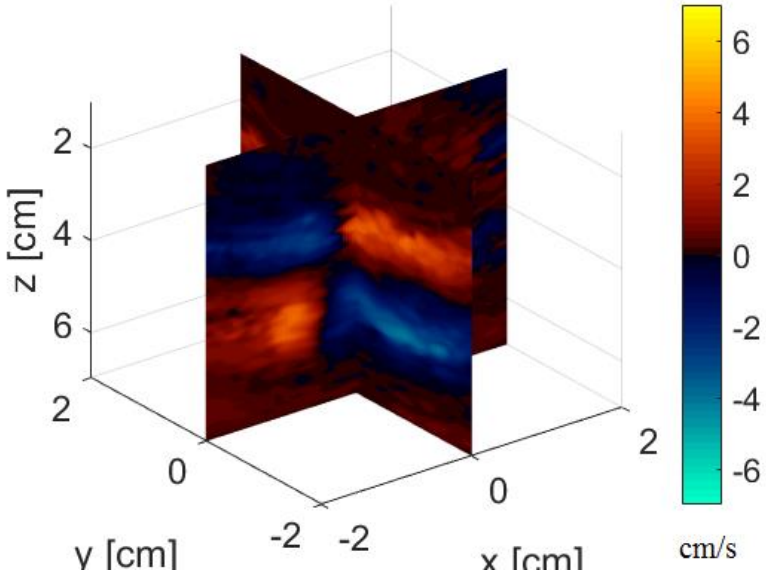

Fig. 19. Cartes de vitesse Doppler pour les plans xz et yz

5.4. Discussion

Nos résultats préliminaires présentent une bonne concordance avec la géométrie et la cinématique des vortex toroïdaux, ce qui tend à indiquer que l'écho-PIV et le Doppler vectoriel par imagerie ultrasonores ultra-rapides peuvent être utilisés avec succès pour évaluer la dynamique des vortex de type cardiaque (Fig. 17). L'étude de la relation entre les vitesses de rotation et de translation a indiqué que ces deux composantes de vitesse sont fortement corrélées (r2 = 0,95, Fig. 18), conformément à la théorie (Tinaikar et al. 2018). Bien que cela montre un comportement stable du fantôme à une position donnée de la

propagation du vortex, une grande limitation de cette étude est que nous n'avons pas comparé nos résultats avec une référence. En raison de la complexité de la dynamique de l'écoulement tourbillonnaire, il n'est pas facile d'en déduire les vitesses théoriques de la vérité au sol. Une solution intéressante pourrait être de comparer la PIV par écho avec la PIV optique comme cela se fait dans l'échographie conventionnelle (Kheradvar et al. 2010). De plus, un prototype du fantôme compatible avec l'IRM permettrait de comparer les vecteurs de vitesse ultrasonore avec la modalité d'imagerie alternative comme cela a été fait pour la vorticité dans (Faurie et al. 2017).

Malgré la difficulté actuelle à fournir une mesure quantitative de la précision, nos résultats prometteurs en 2D nous ont incités à étendre notre étude en 3D. Comme le montre la Fig. 19, en plus de la composante de vitesse Doppler axiale disponible lors de l'utilisation d'une sonde 1D (Fig. 17 B, Vz), les acquisitions avec une sonde 2D permettent également de calculer la composante sagittale. L'extension des approches Doppler et PIV en 3D pourrait ainsi offrir un champ vectoriel tridimensionnel complet.

Les résultats 2D et 3D présentés dans cette section sont très préliminaires, néanmoins, ils indiquent la compatibilité du générateur d'anneaux vortex avec le système ultrasonore.

5.5. Conclusion

L’imagerie ultrasonore à haute cadence d'images peut être utilisée pour estimer des flux vectoriels complexes tels que ceux qui caractérisent les vortex. L'écho 2D PIV et le Doppler vectoriel semblent permettre d’obtenir une estimation des cartes de vitesse des vortex. Les résultats préliminaires du Doppler 3D ont montré que les vitesses Doppler le long des plans xz et yz peuvent être estimées à partir de séries de volumes.

Dans l'ensemble, cette étude a montré que le fantôme de vortex représente un bon candidat pour optimiser et valider les méthodes d'imagerie par ultrasons dans des écoulements complexes tridimensionnels, non stationnaires et contrôlables.

Conclusion générale

Le mouvement cardiaque a été activement étudié au cours des dernières décennies grâce à son potentiel d'évaluation des propriétés de contractilité du myocarde. Malgré les énormes progrès réalisés au cours des dernières années dans le domaine de l'imagerie par échographie cardiaque, qui ont permis d'améliorer ses capacités cliniques actuelles (Chapitre 1), plusieurs aspects pourraient encore être améliorés, comme la cadence d'images et ou encore l'usage de l'imagerie 3D en routine clinique. En réponse, des méthodes à haute cadence d'images ont été proposées et étendues en 3D par la communauté des chercheurs en échographie, comme nous l'avons expliqué au Chapitre 2. L'objectif de cette thèse était d'évaluer ces nouvelles approches dans des conditions réalistes, aussi proches que possible de celles d'une future application clinique.

Dans ce contexte, notre premier objectif était de comparer le MLT et le DW afin de déterminer si une méthode est plus appropriée que l'autre pour l'imagerie 2D cardiaque (Chapitre 3). Les deux méthodes se sont révélées très compétitives, chacune ayant ses avantages et ses limites. Ainsi, aucune conclusion claire ne peut être tirée de nos résultats et le choix d'utiliser l'une ou l'autre méthode doit être adapté en fonction de l'application.

Motivés par nos résultats prometteurs en 2D mais aussi par le potentiel de l'imagerie 3D pour permettre de nouvelles avancées dans le diagnostic, notre deuxième objectif était d'étendre le MLT en 3D. Tout d'abord, nous avons prouvé sa faisabilité dans des conditions statiques et dynamiques. Deuxièmement, nous avons montré qu'une meilleure séparation des faisceaux transmis peut être obtenue en distribuant les faisceaux focalisés simultanément sur l'ensemble du volume. Bien que cela ait eu pour résultat une apparence plus fine des cibles ponctuelles de résolution, le CNR a été affecté et les cartes Doppler étaient plus bruyantes.

Enfin, notre dernier objectif était d'évaluer le potentiel d'un nouveau modèle complexe *in vitro* pour valider des méthodes d'estimation de mouvement à haute cadence d'images. Plus précisément, notre modèle était un générateur de vortex toroïdaux. Bien que nous avons obtenu une bonne concordance avec la géométrie et la cinématique de ces vortex en imagerie 2D et 3D, nos résultats sont encore préliminaires et d'autres travaux sont nécessaires pour une analyse 3D complète.

Dans l'ensemble, dans le cadre de cette thèse, nous avons développé, mis en œuvre et testé des approches d'imagerie cardiaque 2D et 3D à haute cadence d'images afin de révéler leurs avantages, de tester leurs limites et d'aider à la prise de décision en matière de translation clinique.

Denarie, B.., Bjastad, T.. & Torp, H.., 2013. Multi-line transmission in 3-D with reduced crosstalk artifacts: a proof of concept study. *IEEE Transactions on Ultrasonics, Ferroelectrics, and Frequency Control*, 60(8), pp.1708–1718.

Denarie, B. et al., 2013. Coherent Plane Wave Compounding for Very High Frame Rate Ultrasonography of Rapidly Moving Targets. *IEEE Transactions on Medical Imaging*, 32(7), pp.1265–1276.

Fadnes, S. et al., 2017. In vivo intracardiac vector velocity imaging using phased array transducers for pediatric cardiology. *IEEE Transactions on Ultrasonics, Ferroelectrics, and Frequency Control*, pp.1–1.

Faurie, J. et al., 2017. Intracardiac Vortex Dynamics by High-Frame-Rate Doppler Vortography—In Vivo Comparison With Vector Flow Mapping and 4-D Flow MRI. *IEEE Transactions on Ultrasonics, Ferroelectrics, and Frequency Control*, 64(2), pp.424–432.

Ferrari, S. et al., 2018. The Ring Vortex: A Candidate for a Liquid-Based Complex Flow Phantom for Medical Imaging. In Springer, Cham, pp. 893–902.

Gammelmark, K.L. & Jensen, J.A., 2014. 2-D tissue motion compensation of synthetic transmit aperture images. *IEEE Transactions on Ultrasonics, Ferroelectrics, and Frequency Control*, 61(4), pp.594–610.

Hasegawa, H. & Kanai, H., 2011. High-frame-rate echocardiography using diverging transmit beams and parallel receive beamforming. *Journal of Medical Ultrasonics*, 38(3), pp.129–140.

Hasegawa, H. & Kanai, H., High-frame-rate echocardiography using diverging transmit beams and parallel receive beamforming.

Hein, I.A. & O'Brien, W.D., 1993. Current time-domain methods for assessing tissue motion by analysis from reflected ultrasound echoes-a review. *IEEE Transactions on Ultrasonics, Ferroelectrics and Frequency Control*, 40(2), pp.84–102.

Hoskins, P.R., Anderson, T. & McDicken, W.N., 1989. A computer controlled flow phantom for generation of physiological Doppler waveforms. *Physics in medicine and biology*, 34(11), pp.1709–17.

Jensen, J.A. et al., 2016. Ultrasound Vector Flow Imaging: I: Sequential Systems. *IEEE Transactions on Ultrasonics, Ferroelectrics, and Frequency Control*, pp.1–1.

Karaman, M., Pai-Chi Li & O'Donnell, M., 1995. Synthetic aperture imaging for small scale systems. *IEEE Transactions on Ultrasonics, Ferroelectrics and Frequency Control*, 42(3), pp.429–442.

Kasai, C. et al., 1985. Real-Time Two-Dimensional Blood Flow Imaging Using an Autocorrelation Technique. *IEEE Transactions on Sonics and Ultrasonics*, 32(3), pp.458–464.

Kheradvar, A. et al., 2010. Echocardiographic Particle Image Velocimetry: A Novel Technique for Quantification of Left Ventricular Blood Vorticity Pattern. *Journal of the American Society of Echocardiography*, 23(1), pp.86–94.

King, D.M. et al., 2011. Development of a Vessel-Mimicking Material for use in Anatomically Realistic Doppler Flow Phantoms. *Ultrasound in Medicine & Biology*, 37(5), pp.813–826.

Kripfgans, O.D. et al., 2006. Vector Doppler imaging of a spinning disc ultrasound Doppler phantom. *Ultrasound in Medicine & Biology*, 32(7), pp.1037–1046.

Law, Y.F. et al., 1987. Computer-controlled pulsatile pump system for physiological flow simulation. *Medical & biological engineering & computing*, 25(5), pp.590–5.

Loupas, T., Powers, J.T. & Gill, R.W., 1995. An axial velocity estimator for ultrasound blood flow imaging, based on a full evaluation of the Doppler equation by means of a two-dimensional autocorrelation approach. *IEEE Transactions on Ultrasonics, Ferroelectrics and Frequency Control*, 42(4), pp.672–688.

Mallart, R. & Fink, M., 1992. Improved imaging rate through simultaneous transmission of several ultrasound beams. In F. L. Lizzi, ed. pp. 120–130.

Matrone, G. et al., 2017. High Frame-Rate, High Resolution Ultrasound Imaging With Multi-Line Transmission and Filtered-Delay Multiply And Sum Beamforming. *IEEE Transactions on Medical*

Imaging, 36(2), pp.478–486.
Meagher, S. et al., 2007. Anatomical flow phantoms of the nonplanar carotid bifurcation, Part II: Experimental validation with Doppler ultrasound. *Ultrasound in Medicine & Biology*, 33(2), pp.303–310.
Montaldo, G. et al., 2009. Coherent plane-wave compounding for very high frame rate ultrasonography and transient elastography. *IEEE transactions on ultrasonics, ferroelectrics, and frequency control*, 56(3), pp.489–506.
Nagueh, S.F. et al., 1997. Doppler Tissue Imaging: A Noninvasive Technique for Evaluation of Left Ventricular Relaxation and Estimation of Filling Pressures. *Journal of the American College of Cardiology*, 30(6), pp.1527–1533.
Ortega, A. et al., 2016. A Comparison of the Performance of Different Multiline Transmit Setups for Fast Volumetric Cardiac Ultrasound. *IEEE Transactions on Ultrasonics, Ferroelectrics, and Frequency Control*, 63(12), pp.2082–2091.
Papadacci, C. et al., 2014a. High-contrast ultrafast imaging of the heart. *IEEE transactions on ultrasonics, ferroelectrics, and frequency control*, 61(2), pp.288–301.
Papadacci, C. et al., 2014b. High-contrast ultrafast imaging of the heart. *IEEE Transactions on Ultrasonics, Ferroelectrics, and Frequency Control*, 61(2), pp.288–301.
Pedrizzetti, G. et al., 2014. The vortex—an early predictor of cardiovascular outcome? *Nature Reviews Cardiology*, 11(9), pp.545–553.
Petrusca, L. et al., 2018. Fast Volumetric Ultrasound B-Mode and Doppler Imaging with a New High-Channels Density Platform for Advanced 4D Cardiac Imaging/Therapy. *Applied Sciences*, 8(2), p.200.
Poepping, T.L. et al., 2002. An in vitro system for Doppler ultrasound flow studies in the stenosed carotid artery bifurcation. *Ultrasound in medicine & biology*, 28(4), pp.495–506.
Poree, J. et al., 2016. High-Frame-Rate Echocardiography Using Coherent Compounding With Doppler-Based Motion-Compensation. *IEEE Transactions on Medical Imaging*, 35(7), pp.1647–1657.
Provost, J. et al., 2010. Electromechanical Wave Imaging of Normal and Ischemic Hearts In Vivo. *IEEE Transactions on Medical Imaging*, 29(3), pp.625–635.
von Ramm, O.T., Smith, S.W. & Pavy, H.G., 1991. High-speed ultrasound volumetric imaging system. II. Parallel processing and image display. *IEEE Transactions on Ultrasonics, Ferroelectrics and Frequency Control*, 38(2), pp.109–115.
Sandrin, L. et al., 1999. Time-Resolved Pulsed Elastography with Ultrafast Ultrasonic Imaging. *Ultrasonic Imaging*, 21(4), pp.259–272.
Tinaikar, A., Advaith, S. & Basu, S., 2018. Understanding evolution of vortex rings in viscous fluids. *Journal of Fluid Mechanics*, 836, pp.873–909.
Tong, L. et al., 2012. Comparison of conventional parallel beamforming with plane wave and diverging wave imaging for cardiac applications: a simulation study. *IEEE Transactions on Ultrasonics, Ferroelectrics and Frequency Control*, 59(8), pp.1654–1663.
Tong, L. et al., 2014. Multi-Transmit Beam Forming for Fast Cardiac Imaging - Experimental Validation and In Vivo Application. *IEEE Transactions on Medical Imaging*, 33(6), pp.1205–1219.
Tong, L., Gao, H. & D'hooge, J., 2013. Multi-transmit beam forming for fast cardiac imaging-a simulation study. *IEEE Transactions on Ultrasonics, Ferroelectrics, and Frequency Control*, 60(8), pp.1719–1731.
Trahey, G.E. & Nock, L.F., 1992. Synthetic receive aperture imaging with phase correction for motion and for tissue inhomogeneities. II. Effects of and correction for motion. *IEEE Transactions on Ultrasonics, Ferroelectrics and Frequency Control*, 39(4), pp.496–501.
Yiu, B.Y.S. & Yu, A.C.H., 2017. Spiral Flow Phantom for Ultrasound Flow Imaging Experimentation. *IEEE Transactions on Ultrasonics, Ferroelectrics, and Frequency Control*, 64(12), pp.1840–1848.
Zhou, X. et al., 2017. Fabrication of Two Flow Phantoms for Doppler Ultrasound Imaging. *IEEE*

Transactions on Ultrasonics, Ferroelectrics, and Frequency Control, 64(1), pp.53–65.